STUDY OF ORGANIC RANKINE CYCLE WITH ZEOTROPIC MIXTURES AND OPTIMIZATION OF MIXTURE COMPOSITION

by
Alpay Asma
B.S., Mechanical Engineering, Yıldız Technical University, 2011
M.S., Mechanical Engineering, Bogazici University, 2015

Submitted to the Institute for Graduate Studies in
Science and Engineering in partial fulfillment of
the requirements for the degree of
Doctor of Philosophy

Graduate Program in Mechanical Engineering
Bogazici University
2024

ACKNOWLEDGEMENTS

I would like to express my sincere appreciation to my supervisor Prof. Hasan Bedir and my co-supervisor Prof. Günay Anlaş for their support, guidance, patience, advice, motivation, and encouragement to deal with difficulties I have been faced throughout this research. It is an honor to me to study with them and learn from their experiences.

I would also like to acknowledge Prof. Salim Kunt Atalık, Prof. Ahmet Erhan Aksoylu, Assoc. Prof. Hatice Mercan, and Assoc. Prof. Murat Çakan for their advice, comments and sharing their valuable time to review this study as the committee members.

I would like to extend my special thanks to my friends and colleagues Ertuğrul Altun and Hasan Eren Bekiloğlu for their great support and friendship throughout my thesis. Their support and motivation play a crucial role in this work.

I am also grateful to my mother Kıymet Asma and my father Gazanfer Asma for their support, patience and understanding that makes me stronger throughout my life.

Finally, I am grateful to my lovely wife Pınar Demir Asma for her love, patience, great understanding, enormous support, and motivation. She was the only one who keeps me alive throughout this long journey. She always believes in me, and her love and kindness give me a faith that made me stand up in all difficulties I have been faced during these years.

ABSTRACT

STUDY OF ORGANIC RANKINE CYCLE WITH ZEOTROPIC MIXTURES AND OPTIMIZATION OF MIXTURE COMPOSITION

There are two main parts of this study. In the first part of the study, the aim is to develop an accurate ORC model which is validated using reliable steady-state data. For this purpose, tests are conducted at four different heat source temperatures ranging from 80 to 110 ℃ to obtain data in a repeatable manner. The proposed model considers pressure drop and heat transfer correlations to improve the accuracy of model predictions. The results show that the steady-state ORC model is significantly accurate, with ±1% deviations in pressure and ±1 ℃ in temperature, and ±5% in mass flow rate, heat transfer rate and refrigerant pump power predictions. In the second part, the performance of ten different R134a blends with varying mole fractions is evaluated by the modified version of the ORC model developed in the first part. The fluid screening is made for various criteria including low flammability and toxicity indexes, low ODP values, and molecular weight of the pure refrigerant candidates. The parametric performance evaluation of the selected R134a blends with the variable mass fraction is made with respect to two performance indicators including net power output, and the cycle thermal efficiency. Expander outlet pressure and hot fluid inlet temperature are selected as decisive parameters. For the parametric optimization, firstly, all the parameters except the hot fluid inlet temperature are fixed, and R134a blends with varying mass fractions are searched for hot fluid inlet temperature ranging between 363-403 K. Then, the expander outlet pressure is changed between 550-700 kPa for a hot fluid inlet temperature field of 363-393 K to seek the best performing R134a blends with variable compositions in terms of the selected performance indicators. Results show that zeotropic blends with more volatile second components than the pure R134a including R134a/R32, R134a/R143a, and R134a/R125 blends show the best performance in terms of selected performance indicators for all applicable temperatures and the expander outlet pressure range, although they have limited mass fraction of the second components. Besides, azeotropic blends that have closer boiling temperatures to R134a can also provide a better performance than pure R134a.

ÖZET

ORGANİK RANKİN ÇEVRİMİNİN ZEOTROPİK KARIŞIMLAR İLE İNCELENMESİ VE KARIŞIM BİLEŞİMİNİN OPTİMİZASYONU

Bu çalışmanın iki ana bölümü bulunmaktadır. Çalışmanın ilk bölümünde amaç, güvenilir kararlı durum verileri kullanılarak doğrulanan doğru bir ORC modeli geliştirmektir. Bu amaçla, tekrarlanabilir bir şekilde veri elde etmek için 80 ile 110 °C arasında değişen dört farklı ısı kaynağı (yağ) sıcaklığında testler yapılmıştır. Önerilen model, model tahminlerinin doğruluğunu artırmak için basınç düşüşü ve ısı transferi korelasyonlarını dikkate almaktadır. Sonuçlar, kararlı durum ORC modelinin basınçta ±%1 ve sıcaklıkta ±1 °C sapmalarla ve kütle akış hızı, ısı transfer hızı ve soğutucu pompa gücü tahminlerinde ±%5 ile önemli ölçüde doğru olduğunu göstermektedir. İkinci bölümde, değişen mol oranlarına sahip on farklı R134a karışımının performansı, ilk bölümde geliştirilen ORC modelinin modifiye edilmiş versiyonu ile değerlendirilmiştir. Akışkan taraması, düşük yanıcılık ve toksisite indeksleri, düşük ODP değerleri, saf soğutucu akışkan adaylarının moleküler ağırlığı gibi çeşitli kriterlere göre yapılmıştır. Seçilen değişken kütle oranına sahip R134a karışımlarının parametrik performans değerlendirmesi, net güç çıkışı ve çevrim termal verimliliği gibi iki performans göstergesine göre yapılmıştır. Genişletici çıkış basıncı ve sıcak akışkan (yağ) giriş sıcaklığı belirleyici parametreler olarak seçilmiştir. Parametrik performans çalışmasında öncelikle sıcak akışkan giriş sıcaklığı hariç tüm parametreler sabit tutulmuş ve 363-403 K arasında değişen sıcak akışkan giriş sıcaklığı için değişen kütle oranlarına sahip R134a karışımları aranmıştır. Ardından, seçilen performans göstergeleri açısından değişken bileşimlere sahip en iyi performans gösteren R134a karışımlarını aramak için sıcak akışkan giriş sıcaklığı alanı 363-393 K ve genişletici çıkış basıncı 550-700 kPa arasında değiştirilmiştir. Sonuçlar, R134a/R32, R134a/R143a, R134a/R125 karışımları dahil olmak üzere saf R134a'dan daha uçucu ikinci bileşenlere sahip zeotropik karışımların, ikinci bileşenlerin sınırlı kütle oranına sahip olmalarına rağmen, tüm uygulanabilir sıcaklıklar ve genişletici çıkış basıncı aralığı için seçilen performans göstergeleri açısından en iyi performansı gösterdiğini ortaya koymaktadır.

TABLE OF CONTENTS

ACKNOWLEDGEMENTS iii
ABSTRACT iv
ÖZET v
LIST OF FIGURES viii
LIST OF TABLES xv
LIST OF SYMBOLS xviii
LIST OF ACRONYMS / ABBREVIATIONS xxi
1. INTRODUCTION 1
2. LITERATURE REVIEW 8
2.1. General Remarks on ORC 8
2.2. Working Fluid Classification 9
2.2.1. Pure Working Fluids 9
2.2.2. Working Fluid Mixtures 11
2.3. Working Fluid Screening 12
3. EXPERIMENTAL STUDY 15
3.1. Experimental ORC Setup 15
3.2. Steady State Experimental Results for Pure Fluids 18
3.3. Steady-State Experimental Results for Refrigerant Mixtures 22
4. ORC MODEL FOR PURE FLUIDS AND MIXTURES 30
4.1. ORC Model for Pure Fluids 30
4.1.1. Heat Exchanger Model 30
4.1.1.1. Single Phase Regions: Correlations for Subcooled and Superheated Regions 34
4.1.1.2. Two-Phase Region Correlations (For Evaporator) 35
4.1.1.3. Two-Phase Region Correlations (Condenser) 36
4.1.2. Refrigerant Pump Model 38
4.1.3. Pipe Heat Transfer Model 38
4.1.4. Pipe Pressure Drop Model 40
4.2. ORC Model for Refrigerant Mixtures 41
4.2.1. Modified Heat Exchanger Model for Refrigerant Mixtures 42

4.2.1.1. Pressure Drop Correlations in Heat Exchangers 45
4.2.2. Interconnected Cycle Model 46
5. ORC MODEL VALIDATION 48
5.1. Model Validation for Pure Fluids 48
5.1.1. Validation of ORC Component Model 48
5.1.2. Validation of Interconnected ORC Model 52
5.2. Model Validation for Refrigerant Mixtures. 58
5.2.1. Validation of ORC Component Model 58
6. PARAMETRIC PERFORMANCE OPTIMIZATION OF REFRIGERANT MIXTURES 71
6.1. Modeling Constraints and Assumptions. 71
6.2. Working Fluid Screening 74
6.3. Effect of Hot Fluid Inlet Temperature (Study-I) 75
6.4. Effect of Varying Expander Inlet Pressure (Study-II) 86
6.4.1. Hot Fluid Inlet Temperature of 363 K 86
6.4.2. Hot Fluid Inlet Temperature of 373 K 90
6.4.3. Hot Fluid Inlet Temperature of 383 K 95
6.4.4. Hot Fluid Inlet Temperature of 393 K 100
7. SUMMARY & DISCUSSION 106
8. CONCLUSIONS 112
REFERENCES 115
APPENDIX A: EXPERIMENTAL RAW DATA AND UNCERTAINTIES 126
APPENDIX B: WORKING FLUID SCREENING & PROPERTY ESTIMATION. . 131
APPENDIX C: PARAMETRIC PERFORMANCE STUDY RESULTS OF STUDY-I AND STUDY-II 140
APPENDIX D: PARAMETRIC PERFORMANCE STUDY ADDITIONAL FIGURES AND TABLES OF STUDY-I 146
APPENDIX E: PARAMETRIC PERFORMANCE STUDY ADDITIONAL FIGURES OF STUDY-I 152
APPENDIX F: PIPE GEOMETRIES OF ORC TEST SETUP AND MODEL INPUT. 156

LIST OF FIGURES

Figure 2.1. Schematic representation of simple ORC. 9

Figure 2.2. T-s diagram of simple ORC. 9

Figure 2.3. Vapor saturation curves for a) wet b) isentropic c) dry fluids. 10

Figure 2.4. Temperature-composition diagram of a) azeotropic mixtures b) zeotropic mixtures. 11

Figure 2.5. Vapor saturation curve of ORC with zeotropic mixtures. 12

Figure 3.1. The experimental 5 kWe ORC setup in BURET Lab. 16

Figure 3.2. P & ID of the 5 kWe ORC test rig located at Sarıtepe Campus, Bogazici University. 16

Figure 3.3. Detected steady-state zones for various heat source temperatures between 80 - 110 °C, the plot of $T_{hf,in}$, $T_{cw,in}$, $P_{t,o}$. 20

Figure 3.4. Detected steady-state zones for various heat source temperatures between 80 - 110 °C, the plot of $\dot{m}_{wf}$, $\dot{V}_{hf}$ and $\dot{V}_{cw}$, respectively. 20

Figure 3.5. Reference steady state zone at 100 °C, for $T_{hf,in}$, $T_{cw,in}$ and $P_{t,o}$, $\dot{m}_{wf}$, $\dot{V}_{hf}$ and $\dot{V}_{cw}$ (Corresponding to Exp-3 on Figures 3 & 4). 22

Figure 3.6. Detected steady - state zones of the tests with R134a/R236fa mixture, the plot of $T_{hf,in}$, $T_{cw,in}$ and $P_{t,o}$ (Case 13 to 26). 24

Figure 3.7. Detected steady - state zones of the tests with R134a/R236fa mixture, the plot of $\dot{m}_{wf}$, $\dot{V}_{hf}$ and $\dot{V}_{cw}$ (Case 13 to 26). 24

Figure 3.8. Reference steady - state zone at 115 °C, for (a) $T_{hf,in}$, $T_{cw,in}$, $P_{t,o}$ and (b) $\dot{m}_{wf}$, $\dot{V}_{hf}$, $\dot{V}_{cw}$ (Case 21). 25

Figure 3.9. Working fluid pump characteristic curves for R134a (pure) and R236fa / R134a mixture at 1150 rpm ($DP_{pump} - \dot{m}_{wf}$). 29

Figure 4.1. The cycle T - s diagram shows the evaporator zones defined concerning the refrigerant phase (Zone I: subcooled liquid, Zone II: liquid - vapor mixture, Zone III: superheated vapor, $T_7 = T_{cw,in}$). 30

Figure 4.2. Schematic of plate-type heat exchanger. 31

Figure 4.3. Flowchart of the heat exchanger model. 32

Figure 4.4. Pump characteristic curve of the refrigerant pump. 38

Figure 4.5. T - s diagram of the ORC process and the zones of PHEs with respect to phases of (a) pure fluid (b) zeotropic blend of R134a / R245fa(0.65/0.35) and (c) Phase diagram of the zeotropic mixture. 42

Figure 4.6. Flowchart of the modified interconnected ORC model. 47

Figure 5.1. Heat balance in (a) the evaporator (b) the condenser. 49

Figure 5.2. Parity plots of heat flow rate in (a) evaporator and (b) condenser 49

Figure 5.3. Parity plots of (a) R134a temperature at the evaporator outlet, (b) R134a pressure at the evaporator outlet, (c) hot fluid (oil) temperature at the evaporator outlet. 50

Figure 5.4. Parity plots of (a) temperature and (b) pressure in condenser outlet. . . . 50

Figure 5.5. Parity plots of (a) R134a mass flow rate, (b) R134a pressure at the pump inlet, (c) R134a pressure at the pump outlet, (d) work done by the pump. . 51

Figure 5.6. Parity plot of temperature at throttle outlet. 52

Figure 5.7. Schematic of the interconnected ORC model. 52

Figure 5.8. Flowchart of the interconnected ORC model. 54

Figure 5.9. T-s diagram of the ORC. 54

Figure 5.10. Heat transfer in (a) the evaporator (b) the condenser calculated from experimental data. 60

Figure 5.11. Parity plots of heat flow rate in the evaporator for (a) the working fluid and (b) the hot fluid (oil). 61

Figure 5.12. Parity plots of heat flow rate in the condenser for (a) the working fluid and (b) the cooling water. 62

Figure 5.13. Calculated heat duties of the refrigerant and hot fluid (oil) of the evaporator for a) pure fluid (Case 1 to 9) and b) R236fa / R134a mixture (Case 13 to 18) c) R236fa/R134a mixture (Case 19 to 24) with error bars. 64

Figure 5.14. Calculated heat duties of the refrigerant and cooling water (ethylene glycol +water) of the condenser for a) pure fluid (Case 1 to 9) b) R236fa b) R236fa/R134a mixture (Case 13 to 18) and c) R236fa /R134a mixture (Case 19 to 24) with error bars. 65

Figure 5.15. Parity plots of (a) working fluid temperature at the evaporator outlet, (b) hot fluid (oil) temperature at the evaporator outlet (c) pressure at the evaporator outlet. 66

Figure 5.16. Parity plots of (a) working fluid temperature at the condenser outlet, (b) cooling water (ethylene glycol + water) temperature at the condenser outlet, (c) pressure at the condenser outlet. 67

Figure 5.17. An example case for condenser level indicator sub-cooled liquid level (Case 24). 68

Figure 5.18. Variation of a) the condensation temperature b) the condensation heat transfer rate vs the change of condenser area for different test cases (R134a/R236fa vs pure R134a). 69

Figure 6.1. Flowchart of parametric performance study model for refrigerant mixtures. 73

Figure 6.2. Performance indicators for R134a blends with varying mass fractions at a) 363 K b) 373 K c) 383 K d) 393 K e) 403 K heat source temperatures (Study I-a). 76

Figure 6.3. Variation of heat transfer area for the two - phase zone of the condenser ($A_{II,cnd}$) vs the mass fraction of the second component x_2 at $T_{hf,in} = 363$ K. 78

Figure 6.4. Variation of heat transfer area for the two - phase zone of the evaporator ($A_{II,evp}$) vs the mass fraction of the second component (x_2) at $T_{hf,in} = 363$ K. 79

Figure 6.5. Variation of a) the evaporator outlet temperature b) the evaporation heat transfer rate vs the change of mass fraction of the second component x_2 for varying hot fluid inlet temperatures (R134a/R245fa vs pure R134a) 82

Figure 6.6. Performance indicators for R134a blends with varying mass fractions at a) 363 K b) 373 K c) 383 K d) 393 K e) 403 K heat source temperatures (Study I-b). 83

Figure 6.7. The variation of a) the heat duty in the evaporator $Q_{evp,in}$ b) net power Produced $\dot{W}_{net}$ vs the mass fraction of the second component x_2 for $T_{hf,in} = 403$ K. 85

Figure 6.8. Performance indicators of R134a blends with varying expander outlet pressure (kPa) and mass fractions a) 0.8 / 0.2 b) 0.6 / 0.4 c) 0.4 / 0.6 d) 0.2/0.8 e) 0.0/1.0 at a heat source temperature of 363 K. 87

Figure 6.9. Calculated (model) vs theoretical temperature glides in a) the evaporator and b) the condenser for the selected mixtures with different mass fractions of the second component x_2 at $P_{exp,out} = 550$ kPa ($P_{cd,in} = 523$ kPa, $P_{ev,in} = 1949$ kPa). 90

Figure 6.10. Performance indicators of R134a blends with varying expander outlet pressure (kPa) and mass fractions a) 0.8 / 0.2 b) 0.6 / 0.4 c) 0.4 / 0.6 d) 0.2/0.8 e) 0.0/1.0 at a heat source temperature of 373 K. 91

Figure 6.11. Calculated (model) vs theoretical temperature glides in a) the evaporator and b) the condenser for the selected mixtures with different mass fractions of the second component x_2 at $P_{exp,out} = 550$ kPa ($P_{cd,in} = 522$ kPa, $P_{ev,in} = 1949$ kPa). 95

Figure 6.12. Performance indicators of R134a blends with varying expander outlet pressure (kPa) and mass fractions a) 0.8 / 0.2 b) 0.6 / 0.4 c) 0.4 / 0.6 d) 0.2/0.8 e) 0.0/1.0 at a heat source temperature of 383 K. 96

Figure 6.13. Calculated (model) vs theoretical temperature glides in a) the evaporator and b) the condenser for the selected mixtures with different mass fractions of the second component x_2 at $P_{exp,out} = 550$ kPa ($P_{cd,in} = 521$ kPa, $P_{ev,in} = 1949$ kPa). 100

Figure 6.14. Performance indicators of R134a blends with varying expander outlet pressure (kPa) and mass fractions a) 0.8 / 0.2 b) 0.6 / 0.4 c) 0.4 / 0.6 d) 0.2/0.8 e) 0.0/1.0 at a heat source temperature of 393 K. 101

Figure 6.15. Calculated (model) vs theoretical temperature glides in a) the evaporator and b) the condenser for the selected mixtures with different mass fractions of the second component x_2 at $P_{exp,out} = 550$ kPa ($P_{cd,in} = 520$ kPa, $P_{ev,in} = 1949$ kPa). 105

Figure D.1. Pressure difference between the inlet and the outlet of the condenser vs the mass fractions of the second component x_2 of the selected refrigerant mixtures at $T_{hf,in} = 363$ K for Study I-a (for R134a (pure) : $P_{cnd,in} = 575.7$ kPa & $P_{cnd,out} = 568.5$ kPa). 146

Figure D.2. Change of a) condenser inlet pressure b) condenser outlet pressure vs the mass fractions of the second component x_2 of the selected refrigerant mixtures at $T_{hf,in} = 363$ K for Study I-a (for R134a (pure) : $P_{cnd,in} = 575.7$ kPa & $P_{cnd,out} = 568.5$ kPa). 148

Figure D.3. Temperature variation at a) the expander inlet b) the expander outlet vs the mass fraction of the second components for the selected R134 blends ($T_{hf,in} = 373$ K). 149

Figure D.4. Temperature at a) the evaporator outlet b) the condenser outlet vs the mass fraction of the second components for the selected R134 blends ($T_{hf,in} = 373$ K). 150

Figure D.5. Temperature drops at the expander vs the mass fraction of the second components for the selected R134 blends ($T_{hf,in} = 373$ K). 151

Figure E.1. Temperature drops at expander outlet vs the mass fraction of the second components for the selected R134 blends ($P_{exp,out} = 550$ kPa , $T_{hf,in} = 373$ K). 152

Figure E.2. Temperature drops at expander outlet vs the mass fraction of the second component for R134a/R1234yf ($P_{exp,out} = 550$-700 kPa,$T_{hf,in} = 373$ K). 152

Figure E.3. The variation of the condensation phase change areas vs the mass fractions of the second components of R134a / R32 blends for varying expander outlet pressures at $T_{hf,in} = 383$ K. 153

Figure E.4. The variation of the condensation phase change areas vs the mass fractions of the second components of R134a / R143a blends for varying expander outlet pressures at $T_{hf,in} = 383$ K. 153

Figure E.5. The variation of the condensation phase change areas vs the mass fractions of the second components of R134a / R125 blends for varying expander outlet pressures at $T_{hf,in} = 383$ K. 154

Figure E.6. The variation of the condensation phase change areas vs the mass fractions of the second components of R134a / R32 blends for varying expander outlet pressures at $T_{hf,in} = 393$ K. 154

Figure E.7. The variation of the condensation phase change areas vs the mass fractions of the second components of R134a / R143a blends for varying expander outlet pressures at $T_{hf,in} = 393$ K. 155

Figure E.8. The variation of the condensation phase change areas vs the mass fractions of the second components of R134a / R125 blends for varying expander outlet pressures at $T_{hf,in} = 393$ K. 155

LIST OF TABLES

Table 3.1. Characteristics of the equipment of the ORC test system. 17

Table 3.2. Technical information about sensors and measurement equipment. 18

Table 3.3. Parameter values of the experiment. 18

Table 3.4. Data collected at four different heat source temperatures between 80-110 ℃ for a time window of 750sec. 21

Table 3.5. Set values of the experiment. 22

Table 3.6. Experimental scenario of the zeotropic mixture tests. 23

Table 3.7. Original data collected at three different heat source temperatures between 90-115 ℃ (for pure R134a). 26

Table 3.8. Original data collected at three different heat source temperatures between 90-115 ℃ (for R236fa/R134a mixture with varying composition). 27

Table 4.1. Geometrical values of the evaporator and condenser of the ORC set-up. . . 32

Table 4.2. Technical data sheet of Atherma M32 type heat transfer oil. 34

Table 4.3. Governing equations of the performance indicators $\dot{\mathrm{W}}_{\mathrm{net}}$, and n_{th}. 47

Table 5.1. Averaged input parameters used for model validation under steady state operation conditions (working fluid pump speed: 1050 rpm, hot fluid (oil) pump frequency: 40 Hz, $T_{hf,in} = 80 - 110$ ℃ ,$T_{cw,in} = 4$ ℃). 48

Table 5.2. Experimental data with uncertainties vs. model predicted results (time window=750 sec). 55

Table 5.3. Performance comparison of the interconnected ORC model with the literature. 57

Table 5.4. The effect of pipe heat losses and pressure drop on ORC modeling accuracy for Exp-1 & Exp-2 and for Exp-3 & Exp-4. 57

Table 5.5. Averaged experimental input parameters for the validation of pure fluid case (Case 1-9) and R236fa/R134a mixture (Case 13-24). 59

Table 5.6. Experimental vs model results of sub-cooled liquid level at condenser level indicator. 68

Table 6.1. Model parameters and decisive variables. 72

Table 6.2. Model constraints and assumptions. 72

Table 6.3. Physical and environmental properties of working fluid candidates for R134a blends. 74

Table A.1. Statistical values of reference steady-state zones (no time window). 126

Table A.2. Relative standard uncertainty (u_r) vs. sensor accuracy of the experiments. . 128

Table A.3. Absolute uncertainty values of the experimental steady states. 129

Table A.4. Relative standard uncertainties for (a) pure fluid cases (b) R236fa / R134a mixture with varying composition (Case 10 to 18) (c) R236fa / R134a mixture with varying composition (Case 19 to 25). 129

Table B.1. Property calculation methods of selected refrigerant mixtures. 131

Table B.2. Definition and calculation of mixture property in terms of Helmholtz energy derivations [66]. 133

Table B.3. Working fluid candidates for R134a blends (Pre-screening). 138

Table C.1. Variation of performance indicators for R134a blends with respect to varying hot fluid inlet temperature $T_{hf,in}$=363-403 K (Study I-a). 140

Table C.2. Variation of performance indicators for R134a blends with respect to varying hot fluid inlet temperature $T_{hf,in}$=363-403 K (Study I-b). 141

Table C.3. Variation of performance indicators for R134a blends with respect to varying expander outlet pressure $P_{exp,out}$ for heat source temperature $T_{hf,in} = 363$ K. 142

Table C.4. Variation of performance indicators for R134a blends with respect to varying expander outlet pressure $P_{exp,out}$ for heat source temperature $T_{hf,in} = 373$ K. 143

Table C.5. Variation of performance indicators for R134a blends with respect to varying expander outlet pressure $P_{exp,out}$ for heat source temperature $T_{hf,in} = 383$ K. 144

Table C.6. Variation of performance indicators for R134a blends with respect to varying expander outlet pressure $P_{exp,out}$ for heat source temperature $T_{hf,in} = 393$ K. 145

Table D.1. Pressure difference and relative differences of the selected mixtures at $x_{2,max}$ with respect to reference case ($P_{cnd,in,ref} = 575.7$ kPa & $P_{cnd,out,ref} = 568.5$ kPa for pure R134a). 147

Table F.1. Pipe total lengths and elevations for each pipe section ($D_i = 22.1$ mm and $D_o = 25.4$ mm). 156

Table F.2. Pipe lengths and elevations between model components and sensors. 156

Table F.3. Number of pipe connection elements for each pipe section. 157

Table F.4. Loss coefficients (K) with respect to the type of pipe connection elements. . 157

LIST OF SYMBOLS

abs	Absolute
acc	Acceleration (Subscript)
air	Air (Subscript)
a^{idmix}	Helmholtz energy for ideal mixtures
A_{tot}	Total heat transfer area
$A_{tot,req}$	Total required heat transfer area
Bo	Boiling number
cd/cnd	Condenser (Subscript)
$coldin$	Cold inlet (Subscript)
$coldout$	Cold outlet (Subscript)
$comb$	Combined (Subscript)
$conv$	Convective (Subscript)
c_p	Constant pressure specific heat
c_v	Constant volume specific heat
cr	Critical (Subscript)
cw	Cooling water (Subscript)
D_h	Hydraulic diameter
D_p	Port diameter
ele	Elevation (Subscript)
eq	Equivalent (Subscript)
ev/evp	Evaporator (Subscript)
exp	Expander (Subscript)
f	Pipe friction coefficient
f_D	Darcy friction factor
F_{ij}	Generalized factors
fr	Friction (Subscript)
f_{sp}	Fanning friction factor
g	Gas (Subscript)

G	Channel mass flow rate; Gibbs energy
G_{eq}	Equivalent mass flux
h	Enthalpy
Hex	Heat exchanger (Subscript)
hf	Hot fluid (Subscript)
$hotin$	Hot inlet (Subscript)
$hotout$	Hot outlet (Subscript)
i	In (Subscript)
in	Inlet (Subscript)
ins	Insulation (Subscript)
is	Isentropic (Subscript)
k	Thermal conductivity
K_i	Resistance coefficients
k_p	Plate thermal conductivity
l	Liquid (Subscript)
L_p	Length of the pipe
$\dot{m}$	Mass flow rate
maj	Major (Subscript)
max	Maximum (Subscript)
min	Minimum (Subscript)
mix	Mixture (Subscript)
N_{ch}	Number of channels
n_{th}	Cycle thermal efficiency
Nu_{forced}	Nusselt number for forced convection
Nu_{free}	Nusselt number for free convection
o	Out (Subscript)
out	Outlet (Subscript)
p	Pipe (Subscript) ; Pump (Subscript)
pp	Pump
P	Pressure
P_{co}	Corrugation pitch

$P_{pp,i}$	Pressure at the pump inlet
$P_{t,o}$	Pressure at the throttle outlet
Pr	Prandtl number
Pr_w	Prandtl wall number
q	Quality of the fluid
$\dot{Q}_{in}$	Rate of heat transferred into the cycle
R	Universal gas constant
Ra	Rayleigh number
Re	Reynolds number
rad	Radiation (Subscript)
$satl$	Saturated liquid (Subscript)
$satv$	Saturated vapor (Subscript)
sp	Single-phase (Subscript)
t	Throttle valve (Subscript)
tp	Two-phase (Subscript)
T	Temperature
$T_{pp,i}$	Temperature at the pump inlet
T_r	Reduced temperature
U_p	Heat transfer coefficient in the pipe
$\dot{V}$	Volumetric flow rate
$\dot{W}_{net}$	Net power output
wf	Working fluid (Subscript)
x_2	Mass fraction of the second component of the mixture
α	Convective heat transfer coefficient
α^0	Ideal gas contribution of Helmholtz free energy
α^r	Residual gas contribution of Helmholtz free energy
β	Chevron angle
ϵ	Relative roughness
ρ_r	Reduced density
μ	Dynamic viscosity

LIST OF ACRONYMS / ABBREVIATIONS

ASHRAE	American Society of Heating, Refrigerating and Air-Conditioning Engineers
BURET	Boğaziçi University Renewable Energy Technology
CFC	Chlorofluorocarbon
CHP	Combined Heat and Power
CO2	Carbon Dioxide
EXP	Experiment
GERG	European Gas Research Group
GWP	Global Warming Potential
HC	Hydrocarbon
HCFC	Hydrochlorofluorocarbon
HEX	Heat Exchanger
HFC	Hydrofluorocarbon
HFO	Hydrofluoroolefin
ICE	Internal Combustion Engine
IHORC	Organic Rankine Cycle with Internal Heat Exchanger
LMTD	Logarithmic Mean Temperature Difference
LNG	Liquefied Natural Gas
NIST	National Institute of Standards and Technology
NPSH	Net Pump Suction Head
ODP	Ozone Depletion Point
ORC	Organic Rankine Cycle
PFC	Perfluorocarbon
P & ID	Piping and Instrumentation Diagram
PHE	Plate Heat Exchanger
PTORC	Parallel Two Stage Organic Rankine Cycle
RORC	Regenerative Organic Rankine Cycle
RTD	Resistance Temperature Detector
SPR	Single Phase Region

STORC	Series Two Stage Organic Rankine Cycle
TPR	Two Phase Region
VLE	Vapor Liquid Equilibrium
WHR	Waste Heat Recovery

1. INTRODUCTION

Recently, interest in using low-grade heat to generate electricity has been rising due to increasing energy demand and restrictive regulations on greenhouse gas emissions [1,2]. ORC, Kalina, Trilateral Flash, Maloney-Robertson, supercritical CO2 cycles, and thermoelectric generators are examples of techniques available to convert low-grade heat into mechanical work from solar and geothermal energy and waste heat. ORC offers better performance than other technologies of comparable size and operating conditions [3,4]. Thanks to their robustness, simplicity, minimal maintenance cost, and good partial load behavior, ORCs are preferred in the solar energy industry [7, 8, 9, 10], waste heat recovery [11, 12, 13], and combined heat and power (CHP) generation applications [14,15,16]. Detailed information about ORC technology, applications, and different ORC architectures (i.e., regenerative, trans-critical, recuperated) can be found in reviews of Lecompte et al. [5] and Quoilin et al. [6].

Off-design models are used to understand the operational performance of ORC systems in conditions away from their nominal regime. For example, Rech et al. [17] investigated the performance of three different ORC configurations under transient and steady-state conditions using waste heat from dual-fuel diesel engines to show the application of waste heat recovery from the engines on board an LNG carrier. Manente et al. [18] developed an off-design ORC model of geothermal power plants to determine the optimal operational conditions at part-load. Lecompte et al. [19] developed a part-load model to optimize the ORC performance in combined heat and power (CHP) applications regarding thermo-economic indicators such as investment cost. Mazzi et al. [20] developed an off-design dynamic model to assess the system behavior of superheated regenerative ORC systems at steady-state and transient operation conditions. Wang et al. [21] evaluated the performance of the solar-driven ORC using an off-design model, and the results revealed that the system's performance has increased with decreasing environment temperature and increasing mass flow rates of vapor generators and parabolic collectors. Recently, Neto et al. [22] developed an off-design ORC model operating with exhaust gases of stationary diesel engine. Their study illustrated that the combined system results in an increase in thermal efficiency and a decrease in fuel consumption as well as engine out emissions. However, none of the papers cited above mentioned the experimental validation.

The validation of the off-design model with reliable experimental data is crucial to evaluate the model's accuracy. Quoilin et al. [23] developed an experimentally validated complete ORC model with a scroll expander using R123 as a working fluid to examine the part-load behavior. Lemort et al. [24] developed an oil-free scroll expander integrated ORC model with HCFC-123 as a working fluid and verified it with experimental data. Ziviani et al. [25] reported an experimentally verified, control-oriented ORC model with a screw expander and R245fa as working fluid to optimize the operation of the ORC. Fatigati et al. [26] developed a 1-D off-design model using the GT Suite package to evaluate the performance of ORC plants with rotary vane expander exploiting low-grade heat from supercharged ICE. Quoilin et al. [27] developed a transient model of a small-scale ORC with a volumetric expander by focusing on the pipe-in-pipe HEXs and found that evaporation pressure is the most decisive control parameter in evaluating dynamic behavior. Dickes et al. [28] conducted a comparative study of different off-design modeling approaches (constant efficiency, polynomial regression, and semi-empirical models), validated by experimental ORC setup with scroll expander and found that the semi-empirical models are the most reliable ones in off-design conditions. Although many examples of ORC units with scroll-expander and volumetric expanders exist, experimental and numerical ORC studies with expander simulator lines are relatively scarce in the literature. Twomey et al. [29] used an experimental test rig equipped with an expansion valve and heat exchanger to evaluate the off-design performance of their dynamic model.

The reliability of the data used in the model validation emerges as an important criterion in evaluating the model's accuracy. Incorrect determination of the steady-state regime may lead to high errors in the calculation of measured uncertainties and can make the dataset completely useless for model validation. Especially when working with larger datasets, correct identification of steady-state regimes is required. Yet, pre-,and post-processing of the steady-state data are neglected in most of the studies. Lecompte et al. [30] developed a novel steady-state identification methodology for detecting steady-state data and correctly validating a small-scale ORC model with volumetric double screw expander to deal with that issue. Their research proposes a steady-state detection algorithm based on an iterative process of standard deviations in a moving window to detect steady-state zones. The results revealed that their model can predict the net power outputs with $\mp 2\%$ deviation from the experimental data.

Pipe heat and pressure losses that may be significant, especially for test setups with more extended connecting elements, are also neglected in most studies. There are limited interconnected ORC models in the literature that consider pressure drop in heat exchangers, and heat transfer and pressure drop in connecting cycle elements [28, 30, 31–34]. Yet, these either used imposed internal conditions (i.e., degree of sub-cooling, degree of super-heating, liquid receiver level) or assumed exit properties while calculating the thermodynamic state properties. Moradi et al. [33] developed an assumption-free charge-sensitive model that can predict the liquid receiver mass using experimentally measured liquid receiver level. However, it is still not fully predictive since it requires a liquid-receiver level as an input. The first fully deterministic ORC model operating under off-design conditions has been developed by J. Oh et al. [34]. This model uses system boundary conditions and semi-empirical correlations of evaporation pressure as inputs to predict the off-design performance with a maximum error of 8%.

In the literature, several studies compare the model results with experimental data on ORCs. The study conducted by Lecompte et al. [30] is a good example since it shows the importance of using statistically reliable steady-state data in ORC modeling, but the pipe losses are not considered in the modeling process. To the best knowledge of the authors, pipe losses that would be significant in ORC setups are not considered in the literature except for the works of Dickes et al. [31] and J. Oh et al. [34]. Dickes et al. [31] included the pipe losses in their analysis; however, they lumped all losses in the inter-connections to two fictitious elements, one on the evaporator side and another on the condenser side, and the matching accuracy between the model and the experiments is low. Although in the work of J. Oh et al. [34], the accuracy is higher a discussion of the effect of pipe losses is not given.

In the majority of previous studies, pure working fluids have been examined. The pinch point temperature difference, which can be defined as the minimum temperature difference between the working fluid and heat source at the heat exchanger, is one problem that leads to large temperature differences at the end of the condensation and evaporation process. This will cause high irreversibility that reduce cycle efficiency and net power produced from the cycle. This problem can be solved by using refrigerant mixtures providing variable evaporation temperature profiles during phase change [3, 47, 48]. In that sense, zeotropic mixtures which consist of organic blends that have different boiling points would reduce irreversibility greatly, thanks to variable temperature profile they have during evaporation and condensation processes [47].

Recently, zeotropic mixtures have gained huge popularity as they offer a better temperature match compared to pure organic compounds. The performance of zeotropic mixtures varies depending on many factors, from the temperature range studied to the type and mixing ratio of the refrigerants used in the blend. By changing the mixing ratio, it is possible to vary the system performance to a large extent as the physical safety and chemical properties of the mixture are strongly dependent on the mixture composition. Latent heat of condensation stemming from the large temperature glide can be used to preheat working fluids which leads to improvement in the efficiency. Therefore, blend composition and mass fraction of each component should be precisely determined [47]. Further, the heat transfer coefficient should also be predicted correctly since it affects the mixture properties (i.e., thermal conductivity, and viscosity) [48].

In fluid screening, the thermal match between the heat source and the working fluid during evaporation and condensation is crucial as zeotropic mixtures are used. The study conducted by Zhao et al. [25] reveals the significance of heat source temperature on the composition of zeotropic mixtures. Lecompte et al. [49] worked with eight pure organic fluids and their mixtures by selecting second-law efficiency as an optimization criterion. Results showed that the exergy efficiency was increased in the range of 7.1-14.2 % as refrigerant mixtures were used for a heat source temperature of 150°C. Besides, a temperature glide in the condenser was found most critical for performance. Y. Feng et al. [50] conducted a multi-objective parametric study to assess the performance of R245fa and R227ea, and their mixtures in terms of various evaporating bubble point temperature and condensing dew point temperature. According to the results, the best thermal and economic performance was obtained by using R245fa/R227ea (0.7/0.3). Song et al. [51] used different blends of refrigerants (R141b, R11) and hydrocarbons for the WHR of a diesel engine. Results showed that the net power output was raised by 13.3% by selecting the cyclohexane/R141b (0.5/0.5) blend.

Different design configurations are also considered in the multi-objective optimization studies. Sadeghi et al. [52] used three different configurations including ORC, PTORC, and STORC to examine the performance of refrigerant mixtures concerning two objective functions: net power output and turbine sizing parameter. In their study, evaporation pressure, pinch point temperature difference, and superheating degree are selected as decisive parameters. Results show that the net power output from simple ORC, PTORC, and STORC configurations are raised by 27.76%, 24.98%, and 24.79%, respectively, when the refrigerant mixtures are used instead of pure R245fa. The multi-objective study conducted by Nondy et al. [53] compares the performance of different ORC configurations including recuperative ORC (RORC) and basic ORC in terms of net power and exergy efficiency. In their study, Pareto Envelope-based Selection Algorithm-II is used. Results show that RORC provides 16.19% higher net power output, and 15.33% higher exergy efficiency than basic ORC.

Up to now, all the mentioned studies have included studies showing that refrigerant mixtures improve the cycle performance. Yet, there are also studies in the literature that show the usage of refrigerant mixtures can't always lead to a performance increase [88, 89, 90]. The main issues associated with the zeotropic mixtures are the increase of the irreversibility due to the deteriorating thermal match between the phase-change lines of the zeotropic mixture with the heat source and heat sink temperature lines, higher heat transfer area demand for the heat exchangers due to the temperature glide during the phase-change, composition shift, and fractionating, and the deterioration of the heat transfer mechanism [59].

Besides, when the ORC system operates under off-design conditions, it is hard to reach an optimum condition valid for the selected mixtures. Therefore, the cycle performance is also affected by the operating conditions, design configurations, and the performance criteria itself [54, 55, 59]. For instance, Wu et al [88] uses three different zeotropic mixtures (R227ea/R245fa, R600/R245fa, and RC318/R245fa) in their analysis to compare the results with pure R245fa. In their study, the cycle thermal efficiency, net power output, and economic performance are used as performance criteria. Results show that although the net power output and thermal efficiencies increase by using zeotropic mixtures, the economic performance (assessed by net power output vs per unit UA) of the zeotropic mixtures gets worse compared to the pure fluid case. The study conducted by Li et al [90] also shows parallel results to Wu et al's [88] work. In their study, 20 different zeotropic mixtures with varying mole fractions are analyzed in terms of economic performance, and results show that the superiority of the zeotropic mixtures is dependent on the range of operating conditions. Further, the economic performance of the zeotropic mixtures is worse compared to pure fluid cases due to the larger heat transfer area needs of the mixtures to compensate phase-change of the zeotropic mixtures.

Previous studies in the literature also show that the composition of the zeotropic mixtures [54, 55], heat source temperature, and condensation pressure are among the most significant control variables affecting the off-design performance of the cycle [56]. Besides, a detailed ORC model which simulates the experimental process with good accuracy is also needed. The novel study presented here uses statistically reliable data, considers pipe pressure drops and heat transfer losses to validate the ORC model developed for both pure fluids and refrigerant mixtures.

Main objective of the present study is to evaluate the thermodynamic performance of various R134a blends in an ORC system using reliable interconnected ORC model. This thesis is composed of two parts. The first part of the study aims to build an accurate iterative steady state model of an ORC with throttle valve using refrigerant pump mass flow rate, thermal oil volumetric flow rate, cooling water inlet temperature, and volumetric flow rate, throttle valve and refrigerant pump outlet pressures as inputs. The ORC model for pure fluids which presented in Chapter 4, takes piping heat transfer and pressure drop into account, and it models the heat exchange processes in detail without making any exit state assumptions for heat exchangers. Experimental data collected from the BURET Laboratory ORC test rig are used to validate the model. This work contributes to the literature with an ORC model that considers pipe losses which can accurately predict pressures and temperatures at sensor points and sub-model boundaries.

The second part of the study aims to examine the performance of selected R134a blends examined under various restrictive conditions with respect to two different performance indicators: net power output, and the cycle thermal efficiency. However, the ORC model developed for the pure fluid case cannot be used for the refrigerant mixtures directly. Therefore, a modified version of the ORC model, which can calculate the temperature glide that occurs in the phase change of the mixture, is developed (see Chapter 5). The decisive parameters of the study are the maximum cycle temperature reached by heat transfer fluid during evaporation and the expander outlet pressure. Fluid screening is conducted by both considering the thermodynamic performance indicators (i.e., molecular weight, and boiling point) and safety aspects including ODP values, flammability, and toxicity indexes. At the end of the screening process, R134a blends with low toxicity and low flammability indexes, and low and/or moderate molecular weight with low ODP values are selected including R134a/R1234yf, R134a/R143a, R134a/R227ea, R134a/R245fa, R134a/R236ea, R134a/R236fa, R134a/R32, R134a/R125, R134a/R152a, and R134a/R1234ze. The properties of R134a blends are calculated by REFPROP v9.1.

The performance evaluation of selected refrigerant blends is made with respect to two different decisive variables. In the first part of the parametric performance study ten different R134a blends with varying mole fractions are evaluated in terms of $\dot{W}_{net}$ and n_{th} as the hot fluid inlet temperatures are varied between 363-403 K, while the rest of the six independent variables are kept constant. The first study comprises two sub-studies with respect to change of the pump isentropic efficiencies including Study I-a ($n_{pump,is} = 0.3$) and Study I-b ($n_{pump,is} = 0.8$). In the second part (Study-II), five out of 10 best-performing refrigerant blends with varying mass fractions are assessed with respect to expander outlet pressures of 550, 600, 650 and 700 kPa for four different hot fluid inlet temperature of 363, 373, 383 and 393 K. In both studies, the total heat transfer areas of the evaporator and condenser are considered limitations for the determination of the upper limits of the mole fractions of each blend.

2. LITERATURE REVIEW

2.1. General Remarks on ORC

Thanks to its compact structure and robustness, high reliability, ease of maintenance and low investment cost, success in partial loads, and applicability to WHR systems, ORC units would be an appropriate candidate to convert low-grade heat into electricity. Being almost analogous to the steam Rankine cycle, ORC uses working fluids instead of water having higher molecular weight, and lower boiling point, and these make them preferable in converting heat at low temperatures ranging from 60 ℃ to 350 ℃ into electricity. Despite being limited by low thermodynamic efficiencies of up to 20%, their flexibility, and success in partial load conditions makes them excellent choices in low and medium-grade heat conversion systems [57].

ORC is analogous to the steam Rankine cycle and is composed of the same components including a pump, an expansion device, an evaporator, and a condenser. The process starts with a pump, which delivers the working fluid into an evaporator where it changes phase from liquid to vapor form. Then, pressurized organic fluid flows into an expander where it loses enthalpy and power is produced consequently. Finally, passing through the condenser the low-pressure vapor at the expander outlet turns back to liquid form [50]. To raise the thermal efficiency of the cycle and reduce the heat duty of the evaporator regenerative cycle can be used. Differentiating from simple ORC, the vapor at the expander outlet goes into the heat exchanger unit called recuperator where it loses its enthalpy thanks to the supply of cold working fluid coming from the discharge section of the pump. The scheme representing the simple ORC is shown in Figure 2.1. The T-s diagram of simple ORC is given in Figure 2.2.

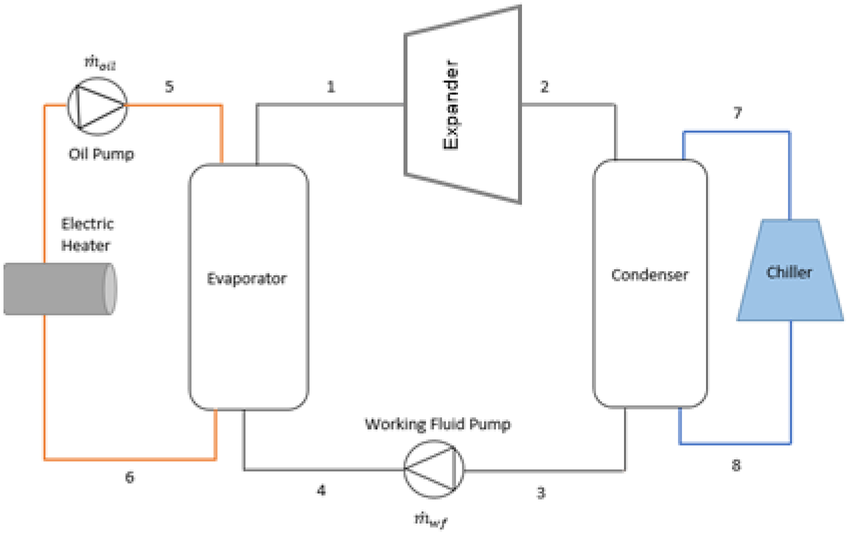

Figure 2.1. Schematic representation of simple ORC.

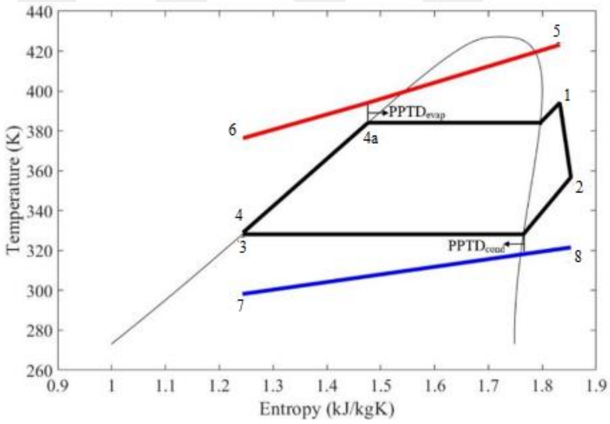

Figure 2.2. T-s diagram of simple ORC.

2.2. Working Fluid Classification

2.2.1. Pure Working Fluids

Working fluids can be classified into three different groups with respect to the slope of the saturation curve: dry, wet, and isentropic. Figure 2.3. shows the temperature (T)-entropy (s) diagram of each working fluid. The fluids having negative slopes are called wet fluids, whereas dry and isentropic fluids are characterized by positive and zero slopes respectively.

Mostly, dry and isentropic fluids are preferred in ORC applications since they don’t require superheating. Wet fluids can also be used in ORCs however superheating would be needed to avoid liquid droplets observed during later expansion period damaging the turbine blades.

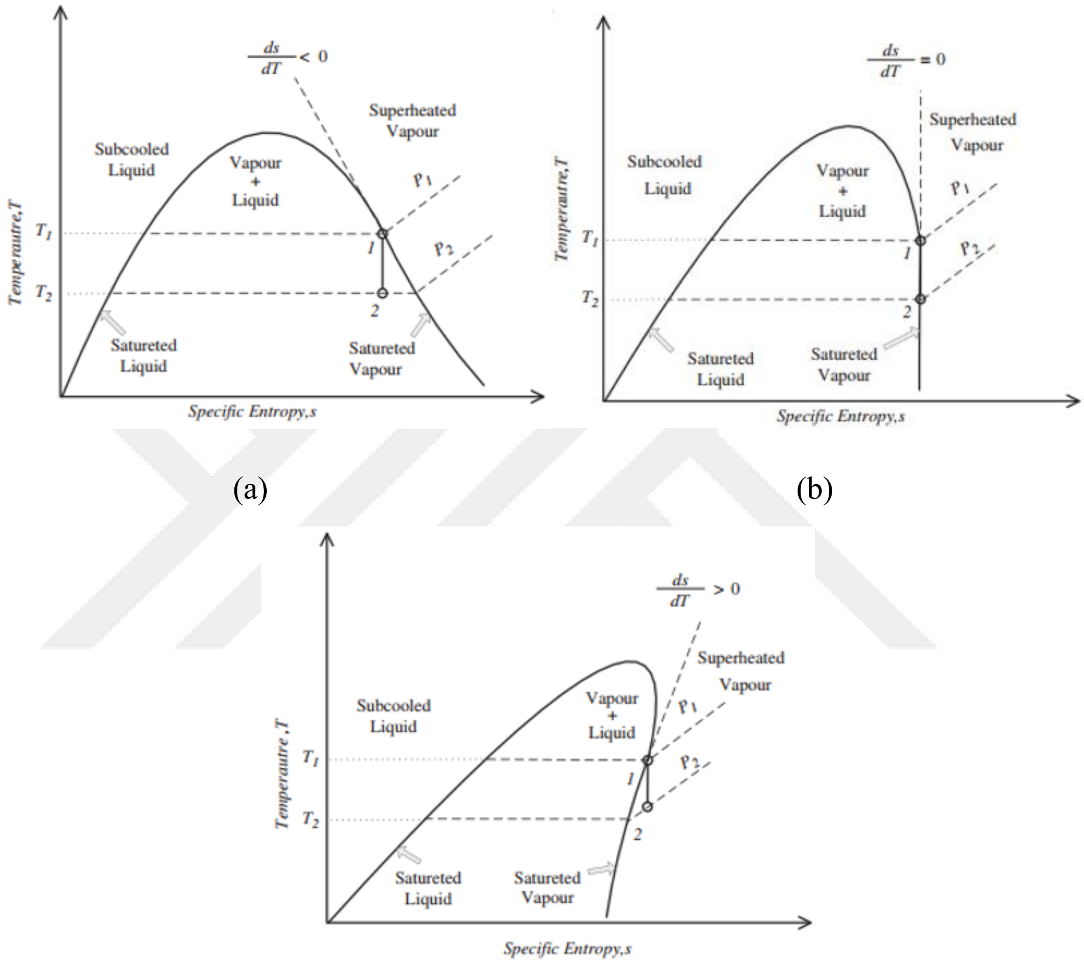

(c)

Figure 2.3. Vapor saturation curves for (a) wet (b) isentropic (c) dry fluids [85].

It is possible to classify the working fluids into seven different groups according to the molecular structure of their atoms. Scientific researches have been carried out for many years to determine what types of organic fluids are most suitable for which type of applications, and no definite conclusion has been reached yet. In the selection of working fluids pre-screening method is the most preferable method [47]. The working fluids with desirable properties (i.e. low toxicity, non-flammable, cheap, and stable) are chosen as candidates. The working fluid candidates available in the literature concerning their molecular structure and desirable properties are tabulated in Table B.3 in Appendix B.

2.2.2. Working Fluid Mixtures

Organic mixtures can be classified into two different categories: azeotropic mixtures, and zeotropic mixtures. The difference between them is that azeotropic mixtures have constant boiling points during the phase change process, whereas zeotropic mixtures do not have constant boiling points.

Zeotropic mixtures, or non-azeotropic mixtures, can be defined as the mixture, composed of components, which don't have a constant boiling or condensation temperature during the phase change process.

The advantage of zeotropic mixtures is the non-isothermal phase change line they have. This can provide a better match between the heat source and working fluid temperatures during the phase change process. In this way, the irreversibility observed in processes such as evaporation and condensation can be reduced [47, 59]. However, the usage of zeotropic mixtures can't always provide a better performance. It would also add the system additional safety precautions and extra cost due to the high-pressure conditions. Figure 2.4. represents the temperature-composition diagrams of ORC with azeotropic and zeotropic mixtures. Vapor-saturation curve of zeotropic mixtures is shown in Figure 2.5.

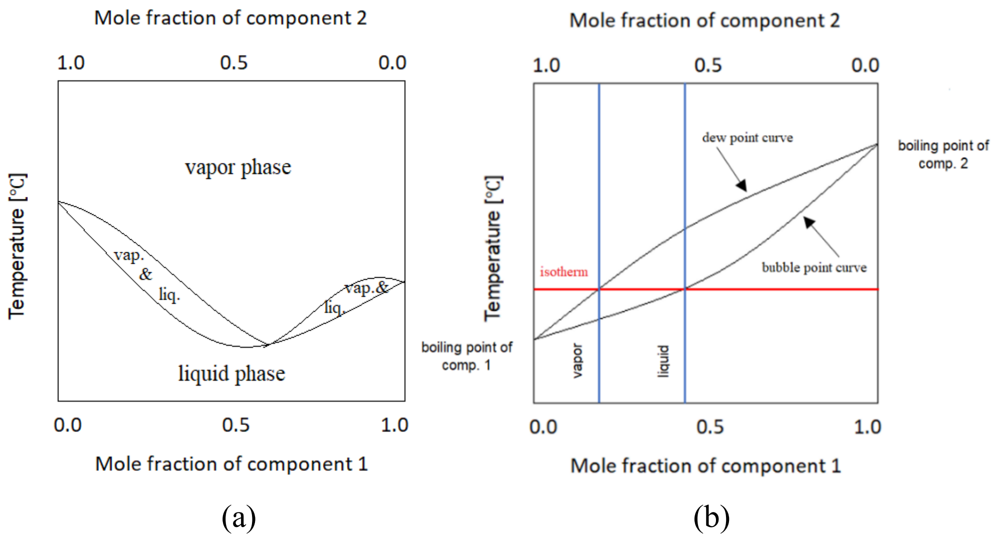

Figure 2.4. Temperature-composition diagram of (a) azeotropic mixtures (b) zeotropic mixtures.

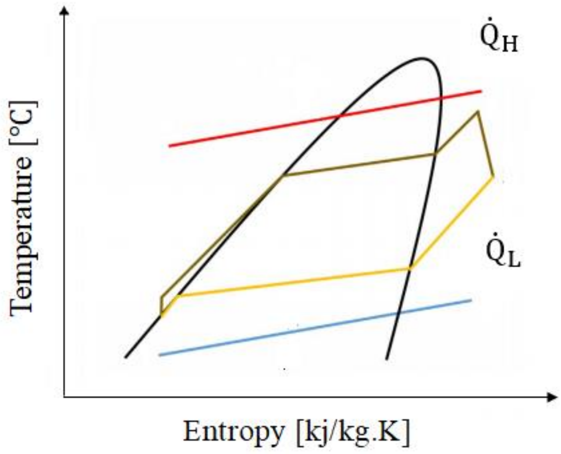

Figure 2.5. Vapor saturation curve of ORC with zeotropic mixtures.

Herein, temperature lines of high heat source and evaporation are shown with red and green lines respectively. Similarly, temperature lines of low-temperature heat source and condensation are denoted by blue and yellow lines respectively.

The performance of zeotropic fluids varies depending on many factors, from the temperature range studied, to the type of fluid used in the blend and to the blend percentage. By changing the mass percentage of the mixture, it is possible to vary the system performance to a large extent as the physical, safety, and chemical properties of the mixture are strongly dependent on the mixture composition.

Latent heat of condensation stemming from the large temperature glide can be used to preheat working fluids which leads to improvement in the efficiency. Therefore, the blend composition and mass fraction of each constituent should be precisely determined [47]. Further, the heat transfer coefficient should also be predicted correctly as it affects the mixture properties such as thermal conductivity, and viscosity [3].

2.3. Working Fluid Screening

Identification of high-performance working fluids providing optimal performance has still been a major issue for ORC technology. A general methodology in the selection of working fluid is to determine working fluid candidates exhibiting favorable chemical, environmental, safety, and economic properties.

Various screening criteria exist in the selection of working fluids: cycle performance, cost, thermal stability, flammability and toxicity, and environmental index. Preferrable criteria in the selection of working fluids are thermal efficiency, positive or isentropic saturation vapor curve, high vapor density, good thermal stability, high conductivity and latent heat of vaporization, low viscosity, high vapor density, low melting point, positive condensing gauge pressure, high safety index, good availability, low ODP and GWP values [6, 58].

There exist different optimization techniques based on various algorithms in the literature. One of the most prominent ways of the determination of working fluid is to conduct experimental studies with pre-selected candidates from commercially available organic compounds (i.e., hydrocarbons, and refrigerants). However, experimental studies are confined by the high costs, and low predictive capabilities they have. Hence, computer-aided tools could provide better screening performance as they enable us to solve the problem more systemically. Besides, more comprehensive models screening a large number of molecules (i.e., Computer Aided Molecular Design) are also used. These methods take the working fluid selection on a molecular basis. Therefore, novel working fluid candidates which are not readily available in online working fluid databases such as NIST can be determined. However, the complexity of that kind of model is very high, and this affects the computational efficiency of the optimization process greatly [48].

Applying pre-screening criteria is the most common methodology used to determine refrigerant mixture candidates and the optimal mole fraction. The study conducted by Z. Kang et al. [60] is targeting to find the optimal refrigerant mixture and its' composition that maximizes the net power delivered from the ORC driven by low & medium-temperature geothermal fluids. In their study, working fluid selection is made from commercially available organic compounds using various screening criteria including low ODP & GWP values, low or no toxicity, low critical temperature (<200 ℃), and reasonable price. 10 different refrigerant mixtures are determined by this methodology, and their effect on ORC performance is investigated. In the study, the mass fraction of each component and evaporator temperature are selected as optimization parameters. Based on this study, R245fa/R600a (0.9/0.1) is determined as the most preferable one.

G. Shu et al. [79] examined the effect of zeotropic mixtures on cycle efficiency and exergy loss for high-temperature ORC applications. In their study, a combination of pure hydrocarbons including benzene, cyclohexane, and cyclopentane with refrigerants (R11 and R123) are used. Results showed that the optimum mixing ratio has considerably changed with respect to evaporator temperature. The maximum cycle efficiency is 16,7% and obtained by Benzene/R11 (0.7/0.3).

H.Xi et al. [86] tried to find the optimal zeotropic fluid composition using 8 different working fluids for two different design configurations: basic ORC, and ORC with internal heat exchanger (IHORC). In their study, the thermodynamic and economic performance of two different ORC configurations with heat source temperature (80-120 ℃). As a result of this study, Isopentane/Isobutane, Isobutane/R152a, and Butane/R227ea blends are recommended as optimal zeotropic mixtures for the heat source temperature varies between 80 and 120 ℃.

A.M. Ahmed et al. [87] examined the effect of critical temperature and working fluid classification (i.e., wet-wet, wet-dry) on the performance of the mixture. In their study, eight working fluids, including R134a, R245fa, R152a, Propane, Pentane, Isobutane, Hexane, and Cyclopropane are evaluated with respect to three different scenarios developed regarding the working fluid classification. Four different cycle operating conditions concerning various evaporation and condensation temperatures are prepared. Thermal efficiencies and net-work outputs of each mixture are calculated. Results show that zeotropic mixtures with high critical temperatures provide better performance compared to ones with low critical temperatures. Further, the mixing ratio and the selection of set temperatures for the evaporator and the condenser are reported as crucial parameters affecting the performance.

3. EXPERIMENTAL STUDY

3.1. Experimental ORC Setup

The test rig consists of on-skid (working fluid pump, oil pump, plate-type heat exchangers, throttle valve) and off-skid equipment (a scroll-type expander, chiller, electric heater, and an expansion vessel). A picture of the setup is given in Figure 3.1; the piping and instrumentation diagram (P&ID) of the ORC setup is given in Figure 3.2. Technical information on components and measurement equipment is provided in Table 3.1. The setup design allows using different hydrocarbons as working fluids in the test rig. The working fluid chosen for this study is R134a. Brazed-type plate heat exchangers evaporate and condense the working fluid. The heat transfer area of the condenser is 6.08 m^2, and the evaporator area is 7.41 m^2. All heat exchangers are thermally insulated with glass wool. A Speck Pumpen SK 2007-LL model side channel pump circulates the working fluid. The pump can pressurize liquid and little gas, transferring working fluid in both phases without damaging the pump's bearings due to dry running. The flow rate of the working fluid is controlled by adjusting the frequency of the electricity supplied to the pump motor by a frequency inverter.

The setup has a semi-hermetic scroll-type expander with 5-kWe capacity and an expander simulator line that utilizes a SAMSON 41-23 type throttle valve. A 100-kW electric heater is used to heat Atherma M32-type thermal oil circulated by a King CC-2214 model internal gear pump. A frequency inverter is used to control the oil mass flow rate. An air-cooled chiller with 100 kW capacity is used to supply cold-water to the condenser. The mass flow rate of water is controlled by globe valves mounted on the ORC grid.

Figure 3.1. The experimental 5 kWe ORC setup in BURET Lab.

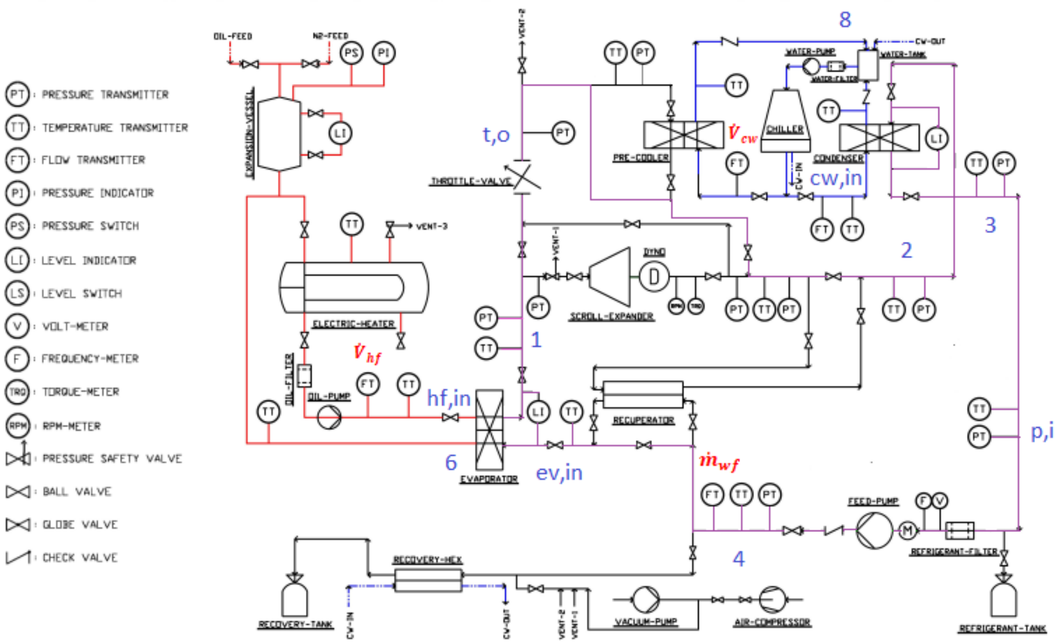

Figure 3.2. P&ID of the 5 kWe ORC test rig located at Sarıtepe Campus, Bogazici University.

Table 3.1. Characteristics of the equipment of the ORC test system.

Component	**Characteristic**	**Unit**	**Value**
PHEs	Model	-	MIT MB 09-H
	Number of plates (N_p)	-	80/66/50
	Dimensions (L x W)	mm	615 x 188
	Port diameter	mm	50
	Plate pitch/ thickness	mm	2.4/0.5
	Temperature range	℃	-196 to 200
	Material	-	Stainless steel (316L)
	Weight	kg	$4.6 + 0.41 * N_p$
	Heat transfer area	m^2	$(N_p - 2) * 0.095$
Refrigerant pump	Model	-	SK 2007-LL
	Nominal speed	rpm	1450
	Total absolute power	kW	2.87
	Flow rate range	m^3/h	0.2-3
	Head range	m	30-156
	Max. operating pressure	bar	26.18
	Material	-	Stainless steel (1.4122)
Internal gear oil pump	Model	-	CC-2214
	Nominal speed	rpm	1450
	Nominal power	kW	0.6
	Flow rate range	m^3/h	0-1
	NPSH	m	1.85
	Operational pressure	bar	3
	Operational temperature	℃	155
Throttle valve	Model	-	Samson 41-23
	Nominal size	-	DN 25
	Setpoint range	bar	4.5-10
	Dimensions	(L x H x ØD)	160 x 410 x 170
	Actuator area	mm^2	4000
	Max. operating temperature	℃	350
	Material	-	Stainless steel
Air-cooled chiller	Model	-	ERA-S 1072
	Compressor type	-	Hermetic scroll
	Evaporator type	-	Shell & tube
	Water volumetric flow rate	m^3/h	18.5
	Power supply	V/ phz/ Hz	400/3/50
	Air volumetric flow rate	m^3/h	34500
	Nominal power	kW	4

Ten pressure, thirteen temperature transmitters, and four flow meters (electromagnetic, vortex, and Coriolis) are installed on the ORC test setup. The transmitters' and flow meters' locations are shown on the P&ID given in Figure 3.2. In addition, the technical information on the sensors and measurement equipment is provided in Table 3.2.

Table 3.2. Technical information about sensors and measurement equipment.

Measurement	Type	#	Accuracy	Measurement range	Unit
$\dot{V}_{cw}$	Electromagnetic	1 1	∓0.4 % ∓0.4 %	0 – 90 0 – 270	m^3/h m^3/h
$\dot{m}_{wf}$	Coriolis	1	∓0.4 %	0 – 1	kg/s
$\dot{V}_{hf}$	Vortex	1	∓0.65 %	0 – 125	m^3/h
P_{wf}	Piezoresistive	6 4	∓0.1 % ∓0.1 %	0 – 10 0 – 40	bar bar
T_{cw}	RTD	2	∓0.5 ℃	0 – 60	℃
T_{wf}	RTD	5 4	∓0.5 ℃ ∓0.5 ℃	0 – 60 0 – 250	℃ ℃
T_{hf}	RTD	2	∓0.5 ℃	0 – 250	℃

3.2. Steady-State Experimental Results for Pure Fluids

In this section, the steady-state results evaluated at each measurement point of the ORC test rig are presented. All data are collected and stored using the 'IpeMotion' Ipetronics Data acquisition module at 1 Hz. During the tests, the hot oil set temperature varied between 80 and 110 ºC, while the oil pump speed, the refrigeration pump speed, cooling water temperature, cooling water flow rate and throttle valve outlet set pressure were fixed. The values used are tabulated in Table 3.3.

Table 3.3. Parameter values of the experiment.

Parameter	Value	Unit
Frequency of oil pump	40	Hz
Refrigerant pump speed	1050	rpm
Expander outlet set pressure	5.75	bar
Cooling water set temperature	4	℃
The flow rate of cooling water	8.6	m^3/h
Amount of R134a filled	19	kg

The whole test lasted approximately 6 h, and each steady-state operation of the cycle continued for at least 40 min. Four steady-state conditions are observed for hot oil set temperatures of 80, 90, 100, and 110 ºC. The hot oil set temperature of 80 ºC is used more than once to check the repeatability and the hot oil set temperature is changed seven times (80, 110, 80, 100, 80, 90, and 80 ºC) in the experiment.

A sudden and drastic change in pressure and temperature values is observed at the beginning of each transition period between steady states, but a new steady state is reached in several minutes.

Pre-processing of the data is crucial to identify the steady-state zones and correctly show the experimental data. Before filtering out the transient or non-steady data, the statistics of original datasets (minimum, maximum, mean values, and standard deviations) are determined for measured temperatures, pressure, and flow rates. Next, using the steady-state criterion of Woodland et al. [36], all the measured quantities are checked to determine whether they are within steady-state thresholds. If, the measured quantities are within the thresholds, then the data is in steady state. Moving windows (window length of 750 sec) is used to determine the steady-state regions.

Moving average means of temperature, pressure, and flow rates are calculated to avoid unwanted noise. The statistics on raw data & uncertainties are given in Appendix A, and the statistical values obtained by moving average means using a 750-second time window are provided in Table 3.4. The data in Table 3.4 are divided into four steady-state segments denoted by Exp-1, Exp-2, Exp-3, Exp-4. All steady-state data are compatible with the steady state criteria of Woodland et al. [36], which states that a cycle is Table operating at a steady state when the temperature fluctuates 0.5 K, and pressure, mass flow rate, and rotating equipment speed values are changed within the range of ±2%. The highest fluctuation is observed for the working fluid mass flow rate, 2.46% for Exp-1. All pressure, temperature, and flow rate measurements are within the threshold limits except for this.

The plots of moving-averaged means of measured quantities are given as a function of time in Figure 3.3 and Figure 3.4 for the whole experiment. They are plotted to see whether the experiment's steady-state conditions are reached as intended. A sample of raw data showing the temporal fluctuation of oil inlet temperature, cooling water inlet temperature, pressure at the throttle valve outlet, working fluid mass flow rate, oil volumetric flow rate, and cooling water volumetric flow rate measured at 100 ºC are plotted in Figure 3.5. The hot fluid (hot oil) temperature fluctuates around the set temperature as the heater goes on & off by the thermostat in a repeatable manner, as shown in the figure. Compatible with hot fluid inlet temperature fluctuations, all the other measurements fluctuate similarly even though the cycle operates in the steady state.

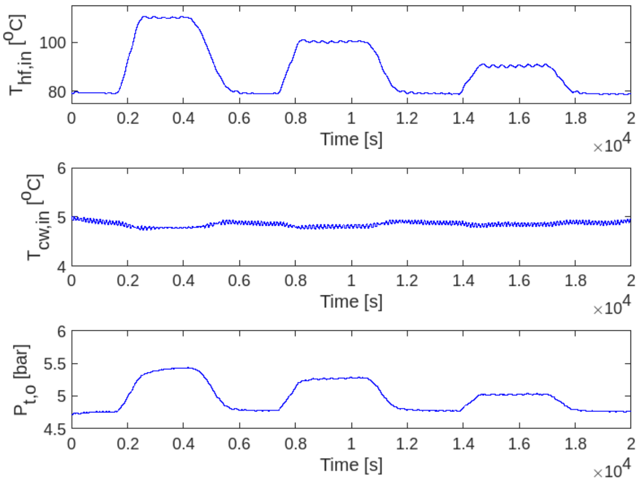

Figure 3.3. Detected steady-state zones for various heat source temperatures between 80-110 °C, the plot of $T_{hf,in}$, $T_{cw,in}$, $P_{t,o}$.

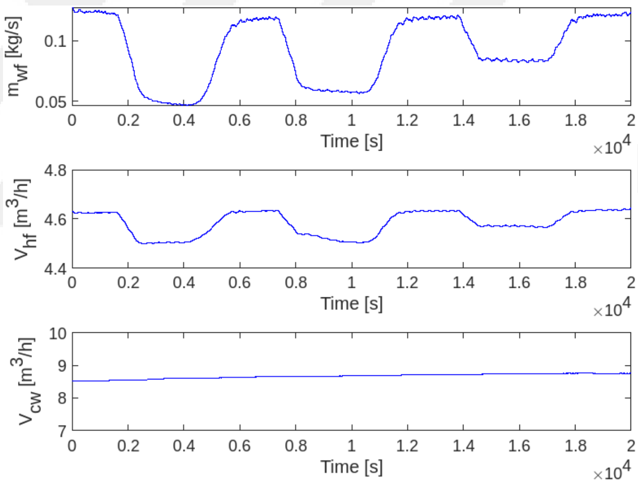

Figure 3.4. Detected steady-state zones for various heat source temperatures between 80-110 °C, the plot of $\dot{m}_{wf}$, $\dot{V}_{hf}$ and $\dot{V}_{cw}$, respectively.

Table 3.4. Data collected at four different heat source temperatures between 80-110 ℃ for a time window of 750sec.

Variable	Exp-1				Exp-2				Exp-3				Exp-4			
	Min	**Max**	**Ave**	σ	**Min**	**Max**	**Ave**	σ	**Min**	**Max**	**Ave**	σ	**Min**	**Max**	**Ave**	σ
$T_{pp,i}$(℃)	5.59	5.65	5.62	0.01	6.22	6.39	6.31	0.06	6.26	6.35	6.31	0.03	5.99	6.07	6.04	0.02
T_1(℃)	73.8	74.2	74.0	0.09	96.6	96.9	96.8	0.07	89.8	90.2	90.1	0.10	82.9	83.5	83.2	0.14
T_2(℃)	57.1	57.3	57.2	0.06	72.0	72.2	72.1	0.08	68.1	68.2	68.1	0.02	64.3	64.8	64.5	0.13
T_3(℃)	5.38	5.44	5.41	0.01	5.70	5.76	5.73	0.02	5.70	5.77	5.74	0.02	5.61	5.66	5.64	0.01
$T_{ev,in}$(℃)	12.39	12.53	12.46	0.03	20.45	22.48	21.61	0.65	19.85	20.38	20.13	0.17	15.86	16.23	16.08	0.12
$T_{cw,in}$(℃)	4.79	4.92	4.86	0.02	4.73	4.82	4.78	0.02	4.75	4.87	4.81	0.03	4.78	4.90	4.84	0.03
T_8(℃)	7.46	7.59	7.52	0.02	5.86	5.98	5.92	0.02	6.12	6.21	6.16	0.02	6.71	6.81	6.76	0.02
$T_{hf,in}$(℃)	78.5	79.6	79.1	0.25	109.4	110.6	110.0	0.31	99.6	100.5	100.1	0.27	89.4	90.7	90.1	0.37
T_6(℃)	66.3	67.1	66.7	0.19	104.0	104.9	104.5	0.21	93.1	94.3	93.8	0.27	80.8	82.0	81.4	0.33
T_4(℃)	12.28	12.42	12.35	0.03	20.74	22.53	21.76	0.58	19.76	20.24	20.01	0.16	15.70	16.03	15.90	0.10
$P_{pp,i}$(bar)	5.328	5.400	5.368	0.016	6.337	6.386	6.364	0.012	6.178	6.208	6.195	0.007	5.822	5.872	5.849	0.012
P_1(bar)	14.518	14.706	14.621	0.042	16.607	16.672	16.635	0.017	16.369	16.419	16.398	0.012	15.712	15.830	15.770	0.027
$P_{t,o}$(bar)	5.729	5.771	5.752	0.009	6.384	6.433	6.411	0.012	6.256	6.282	6.271	0.006	6.005	6.038	6.022	0.007
P_2(bar)	5.375	5.436	5.410	0.014	6.347	6.402	6.378	0.014	6.201	6.230	6.216	0.007	5.858	5.903	5.882	0.010
P_3(bar)	5.257	5.329	5.298	0.016	6.267	6.317	6.295	0.012	6.108	6.138	6.125	0.007	5.752	5.802	5.779	0.012
P_4(bar)	14.452	14.642	14.555	0.043	16.450	16.509	16.475	0.014	16.204	16.253	16.234	0.011	15.564	15.681	15.621	0.027
$\dot{m}_{wf}$(kg/s)	0.119	0.125	0.122	0.001	0.047	0.050	0.048	0.001	0.057	0.059	0.058	0.000	0.082	0.085	0.084	0.001
$\dot{V}_{hf}$(m^3/h)	4.61	4.63	4.62	0.00	4.500	4.509	4.505	0.002	4.50	4.51	4.50	0.002	4.56	4.57	4.57	0.00
$\dot{V}_{cw}$(m^3/h)	8.53	8.55	8.54	0.00	8.57	8.60	8.59	0.00	8.66	8.68	8.67	0.006	8.73	8.74	8.74	0.00

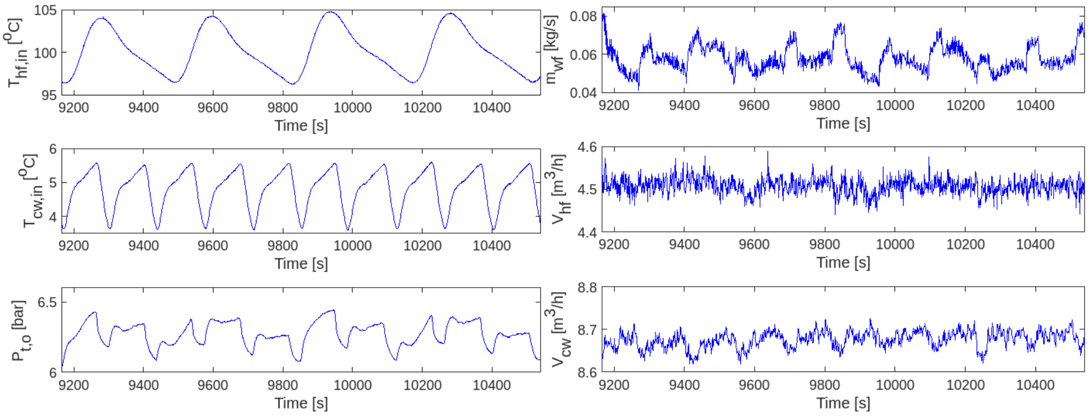

Figure 3.5. Reference steady state zone at 100 °C, for $T_{hf,in}$, $T_{cw,in}$ and $P_{t,o}$, $\dot{m}_{wf}$, $\dot{V}_{hf}$ and $\dot{V}_{cw}$ (Corresponding to Exp-3 on Figures 3 & 4).

3.3. Steady State Experimental Results for Refrigerant Mixtures

In this section, steady state results of tests with zeotropic mixture (R134a/R236fa) are presented. The results are provided at each measurement point of the ORC test set-up. The test data are collected and stored using data acquisition module at 1 Hz. The main aim of the test is to understand the effect of the zeotropic mixture on the ORC system performance. During the tests, the mass fraction of the mixture, the hot fluid (oil) inlet temperature set value, working fluid pump speed (rpm) and the oil pump frequency (Hz) are changed in different steps, while the throttle valve outlet set pressure, cooling water flow rate, cooling water temperature were fixed. The set values of the experiment are shown in Table 3.5. The experimental scenario that is prepared for the tests are provided in Table 3.6.

Table 3.5. Set values of the experiment.

Parameter	**Value**	**Unit**
Expander outlet set pressure	5.75	bar
Cooling water set temperature	2	°C
The flow rate of cooling water	8	m^3/h

Table 3.6. Experimental scenario of the zeotropic mixture tests.

Case No	**Total Mass (kg)**	**R134a (kg)**	**R236fa (kg)**	**R134a/R236fa**	$T_{hf,in}$ (℃)	**WF Pump Speed (rpm)**	**HF Pump Speed (Hz)**
1	20	20	0	1.0/0.0	90	1125	45
2	19	19	0	1.0/0.0	90	1125	45
3	18	18	0	1.0/0.0	90	1125	45
4	18	18	0	1.0/0.0	100	1125	45
5	17	17	0	1.0/0.0	100	1125	45
6	16	16	0	1.0/0.0	115	1125	50
7	15	15	0	1.0/0.0	115	1125	50
8	17	17	0	1.0/0.0	115	1125	45
9	17	17	0	1.0/0.0	115	1125	50
10	14	4.23	9.77	0.302/0.698	90	1050	50
11	15	5.23	9.77	0.348/0.652	90	1050	50
12	16	6.23	9.77	0.389/0.611	90	1050	50
13	16	6.23	9.77	0.389/0.611	100	1125	50
14	16	6.23	9.77	0.389/0.611	115	1125	50
15	17	7.23	9.77	0.425/0.575	115	1125	45
16	17	7.23	9.77	0.425/0.575	100	1125	45
17	17	7.23	9.77	0.425/0.575	90	1125	45
18	18	8.23	9.77	0.457/0.543	90	1125	45
19	18	8.23	9.77	0.457/0.543	100	1125	45
20	18	8.23	9.77	0.457/0.543	115	1125	45
21	19	9.23	9.77	0.485/0.515	115	1125	45
22	19	9.23	9.77	0.485/0.515	100	1125	45
23	19	9.23	9.77	0.485/0.515	90	1125	45
24	20	10.23	9.77	0.511/0.489	90	1125	45
25	20	10.23	9.77	0.511/0.489	100	1125	45
26	20	10.23	9.77	0.511/0.489	100	1050	45

The tests were completed in two days on 17/05/2024 and 24/05/2024 in a total of 13h. Each steady-state operation continued for at least 30 min for all 26 test cases (see Table 3.6). The steady-state conditions are obtained for varying compositions of the R236fa/R134a mixture while the hot fluid (oil) set temperatures are changed between 90 and 115 ºC. The working fluid pump speed of 1050 and 1125 rpm, and the oil pump frequencies of 45 and 50 Hz are also varied during the tests. Similar to the previous tests with pure fluid (R134a), a continuous test approach, which shows not only the steady states but also the transition periods between each steady state, is used for the experimental study with R134a/R236fa zeotropic mixture. In Figures 3.6 to 3.7, the steady-state zones with transition periods are provided for R134a/R236fa mixture for test cases range between Case-13 to 26.

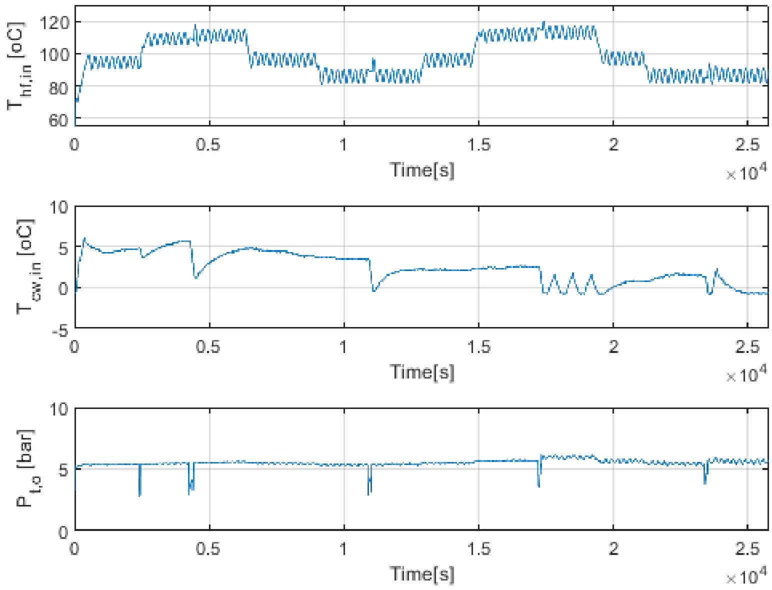

Figure 3.6. Detected steady-state zones of the tests with R134a/R236fa mixture, the plot of $T_{hf,in}$, $T_{cw,in}$ and $P_{t,o}$ (Case 13 to 26).

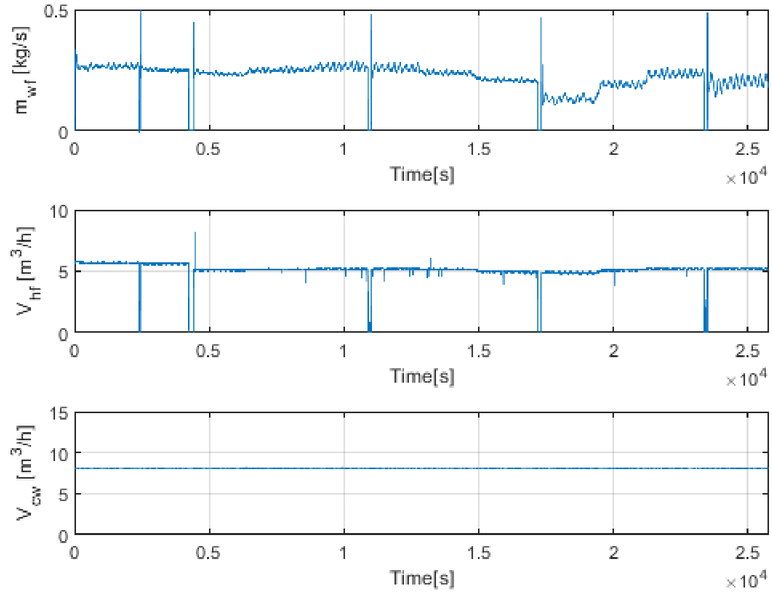

Figure 3.7. Detected steady-state zones of the tests with R134a/R236fa mixture, the plot of $\dot{m}_{wf}$, $\dot{V}_{hf}$ and $\dot{V}_{cw}$ (Case 13 to 26).

Before filtering out the transient or non-steady data, the statistics of original datasets (mean values and standard deviations) are determined for measured temperatures, pressure, and flow rates. Next, using the steady-state criterion of Woodland et al. [36], all the measured quantities are checked to determine whether they are within steady-state thresholds. If, the measured quantities are within the thresholds, then the data is in steady state. Figure 3.8 shows the variation of the selected experimental parameters for a reference steady-state case (Case-21). The steady-state test results for pure fluid cases and R236fa/R134a mixture with varying compositions are presented in Table 3.7 and Table 3.8 respectively.

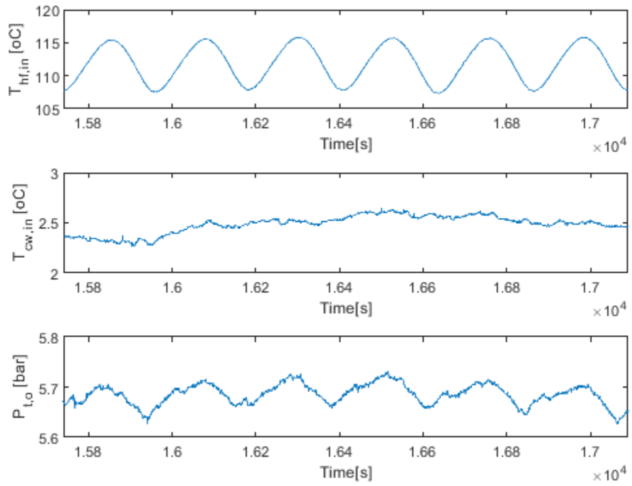

(a)

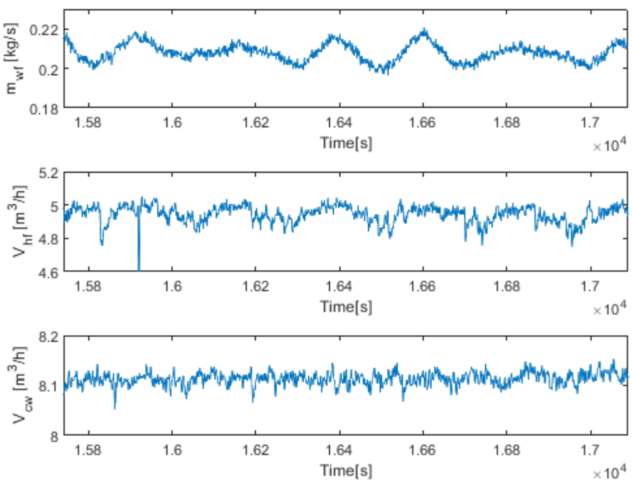

(b)

Figure 3.8. Reference steady state zone at 115 °C, for (a) $T_{hf,in}$, $T_{cw,in}$, $P_{t,o}$ and (b) $\dot{m}_{wf}$, $\dot{V}_{hf}$ and $\dot{V}_{cw}$ (Case 21).

Table 3.7. Original data collected at three different heat source temperatures between 90-115 °C (for pure R134a).

Variable	Case-1		Case-2		Case-3		Case-4		Case-5		Case-6		Case-7		Case-8		Case-9	
	Ave	**σ**	**Ave**	**σ**	**Ave**	**σ**	**Ave**	**σ**	**Ave**	**σ**	**Ave**	**σ**	**Ave**	**σ**	**Ave**	**σ**	**Ave**	**σ**
$T_{pp,i}$(°C)	2.6	0.63	2.4	0.33	3.3	0.27	2.6	0.03	4.6	0.46	5.0	0.26	6.5	0.35	5.0	0.75	5.0	0.75
T_1(°C)	82.3	1.41	80	3.10	74.3	3.55	89.0	2.75	89.0	3.26	102.5	2.45	103.4	1.94	102.5	0.84	102.5	0.84
T_2(°C)	61.6	0.57	64.1	1.45	58.7	2.48	73.1	1.50	74.5	1.84	88.0	1.53	89.0	1.07	88.0	1.44	88.0	1.44
T_3(°C)	1.7	0.88	1.8	0.31	2.8	0.27	2.2	0.03	4.2	0.48	4.6	0.26	5.6	0.40	4.6	0.56	4.6	0.56
$T_{ev,in}$(°C)	11.6	0.50	9.1	0.50	9.3	0.39	8.6	0.04	10.8	0.55	11.2	0.33	12.2	0.44	11.2	0.55	11.2	0.55
$T_{cw,in}$(°C)	0.7	1.10	0.5	0.28	1.6	0.24	1.0	0.04	2.8	0.49	3.1	0.27	2.9	0.54	3.1	0.0	3.1	0.0
T_8(°C)	3.9	0.96	5.1	0.23	6.4	0.23	6.0	0.04	7.7	0.41	8.4	0.23	8.2	0.43	8.4	1.01	8.4	1.01
$T_{hf,in}$(°C)	88.3	2.86	86.4	2.97	87.0	2.90	96.7	3.13	96.6	2.98	111.3	2.96	110.8	3.05	111.3	4.86	111.3	4.86
T_6(°C)	76.5	2.85	70.7	2.67	70.2	2.40	78.9	2.50	79.2	2.57	93.9	2.47	93.5	2.53	93.9	4.13	93.9	4.13
T_4(°C)	10.9	0.56	8.7	0.48	9.1	0.38	8.4	0.05	10.5	0.56	10.9	0.32	11.9	0.45	10.9	0.55	10.9	0.55
$P_{pp,i}$(bar)	5.495	0.186	4.785	0.075	4.956	0.051	4.637	0.031	4.602	0.054	4.543	0.031	4.401	0.051	4.543	0.083	4.543	0.083
P_1(bar)	16.399	0.376	14.657	0.203	14.157	0.169	14.389	0.099	14.284	0.127	14.276	0.084	14.171	0.116	14.276	0.280	14.276	0.280
$P_{t,o}$(bar)	5.833	0.114	5.636	0.021	5.590	0.015	5.625	0.010	5.617	0.012	5.631	0.007	5.507	0.011	5.631	0.020	5.631	0.020
P_2(bar)	5.520	0.178	4.935	0.063	4.781	0.042	4.829	0.025	4.813	0.044	4.792	0.025	4.656	0.041	4.792	0.054	4.792	0.054
P_3(bar)	5.421	0.187	4.714	0.075	4.527	0.050	4.567	0.031	4.533	0.053	4.473	0.030	4.331	0.050	4.473	0.084	4.473	0.084
P_4(bar)	16.310	0.362	14.601	0.197	14.119	0.164	14.324	0.097	14.215	0.124	14.178	0.083	14.070	0.113	14.178	0.279	14.178	0.279
$\dot{m}_{wf}$(kg/s)	0.122	0.012	0.173	0.008	0.185	0.007	0.179	0.004	0.179	0.005	0.177	0.004	0.174	0.004	0.177	0.016	0.177	0.016
$\dot{V}_{hf}$(m^3/h)	5.180	0.024	5.180	0.029	5.150	0.037	5.050	0.037	5.040	0.042	5.290	0.050	5.270	0.054	5.290	0.029	5.290	0.029
$\dot{V}_{cw}$(m^3/h)	8.010	0.025	8.010	0.012	7.910	0.016	7.880	0.012	7.920	0.015	7.690	0.013	7.550	0.015	7.690	0.034	7.690	0.034

Table 3.8. Original data collected at three different heat source temperatures between 90-115 ℃ (for R236fa/R134a mixture with varying composition).

Variable	Case-10		Case-11		Case-12		Case-13		Case-14		Case-15		Case-16		Case-17		Case-18	
	Ave	σ	Ave	σ	Ave	σ	Ave	σ	Ave	σ	Ave	σ	Ave	σ	Ave	σ	Ave	σ
$T_{pp,i}$(℃)	8.7	0.45	3.1	0.33	2.8	0.61	6.0	0.13	6.4	0.30	4.8	0.38	5.6	0.12	5.2	0.09	3.5	0.17
T_1(℃)	55.3	0.67	54.3	0.56	58.5	0.77	61.9	0.52	74.7	1.56	80.7	1.93	64.3	1.48	60.3	0.85	60.9	1.01
T_2(℃)	31.5	1.82	29.4	1.70	29.4	2.22	42.9	1.44	59.8	1.11	65.4	1.31	47.5	1.53	33.0	2.12	33.8	2.30
T_3(℃)	7.7	0.62	2.7	0.44	2.4	0.66	5.8	0.14	6.2	0.30	4.5	0.41	5.4	0.12	4.9	0.10	3.2	0.17
$T_{ev,in}$(℃)	11.3	0.62	6.6	0.26	6.7	0.60	10.3	0.14	10.9	0.33	9.6	0.40	10.3	0.12	9.6	0.10	8.0	0.22
$T_{cw,in}$(℃)	3.3	0.77	0.3	0.35	0.6	0.61	4.4	0.15	5.2	0.30	3.6	0.43	4.2	0.16	3.5	0.05	2.0	0.16
T_8(℃)	8.7	0.74	5.9	0.35	6.3	0.61	9.9	0.14	10.8	0.29	9.1	0.40	9.7	0.14	8.9	0.05	7.4	0.16
$T_{hf,in}$(℃)	86.1	2.89	85.5	2.78	85.3	2.82	95.0	2.47	109.1	2.46	111.4	2.58	96.3	2.74	86.3	2.85	86.3	2.90
T_6(℃)	68.9	2.33	67.9	2.27	67.4	2.32	76.9	2.14	90.7	2.12	91.3	2.21	77.0	2.33	67.4	2.31	67.4	2.44
T_4(℃)	11.2	0.66	6.4	0.30	6.6	0.61	10.1	0.15	10.7	0.33	9.4	0.40	10.1	0.13	9.4	0.12	7.9	0.21
$P_{pp,i}$(bar)	2.827	0.079	2.793	0.044	3.030	0.081	3.517	0.039	3.786	0.041	4.113	0.055	3.891	0.068	3.549	0.093	3.808	0.131
P_1(bar)	9.230	0.198	9.361	0.182	10.872	0.274	11.681	0.173	12.394	0.098	13.133	0.125	12.421	0.194	11.670	0.322	12.169	0.376
$P_{t,o}$(bar)	5.077	0.023	5.089	0.023	5.244	0.027	5.357	0.015	5.458	0.015	5.554	0.017	5.467	0.024	5.334	0.046	5.402	0.043
P_2(bar)	3.490	0.035	3.487	0.034	3.630	0.052	3.908	0.023	4.131	0.033	4.399	0.045	4.205	0.051	3.924	0.070	4.103	0.099
P_3(bar)	2.755	0.075	2.716	0.043	2.954	0.081	3.443	0.038	3.712	0.039	4.039	0.055	3.818	0.068	3.475	0.093	3.734	0.130
P_4(bar)	9.469	0.191	9.583	0.175	11.041	0.265	11.827	0.164	12.460	0.093	13.147	0.119	12.484	0.185	11.790	0.312	12.265	0.360
$\dot{m}_{wf}$(kg/s)	0.274	0.012	0.273	0.012	0.277	0.010	0.265	0.006	0.250	0.004	0.236	0.004	0.251	0.006	0.265	0.011	0.257	0.011
$\dot{V}_{hf}$(m^3/h)	5.650	0.074	5.700	0.049	5.730	0.030	5.670	0.024	5.610	0.022	5.090	0.021	5.150	0.025	5.190	0.033	5.190	0.046
$\dot{V}_{cw}$(m^3/h)	7.890	0.020	7.830	0.013	7.810	0.013	8.120	0.013	8.130	0.013	8.110	0.014	8.130	0.013	8.130	0.012	8.130	0.011

Table 3.8. Original data collected at three different heat source temperatures between 90-115 ℃ (for R236fa/R134a mixture with varying composition). (cont.)

Variable	Case-19		Case-20		Case-21		Case-22		Case-23		Case-24		Case-25		Case-26	
	Ave	**σ**	**Ave**	**σ**	**Ave**	**σ**	**Ave**	**σ**	**Ave**	**σ**	**Ave**	**σ**	**Ave**	**σ**	**Ave**	**σ**
$T_{pp,i}$(℃)	3.7	0.02	4.0	0.07	2.6	0.51	2.3	0.31	3.2	0.07	1.9	0.55	4.0	1.79	10.3	0.88
T_1(℃)	67.0	2.34	94.4	2.79	105.4	1.39	88.7	3.32	63.6	1.24	73.2	5.67	83.8	1.89	84.3	1.37
T_2(℃)	49.8	1.63	79.0	1.69	86.8	0.57	72.9	1.69	40.5	2.75	53.1	3.69	54.3	2.47	41.8	1.58
T_3(℃)	3.4	0.02	3.6	0.07	1.7	0.60	1.8	0.33	2.8	0.07	1.3	0.54	1.9	0.59	4.3	0.68
$T_{ev,in}$(℃)	8.6	0.05	9.8	0.09	11.9	0.53	8.8	0.27	8.4	0.10	8.3	0.73	12.2	3.28	309	1.64
$T_{cw,in}$(℃)	2.1	0.03	2.4	0.09	-0.1	0.74	0.5	0.34	1.6	0.08	-0.2	0.51	-0.7	0.01	0.0	0.89
T_8(℃)	7.6	0.04	7.8	0.09	3.5	0.67	5.3	0.33	6.7	0.09	4.6	0.42	0.1	1.48	0.4	1.16
$T_{hf,in}$(℃)	96.4	2.82	111.9	2.71	113.1	2.83	96.7	2.93	86.4	2.95	86.9	2.91	99.4	2.72	101.5	2.28
T_6(℃)	77.3	2.36	92.2	2.24	100.0	2.87	79.7	2.53	68.7	2.45	70.7	2.71	93.9	7.19	99.3	2.13
T_4(℃)	8.4	0.05	9.5	0.09	11.4	0.61	8.4	0.30	8.1	0.11	7.9	0.75	13.6	4.41	33.2	1.36
$P_{pp,i}$(bar)	4.139	0.087	4.540	0.056	5.528	0.174	4.707	0.193	4.196	0.198	4.714	0.302	6.997	0.542	7.065	0.104
P_1(bar)	13.043	0.214	14.279	0.153	16.926	0.341	14.858	0.373	13.197	0.449	14.580	0.735	19.312	0.873	17.604	0.104
$P_{t,o}$(bar)	5.504	0.034	5.685	0.019	5.944	0.110	5.645	0.097	5.457	0.096	5.612	0.115	7.002	0.413	6.998	0.099
P_2(bar)	4.378	0.070	4.762	0.046	5.635	0.164	4.898	0.173	4.421	0.167	4.853	0.262	6.988	0.519	7.021	0.103
P_3(bar)	4.065	0.087	4.466	0.055	5.453	0.174	4.631	0.193	4.123	0.198	4.639	0.302	6.926	0.543	6.988	0.104
P_4(bar)	13.079	0.205	14.222	0.147	16.747	0.332	14.762	0.362	13.318	0.430	14.546	0.706	19.136	0.852	17.450	0.099
$\dot{m}_{wf}$(kg/s)	0.239	0.005	0.209	0.005	0.133	0.010	0.192	0.009	0.234	0.010	0.200	0.018	0.032	0.037	0.025	0.003
$\dot{V}_{hf}$(m^3/h)	5.150	0.034	4.950	0.063	4.890	0.046	5.090	0.061	5.190	0.031	5.190	0.025	5.080	0.086	5.010	0.033
$\dot{V}_{cw}$(m^3/h)	8.110	0.014	8.110	0.012	8.070	0.019	8.080	0.014	8.100	0.012	8.080	0.014	8.040	0.043	8.060	0.026

Relative standard uncertainty analysis is also conducted for pressure, temperature, and flow rate measurements. Relative standard uncertainties of each experimental cases are calculated with respect to original data set (see Table A.4). The highest relative uncertainties are observed for mass flow rates at the refrigerant pump outlet with maximum 9.03% for Case-24, and the pressure at the condenser outlet & pump inlet for both pure R134a cases (Case-1 to 9), and R236fa/R134a mixture cases (Case-10 to 24). Except these, the relative standard uncertainties of all measurement points are compatible with the sensor accuracy values. The results clearly show that the original experimental data set is statistically reliable and can be used to test the model validation without any post-processing (i.e., moving average mean).

Due to the zeotropic behavior of R236fa/R134a blend, the operating conditions of the working fluid pump changes. The change in operation regime especially becomes more visible for the zeotropic mixture components with different densities. The experimental test results are also significant as it shows the operation of the working fluid pump for the refrigerant mixtures. Figure 3.9 shows the pump characteristic ($\mathrm{DP} - \dot{\mathrm{m}}_{\mathrm{wf}}$) curves for both pure R134a and R236fa/R134a zeotropic mixture. Pump characteristic curves for pure R134a and R236fa/R134a mixture are respectively obtained by using third and fourth-order polynomial fit to the experimental data.

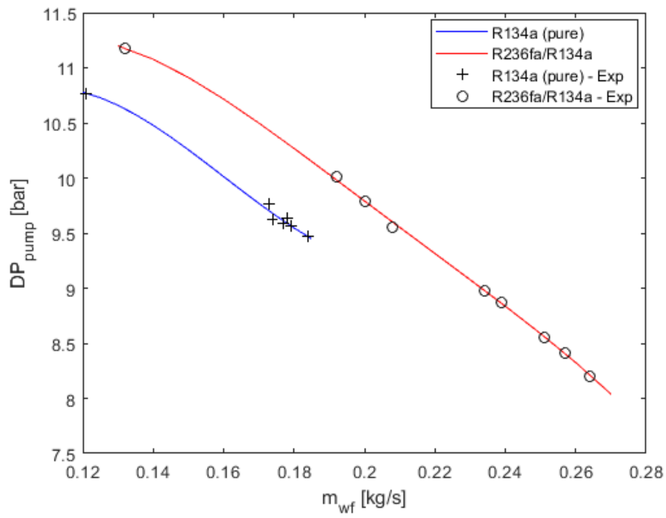

Figure 3.9. Working fluid pump characteristic curves for R134a (pure) and R236fa/R134a mixture at 1150 rpm ($\mathrm{DP}_{\mathrm{pump}} - \dot{\mathrm{m}}_{\mathrm{wf}}$).

4. ORC MODEL FOR PURE FLUIDS AND MIXTURES

4.1. ORC Model for Pure Fluids

In this section, an interconnected steady-state model of the ORC setup is built. Starting from sub-models that include a detailed heat exchanger model, a pump characteristic curve, and a throttle valve model coupled with pipe elements that allow heat and pressure losses. First, component models will be discussed.

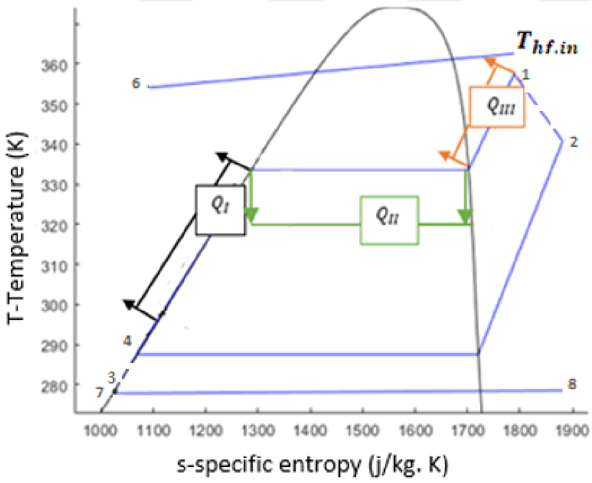

Figure 4.1. The cycle T-s diagram shows the evaporator zones defined concerning the refrigerant phase (Zone I: subcooled liquid, Zone II: liquid-vapor mixture, Zone III: superheated vapor,

$T_7 = T_{cw,in}$.

4.1.1. Heat Exchanger Model

The heat exchanger is divided into three zones (subcooled, two-phase, and superheated) regarding the state of refrigerant flowing inside (see Figure 4.1). The fluid properties in single-phase zones (sub-cooled and superheated) are evaluated at mean temperature values of the inlet and outlet of each region. Using the LMTD method, each single-phase region's required heat transfer area is accurately calculated. In the two-phase zone, fluid properties change drastically due to change in the mixture quality.

Therefore, the two-phase region is divided into smaller segments where fluid properties can be assumed constant. The size of each segment is adjusted to give the same enthalpy change.

The properties are calculated by knowing each segment's enthalpy and pressure values. Properties of the working fluid and cooling water are obtained by using REFPROP v9.1 software [35]. The schematic representation of the plate-type heat exchanger is shown in Figure 4.2. The geometrical information of PHEs available in BURET laboratory is provided in Table 4.1.

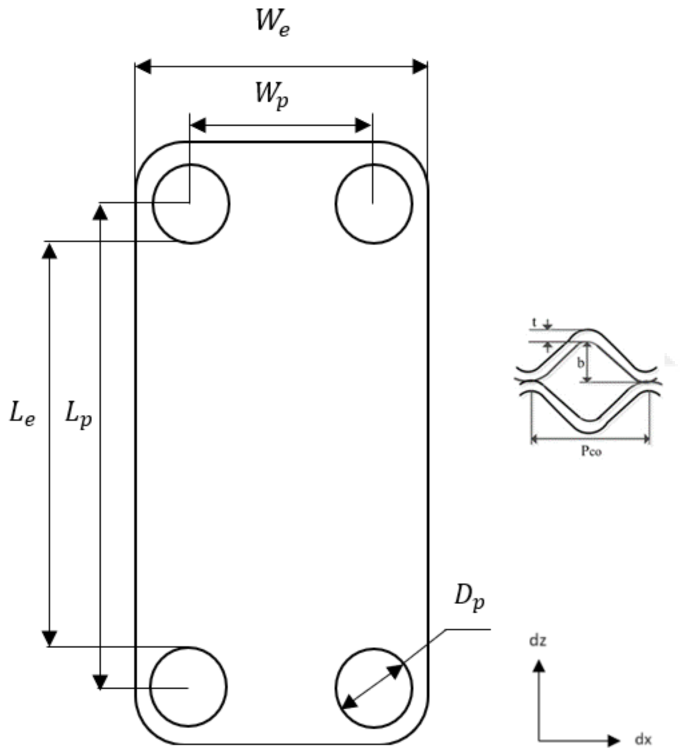

Figure 4.2. Schematic of plate-type heat exchanger.

Table 4.1. Geometrical values of the evaporator and condenser of the ORC set-up.

Geometrical Values	**Unit**	**Evaporator**	**Condenser**
Heat exchanger length (L)	m	0.615	0.615
Heat exchanger width (W)	m	0.188	0.188
Port diameter (D_p)	m	0.05	0.05
Port to port length (L_p)	m	0.519	0.519
Port to port width (W_p)	m	0.092	0.092
Effective length (L_e)	m	0.469	0.469
Effective width (W_e)	m	0.142	0.142
Corrugation pitch (P_{co})	m	0.00658	0.00658
Plate thickness (t)	mm	0.4	0.4
Plate pitch (p)	mm	1.4	1.4
Mean plate spacing (b)	mm	1	1
Chevron angle (β)	°	60	60
Total number of plates (N_p)	-	80	66

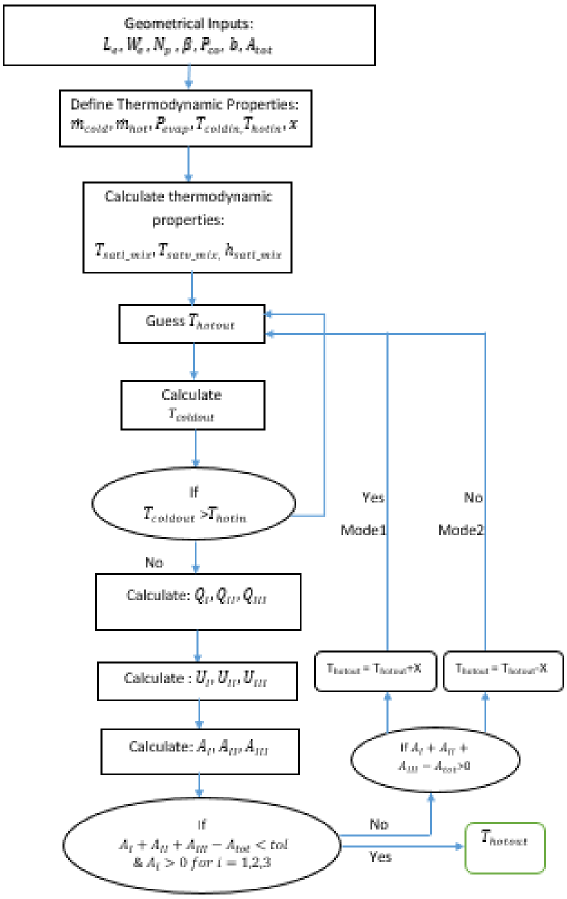

Figure 4.3. Flowchart of the heat exchanger model.

The geometrical properties of the heat exchangers, including chevron angle, length, width, port diameter, plate spacing, corrugation pitch, and the number of plates, are introduced in the model. The heat exchanger model uses an iterative process.

First, the total heat transfer area for the evaporator and the condenser are calculated using the mass flow rate of hot oil, working fluid and cooling water, evaporation pressure, evaporation temperature, and setting the initial oil outlet temperature for the evaporator and cooling water outlet temperature for the condenser. Then, the outlet temperatures are changed iteratively to match the calculated heat transfer areas to the actual equipment heat transfer areas of the evaporator and the condenser with a small tolerance. The flowchart of the heat exchanger model is shown in Figure 4.3.

Chisholm and Wanniarachchi correlations, valid for chevron-type heat exchangers, are used in single-phase regions calculations. For the two-phase regions, Han et al. correlations are used [38, 41].

In the calculations, the working fluid side of the evaporator is divided into three regions as follows: subcooled region (SPR1), two-phase region (TPR), and superheated region (SPR2). The heat source of the evaporator is Atherma M32 type thermal oil. The properties of working fluid and oil are determined by REFPROP v9.1 and the technical data sheet of Atherma M32 thermal oil (see Table 4.2) , respectively. Then, adopting the numerical strategy summarized in Figure 3.7, the heat transfer processes in each region are modeled. For single-phase regions (including subcooled and superheated regions), the heat transfer can be modeled directly by the LMTD method. However, for the two-phase regions, it is required to divide the region into an adequate number of sub-regions to adopt the LMTD method.

LMTD methodology equations can be given as

$$A_{tot,req} = \sum A_i \quad A_i = \frac{\dot{Q}_i}{U_i LMTD_i}, \tag{4.1}$$

$$LMTD_i = \frac{\left(T_{hotin,i} - T_{coldout,i}\right) - \left(T_{hotout,i} - T_{coldin,i}\right)}{ln\left(\frac{T_{hotin,i} - T_{coldout,i}}{T_{hotout,i} - T_{coldin,i}}\right)}, \tag{4.2}$$

$$\frac{1}{U_i} = \frac{1}{\alpha_{cold,i}} + \frac{t_p}{k_p} + \frac{1}{\alpha_{hot,i}}, \tag{4.3}$$

where α and k_p are convective heat transfer coefficient and plate thermal conductivity, respectively.

In the calculations, t_p/k_p the term is negligibly small $(t_p/k_p \approx 0)$, so it can be neglected. The correlations needed to calculate the heat transfer area and the pressure drop in the PHEs are summarized below.

Table 4.2. Technical data sheet of Atherma M32 type heat transfer oil.

Temp. (°C)	$\boldsymbol{\rho_{hf}}$ $(\boldsymbol{kg/m^3})$	$\boldsymbol{c_{p,hf}}$ $(\boldsymbol{kj/kg.K})$	$\boldsymbol{k_{hf}}$ $(\boldsymbol{W/m.K})$	$\boldsymbol{Pr_{hf}}$ (-)
0	871	1.962	0.136	3451
20	858	2.049	0.135	1003
40	845	2.137	0.133	393
100	804	2.400	0.129	76
150	773	2.619	0.125	37
200	741	2.838	0.121	24
250	708	3.058	0.118	18
300	676	3.277	0.114	15
340	651	3.452	0.111	14

4.1.1.1. Single Phase Regions: Correlations for Subcooled and Superheated Regions. Chisholm and Wanniarachchi et al.'s correlation is selected to calculate the Nusselt number.

Nusselt number in single phase regions can be calculated by [37]

$$Nu_{sp} = \frac{D_h \alpha}{k_f} = 0.724 \left(\frac{6\beta}{\pi}\right)^{0.646} Re^{0.583} Pr^{0.33} , \tag{4.4}$$

where β is chevron angle in rad, Re is the Reynolds number, and Pr is the Prandtl number.

Reynolds and Prandtl numbers can be calculated by

$$Re = \frac{GD_h}{\mu} \; ; \; Pr = \frac{c_p \mu}{k_f} , \tag{4.5}$$

where G, μ, and c_p are mass velocity, dynamic viscosity, and constant pressure-specific heat, respectively. To calculate the working fluid properties, the bulk temperatures at each region's inlet and the outlet are averaged.

Mass velocity G is the channel mass flow rate per cross-sectional area, and can be determined as

$$G = \frac{\dot{m}}{N_{ch} b W_e} \, . \tag{4.6}$$

The frictional pressure drop is considered for the pressure drop calculations in subcooled and superheated regions which can be calculated by [39, 40]

$$\Delta P_{sp} = \frac{4 f_{sp} N_{ch} G^2 L_r}{2 \rho D_h} \, , \tag{4.7}$$

where L_r is the length of the region along with the flow direction, and f_{sp} is the fanning friction factor which can be calculated as

$$f_{sp} = \frac{0.572}{Re^{0.217}} \; for \; Re > 550 \, . \tag{4.8}$$

<u>4.1.1.2. Two-Phase Region Correlations (For Evaporator).</u> The two-phase region is divided into a small number of regions, j, in such a way that the change of enthalpy would be negligibly small to assume constant properties. In the calculation of the Nusselt number Han et al.'s correlation is used [38].

Han et al.'s correlations for two-phase region are

$$Nu_{tp,j} = \frac{D_h \alpha}{k_l} = Ge_1 Re_{eq,j}^{Ge_2} Bo_{eq,j}^{0.3} Pr_l^{0.4} \, , \tag{4.9}$$

$$Ge_1 = 2.81 \left(\frac{P_{co}}{D_h}\right)^{-0.041} \left(\frac{\pi}{2} - \beta\right)^{-2.83} , \tag{4.10}$$

$$Ge_2 = 0.746 \left(\frac{P_{co}}{D_h}\right)^{-0.082} \left(\frac{\pi}{2} - \beta\right)^{0.61} , \tag{4.11}$$

where Prandtl number Pr_l is calculated by using saturated liquid properties, and P_{co} is the plate corrugation pitch for a given geometry.

The Reynolds and Boiling numbers required for the two-phase region can be evaluated by

$$Re_{eq,j} = \frac{G_{eq,j} D_h}{\mu_l} \ ; \quad Bo_{eq,j} = \frac{q_j''}{G_{eq,j} h_{lg}} \ , \tag{4.12}$$

where G_{eq}, q_j'', and h_{lg} are equivalent mass flux, heat flux, and enthalpy of vaporization, respectively.

The equivalent mass flux can be computed by

$$G_{eq,j} = G\left[1 - q_j + q_j\left(\frac{\rho_l}{\rho_g}\right)\right] . \tag{4.13}$$

Herein q, ρ_l, and ρ_g are the selected working fluid's quality, liquid, and vapor density. The pressure drop in the two-phase region is related to the friction losses, elevation change, acceleration of the working fluid, and inlet and outlet flow port losses.

The friction factor in the two-phase region during the condensation, is calculated by Han et al.'s correlation which can be calculated by [38]

$$f_{tp,j,ev} = Ge_3 Re_{eq}^{Ge_4}, \tag{4.14}$$

$$Ge_3 = 64710\left(\frac{P_{co}}{D_h}\right)^{-5.27}\left(\frac{\pi}{2} - \beta\right)^{-3.03}, \tag{4.15}$$

$$Ge_4 = -1.314\left(\frac{P_{co}}{D_h}\right)^{-0.62}\left(\frac{\pi}{2} - \beta\right)^{-0.47}. \tag{4.16}$$

<u>4.1.1.3. Two-Phase Region Correlations (For Condenser).</u> The two-phase region is divided into a small number of regions, j, like in the evaporator.

Nusselt number during condensation can be calculated by [41]

$$Nu_{tp,j} = \frac{D_h \alpha}{k_l} = Ge_5 Re_{eq,j}^{Ge_6} Pr_l^{0.33} \ , \tag{4.17}$$

$$Ge_5 = 11.22\left(\frac{P_{co}}{D_h}\right)^{-2.83}\left(\frac{\pi}{2} - \beta\right)^{-4.5}, \tag{4.18}$$

$$Ge_6 = 0.35 \left(\frac{P_{co}}{D_h}\right)^{0.23} \left(\frac{\pi}{2} - \beta\right)^{1.48} . \tag{4.19}$$

The friction factor in the two-phase region during the condensation is calculated by Han et al.'s correlation which can be defined as [41]

$$f_{tp,j,cd} = Ge_7 Re_{eq}^{Ge_8} , \tag{4.20}$$

$$Ge_7 = 3521.1 \left(\frac{P_{co}}{D_h}\right)^{4.17} \left(\frac{\pi}{2} - \beta\right)^{-7.75} , \tag{4.21}$$

$$Ge_8 = -1.024 \left(\frac{P_{co}}{D_h}\right)^{0.0925} \left(\frac{\pi}{2} - \beta\right)^{-1.3} . \tag{4.22}$$

Pressure drop due to friction loss can be evaluated by

$$\Delta P_{fr,j} = \frac{f_{tp,j} N_{ch} {G_{eq}}^2 L_{r,j}}{\rho_l D_h} . \tag{4.23}$$

Port pressure drop is determined by

$$\Delta P_{port} = 1.4 \frac{G_{port}^2}{2\rho_{mean}} \; ; \; \rho_{mean} = \left(\frac{x}{\rho_g} + \frac{1-x}{\rho_l}\right)^{-1} , \tag{4.24}$$

where G_{port} is the port mass velocity and determined as

$$G_{port} = \frac{4\dot{m}_{eq}}{\pi D_p^2} \; ; \quad \dot{m}_{eq} = \dot{m}_{wf} \left[1 - x + x\left(\frac{\rho_l}{\rho_g}\right)^{0.5}\right] . \tag{4.25}$$

Pressure drop due to elevation is obtained by

$$\Delta P_{ele,j} = \rho_m g L_{r,j} . \tag{4.26}$$

Pressure drop due to acceleration is obtained by

$$\Delta P_{acc} = \left(\frac{G_{eq}^2 x}{\rho_l - \rho_g}\right)_{in} - \left(\frac{G_{eq}^2 x}{\rho_l - \rho_g}\right)_{out} . \tag{4.27}$$

Pressure drop in a two-phase region can be calculated via

$$\Delta P_{tp} = \Delta P_{fr} + \Delta P_{port} + \Delta P_{ele} + \Delta P_{acc} \,. \tag{4.28}$$

Total pressure drop across the heat exchanger can be evaluated by

$$\Delta P_{Hex} = \Delta P_{sp} + \Delta P_{tp} \,. \tag{4.29}$$

4.1.2. Refrigerant pump model

The characteristic curve of the SK2007-LL model side channel pump shown in Figure 4.4 is used in the refrigerant pump model. A fourth-order polynomial is fitted to the pump efficiency-volumetric flow rate data, and a third-order polynomial is fitted to the pressure-volumetric flow rate data.

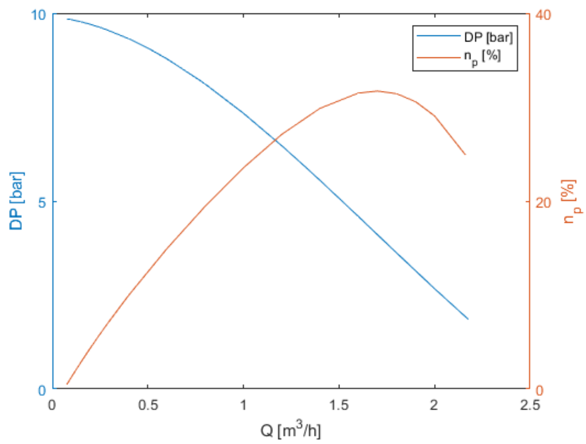

Figure 4.4. Pump characteristic curve of the refrigerant pump.

4.1.3. Pipe Heat Transfer Models

Heat transfer in the pipe is calculated with respect to resistance model which can be evaluated by [44]

$$U_p = 1/(R_i + R_p + R_{ins} + 1/h_{air}) \,, \tag{4.30}$$

where R_i, R_p, and R_{ins} are the resistance of the inner cylinder, between the inner and outer radius and outer surface to insulation which are given as

$$R_i = \frac{1}{h_{conv,wf}\pi r_i L_p}\,, \tag{4.31}$$

$$R_p = \frac{r_{ins} log(r_o/r_i\,)}{2\pi k_p L_p}\,, \tag{4.32}$$

$$R_{ins} = \frac{r_{ins} log(r_{ins}/r_o\,)}{2\pi k_p L_p}\,, \tag{4.33}$$

$$R_o = \frac{1}{h_{air}\pi r_{ins} L_p}\,. \tag{4.34}$$

Convective loss between the outer surface and the environment is

$$h_{air} = h_{rad} + (Nu_{comb} k_{air}/r_{ins})\,, \tag{4.35}$$

where the combined Nusselt number is

$$Nu_{comb} = \left(Nu_{forced}^4 + Nu_{free}^4\right)^{0.25}\,. \tag{4.36}$$

Churchill and Bernstein's correlation used for the heat transfer from forced convection which can be calculated by [42]

$$Nu_{forced} = 0.3 + \left[\frac{0.62 {Re_{air}}^{0.5} {Pr_{air}}^{1/3}}{(1 + 0.4 Pr_{air})^{2/3}}\right]^{0.25} \left[1 + (Re_{air}/282000)^{5/8}\right]^{0.8}\,. \tag{4.37}$$

Churchill and Chu's correlation for the heat transfer from free convection is [43]

$$Nu_{free} = \left[\frac{\left(0.6 + 0.387 {Ra_{air}}^{1/6}\right)}{\left(1 + 0.559 {Pr_{air}}^{9/16}\right)^{8/27}}\right]^2\,. \tag{4.38}$$

Convective heat transfer coefficient of the fluid in the pipe, $h_{conv,wf}$ can be calculated by

$$h_{conv,wf} = \frac{Nu_{wf} k_{wf}}{D_h} \text{for } Re_{wf} \geq 3000\,, \tag{4.39}$$

$$h_{conv,wf} = \frac{4.36k_{wf}}{D_h} \text{ for } Re_{wf} < 3000\,. \quad (4.40)$$

Nusselt number of the working fluid at turbulent flow, Nu_{wf} can be calculated by Gnielinski correlation which can be defined as [44]

$$Nu_{wf} = \frac{(f/8)\left(Re_{wf} - 1000\right)Pr_{wf}}{\left(1 + 12.7(f/8)^{0.5}\left({Pr_{wf}}^{2/3} - 1\right)\right)}\left(1 + \left(r_i/L_p\right)^{2/3}\right)\left(Pr_{wf}/Pr_w\right)^{0.11}, \quad (4.41)$$

which is valid for $3000 \leq Re_{wf} \leq 5 \times 10^6$ and 0.5$\leq Pr_{wf} \leq 2000$), and Pr_w is the wall Prandtl number, r_i and L_p are inner radius and pipe length, respectively, and f is pipe friction coefficient which is calculated via

$$f = \left(0.79ln\left(Re_{wf}\right) - 1.64\right)^{-2}. \quad (4.42)$$

Finally, the heat transfer and the temperature drop due to heat transfer in the pipe are

$$\dot{Q}_p = U_p(T_e - T_s)\,, \quad (4.43)$$

$$\Delta T_p = \frac{Q_p}{c_p\dot{m}_{wf}}\,, \quad (4.44)$$

where T_e is environmental temperature, T_s is surface temperature of the pipe.

4.1.4. Pipe Pressure Drop Model

In the calculation of pipe pressure drop, there are two types of losses affecting the pressure drop in the pipe section: major loss stemming from pipe friction and minor losses for each connection element (i.e., valve, tee, and elbow).

Total pressure drop can be expressed as

$$\Delta P_p = \Delta P_{maj} + \Delta P_{min}\,. \quad (4.45)$$

Pipe major pressure loss due to Darcy friction factor can be calculated by

$$\Delta P_{maj} = \frac{f_D L_p \rho_{wf} v_p^2}{2D_h}\,, \tag{4.46}$$

where L_p, ρ_{wf}, v_p and D_h are pipe length, the density of the working fluid, the velocity of working fluid in the pipe section, and the hydraulic diameter of the pipe, respectively, whereas f_D term is the darcy friction factor which can be found iteratively by using [45]

$$f_D = \frac{64}{Re_{wf}} \text{for } Re_{wf} < 2300\,. \tag{4.47}$$

Colebrook equation for pipelines in turbulent flow ($\epsilon = 5 \times 10^{-6}$) is [46]

$$f_{D,i+1} = \left\{-2ln\left(\frac{\epsilon}{3.7D_h} + \frac{2.51}{Re_{wf}\sqrt{f_{D,i}}}\right)\right\}^{-2} \quad \text{for } Re_{wf} < 4000\,. \tag{4.48}$$

Pipe minor pressure loss due to each connection element can be calculated by

$$\Delta P_{min} = \frac{\sum_i n_i\, K_i {v_p}^2 \rho_{wf}}{2}\,, \tag{4.49}$$

where K_i, represent the resistance coefficients for pipe entrances, exits, and connecting elements (i.e., tees, elbows, valves), and n_i represent the number of connecting elements in the pipe section.

4.2. ORC Model for Refrigerant Mixtures

The ORC model for the refrigerant mixtures is introduced in this chapter. Like the model for pure fluids, the ORC model for refrigerant mixtures includes a detailed heat exchanger model for PHEs, and connection pipes. The model uses isentropic efficiency models for the refrigerant pump and the expander. A modified form of the PHE model of the pure fluids is used to calculate the mixture properties and the temperature glide in the two-phase region of the heat exchanger. The fluid screening criteria and the selected refrigerant mixtures are provided in this chapter. The vapor and liquid phase properties of the selected mixtures are determined by using Refprop v9.1. Mixture property correlations and the working fluid candidates are provided in Appendix B.

4.2.1. Modified Heat Exchanger Model for Refrigerant Mixtures

A modified form of the proposed PHE model should be used for the refrigerant mixtures. It can be seen from Figure 4.5a and b that the adaptation of the three-zone modelling approach to the refrigerant mixtures would need careful consideration for the property calculation of each compound in the two-phase zone. This is mainly stemming from the zeotropic nature of some refrigerant mixtures.

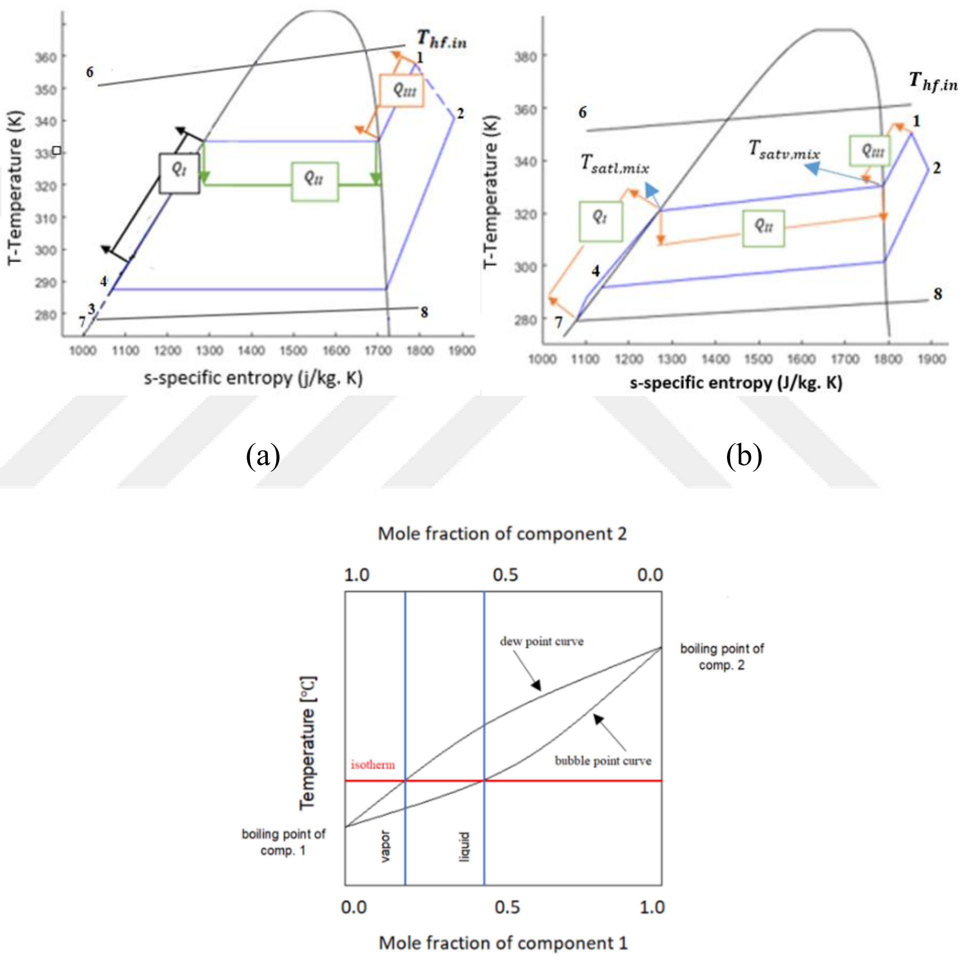

(a) (b)

(c)

Figure 4.5. T-s diagram of the ORC process and the zones of PHEs with respect to phases of (a) pure fluid (b) zeotropic blend of R134a/R245fa(0.65/0.35) and (c) Phase diagram of the zeotropic mixture.

For zeotropic mixtures, the boiling temperature of each component of the mixture varies during the phase change process that occurs in the two-phase zone of the heat exchanger. Therefore, the model developed in the study conducted by Asma et al. [91] is modified in such a way that the property calculation of selected mixture compounds will be made by considering the liquid phase and vapor phase properties separately. In the modelling, the moving boundary type model suitable for chevron-type plate heat exchangers is selected to simulate the heat transfer process in the evaporator and condenser. In the model, the heat exchanger is divided into three zones with respect to the state of the refrigerant. These are subcooled, two-phase, and superheated zones.

The model calculates the required heat transfer area in each zone, using the geometrical inputs, and bulk temperatures at the inlet conditions. Fluid properties in the single-phase zones (sub-cooled and superheated) are evaluated at the mean temperature values obtained by averaging the bulk temperature values at the inlet and outlet of each zone. By the LMTD method, the required heat transfer area of each single-phase zone can be calculated like the pure fluid PHE model.

However, in the two-phase zone, due to the vaporization of the working fluid, fluid properties change drastically as a function of the quality of the mixture. The fluid properties are calculated by dividing the two-phase zone into smaller parts. Regarding it, each small segment of the region has an enthalpy change, and the properties of the zone can be calculated by knowing the enthalpy and pressure values of each segment. The accuracy of the calculations is dependent on the selection of grid numbers in the two-phase zone. Therefore, the number of increments $'j'$ should be selected in such a way that the properties can be calculated for each increment of the two-phase zone.

Further, another problem in the two-phase zone arises from the prediction of mixture composition. The original correlations at the two-phase zone need to be modified to capture the temperature glide in the two-phase zone. The properties of the mixture in the two-phase zone change depending on the liquid and vapor phase properties, and the liquid and vapor phase mass fractions of each pure component of the mixture. The properties of each pure constituent of the mixture are determined by using REFPROP v9.1 [23]. Using the liquid and vapor phase mass fractions (x, y) of each component $'i'$ of the refrigerant mixture, the liquid and vapor phase properties in the two-phase zone of the PHE can be calculated. Then, the heat transfer coefficient, pressure drop, and the heat transfer area in the two-phase zone can be calculated. For the mixtures, the liquid and vapor phase properties in the two-phase zone are changed in each computational step, j. Therefore, the determination of vapor and liquid phase mass fractions is required to calculate the liquid and vapor phase properties correctly. The liquid and vapor phase mass fractions (x_i, y_i) can be directly determined by using Refprop v9.1.

Then, liquid and vapor phase properties μ_l, $k_{f,l}$, $c_{p,l}$, ρ_l and ρ_g can be calculated as

$$c_{p,l} = c_{p,l,x_1} x_1 + c_{p,l,x_2} x_2 \,, \tag{4.50}$$

$$\mu_l = \mu_{l,x_1} x_1 + \mu_{l,x_2} x_2 \,, \tag{4.51}$$

$$k_{f,l} = k_{f,l,x_1} x_1 + k_{f,l,x_2} x_2 \,, \tag{4.52}$$

$$\rho_l = \rho_{l,x_1} x_1 + \rho_{l,x_2} x_2 \,, \tag{4.53}$$

$$\rho_g = \rho_{g,x_1} x_1 + \rho_{g,x_2} x_2 \,, \tag{4.54}$$

where x_1 [-] and x_2 [-] are mass fractions of each component of the mixture, and sub-indices l and v show the liquid & vapor properties, respectively.

The refrigerant mixture does not experience phase change in single-phase zones, therefore, the LMTD methodology can be used for refrigerant mixtures as in pure fluids. Using the LMTD method, the heat transfer area of each zone $\mathrm{A_i}$ can be calculated by knowing the logarithmic mean temperature difference between hot and cold temperature sources, and the heat transfer coefficients for hot and cold sources for each zone.

LMTD methodology equations can be given as

$$A_{tot,req} = \sum A_i \quad A_i = \frac{\dot{Q}_i}{U_i LMTD_i} \,, \tag{4.55}$$

$$LMTD_i = \frac{\left(T_{hotin,i} - T_{coldout,i}\right) - \left(T_{hotout,i} - T_{coldin,i}\right)}{ln\left(\frac{T_{hotin,i} - T_{coldout,i}}{T_{hotout,i} - T_{coldin,i}}\right)} \,, \tag{4.56}$$

$$\frac{1}{U_i} = \frac{1}{\alpha_{cold,i}} + \frac{1}{\alpha_{hot,i}} \,, \tag{4.57}$$

where α and k_p are convective heat transfer coefficient and plate thermal conductivity, respectively.

4.2.1.1. Pressure Drop Correlations in Heat Exchangers. Pressure drop due to friction loss can be evaluated by

$$\Delta P_{fr,mix,j} = \frac{f_{tp,mix,j} N_{ch} {G_{eq,mix,j}}^2 L_{r,j}}{\rho_{l,mix} D_h} . \tag{4.58}$$

Port pressure drop is determined by

$$\Delta P_{port,mix} = 1.4 \frac{G_{port,mix}^2}{2\rho_{mean,mix}} , \tag{4.59}$$

where $\rho_{mean,mix}$, the mean density in the two-phase region in each computational step is

$$\rho_{mean,mix} = \left(\frac{x}{\rho_{g,mix}} + \frac{1-x}{\rho_{l,mix}} \right)^{-1} , \tag{4.60}$$

where $G_{port,mix}$ is the port mass velocity and determined as

$$G_{port,mix} = \frac{4\dot{m}_{eq,mix}}{\pi D_{port}^2} , \tag{4.61}$$

where $\dot{m}_{eq,mix}$ equivalent mass flow rate of the mixture which can be given as

$$\dot{m}_{eq,mix} = \dot{m}_{wf} \left[1 - x + x \left(\frac{\rho_{l,mix}}{\rho_{g,mix}} \right)^{0.5} \right] . \tag{4.62}$$

Pressure drop due to elevation is obtained by

$$\Delta P_{ele,mix,j} = \rho_{mean,mix} g L_{r,j} . \tag{4.63}$$

Pressure drop due to acceleration is obtained by

$$\Delta P_{acc,mix} = \left(\frac{G_{eq,mix}^2 x}{\rho_{l,mix} - \rho_{g,mix}} \right)_{in} - \left(\frac{G_{eq,mix}^2 x}{\rho_{l,mix} - \rho_{g,mix}} \right)_{out} . \tag{4.64}$$

Pressure drop in a two-phase region can be calculated via

$$\Delta P_{tp,mix} = \Delta P_{fr,mix} + \Delta P_{port,mix} + \Delta P_{ele,mix} + \Delta P_{acc,mix} \,. \tag{4.65}$$

The total pressure drop across the heat exchanger can be evaluated by

$$\Delta P_{Hex,mix} = \Delta P_{sp,mix} + \Delta P_{tp,mix} \,. \tag{4.66}$$

The code developed in MATLAB uses a modified version of Chisholm and Wanniarachchi, and Han et al.'s correlations for the two-phase regions of the evaporator and the condenser. The model is based on an iterative process to calculate the required area for the evaporator and the condenser. The only modification made is the calculation of liquid phase and vapor phase properties in the two-phase region of the heat exchanger. Since the properties of the zeotropic mixture changed during the phase change process, the accuracy of the calculations is dependent on the selection of grid numbers in the two-phase region. Therefore, the number of increments $'j'$ should be selected in such a way that the properties can be calculated from the mixing rules for each increment of the two-phase region. Using the liquid and vapor phase mass fractions (x, y) of each component $'i'$ of the refrigerant mixture, the liquid and vapor phase properties in the two-phase region of the PHE can be calculated. The properties of the selected refrigerant mixtures are determined using Refprop v9.1 [35]. Then, the heat transfer coefficient, pressure drop, and the heat transfer area in the two-phase region can be calculated.

LMTD methodology is valid for single-phase regions, therefore, the properties of the refrigerant mixture in single-phase regions and cooling water can directly be determined by Refprop v9.1. The rest is like the model proposed for pure fluids [91].

4.2.2. Interconnected Cycle Model

The interconnected ORC model [91] is modified and used for the parametric performance study conducted within the scope of this work. The model consists of component sub-models including the evaporator, condenser, working fluid pump, and expander. Pipe heat loss and pressure drop correlations are also added to the cycle to increase the realism of the model. The model uses seven decisive variables including cooling water inlet temperature, hot fluid inlet temperature, expander outlet pressure, working fluid mass flow rate, volumetric flow rates of hot fluid and cooling water, and the pump outlet pressure to calculate pressure and temperatures at component boundaries. The modified version of heat exchanger correlations is used to calculate the temperature glide that occurs during two-phase zones of evaporation and condensation processes. In the calculation of heat exchanger areas, the heat exchanger geometries of the experimental ORC setup in our laboratory are used. Therefore, the parametric performance study is conducted with respect to geometrical limitations (i.e., total heat transfer areas of the evaporator $A_{tot,ev}$ and condenser $A_{tot,cd}$) of the experimental setup. The same approach is also used in the connection pipes model. The isentropic efficiency models for the expander and the refrigerant pump are used.

The flowchart of the modified version of the interconnected ORC model is shown in Figure 4.6. Governing equations used in the cycle performance analysis are given in Table 4.3.

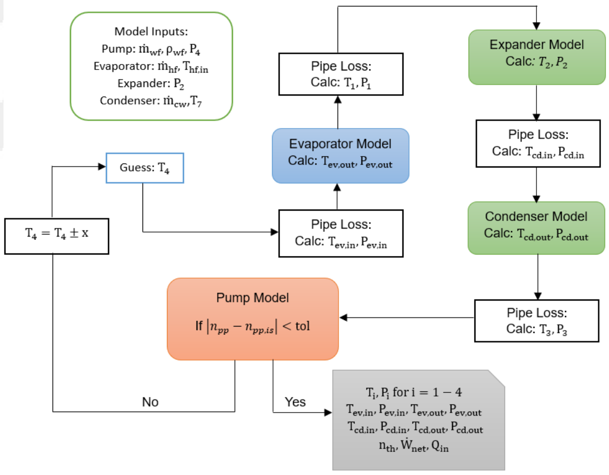

Figure 4.6. Flowchart of the modified interconnected ORC model.

Table 4.3. Governing equations of the performance indicators $\dot{W}_{net}$, and n_{th}.

Component	**Work and Heat Duties [kW]**	**Efficiency [-]**
Pump	$\dot{W}_{pp} = \dot{m}_{wf}(h_{4,is} - h_3)/n_{pp}$	$n_{pp} = \dfrac{h_{4,is} - h_3}{h_4 - h_3}$
Evaporator	$\dot{Q}_{in} = \dot{m}_{wf}(h_{evp,out} - h_{evp,in})$	-
Condenser	$\dot{Q}_{out} = \dot{m}_{wf}(h_{cnd,in} - h_{cnd,out})$	-
Expander	$\dot{W}_{exp} = \dot{m}_{wf}(h_1 - h_{2,is})n_{exp}$	$n_{exp} = \dfrac{h_1 - h_2}{h_1 - h_{2,is}}$
Overall Cycle	$\dot{W}_{net} = \dot{W}_{exp} - \dot{W}_{pp}$	$n_{th} = \dfrac{\dot{W}_{net}}{\dot{Q}_{in}}$

5. ORC MODEL VALIDATION

5.1. Model Validation for Pure Fluids

5.1.1. Validation of the ORC Component Model

In this section, validations of each component models are conducted by comparing the model results with experimental data. The steady state data tabulated in Table 5.1 are used to assess the model's predictive capability.

Table 5.1. Averaged input parameters used for model validation under steady state operation conditions (working fluid pump speed: 1050 rpm, hot fluid (oil) pump frequency: 40 Hz, $T_{hf,in} = 80 - 110$ °C ,$T_{cw,in} = 4$ °C).

Experimental inputs	**Exp-1**	**Exp-2**	**Exp-3**	**Exp-4**
$\dot{m}_{wf}$ (kg/s)	0.122	0.048	0.058	0.084
$\dot{V}_{cw}$ (m^3/h)	8.54	8.59	8.67	8.74
$\dot{V}_{hf}$ (m^3/h)	4.62	4.50	4.50	4.57
$T_{hf,in}$ (°C)	79.1	110.0	100.1	90.1
$T_{cw,in}$ (°C)	4.86	4.78	4.81	4.84
T_4 (°C)	12.35	21.61	20.13	16.08
P_4 (bar)	14.555	16.475	16.234	15.621
$P_{t,o}$ (bar)	5.752	6.411	6.271	6.022

First, the results for heat exchangers, including the evaporator and condenser used in the ORC setup, are presented. Figure 5.1 shows the parity plots of heat balance at the evaporator and condenser units. Parity plots for the heat flow rate at the evaporator and condenser units are given in Figure 5.2. Parity plots of pressure and temperatures at the outlet of heat exchangers are shown in Figure 5.3 and Figure 5.4. The results show a good match between experimental data and the model results. For all cases, the deviations are within ±5% error limits for heat balances, and ±1% and ±2% for pressures, temperatures, and heat fluxes, respectively, in all heat exchangers.

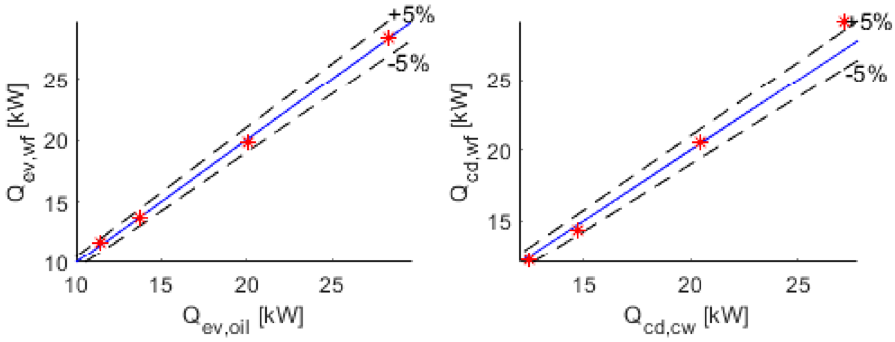

(a) (b)

Figure 5.1. Heat balance in (a) the evaporator (b) the condenser.

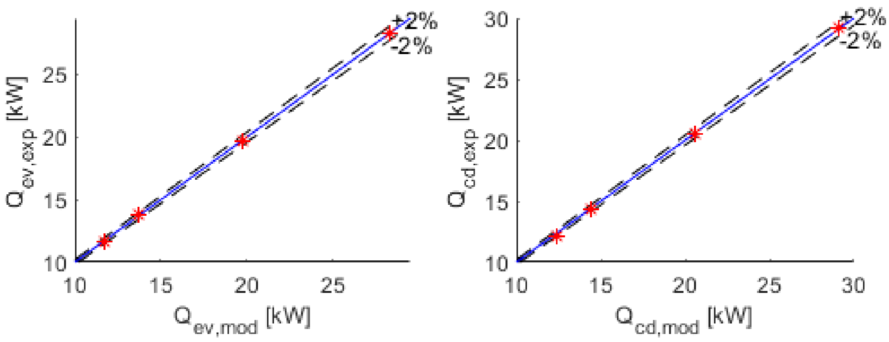

(a) (b)

Figure 5.2. Parity plots of heat flow rate in (a) evaporator and (b) condenser.

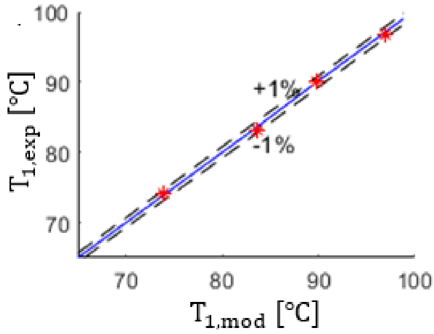

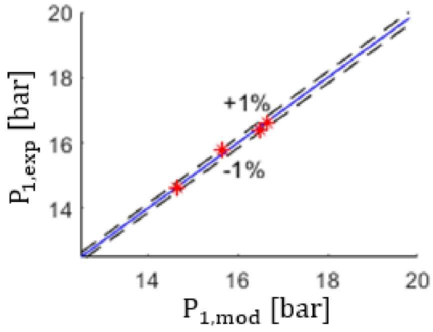

(a) (b)

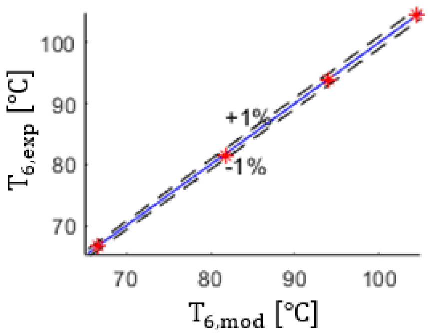

(c)

Figure 5.3. Parity plots of (a) R134a temperature at the evaporator outlet, (b) R134a pressure at the evaporator outlet, (c) hot fluid (oil) temperature at the evaporator outlet.

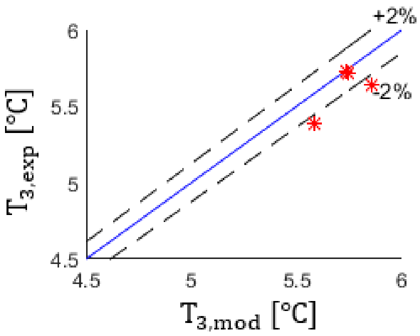

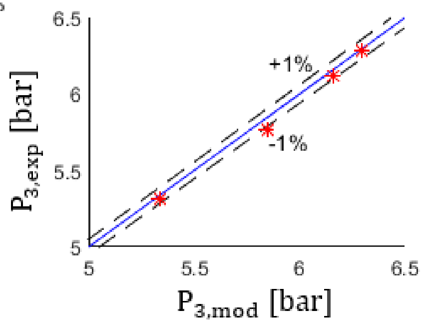

(a) (b)

Figure 5.4. Parity plots of (a) temperature and (b) pressure in condenser outlet.

Next, parity plots of mass flow rate, pumping pressures, and pump work are given in Figure 5.5. A good match between experimental and ORC model data is observed.

For all cases, the deviations from experimental data lie in ±5% for flow rate and pump work and ±2% for the pressure values.

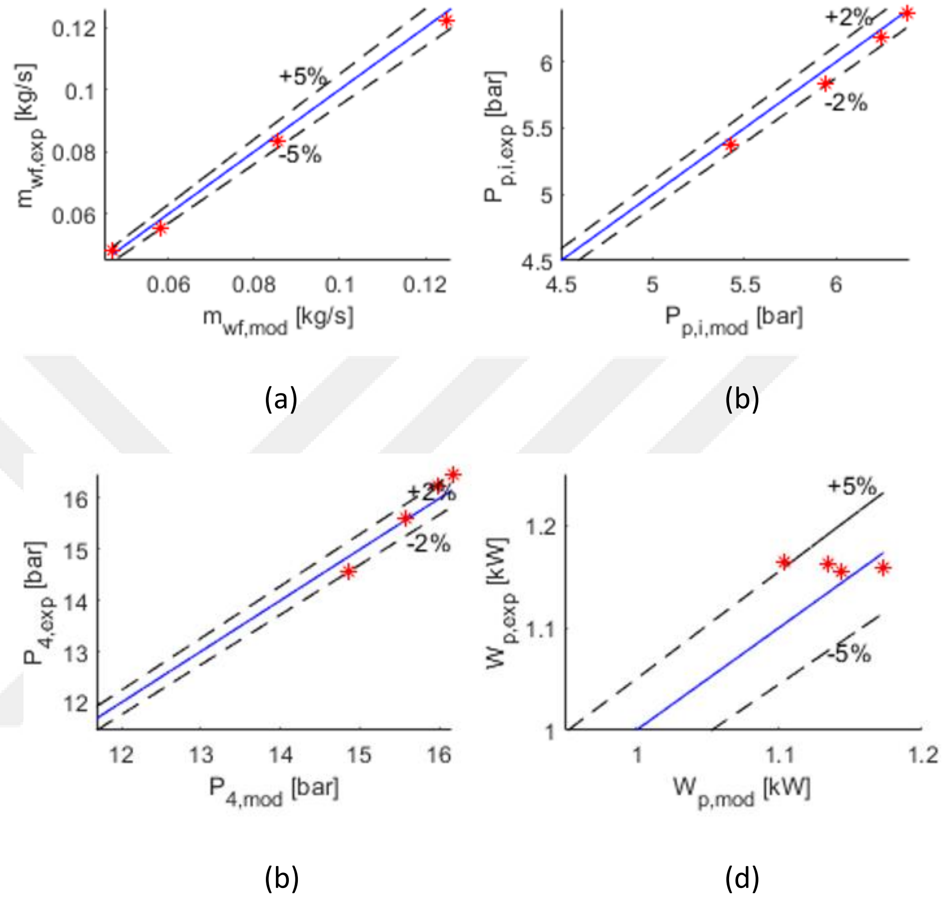

Figure 5.5. Parity plots of (a) R134a mass flow rate, (b) R134a pressure at the pump inlet, (c) R134a pressure at the pump outlet, (d) work done by the pump.

Finally, the parity plot in Figure 5.6 shows the accuracy of the model in comparison to the experimental results under four different heat source temperatures. The results obtained for throttle outlet temperature are within ±2% limits.

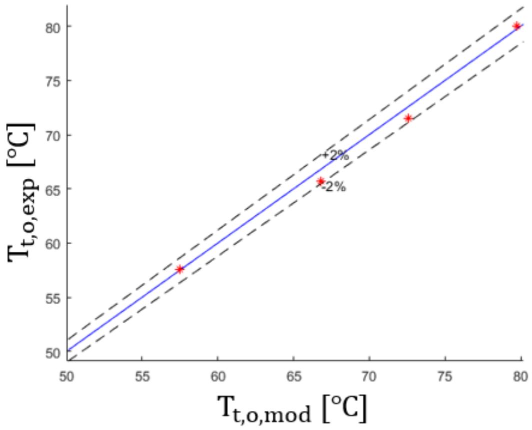

Figure 5.6. Parity plot of temperature at throttle outlet.

5.1.2. Validation of Interconnected ORC model

Components are connected by pipes; therefore, the pressure drop and heat transfer from connecting pipes are considered in the ORC model. The loss calculations for each connecting pipe are conducted iteratively. The model needs the working fluid, hot fluid (oil), and cooling water mass flow rates, the inlet temperatures of cooling water and oil, the pressures at the outlet of the pump and throttle valve, and the pump curve. The temperature at the pump outlet is selected as the cycle iteration parameter. Iterations continue until the difference between the calculated efficiency of the pump and its efficiency obtained from the pump curve is lower than a set tolerance. In the calculations, both the sensor points (T_i, P_i) and the boundaries of components are considered for more realistic assessment and better predictive capability.

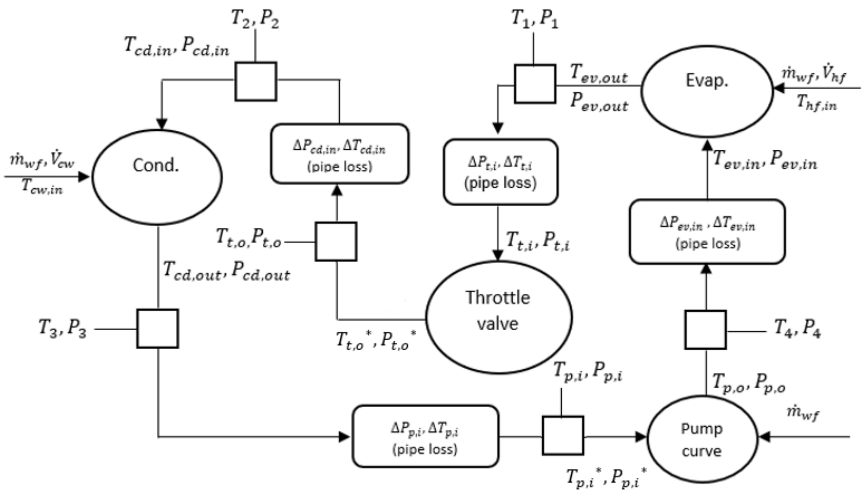

Figure 5.7. Schematic of the interconnected ORC model.

The schematic of the interconnected ORC model is given in Figure 5.7, the flowchart of the interconnected ORC model is shown in Figure 5.8. Energy equations of the model are given below.

Energy equations for refrigerant pump (boundaries) are

$$\dot{W}_p = \dot{m}_{wf}(h_{p,o} - h_{p,i}{}^*) \, , \tag{5.1}$$

$$n_p = \dot{m}_{wf}(h_{p,o,is} - h_{p,i}{}^*) \, / \, \dot{W}_p \, . \tag{5.2}$$

Energy equations for refrigerant pump (sensor points) are

$$\dot{W}_p = \dot{m}_{wf}(h_4 - h_{p,i}) \, , \tag{5.3}$$

$$n_p = \dot{m}_{wf}(h_{4,is} - h_{p,i}) \, / \, \dot{W}_p \, . \tag{5.4}$$

Energy equations for evaporator (boundaries) are

$$\dot{Q}_{ev,wf} = \dot{m}_{wf}(h_{ev,out} - h_{ev,in}) \, , \tag{5.5}$$

$$\dot{Q}_{ev,hf} = \dot{m}_{hf} c_{p,hf}(T_{hf,in}{}^* - T_6{}^*) \, . \tag{5.6}$$

Energy equations for evaporator (sensor points) are

$$\dot{Q}_{ev,wf} = \dot{m}_{wf}(h_1 - h_4) \, , \tag{5.7}$$

$$\dot{Q}_{ev,hf} = \dot{m}_{hf} c_{p,hf}(T_{hf,in} - T_6) \, . \tag{5.8}$$

Energy equation for throttle valve (boundaries) is

$$h_{t,i}\left(T_{t,i}, P_{t,i}\right) = h_{t,o}(T_{t,o}{}^*, P_{t,o}{}^*) \, . \tag{5.9}$$

Energy equation for throttle valve (sensor points) is

$$h_1(T_1, P_1) = h_{t,o}(T_{t,o}, P_{t,o}) \, . \tag{5.10}$$

Energy equations for condenser (boundaries) are

$$\dot{Q}_{cd,wf} = \dot{m}_{wf}(h_{cd,in} - h_{cd,out}) \, , \tag{5.11}$$

$$\dot{Q}_{cd,cw} = \dot{m}_{cw} c_{p,cw} (T_8{}^* - T_{cw,in}{}^*) \ . \tag{5.12}$$

Energy equations for condenser (boundaries) are

$$\dot{Q}_{cd,wf} = \dot{m}_{wf} (h_2 - h_3) \ , \tag{5.13}$$

$$\dot{Q}_{cd,cw} = \dot{m}_{cw} c_{p,cw} (T_8 - T_{cw,in}) \ . \tag{5.14}$$

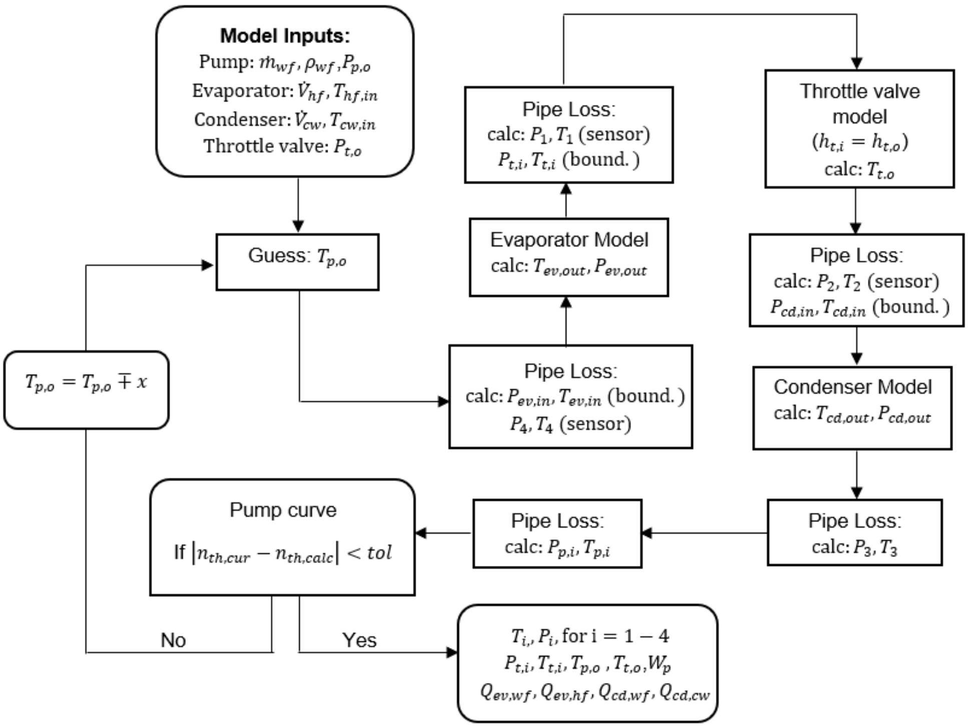

Figure 5.8. Flowchart of the interconnected ORC model.

Piping losses, including pressure and temperature drops in each line, are calculated using the relevant heat transfer equations. The T-S diagram in Figure 5.9 shows the negligible difference between experimental and model-predicted data for the experimental test conducted in a hot fluid temperature of 100 ºC.

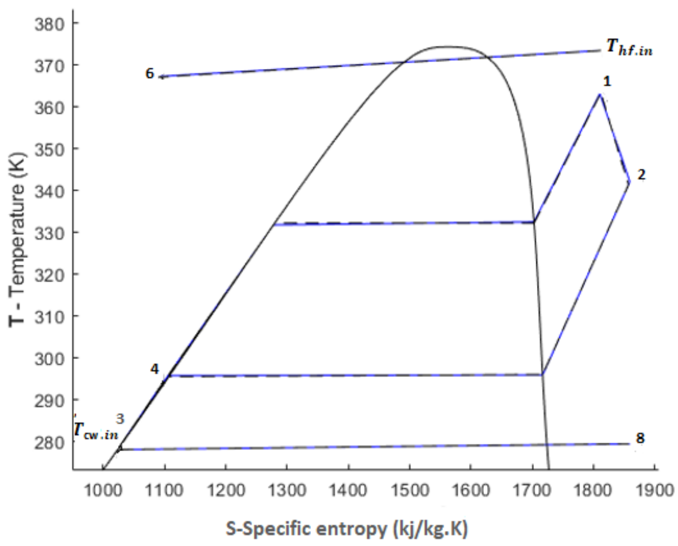

Figure 5.9. T-s Diagram of the ORC (— : model, --- : experiment, $T_{hf,in}$ = 100 °C).

Table 5.2. Experimental data with uncertainties vs. model predicted results (time window=750 sec).

Exp. Variable	Exp-1 Exp1∓U	Mod	Exp-2 Exp2∓U	Mod	Exp-3 Exp3∓U	Mod	Exp-4 Exp4∓U	Mod
$T_{pp,i}$(°C)	5.62∓0.01	5.94	6.31∓0.06	6.63	6.04∓0.02	6.51	6.31∓0.02	6.62
T_1(°C)	74.5∓0.09	74.0	96.8∓0.07	96.8	83.2∓0.14	83.5	90.0∓0.10	89.8
$T_{t,o}$(°C)	57.5∓0.02	57.5	80.0∓0.18	79.7	65.6∓0.16	66.8	71.5∓0.03	72.6
T_2(°C)	57.2∓0.06	56.6	72.1∓0.08	72.8	64.5∓0.13	65.7	68.1∓0.02	68.7
T_3(°C)	5.41∓0.01	5.59	5.73∓0.01	5.7	5.64∓0.01	5.86	5.74∓0.01	5.74
T_8(°C)	7.52∓0.02	7.72	5.92∓0.02	5.9	6.76∓0.02	6.76	6.16∓0.02	6.13
T_6(°C)	66.7∓0.19	66.7	104.5∓0.21	104.5	81.4∓0.33	81.8	93.8∓0.27	94.0
$P_{pp,i}$(bar)	5.368∓0.016	5.42	6.364∓0.018	6.38	5.849∓0.012	5.94	6.195∓0.007	6.24
P_1(bar)	14.621∓0.04	14.63	16.635∓0.01	16.67	15.770∓0.02	15.65	16.398∓0.01	16.51
P_2(bar)	5.410∓0.014	5.41	6.378∓0.014	6.34	5.882∓0.010	5.88	6.216∓0.007	6.20
P_3(bar)	5.298∓0.016	5.34	6.295∓0.012	6.30	5.779∓0.012	5.85	6.125∓0.007	6.16
P_4(bar)	14.555∓0.043	14.85	16.475∓0.014	16.16	15.621∓0.027	15.58	16.234∓0.01	15.99
$\dot{m}_{wf}$(kg/s)	0.122∓0.001	0.125	0.048∓0.001	0.047	0.084∓0.001	0.085	0.058∓0.001	0.055
ΔP_{pp}(bar)	9.187∓0.059	9.43	10.111∓0.032	9.78	9.772∓0.039	9.64	10.039∓0.01	9.75
$\dot{Q}_{ev,wf}$(kW)	28.32∓0.34	28.29	11.70∓0.17	11.70	19.73∓0.19	19.76	13.74∓0.09	13.72
$\dot{Q}_{ev,hf}$(kW)	28.27∓0.59	28.23	11.45∓0.48	11.26	20.07∓0.49	19.82	13.74∓0.47	13.46
$\dot{Q}_{cd,wf}$(kW)	29.14∓0.35	29.07	12.19∓0.17	12.37	20.53∓0.19	20.60	14.39∓0.09	14.43
$\dot{Q}_{cd,cw}$(kW)	27.20∓0.01	29.07	12.46∓0.01	12.37	20.48∓0.01	20.60	14.72∓0.01	14.43
$\dot{W}_p$(kW)	1.155∓0.015	1.143	1.163∓0.042	1.103	1.159∓0.024	1.173	1.162∓0.010	1.134

Table 5.2 shows results predicted by the ORC model and experimental data with absolute uncertainty value. The pressure and temperature at the inlet and outlet of each component (i.e., refrigerant pump, throttle valve), the mass flow rate, heat flow rates of heat exchangers, and power consumed in the refrigerant pump are tabulated. The maximum deviation observed for working fluid mass flow rate is 5.17% (Exp-4), and power consumed by the pump is 5.15% (Exp-2), whereas all remaining deviations for mass flow rate and pump power consumption is less than ±5%.

All pressure and temperature deviations are within ±2%. The maximum deviation for differential pressure of the refrigerant pump is 3.27% (Exp-2), whereas all remaining deviations observed for refrigerant pump differential pressure is smaller than 3%.

The model also evaluates the heat transfer rates of working fluid, hot fluid (oil), and cooling water during evaporation and condensation. The results indicated that the maximum error is observed for heat transfer rates of cooling water at condenser with 6.87% (Exp-1); except this, all the heat transfer rate deviations are within ∓2%. The deviation observed from experimental data is consistent with experimental uncertainties of temperature and pressure sensors.

The highest relative uncertainty values are observed for refrigerant pump inlet and evaporator outlet temperatures of 0.93% and 3.87%, respectively, whereas the highest uncertainty in pressure is observed at the pump inlet and hot fluid at the evaporator outlet with 0.29%. The main reasons for the deviation are the fluid property calculations' uncertainties and each sensor's measurement accuracy.

Data in Table 5.2 also reveal that the highest absolute uncertainty is calculated for heat transfer rates of hot fluid in the evaporator. For better understanding, absolute uncertainties are converted into relative uncertainties by dividing them by experimental pressure, temperature, flow rate values, and experimental heat transfer rates calculated from those values. The maximum relative uncertainty observed for heat transfer rate at the evaporator is 4.19% (Exp-2), followed by 3.42%, 2.44%, and 2.08% observed for Exp-4, Exp-3, and Exp-1, respectively. Except for those, all the remaining relative uncertainties for heat transfer rates are smaller than 2%.

The effect of adding pipe pressure drop and heat transfer losses into the model are also shown. Results tabulated in Table 5.3 show the model's prediction accuracy vs. the ones available in the literature. The interconnected cycle model predicts the pressures of the working fluid within ±1% and calculates the heat transfer rates within ±5% accuracy. The maximum deviation between the model-predicted temperature and the experimental result is 1.1 ℃ (within ∓2%) at the condenser inlet. The deviations for the remaining temperatures predicted at all sensors are less than 1 ℃, much lower than the maximum absolute error of 7

℃ found in the literature [23]. The increased accuracy is achieved by incorporating piping pressure losses and temperature drops into the interconnected cycle model.

Results tabulated in Table 5.4 show the effect of the pipe pressure drop and heat losses on the model's accuracy. The difference between the model prediction and the experimental measurement is calculated and tabulated in the table. The results show that the model that considers the losses predicts the temperature and the pressure more accurately, revealing the significance of the pipeline losses.

Table 5.3. Performance comparison of the interconnected ORC model with the literature.

Source (year)	**Verification**	**Prediction error**	**Reference**
Quoilin et al. (2016)	Power output Exhaust temperature	±10% 7 ℃	[23]
Dickes et al. (2017)	Thermodynamic states Computational cost	±8.3%	[28]
Lecompte et al. (2018)	Net power output Heat balance	±2% ±5%	[30]
Dickes et al. (2018)	Expander work Pump work	±15% ±15%	[31]
Ziviani et al. (2016)	Energy balance	±20%	[32]
Moradi et al. (2021)	Temperature Pressure Power output	±10% ±5% ±15%	[33]
J. Oh et al. (2022)	Thermodynamic states Energy balance Computational cost	±7.9%	[34]
Present study	Temperature Pressure Heat transfer rates	1.1 ℃ ±1% ±5%	[91]

Table 5.4. The effect of pipe heat losses and pressure drop on ORC modeling accuracy for Exp-1 & Exp-2 and Exp-3 & Exp-4.

Exp. Var.	**Exp-1**					**Exp-2**				
	Exp. Data	**No pipe loss**	**With pipe loss**	**Abs. Diff.-1**	**Abs. Diff.-2**	**Exp. Data**	**No pipe loss**	**With pipe loss**	**Abs. Diff.-1**	**Abs. Diff.-2**
$T_{pp,i}$(℃)	5.6	8.7	5.9	3.1	0.3	6.3	11.8	6.6	5.5	0.3
T_1(℃)	74.5	75.3	74.0	0.8	0.5	96.8	97.0	96.8	0.2	0.0
$T_{t,o}$(℃)	57.5	61.6	57.5	4.1	0.0	80.0	84.7	79.7	4.7	0.3
T_2(℃)	57.2	61.6	56.6	4.4	0.6	72.1	84.7	72.8	12.6	0.7
T_3(℃)	5.4	8.7	5.6	3.3	0.2	5.7	11.8	5.7	6.1	0.0
T_8(℃)	7.5	7.6	7.7	0.1	0.2	5.9	5.8	5.9	0.1	0.0
T_6(℃)	66.7	66.8	66.7	0.1	0.0	104.5	104.3	104.5	0.2	0.0
$P_{pp,i}$(bar)	5.37	5.68	5.41	0.31	0.04	6.36	6.37	6.38	0.01	0.02
P_1(bar)	14.62	14.66	14.63	0.04	0.01	16.63	16.71	16.67	0.08	0.04
P_2(bar)	5.410	5.75	5.41	0.34	0.00	6.37	6.41	6.34	0.04	0.03
P_3(bar)	5.30	5.68	5.34	0.38	0.04	6.29	6.37	6.30	0.08	0.01
P_4(bar)	14.55	14.55	14.85	0.00	0.30	16.47	16.47	16.16	0.00	0.31

Table 5.4. The effect of pipe heat losses and pressure drop on ORC modeling accuracy for Exp-1 & Exp-2 and Exp-3 & Exp-4. (cont.)

Exp. Var.	Exp-3					Exp-4				
	Exp. Data	**No pipe loss**	**With pipe Loss**	**Abs. Diff.-1**	**Abs. Diff.-2**	**Exp. Data**	**No pipe loss**	**With pipe loss**	**Abs. Diff.-1**	**Abs. Diff.-2**
$T_{pp,i}$(°C)	6.0	8.5	6.5	2.5	0.5	6.3	11.0	6.6	4.7	0.3
T_1(°C)	83.2	84.3	83.5	1.1	0.3	90.0	90.3	89.8	0.3	0.2
$T_{t,o}$(°C)	65.6	70.9	66.8	5.3	1.2	71.5	76.8	72.6	5.3	1.1
T_2(°C)	64.5	70.9	65.7	6.4	1.2	68.1	76.8	68.7	8.7	0.6
T_3(°C)	5.6	8.5	5.8	2.9	0.2	5.7	11.0	5.7	5.2	0.0
T_8(°C)	6.7	6.6	6.7	0.1	0.0	6.1	6.0	6.1	0.1	0.0
T_6(°C)	81.4	81.8	81.8	0.4	0.4	93.8	93.8	94.0	0.0	0.2
$P_{pp,i}$(bar)	5.85	5.99	5.94	0.14	0.09	6.19	6.23	6.24	0.04	0.05
P_1(bar)	15.77	15.68	15.65	0.09	0.12	16.39	16.52	16.51	0.12	0.12
P_2(bar)	5.88	6.02	5.88	0.14	0.00	6.21	6.27	6.20	0.06	0.01
P_3(bar)	5.78	5.99	5.85	0.21	0.07	6.12	6.23	6.16	0.11	0.04
P_4(bar)	15.62	15.62	15.58	0.00	0.04	16.23	16.23	15.99	0.00	0.24

Abs. Diff.-1 & Abs.Diff.-2 are the absolute difference between the experimental data and the model without and with pipe losses.

The steady-state model developed in this work accurately predicts the outcome of the experiments as shown in the previous sections. The details of the model are explained in Chapter 4. As shown in the preceding discussion, the reason for the improved prediction accuracy is that the model includes the connection pipes in addition to the regular units of the ORC, like the evaporator, condenser, pump, and throttle valve. So, the inlet conditions of these units are estimated with a better precision and consequently the outlet conditions are calculated precisely. Furthermore, the input parameters of the model are specifically selected as refrigerant pump mass flow rate, thermal oil pump volumetric flow rate, cooling water inlet temperature and volumetric flow rate, and the throttle valve outlet set pressure since these are the actual parameters that are set in each experiment. The model, therefore, can replicate the experiment and enables the prediction of the experimental results. Therefore, the present model facilitates a reduction of the experimental effort in the selection of working fluid for different heat input temperatures.

5.2. Model Validation for Refrigerant Mixtures

5.2.1. Validation of ORC Component Model

In this section, model validation results of each component ORC are presented. The steady-state data used to evaluate the model accuracy for R236fa/R134a with varying composition are tabulated in Table 5.5.

Table 5.5. Averaged experimental input parameters for the validation of pure fluid cases (Case 1-9) and R236fa/R134a mixture (Case 13-24).

Model Inputs	**Case No**								
	1	**2**	**3**	**4**	**5**	**6**	**7**	**8**	**9**
$T_{cw,in}$ (°C)	0.7	0.5	1.6	1.0	2.8	3.1	2.9	3.1	3.1
$T_{hf,in}$ (°C)	88.3	86.4	87.0	96.7	96.6	111.3	110.8	111.3	111.3
$T_{ev,in}$ (°C)	11.6	9.1	9.3	8.6	10.8	11.2	12.2	11.2	11.2
P_4 (bar)	16.31	14.60	14.11	14.32	14.21	14.17	14.07	14.17	14.17
$P_{t,o}$ (bar)	5.88	5.63	5.59	5.62	5.61	5.63	5.50	5.63	5.63
$\dot{m}_{wf}$(kg/s)	0.122	0.173	0.185	0.179	0.179	0.177	0.174	0.177	0.177
$\dot{V}_{hf}$(m^3/h)	5.18	5.18	5.15	5.05	5.04	5.29	5.27	5.29	5.29
$\dot{V}_{cw}$(m^3/h)	8.01	8.01	7.91	7.88	7.92	7.69	7.55	7.69	7.69

Table 5.5. Averaged experimental input parameters for the validation of pure fluid cases (Case 1-9) and R236fa/R134a mixture (Case 13-24). (cont.)

Model Inputs	**Case No**											
	13	**14**	**15**	**16**	**17**	**18**	**19**	**20**	**21**	**22**	**23**	**24**
$T_{cw,in}$ (°C)	4.4	5.2	3.6	4.2	3.5	2.0	2.1	2.4	0.0	0.50	1.6	0.0
$T_{hf,in}$ (°C)	95.0	109.1	111.4	96.3	86.3	86.3	96.4	111.9	113.1	96.7	86.4	86.9
$T_{ev,in}$ (°C)	10.3	10.9	9.6	10.3	9.6	8.0	8.6	9.8	11.9	8.8	8.4	8.3
P_4 (bar)	11.82	12.46	13.14	12.48	11.79	12.26	13.07	14.22	16.74	14.76	13.31	14.54
$P_{t,o}$ (bar)	5.35	5.45	5.55	5.46	5.33	5.40	5.50	5.68	5.94	5.64	5.45	5.61
$\dot{m}_{wf}$(kg/s)	0.265	0.250	0.236	0.251	0.265	0.257	0.239	0.209	0.133	0.192	0.234	0.200
$\dot{V}_{hf}$(m^3/h)	5.67	5.61	5.09	5.15	5.19	5.19	5.15	4.95	4.89	5.09	5.19	5.19
$\dot{V}_{cw}$(m^3/h)	8.12	8.13	8.11	8.13	8.13	8.13	8.11	8.11	8.07	8.08	8.10	8.08

Firstly, the validation results for the evaporator and condenser units are presented. Heat balance parity plots at the evaporator and the condenser are shown in Figure 5.10, whereas heat flow rates at the evaporator and condenser for each specific cases are provided in Figures 5.11 and 5.12. The results reveal that, the deviations are within $\mp 10\%$ error limits for heat balances and heat flow rates for most of the cases.

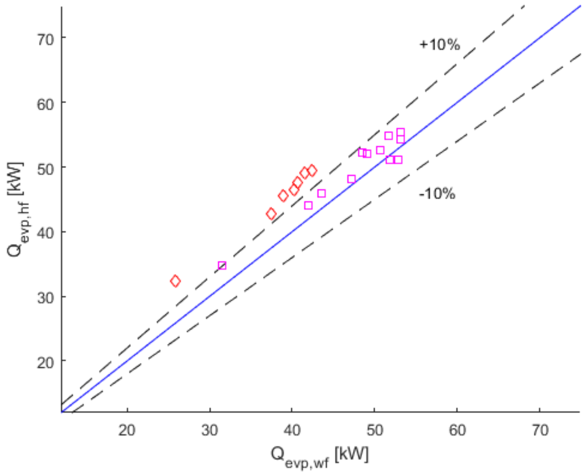

(a)

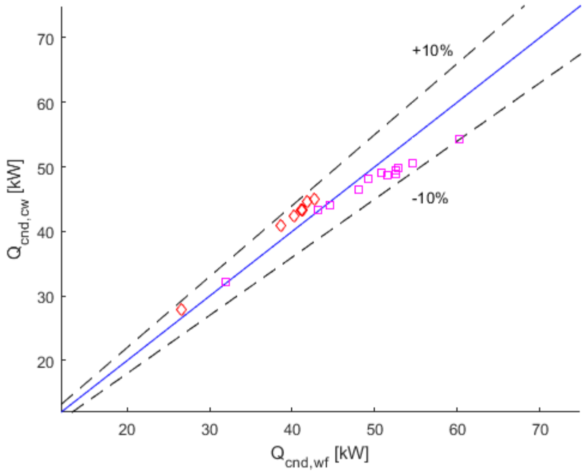

(b)

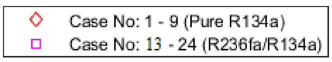

Figure 5.10. Heat transfer in (a) the evaporator (b) the condenser calculated from experimental data.

Figure 5.10 shows the variation of heat balances in the evaporator and condenser units for the experimental data obtained by each case. In Figure 5.10a heat balance in the evaporator for both working fluid side and oil side is provided. The results reveal that a good match between the experimental heat flow rates of the hot fluid (oil) and the working fluid side is obtained for most cases. Interestingly, heat flow rate deviations between the hot fluid and working fluid sides becomes smaller as the zeotropic mixture (R236fa/R134a) is used (see Case 13 to 24; Figure 5.10a). This is mainly stemmed from that the relative uncertainty values of the pure fluid tests (Case 1 to 9) for working fluid mass flow rates are much higher than cases with R236fa/R134a mixture (Case 13 to 24).

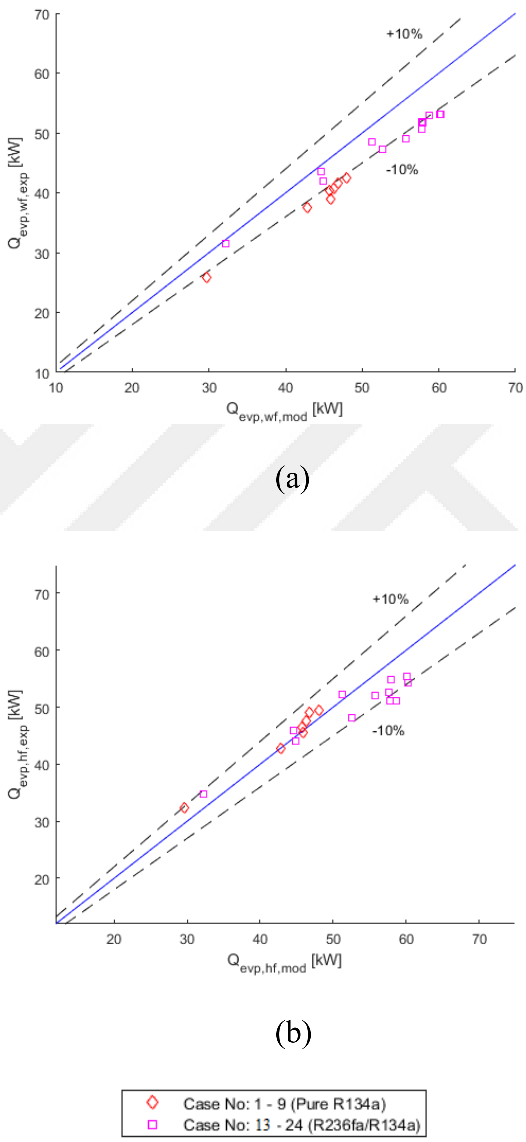

Figure 5.11. Parity plots of heat flow rate in the evaporator for (a) the working fluid and (b) the hot fluid (oil).

The heat balances in the condenser for each case are provided in Figure 5.10b. The results show that the deviations in experimental heat flow rates of the working fluid and cooling water are within $\pm 10\%$ error margins for all cases including pure fluid and the zeotropic mixture tests.

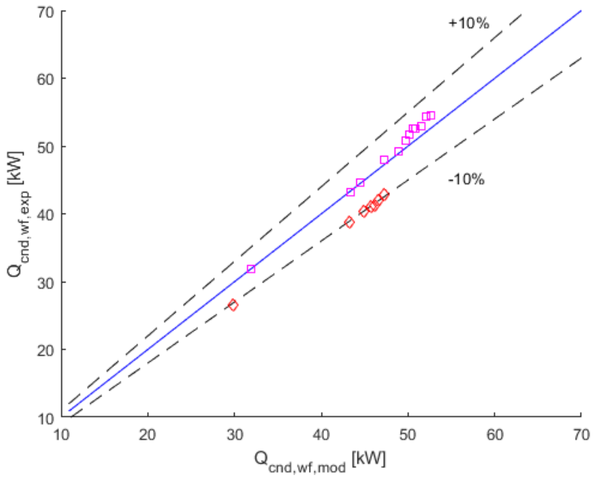

(a)

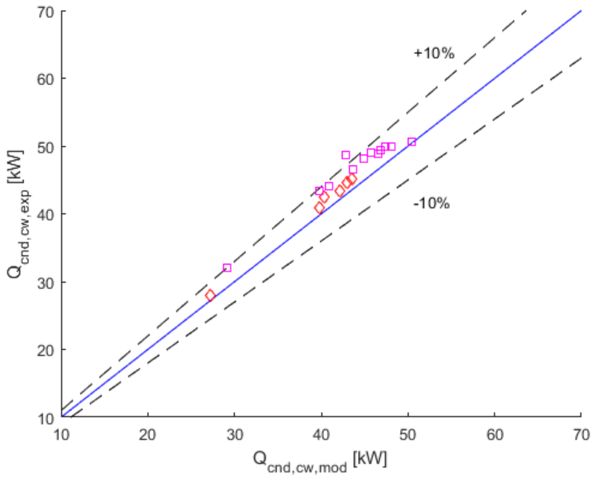

(b)

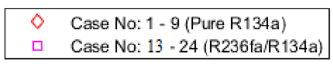

Figure 5.12. Parity plots of heat flow rate in the condenser for (a) the working fluid and (b) the cooling water.

Results provided in Figure 5.11 and Figure 5.12 show the change of calculated heat transfer rates of cooling water, hot fluid (oil) and the working fluid with respect to experimental heat transfer rates during the evaporation and condensation. Result indicated that the maximum deviation from the experimental data is observed for heat transfer rates of the working fluid during the evaporation with 18% (Case-3), whereas Case-20, Case-21 and

Case-22 provide the best modeling accuracy by respectively providing 5.8%, 2.2% and 2.5% deviation from the experimental data (see Figure 5.11).

In Figure 5.12, the variation of condensation heat duties of the model vs the experimental data is shown. The results show that the maximum deviation is observed for Case-2 with %12, which is followed by Case-1 with 11.9%. In between Case-13 to 21, all deviations in heat flow rates of the mixture are within ±5% error limits for the condenser sub-model. Results in Figure 5.12 also show that, for most cases a better match between experimental data vs the condenser sub-model is obtained when R236fa/R134a mixture is used instead of pure R134a. This is mainly due that the relative uncertainty values of the cooling water inlet and outlet temperatures of the mixture tests (Case 13 to 24) are comparably lower than pure fluid tests (Case 1 to 9) for most of the cases.

In terms of heat transfer rates of hot fluid (oil) and cooling water similar results are observed. The highest deviation from the experimental heat transfer rates of the oil during the evaporation are respectively obtained for Case-17 with 14.6% , and Case-18 with 12.8%, and Case-13 with 11.2%. Except these, all deviations are within ±10% error limits. Similar to the evaporator, all heat transfer rates of cooling water values are within ±10% threshold for the condenser sub-model except Case-18.

The ORC model calculates the evaporation and condensation heat transfer rates for hot fluid (oil), cooling water and the refrigerant sides. Figure 5.13 shows the calculated heat transfer rates for both the working fluid and hot fluid (oil) sides of the evaporator with error bars that shows the deviation of the model from the experimental data. In Figure 5.14, the heat duties of the working fluid and cooling water (ethylene glycol 20% + water 80%) of the condenser with error bars are shown.

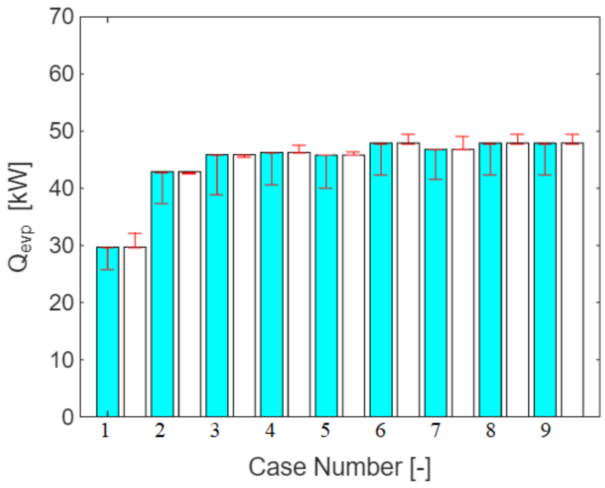

(a)

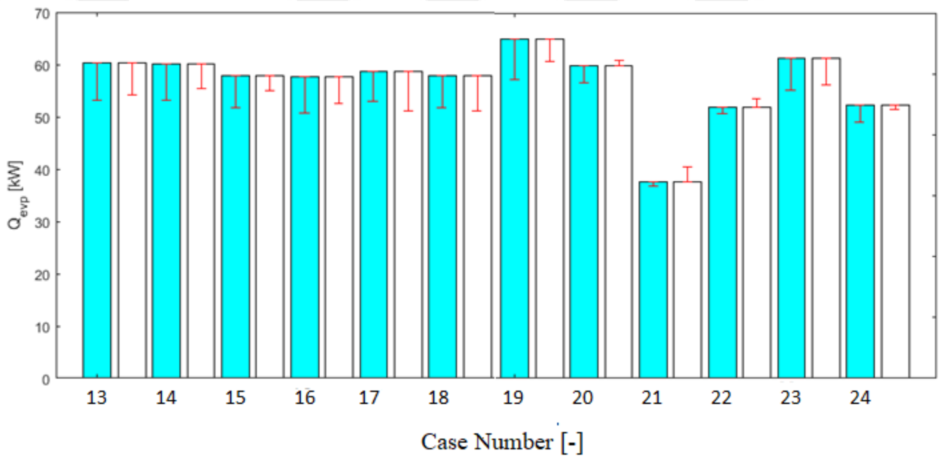

(b)

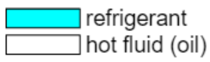

Figure 5.13. Calculated heat duties of the refrigerant and hot fluid (oil) of the evaporator for (a) pure fluid (Case 1 to 9) and (b) R236fa/R134a mixture (Case 13 to 24) with error bars.

Figure 5.13 shows the variation of the calculated and experimental heat duties of the evaporator for both the working fluid and hot fluid (oil) sides. The results provided in Figure 5.13 clearly show that the evaporation heat duties of the refrigerant predicted by the model are higher than experimental data for all cases. In terms of evaporator model accuracy, Case 21 and Case 22 provides the best performance. The accuracy of the evaporator model decreases for cases which have large differences between experimental heat duties of the refrigerant and hot fluid (oil) sides.

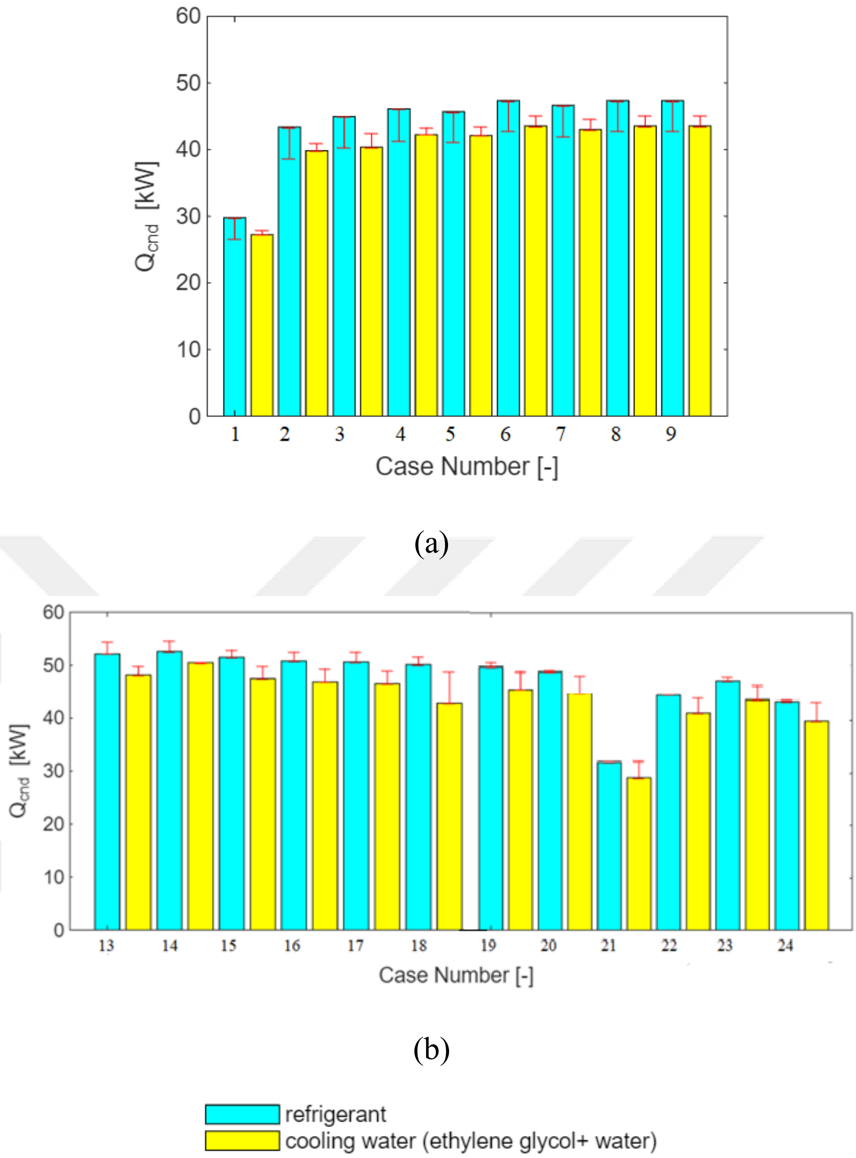

(a)

(b)

Figure 5.14. Calculated heat duties of the refrigerant and cooling water (ethylene glycol +water) of the condenser for (a) pure fluid (Case 1 to 9) and (b) R236fa/R134a mixture (Case 13 to 24) with error bars.

The change of the model based and experimental heat duties of the condenser for both the working fluid and cooling water sides is shown in Figure 5.14. Similar to evaporator model, the accuracy of the condenser model decreases for cases which have high discrepancies of condensation heat duties between cooling water and refrigerant sides.

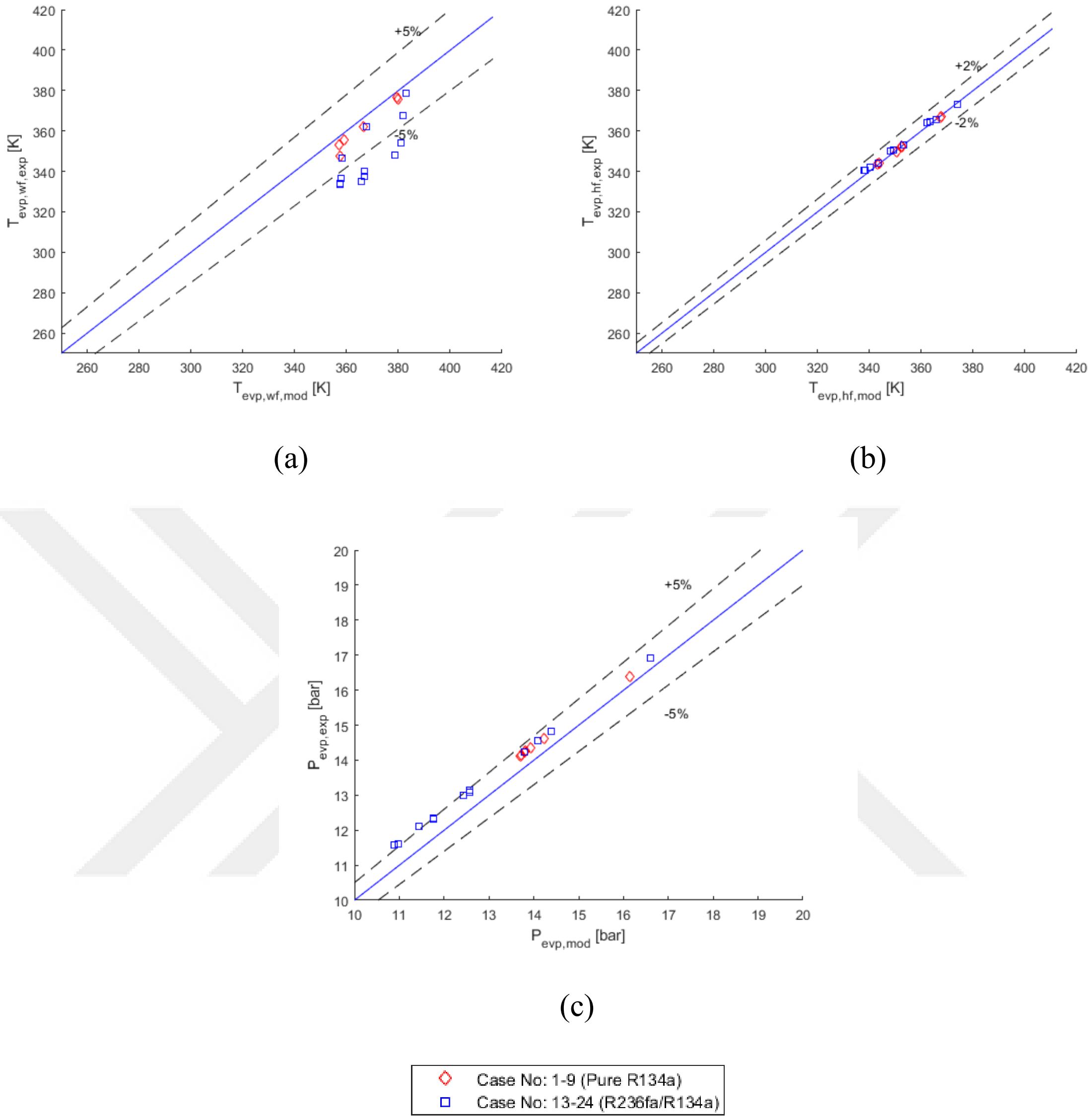

Figure 5.15. Parity plots of (a) working fluid temperature at the evaporator outlet, (b) hot fluid (oil) temperature at the evaporator outlet (c) pressure at the evaporator outlet.

Parity plots of pressure and temperatures at the outlet of the evaporator and condenser are prob in Figure 5.15 and Figure 5.16. The results show a good match between experimental data and the model results. For most cases, including pure fluid and R236fa/R134a mixture, the deviations are within ±5% error limits for evaporator outlet temperatures and pressures, and ±1% and ±2% for outlet pressures and temperatures of cooling water and hot fluid (oil) of the condenser & evaporator respectively.

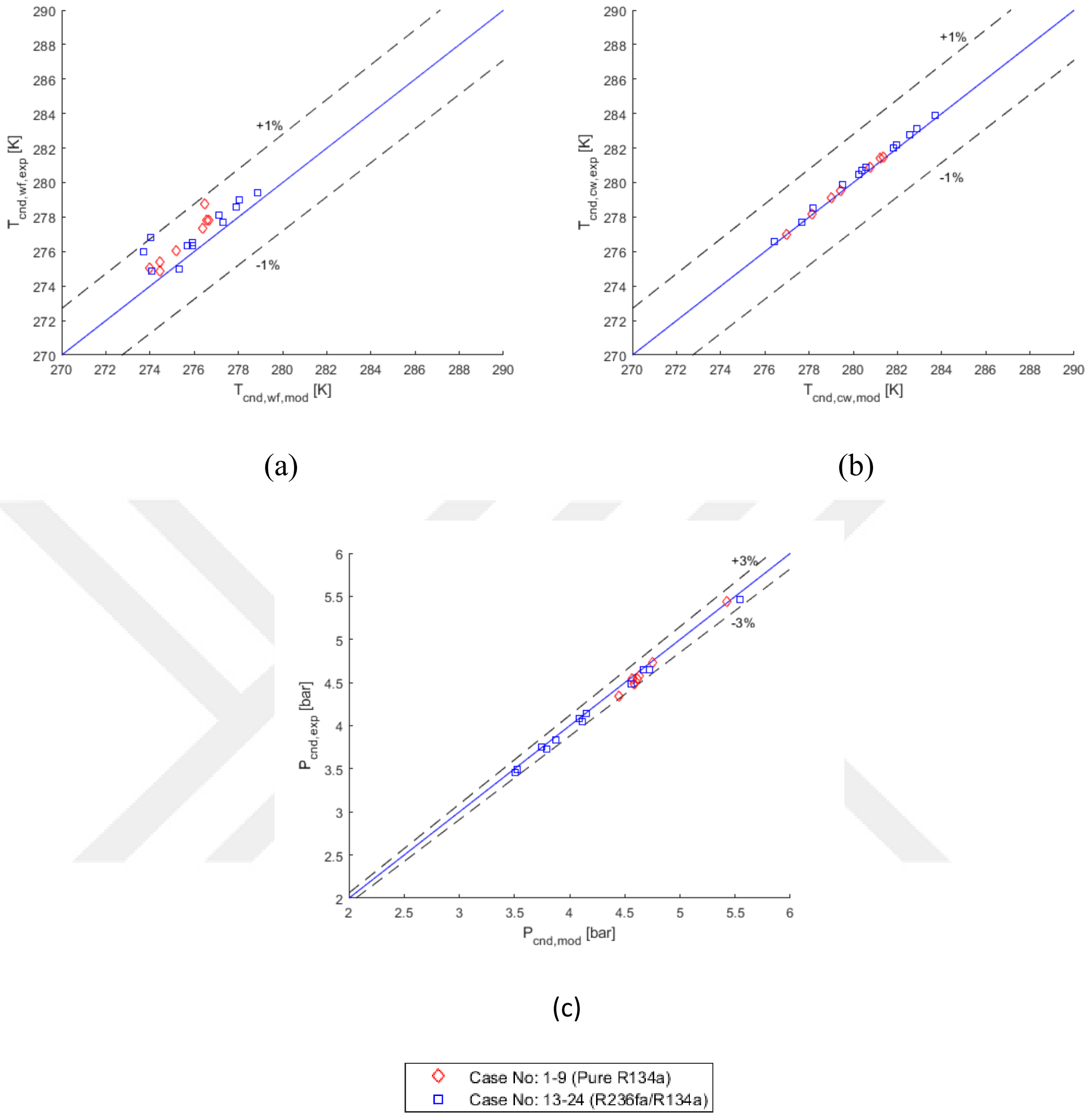

Figure 5.16. Parity plots of (a) working fluid temperature at the condenser outlet, (b) cooling water (ethylene glycol + water) temperature at the condenser outlet, (c) pressure at the condenser outlet.

The results provided in Figure 5.16 shows that the condenser model can predict the working fluid and cooling water (ethylene glycol + water) outlet temperatures within $\pm 1\%$, and condenser outlet pressures within $\pm 3\%$, error limits for all cases (Case 1 to 24).

The accuracy of the heat exchanger model is also tested in terms of the distribution of the heat transfer area based on the fluid phase. The level of sub-cooled mixture at the condenser level indicator are measured during the experimental tests.

In Figure 5.17, an example (Case-24) that shows the sub-cooled liquid level at the condenser is provided. Results tabulated in Table 5.6 shows the measured liquid level vs the model predicted data.

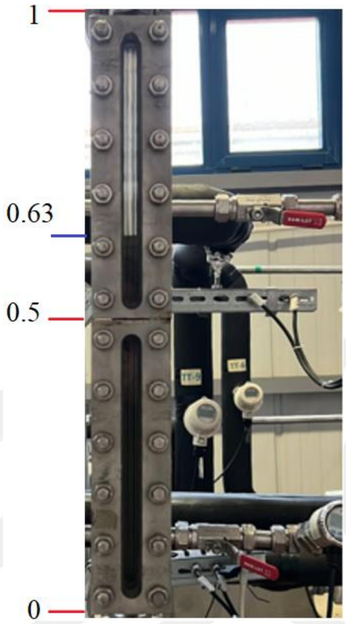

Figure 5.17. An example case for condenser level indicator sub-cooled liquid level (Case 24).

Table 5.6. Experimental vs model results of sub-cooled liquid level at condenser level indicator.

Case Number	**SC Region Area (m^2)**	**LI Liquid Level**		**Relative Error (%)**
	Mod.	**Exp.**	**Mod.**	
13	3.63	0.32	0.59	85.4
14	3.84	0.41	0.63	52.0
15	4.23	0.50	0.69	39.0
16	3.93	0.42	0.64	53.8
17	3.68	0.38	0.60	57.9
18	4.02	0.42	0.66	55.5
19	4.29	0.54	0.70	28.6
20	3.16	0.60	0.51	13.7
21	5.22	0.74	0.85	15.7
22	4.21	0.62	0.69	11.6
23	4.37	0.52	0.71	37.4
24	4.10	0.64	0.67	5.3

The condensation temperature and heat transfer rate are significant parameters to evaluate the effect of the zeotropic blend on the ORC performance. In Figure 5.18, the change of condensation temperature and heat transfer rates for different test cases are shown in comparison to their corresponding pure fluid cases (Case 4 for Case 22; Case 8 for Case 20).

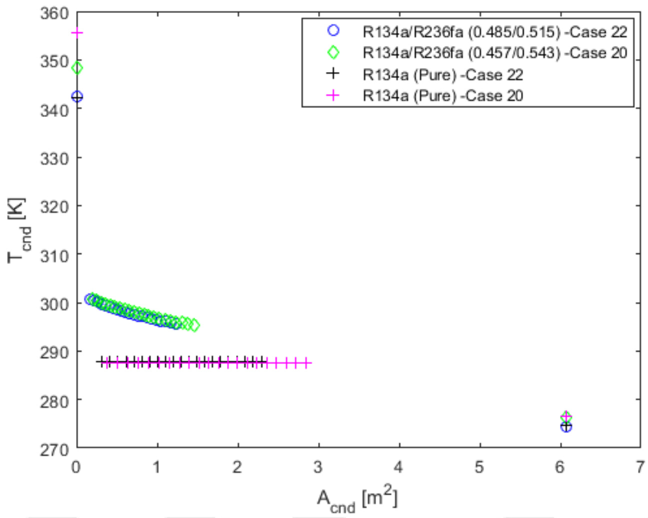

(a)

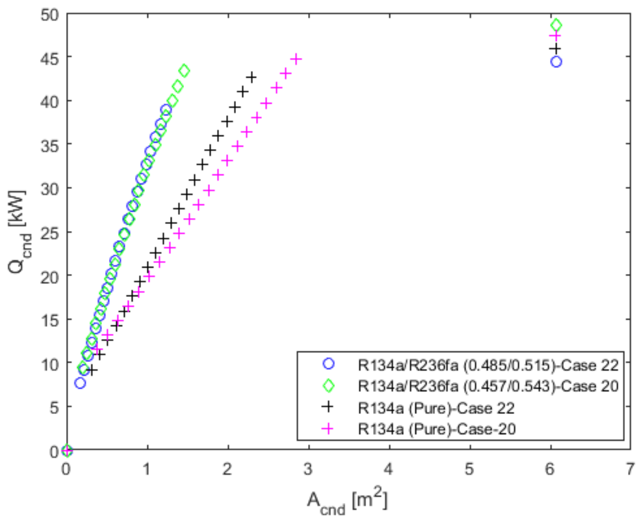

(b)

Figure 5.18. Variation of (a) the condensation temperature b) the condensation heat transfer rate vs the change of condenser area for different test cases (R134a/R236fa vs pure R134a).

The condensation temperature variation vs heat exchanger area A_{cnd} for R134a/R236fa for Case 20 and Case 22 are shown in Figure 5.18. The zeotropic behavior of R134a/R32 mixture can be seen in Figure 5.18. The temperature glides of the condenser $\Delta T_{gl,evp}$ for Case 20 & Case 22 are 5.2 K and 4.9 K, respectively (see Figure 5.18-a). Further, Figure 5.18-a also shows that the condensation area for the phase change of R134a/R236fa blend is smaller than pure R134a.

Figure 5.18-b shows the change in the heat duty of the condenser vs the variation of the condenser area calculated in each computational step. Results provided in Figure 5.18b show that usage of zeotropic mixture R134a/R236fa instead of pure R134a could lead to the deterioration of the heat transfer (Case 22). Besides, the heat transfer rate at the condenser $\dot{Q}_{cnd}$ becomes smaller when the zeotropic mixture R134a/R236fa is used instead of pure R134a (for Case 22). Yet, the usage of zeotropic mixture may also enhance the heat transfer rates (see Figure 5.18b; Case 20). The results provided in Figure 5.18b clearly shows that the mixture composition is one of the main factors which affects the heat transfer mechanism.

6. PARAMETRIC PERFORMANCE STUDIES WITH REFRIGERANT MIXTURES

In this section, parametric performance studies of R134a blends are made to find the best-performing mixtures for the selected regions of pressure and temperature. Firstly, the performance of each selected blend is examined in terms of net power produced and thermal efficiency for a hot fluid temperature range of 363-403 K. The aim is to determine the best performing R134a blends and their mass fraction of the selected mixtures in terms of performance indicators n_{th} and $\dot{W}_{net}$ for the hot source temperatures between 363 and 403 K. In the second part of the study, the parametric performance study is made with respect to the various condenser inlet pressures (550, 600, 650, and 700 kPa) for a hot fluid range of 363 to 393 K.

6.1. Modelling Constraints and Assumptions

The performance of the cycle varies depending on multiple parameters including selected operating conditions, design constraints and the mixture's composition, therefore, it is significant to carry out the performance study by taking all these parameters into account for better prediction accuracy.

In this study, the hot fluid inlet temperature and the expander outlet pressure are selected as decisive variables, whereas the remaining five, including the cooling water inlet temperature, mass flow rate of the working fluid mixture, mass flow rates of the hot fluid (oil) and the cooling water, and the pump outlet pressure, are kept constants for all selected zeotropic blends and processes. The maximum cycle pressure limit is selected as $0.9P_{cr,mix}$ to avoid working in supercritical cycle conditions, whereas the minimum cycle pressure is set to $P_{cnd,out} = P_{cnd,in} - \Delta P_3$ and the phase of each selected mixture at condenser inlet is checked to whether it is superheated vapor using the condenser inlet pressure $P_{cnd,in}$. In the first part of the study, the temperature range for the hot fluid inlet temperature is selected between $T_{hf,in} = 363 - 403\ \mathrm{K}$ to search for the best-performing mixtures at pump isentropic efficiencies of 0.3 and 0.8.

In the second part of the study, both the expander outlet pressures ($P_2 = 550 - 700$ kPa) and hot fluid inlet temperatures ($T_{hf,in} = 363 - 393$ K) are varied to determine the best performing mixtures. The upper limit of the mass fraction of the second component $x_{2,max}$ of each selected R134a blend is determined with respect to the total area needed for the evaporation $A_{tot,ev}$ and condensation $A_{tot,cd}$ processes. The model fixed parameters and decisive variables are presented in Table 6.1, whereas modelling constraints & assumptions are tabulated in Table 6.2. The flowchart of the parametric performance-based study of the ORC model with refrigerant mixtures is shown in Figure 6.1.

Table 6.1. Model parameters and decisive variables.

	Parameters and Decisive Variables		
Variable	**Study I-a**	**Study I-b**	**Study II**
$T_{hf,in}$ (K)	363-403	363-403	363-393
T_7 (K)	277	277	277
P_2 (kPa)	600	600	550-700
P_4 (kPa)	1950	1950	1950
x_2 [−]	$0 \leq x_2 \leq x_{2,max}$	$0 \leq x_2 \leq x_{2,max}$	$0 \leq x_2 \leq x_{2,max}$
$\dot{m}_{wf}$ (kg/s)	0.1	0.1	0.1
$\dot{m}_{hf}$ (m^3/h)	4.5	4.5	4.5
$\dot{m}_{cw}$ (m^3/h)	8.5	8.5	8.5

Table 6.2. Model constraints and assumptions.

Model Constraints and Assumptions
Model Constraints: Superheated vapor: Check for $P_{cd,in} = P_2 - \Delta P_{cd,in}$ Subcritical Cycle: Check $P_{max} = \min(0.9P_{cr,mix}, 1950\text{ kPa})$ Condensed liquid phase: $T_3 = T_{cd,out} + \Delta T_3$ & $T_4 = f(\eta_{pp}, \dot{V}_{wf,mix})$
Mass fraction limit : $x_{2,max} = f(A_{tot,ev}, A_{tot,cd})$
Assumptions: $n_{is,exp} = 0.75$; $n_{pump,is} = 0.3$; T_e=16 °C (Study I-a) $n_{is,exp} = 0.75$; $n_{pump,is} = 0.8$; T_e=16 °C (Study I-b) $n_{is,exp} = 0.75$; $n_{pump,is} = 0.8$; T_e=16 °C (Study II)

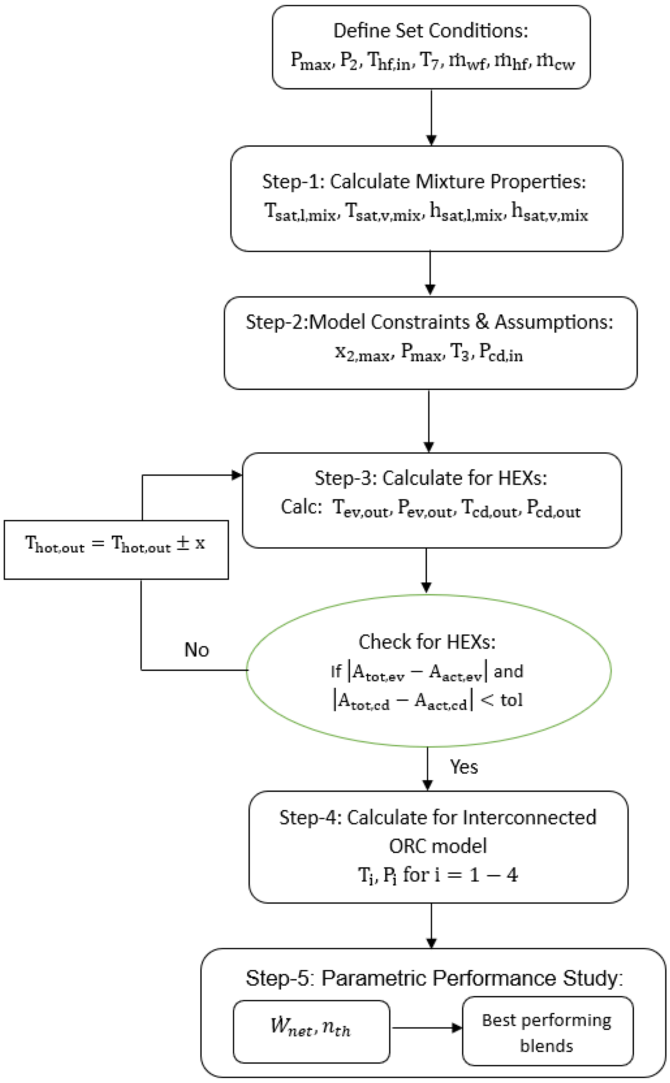

Figure 6.1. Flowchart of parametric performance study model for refrigerant mixtures.

The main aim of this study is to evaluate the performance of the selected R134a blends with varying mass fractions of the second component, x_2. The study split into two distinct parts. In the first part, a parametric performance study with the selected R134a blends for varying mass fractions is made as the hot fluid inlet temperature varies between $T_{hf,in} = 363 - 403$ K for the model parameters and decisive variables in Table 5.4. The first study is split into two sub-studies with respect to the selected pump isentropic efficiencies: Study I-a ($n_{pump,is} = 0.3$) and Study I-b ($n_{pump,is} = 0.8$). The initial aim of the first study (Study I) is to determine the five best performing R134a blends for the given set and decisive parameters. Then, in the second study (Study-II), the parametric performance study is extended for varying expander outlet pressures $P_{exp,out} = 550 - 700$ kPa as the hot fluid inlet temperature varies between $363 - 393$ K using the five best-performing refrigerant mixtures from Study-I. Each analysis in this work is conducted via the ORC model developed in the MATLAB R2021 environment. The parametric performance studies within the scope of this study are made by using a deterministic approach.

6.2. Working Fluid Screening

In this study, R134a is fixed as the first component of the mixture due to its' ease of applicability and supply, low cost, and environmentally friendly nature for laboratory scale applications. The second blend of the mixture is determined by screening out the pure refrigerant candidates with respect to several criteria including toxicity and flammability indexes, ODP and GWP values, and critical pressures. The refrigerant candidates used in pre-screening are provided in Appendix B (see Table B.3).

The following criteria are used in the fluid screening:

1. The working fluids with high toxicity and/or flammability (B2, B3, A3) indexes are eliminated.
2. Hydrochlorofluorocarbons (HCFCs) are not considered in the selection as their usage is restricted due to the Montreal Protocol.
3. Hydrocarbons (HCs) are phased out from screening due to their high flammability.
4. Predefined mixtures in the NIST database (i.e., R410a, R440a) are not considered, and only pure refrigerants are used in the fluid screening.

Table 6.3. Physical and environmental properties of working fluid candidates for R134a blends.

Fluid No	Fluid Name	Mol. Weight (kg/kmol)	T_{cr} (°C)	P_{cr} (bar)	T_{bp} (°C)	ODP[a]	GWP[b] (100 years)	Safety Data[c]	Fluid Type	References Used
1st	R134a	102	101	40.6	-26	0	1430	A1	Isentropic	[30, 34, 35, 36]
2nd	R245fa	134	153	36.1	+15	0	950	B1	Dry	[2, 4, 6, 30, 31]
	R227ea	170	102	29.2	-16	0	3220	A1	Dry	[2, 4, 6, 13, 30]
	R1234yf	114	95	33.8	-29	0	<4.4	A2L	Isentropic	[30, 42, 43, 44]
	R1234ze	114	110	36.3	-19	0	6	A2	Isentropic	[30]
	R236ea	152	139	34.1	+6	0	1200	A2	Dry	[30, 32, 33,37]
	R236fa	152	125	32.0	-2	0	9810	A1	Dry	[2, 13, 30, 38]
	R143a	84	73	38.0	-47	0	3800	A2L	Wet	[2, 13, 30,32,37]
	R152a	66	112	44.5	-24	0	124	A2	Wet	[30]
	R32	52	78	57.8	-51	0	716	A2	Wet	[30,47]
	R125	120	66	36.3	-48	0	3170	A1	Isentropic	[2]

a: ODP relative to R11 [19], b: GWP relative to CO_2 [19], c: ASHRAE Standard 34- [30].

Pure refrigerants listed in Table 6.3 including R245fa, R227ea, R1234yf, R236ea, R236fa, R143a, R32, R125, R1234ze and R152a are selected as second component of R134a blends for the optimization study. The performance of each R134a blend with various mixing ratios is evaluated for the selected operating region in terms of selected performance outputs including net power produced in the cycle $\dot{W}_{net}$, and thermal efficiency n_{th}.

6.3. Effect of Hot Fluid Inlet Temperature (Study-I)

In this section, the performance of each R134a blend is evaluated with respect to the selected hot fluid inlet temperature range. The simulations are made for each specific R134a blend with varying applicable mass fractions for hot fluid inlet temperatures of 363, 373, 383, 393, and 403 K. Set values and decisive parameters are shown in Table 5.4 (see Study I-a and Study I-b). $\dot{W}_{net}$ and n_{th} are used as performance indicators for the parametric performance study. The first study splits into two sub-studies with respect to the change of the pump isentropic efficiency assumption ($n_{pp,is} = 0.3$ for Study I-a; $n_{pp,is} = 0.8$ for Study I-b). The aim of Study-I is to determine the top five best-performing R134a blends and the maximum reachable mass fraction limits for each mixture for the selected heat source temperatures and ORC geometry. Results for Study I-a are given in Figure 6.2 to 6.6, and Study I-b are shown in Figure 6.6 to 6.7.

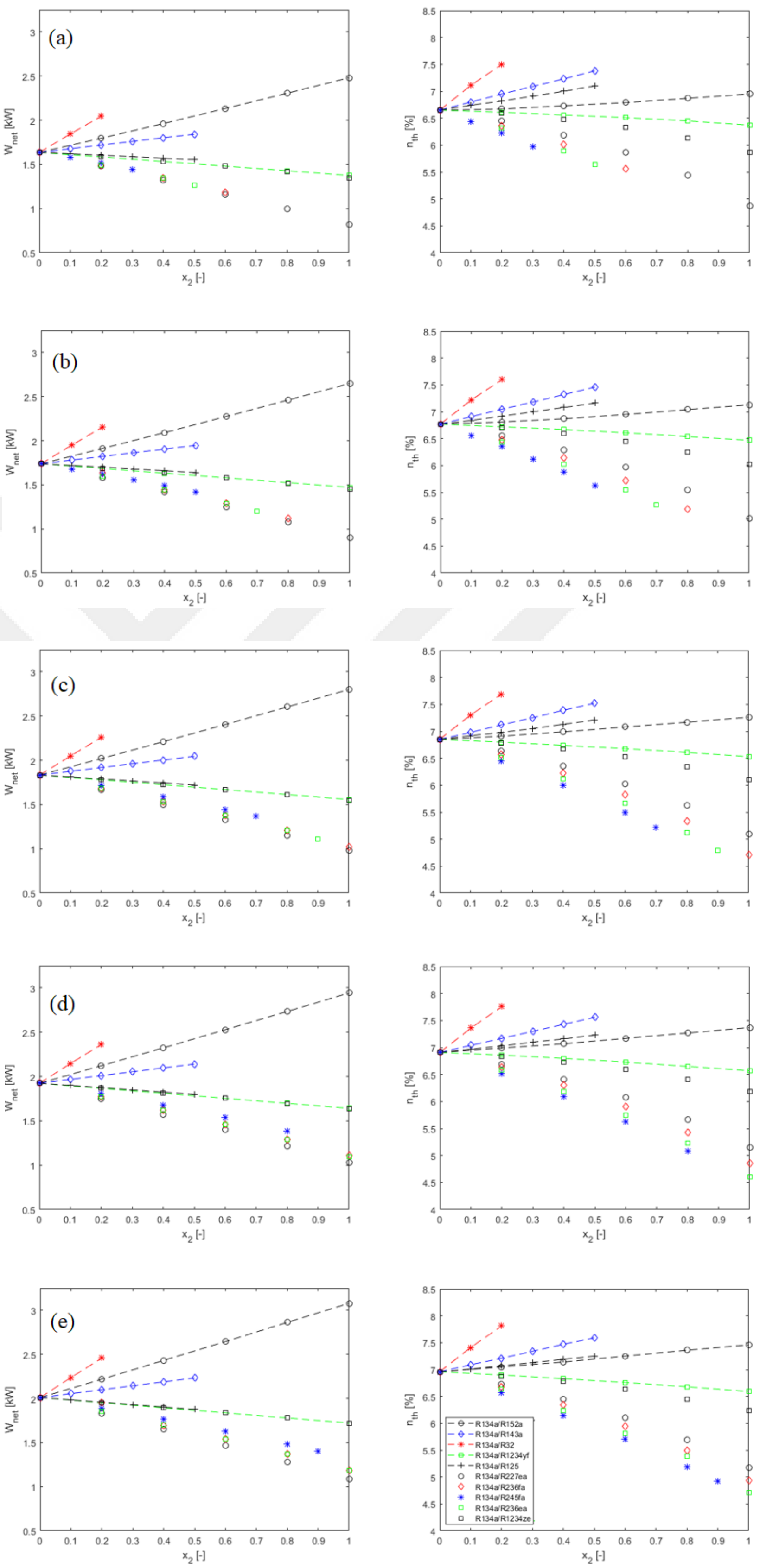

Figure 6.2. Performance indicators for R134a blends with varying mass fractions at (a) 363 K (b) 373 K (c) 383 K (d) 393 K (e) 403 K heat source temperatures (Study I-a).

The results in Figure 6.2 show the variation of performance indicators $\dot{W}_{net}$ and n_{th} for ten different R134a blends with respect to different heat source (oil) temperatures. The results show that the thermal efficiencies and net power production values are changed drastically for all selected refrigerant mixtures as the mixture composition varies from pure R134a. For four out of the ten selected R134a blends including R134a/R32, R134a/R143a, R143a/R125, and R134a/R152a, n_{th} values increase with the increasing mass fraction of the second component x_2, whereas for the remaining six refrigerant blends thermal efficiencies decrease with increasing x_2. The best performance in terms of cycle thermal efficiency is observed for the R134a/R32 blend for all the hot fluid temperature ranges. R134a/R143a and R134a/R125 blends are the second and third best-performing blends (provide better n_{th} than pure R134 case) among the ten selected refrigerant mixtures. The maximum thermal efficiency is observed for R134a/R32 (0.8/0.2) with 7.81 at $T_{hf,in} = 403$ K, which is followed up by R134a/R143a (0.5/0.5) with a thermal efficiency of 7.59, and R134a/R125 (0.5/0.5) with a thermal efficiency of 7.25 at a hot fluid inlet temperature of 403 K. Similar results are also observed for $\dot{W}_{net}$ values for the selected mixtures except for R134a/R125 blend.

The common feature of the top three best-performing blends (R134a/R32, R134a/R143a, and R134a/R125) is the zeotropic behavior they show during the phase change process. As the boiling points of the mixture components differ from each other, the phase change process occurs in a temperature region instead of a constant temperature which is called temperature glide. For R134a/R32, R134a/R143a, and R134a/R125 blends, the increase of thermal efficiency by the increasing mass fraction of the second component x_2 can be explained by the zeotropic behavior. The temperature glide of the evaporation $\Delta T_{gl,evp}$ is 4.1 K, whereas a temperature glide of condenser $\Delta T_{gl,cnd}$ is calculated as 5.5 K for R134a/R32 (0.8/0.2) blend.

However, the utilization of the zeotropic mixture would be confined by the heat transfer area limits of the evaporator and the condenser. The condensation area required for the phase change of R134a/R32 (0.8/0.2) blend ($A_{II,cnd} = 3.63\ m^2$) is much higher than pure R134a ($A_{II,cnd} = 0.90\ m^2$). This means that as the mass fraction of the second component (R32) increases beyond 0.2 ($x_2 > 0.2$), the total condenser area $A_{tot,cd} = 6.08$ would be insufficient to obtain a subcooled liquid mixture at the condenser outlet.

Therefore, the mass fractions of the second components for R134a blends are limited due to inadequate heat exchanger areas stemming from the suppression of the total heat transfer area of the heat exchanger by the heat transfer area of the two-phase zone. For R134a/R32 (0.8/0.2) blend, the total area needed for the two-phase zone $A_{II,cnd} = 3.5$ m^2 is much higher than R134a pure case ($A_{II,cnd} = 0.864$). A similar effect is also seen for the other zeotropic mixtures R134a/R143a and R134a/R125. Figure 6.3 shows the variation of condenser area required for the two-phase zone vs the mass fraction of the second component for R134a/R32, R134a/R143a, and R134a/R125 mixtures at hot fluid inlet temperature of 363 K. In Figure 6.3, the required condensation areas for the phase-change are in the tendency to increase with increasing x_2, and reach a maximum for R134a/R143a (0.5/0.5) with $A_{II,cnd} = 4.98$ m^2 and for R134a/R125 (0.5/0.5) with $A_{II,cnd} = 3.72$ m^2. Therefore, the maximum reachable mass fraction limits of the second component of R134a/R143a and R134a/R125 are $x_{2,max} = 0.5$ for both mixtures.

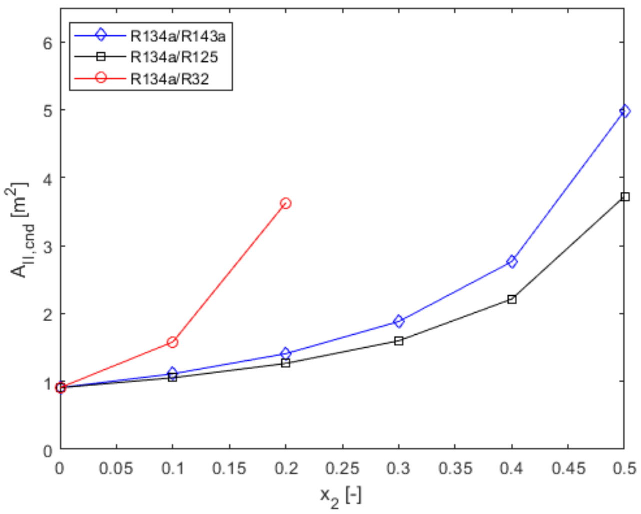

Figure 6.3. Variation of heat transfer area for the two-phase zone of the condenser ($A_{II,cnd}$) vs the mass fraction of the second component (x_2) at $T_{hf,in} = 363$ K.

The evaporation and condensation temperature glides contribute to the cycle performance (see Figure 6.2) for R134a/R32, R134a/R125, and R134a/R143a blends, yet this does not mean that all zeotropic blends can provide better performance than their pure solutions. Depending on the cycle operating conditions and geometrical features of the heat exchangers, the use of zeotropic mixtures can lead to a worse performance than pure refrigerants. The cycle thermal efficiency values for R134a/R245fa, R134a/R236ea, and

R134a/R236fa drastically decrease with increasing x_2 for all the hot fluid temperature ranges (see Figure 6.2). A similar trend is also observed for $\dot{W}_{net}$ values for these three mixtures.

Besides, the mass fraction of the second component can also be limited by the insufficient total evaporator area caused by the increase of the heat transfer area needed for the phase-change process of the evaporator $\left(A_{II,evp}\right)$. Figure 6.4 shows the change of $A_{II,evp}$ vs mass fraction of the second components for R134a/R236ea, R134a/R236fa, and R134a/R245fa, mixtures at $T_{hf,in} = 363$ K. The results in Figure 6.4 show the increasing trend of the required heat transfer area for the phase change at the evaporator with increasing x_2. The mass fraction limits of the second components of R134a/R236ea and R134a/R236fa are obtained as $x_{2,max} = 0.5$ for both mixtures, whereas it is calculated as $x_{2,max} = 0.3$ for R134a/R245fa at $T_{hf,in} = 363$ K.

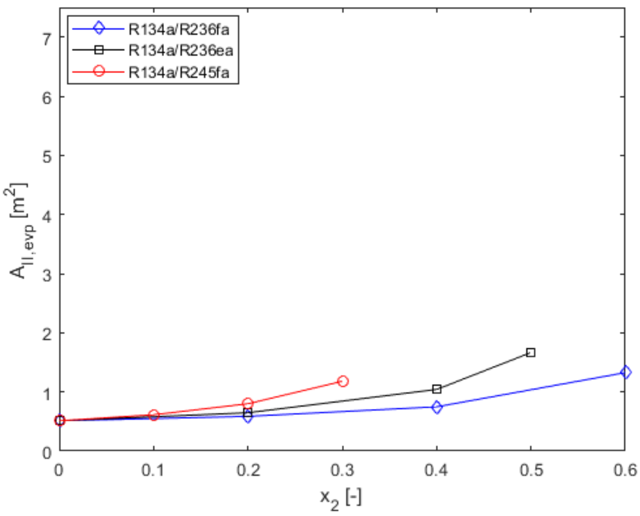

Figure 6.4. Variation of heat transfer area for the two-phase zone of the evaporator ($A_{II,evp}$) vs the mass fraction of the second component (x_2) at $T_{hf,in} = 363$K.

R134a/R245fa is the worst-performing blend among the ten selected R134a blends with all applicable mass fractions of x_2 for the hot fluid inlet temperature range of 363 K to 403 K. As the mass fraction of x_2 increases, the thermal efficiency and the net power delivered from the cycle values are in tendency decrease drastically compared to the pure R134a case. The increase of hot fluid inlet temperature also reinforces this effect. An evaporation temperature glide of 6.2 K and 9.2 K are obtained by R134a/R245fa (0.7/0.3) at $T_{hf,in} = 363$ K, and R134a/R245fa (0.3/0.7) at $T_{hf,in} = 383$ K, respectively.

In terms of net power produced from the cycle $\dot{W}_{net}$, R134a/R152a, R134a/R32, and R134a/R143a blends tend to increase with the increasing mass fraction of x_2, whereas the remaining 7 blends lead to decrease in $\dot{W}_{net}$ of all hot fluid inlet temperature values. Among ten refrigerant blends, R134a/R152a is the high performing blend of the selected range of hot fluid inlet temperature $(T_{hf,in} = 363 - 403\ K)$, when the mass fraction of the second component is higher than 0.2 ($x_2 > 0.2$). The highest obtainable $\dot{W}_{net}$ in Study I-a is obtained for pure R152a case for the hot fluid inlet temperature of 403 K ($\dot{W}_{net}$=3.08 kW). For the selected hot fluid inlet temperature range, R134a/R32 would be the second high-performing mixture for $x_2 > 0.2$, whereas as the mass fraction of R32 is smaller than 0.2 ($x_2 \leq 0.2$), R134a/R32 becomes the best-performing blend in terms of $\dot{W}_{net}$. R134a/R227ea, R134a/R236fa, and R134a/R236ea are the top three worst-performing refrigerant mixtures in terms of net power produced. The lowest $\dot{W}_{net}$ value is provided by pure R227ea for the hot fluid temperature of 403 K ($\dot{W}_{net}$=0.819 kW).

Figure 6.2 also shows that net power output decreases with increasing mass fraction of the second component for most of the refrigerant mixtures selected. Especially, for the zeotropic mixtures with high evaporation and condensation temperature glides such as R134a/R245fa, R134a/R236ea, R134a/R236fa, R134a/R227ea, net power produced from the cycle values decrease more compared to refrigerant mixtures which show near-azeotropic behavior (R134a/R1234yf and R134a/R1234ze). This is due to the reason that, when the evaporation or condensation temperature glides high compared to the temperature differences between the heat source and the heat sink, it results in a decrease in the evaporation pressure or an increase in condensation pressure [49].

In our study, the condensation pressure (P_{cnd}) is almost fixed for all mass fractions of the selected R134a blends (see Figure D.1 & Table D.1), and the heat transfer areas of the evaporator and condenser are also fixed with the geometries of the experimental ORC set-up available in our laboratory. Therefore, condensation temperature increases with increasing mass fraction of the second component. This caused by the limitation of the calculated total heat transfer area by the actual heat transfer areas of the evaporator and the condenser available in our laboratory. When the heat transfer area of the evaporator $A_{tot,ev}$ is inadequate for the selected refrigerant mixture and its composition, the area required for the phase change during the evaporation A_{II} increases. This can lead to a limited contribution of the super-heated zone A_{III} to the total calculated heat transfer area and the rate of heat transfer. Further, when the difference in the boiling points of the two components of the zeotropic mixture increases, the evaporator outlet temperatures also increase due to the deterioration of the heat transfer mechanism. Figure 6.5-b shows the change in the heat duty of the evaporator vs the variation of the mass fraction of the second component of R134a/R245fa mixture. Results provided in Figure 6.5-b clearly show the deterioration of the heat transfer as the zeotropic blend R134a/R245fa is used. Besides, the heat transfer rate at the evaporator $\dot{Q}_{evp}$ becomes smaller when the zeotropic mixture R134a/R245fa is used instead of pure R134a. Although, the temperature at the evaporator outlet $T_{evp,out}$ increases compared to the pure R134 case (see Figure 6.5-a). This effect is also seen for R134a/R236ea and R134a/R236fa which have large boiling point differences.

The variation of the evaporator outlet temperatures of the selected refrigerant blends are shown in Figure D.4-(a) in Appendix D. Results show that the temperature at the evaporator outlet values for zeotropic blends such as R134a/R245fa, R134a/R236ea, and R134a/R236fa are in the tendency to increase with the increasing mass fraction of the second component. Interestingly, these three blends are among the worst performing blends in terms of net power outputs. The increase in the evaporator outlet temperature also leads to an increase in the condenser inlet temperatures (see Figure D.4-(b)). Similarly, as the condensation heat transfer area is insufficient to meet the increased heat transfer area demand provided by the zeotropic mixture, this would lead to an increase in condenser outlet temperature due to the deterioration of the heat transfer mechanism. This will result in a smaller temperature difference (see Figure D.5) and the enthalpy drop at the expander during expansion. Since the mass flow rate of the mixtures is fixed, net power output only changes depending on the enthalpy drop caused by the temperature difference at the expander, therefore, $\dot{W}_{net}$ values decrease as a function of the enthalpy difference caused by the evaporation and the condensation temperatures. Therefore, the net power produced from the ORC decreases.

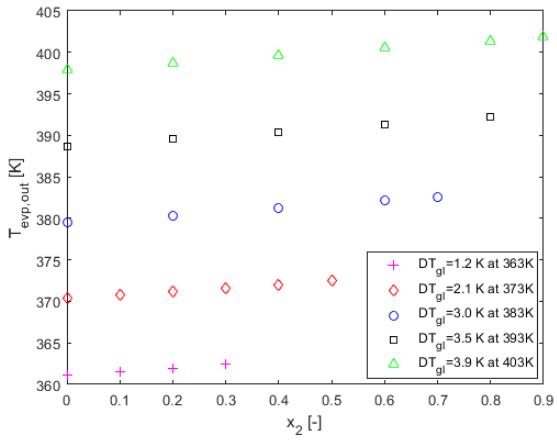

(a)

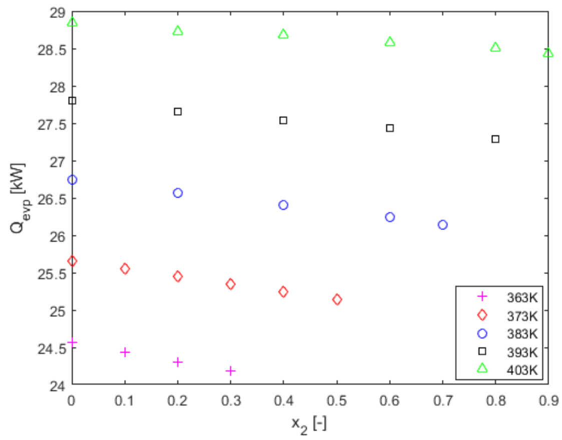

(b)

Figure 6.5. Variation of (a) the evaporator outlet temperature (b) the evaporation heat transfer rate vs the change of mass fraction of the second component x_2 for varying hot fluid inlet temperatures (R134a/R245fa vs pure R134a).

Comparable results are also observed in the study conducted by Y. Li et al. [49], as they fixed the condensation pressure and compared the performance of refrigerant mixtures with pure working fluids. In their study, compatible with the findings of our study, the net power output values for refrigerant mixtures with large temperature glides are usually lower than the pure fluids as the condensation pressure is fixed. However, as they fixed the condensation dew point temperature, the refrigerant mixtures have given better performance in terms of both net power output and thermal efficiency. In this case, the larger temperature glides lead to a better performance due to the better thermal match they provide in the evaporator and the condenser [49].

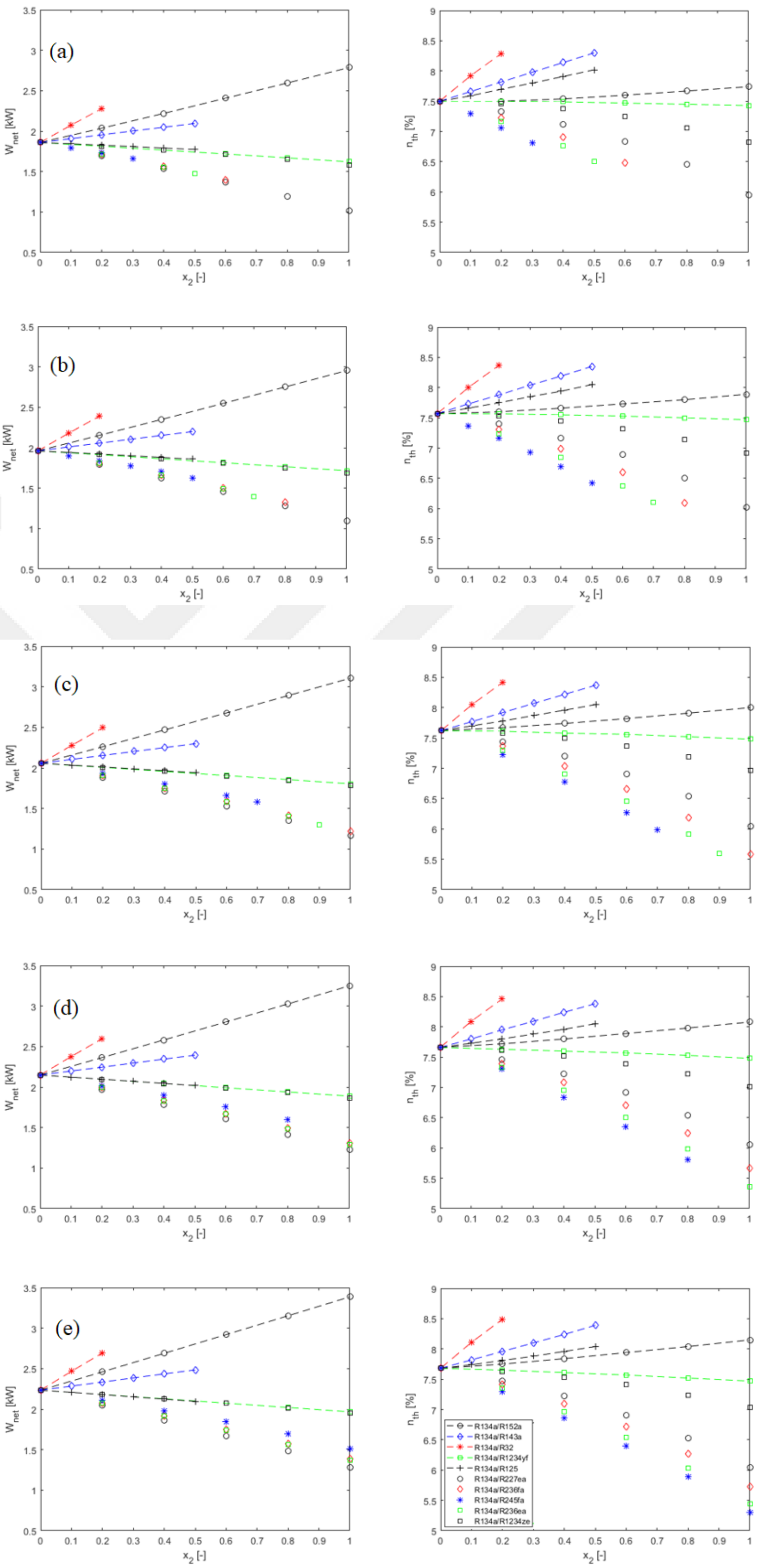

Figure 6.6. Performance indicators for R134a blends with varying mass fractions at (a) 363 K (b) 373 K (c) 383 K (d) 393 K (e) 403 K heat source temperatures (Study I-b).

Figure 6.6 shows the simulation results for ten different R134a blends with varying mixture compositions for Study I-b. The results in Figure 6.6 show the variation in performance indicators $\dot{W}_{net}$ and n_{th} for the selected R134a blends with respect to different heat source (oil) temperatures. Like Study I-a, the thermal efficiencies and cycle net power values change for all selected refrigerant mixtures as the mixture composition varies, except R134a/R1234yf and R134a/R1234ze. R134a/R32, R134a/R143a, R134a/R125, and R134a/R152a are the top four best performing mixtures that provide the highest thermal efficiency and net power output for the whole selected hot fluid inlet temperature range ($T_{hf,in} = 363 - 403$ K). The best performance in terms of n_{th} is obtained for R134a/R32 blend for the whole hot fluid inlet temperature spectrum. R134a/R143a and R134a/R125 are the second and the third best performing blends that provide better thermal efficiency than the pure R134a. The maximum thermal efficiency obtained by R134a/R32 (0.8/0.2) with 8.49% at $T_{hf,in} = 403$ K, followed up by R134a/R143a (0.5/0.5) with a thermal efficiency of 8.39%, and R152a (pure) with a thermal efficiency of 8.15 at a hot fluid inlet temperature of 403 K. Among the ten selected refrigerant mixtures, only five out of ten R134a blends including R134a/R227ea, R134a/R1234yf, R134a/R1234ze, R134a/R152a, and R134a/R245fa (only for $T_{hf,in} = 403$ K) can be used as pure solutions for both components, and R152a is the only one that provides better thermal efficiency than pure R134a case. R134a/R143a and R134a/R32 are the two refrigerant mixtures that can provide a better performance than pure solutions of R152a.

In terms of net power produced from the cycle $\dot{W}_{net}$, are in the tendency to increase with increasing mass fraction of x_2 for R134a/R152a, R134a/R32, and R134a/R143a blends. For the remaining seven blends $\dot{W}_{net}$ values for all hot fluid inlet temperatures decrease with increasing mass fraction of x_2 (see Figure 6.7b) Like Study I-a, R134a/R152a is the highest performance blend among the selected mixtures for the selected range of hot fluid inlet temperature $(T_{hf,in} = 363 - 403\ K)$, when the mass fraction of the second component is higher than 0.2 ($x_2 > 0.2$). In Study I-b, the maximum reachable $\dot{W}_{net}$ is obtained for R152a (pure) solution for a hot fluid inlet temperature of 403 K ($\dot{W}_{net}$=3.38 kW). R134a/R32 would be the second-best performing blend for $x_2 > 0.2$. However, when the mass fraction of R32 is smaller than 0.2 ($x_2 \leq 0.2$), R134a/R32 becomes the best performing blend in terms of $\dot{W}_{net}$. R134a/R227ea, R134a/R236fa, and R134a/R236ea are the top three worst performing refrigerant mixture in terms of net power produced. The lowest $\dot{W}_{net}$ value is obtained by

R227ea (pure) for hot fluid temperature of 403 K ($\dot{W}_{net}$=1.01 kW). Interestingly, although R134a/R227ea mixture provides the lowest net cycle power, the worst cycle thermal efficiency is obtained by R134a/R245fa blend with $x_2 \geq 0.8$.

The lowest cycle thermal efficiency is obtained for R245fa (pure) case with n_{th} = 5.3% for $T_{hf,in}$ = 403 K. This can be explained by the change of heat transfer rates during the evaporation process. The heat duties of the evaporator $Q_{evp,in}$ for R134a/R245fa remain almost constant (see Figure 6.7-a) for increasing mass fractions of x_2, whereas $\dot{W}_{net}$ decrease drastically with increasing mass fractions of R245fa.

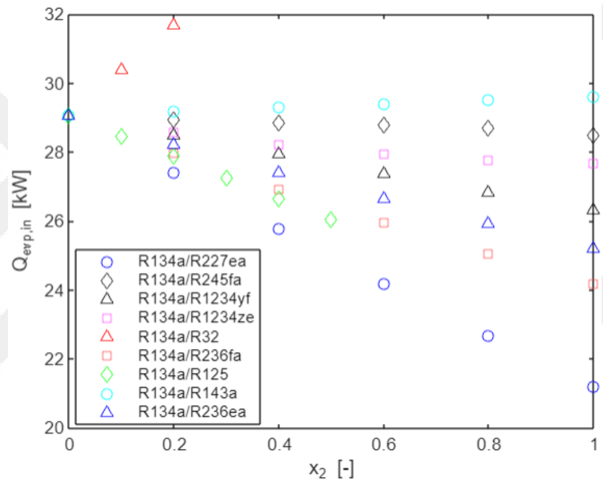

(a)

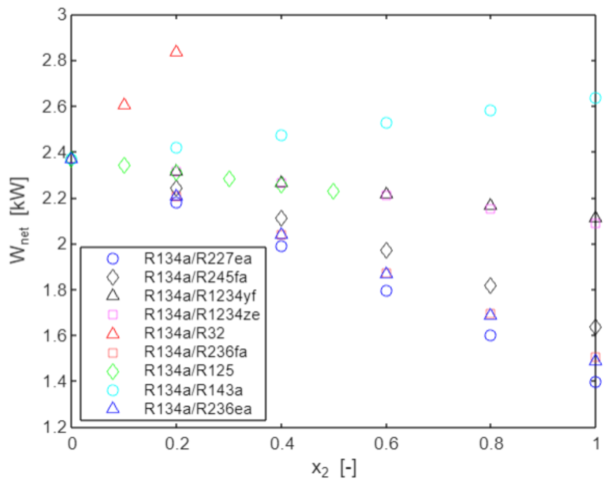

(b)

Figure 6.7. The variation of (a) the heat duty in the evaporator $Q_{evp,in}$ (b) net power produced $\dot{W}_{net}$ vs the mass fraction of the second component x_2 for $T_{hf,in}$ = 403 K.

6.4. Effect of Varying Expander Outlet Pressure (Study-II)

The scope of the study has been expanded to find mixture blends maximizing the selected performance parameters for different pressure ratios in the hot fluid inlet temperature range of 363-393 K. The parametric performance study is made for hot fluid inlet temperatures of 363 K, 373 K, 383 K, 393 K, and expander outlet pressures of 550 kPa, 600 kPa, 650 kPa, and 700 kPa. Top five best performing R134a blends from Study-I including R134a/R152a, R134a/R143a, R134a/R32, R134a/R125 and R134a/R1234yf are used in Study-II. The permissible mass fractions are determined considering the actual geometries of connection pipes, and heat transfer areas for the evaporator and condenser.

6.4.1. Hot Fluid Inlet Temperature of 363 K

Figure 6.8 shows the variation of performance indicators of selected refrigerant blends with respect to the change of expander outlet pressure for various mass fractions.

As it can be seen from Figure 6.8a to 6.8e, four out of five mixtures including R134a/R143a, R134a/R32, R134a/R125, and R134a/R152a lead to an increase in the thermal efficiency of the cycle for the whole selected expander outlet pressure range with the increasing mass fraction of the second component. Among the five selected mixtures, R134a/R1234yf is the only refrigerant mixtures which leads to a decrease in the cycle thermal efficiency when the mass fraction of R1234yf increases. Results also show that only two refrigerant mixtures including R134a/R152a and R134a/R1234yf have remained from the five as the mass fraction of the second component $x_2 \geq 0.6$. Although R134a/R152a and R134a/R1234yf are the top two worst-performing mixture when the mass fraction of the second component of the mixture is lower than $x_2 < 0.6$, they can be used for the entire composition including the pure cases for each mixture component. This is due to the azeotropic behavior they show during the phase change. The azeotropic nature makes temperature glides in the evaporation and condensation close to zero for both R134a/R152a ($\Delta T_{gl,ev,max} = 0.1$ & $\Delta T_{gl,cd,max} = 0.12$) and R134a/R1234yf ($\Delta T_{gl,ev,max} = 0.01$ & $\Delta T_{gl,cd,max} = 0.01$) (see Figure 6.9).

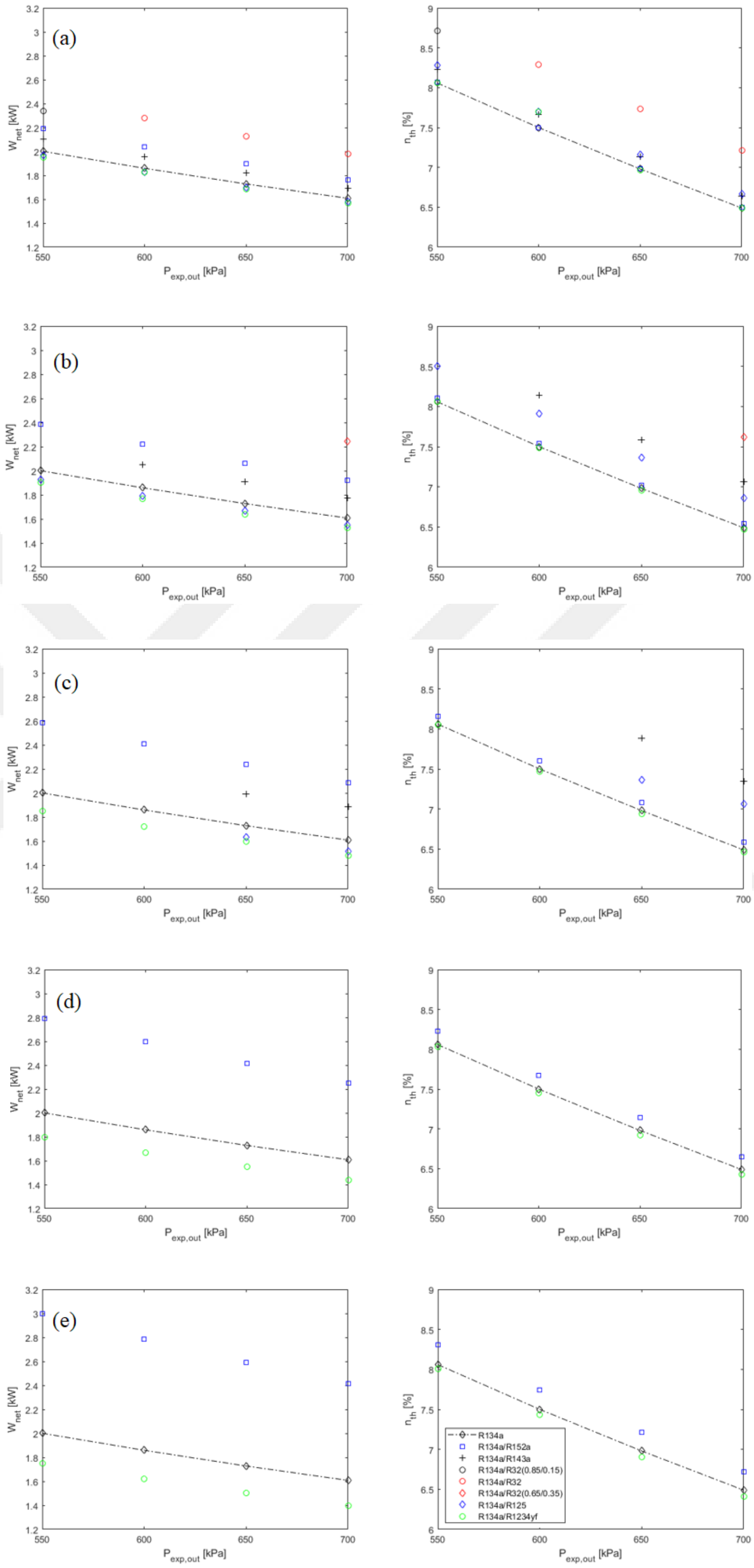

Figure 6.8. Performance indicators of R134a blends with varying expander outlet pressure (kPa) and mass fractions (a) 0.8/0.2 (b) 0.6/0.4 (c) 0.4/0.6 (d) 0.2/0.8 (e) 0.0/1.0 at a heat source temperature of 363 K.

The highest achievable thermal efficiency of the ORC is 8.71% and obtained for R134a/R32 (0.85/0.15) at an expander outlet pressure of 550 kPa. The second highest achievable thermal efficiency of the ORC is 8.58% and obtained for R134a/R143a (0.7/0.3) at an expander outlet pressure of 550 kPa. The third blend that provide a higher efficiency than R134a (pure) case is R134a/R125 (0.6/0.4) with n_{th} =8.5% ($P_{exp,out} = 550$ kPa), whereas the lowest n_{th} is 6.4% and obtained from R1234yf (pure) at $P_{cnd,in} = 700$ kPa.

In Figure 6.9a to 6.9e, the net power produced from the cycle values are also provided for each selected mass fraction. The highest net power output is obtained for R152a (pure) case with $\dot{W}_{net} = 2.99$ kW as the expander outlet pressure is set to 550 kPa. The second high net power output that gives high performance than R134a (pure) is obtained by R134a/R32 (0.85/0.15) with $\dot{W}_{net} = 2.34$ kW. The third best-performing blends that give high net power output than R134a (pure) case is R134a/R143a (0.7/0.3) with $\dot{W}_{net} = 2.15$ kW. Despite providing the second-best performance in terms of net power output, due to the zeotropic behavior of R134a/R32 blend can only be used for a limited mass fraction of R32. This is caused by the area needed to obtain a sub-cooled mixture surpassing the total condenser area limit $A_{tot,cd} = 6.08$ m^2 when the mass fraction of R32 increases beyond $x_2 > 0.15$. This is also valid for R134a/R143a blend as the mass fraction of R143a exceeds 0.3.

The present study not only shows the mass fractions that give the maximum performance for each selected mixture but also evaluates the performance of the selected R134a blends when the same mass fraction is applied. The results tabulated in Table C.3 show the variation of the selected performance indicators n_{th} and $\dot{W}_{net}$ for the selected expander outlet pressures for each specific mass fraction. The highest net power output is obtained by R152a for each specific mass fraction including $x_2 = 0.2$ with 2.19 kW, $x_2 = 0.4$ with 2.38 kW, $x_2 = 0.6$ with 2.58 kW, $x_2 = 0.8$ with 2.79 kW, and $x_2 = 1$ with 2.99 kW. The highest thermal efficiencies in each specific mass fraction are obtained by R134a/R143a with 8.41% at $x_2 = 0.2$, R134a/R25 with 8.39% at $x_2 = 0.4$, R134a/R152a with 8.16% at $x_2 = 0.6$, R134a/R152a with 8.23% at $x_2 = 0.8$, and R134a/R152a with 8.31% at $x_2 = 1$.

Increasing the expander outlet pressure results in a decrease in thermal efficiencies and net power outputs, however, it also causes an increase in the maximum mass fraction limits of the second component of the selected mixtures. The results provided in Table C.3 clearly show that as the expander outlet pressure is set to 600 kPa the maximum mass fraction limit of the second component x_2 of R134a/R143a increases from 0.3 to 0.5. R134a/R143a (0.5/0.5) at $P_{exp,out} = 600$ kPa also coincides with the maximum reachable thermal efficiency point at this expander outlet pressure. Due to the increase of x_2 at $P_{exp,out} = 600$ kPa condition, an additional increase of 0.32% in thermal efficiency can be provided by using R134a/R143a (0.5/0.5) instead of R134a/R143a (0.7/0.3) (see Table C.3).

Similarly, as the expander outlet pressure of 650 kPa is used maximum reachable mass fraction of R32 reaches 0.3, whereas R143a and R125 reach 0.6. The maximum achievable mass fractions for R143a ($x_2 = 0.75$) and R125 ($x_2 = 0.75$) are obtained at an expander outlet pressure of 700 kPa. R134a/R143 (0.5/0.5) coincides with the maximum efficiency point at $P_{exp,out} = 700$ kPa, and the additional increase of the mass fraction of R143a from 0.6 ($P_{exp,out} = 650$ kPa) to 0.75 can provide an additional increase of 0.21% in thermal efficiency compared to R134a/R143a (0.4/0.6) at $P_{exp,out} = 700$ kPa.

Further, R134a/R143a (0.25/0.75) at $P_{exp,out} = 700$ kPa provides a better thermal efficiency than R134a/R1234yf and R134a/R152a for the whole composition including their pure components, and R134a/R125 with a mass fraction of $x_2 \leq 0.5$.

Figure 6.9 shows the temperature glides of the evaporator and the condenser for the selected refrigerant mixtures with various mass fractions of the second component x_2. The calculation of the theoretical temperature glides is made for the pressure corresponding to the evaporator inlet $P = P_{ev,in}$ and the condenser inlet $P = P_{cd,in}$ for the expander outlet pressure of 550 kPa. For the calculation of the theoretical temperature glides, the liquid saturation temperature $T_{sat,l,mix}$ and vapor saturation temperature $T_{sat,v,mix}$ for both the evaporator and the condenser are determined using Refprop v9.1 using the corresponding evaporator and condenser inlet values obtained from the ORC model [45]. Then, the theoretical temperature glides of the evaporation and condensation can be calculated by taking the difference between vapor and liquid saturation temperatures ($\Delta T_{gl} = T_{sat,v,mix} - T_{sat,l,mix}$). However, the more realistic temperature glide curves that show the maximum available mass fraction limit of the second component $x_{2,max}$ for the selected mixtures. Therefore, the model-predicted temperature glides of the evaporation and condensation are also provided with their maximum achievable mass fraction limits to interpret the results more accurately.

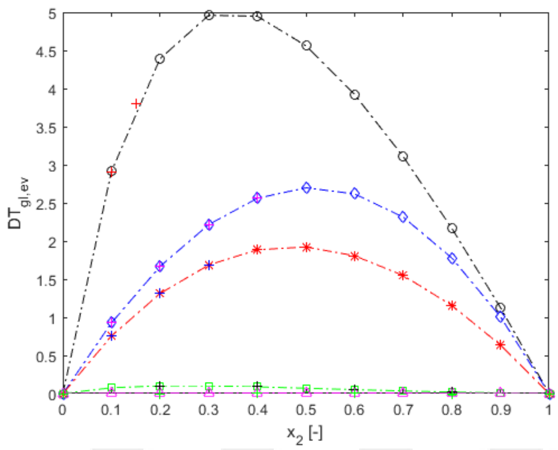

(a)

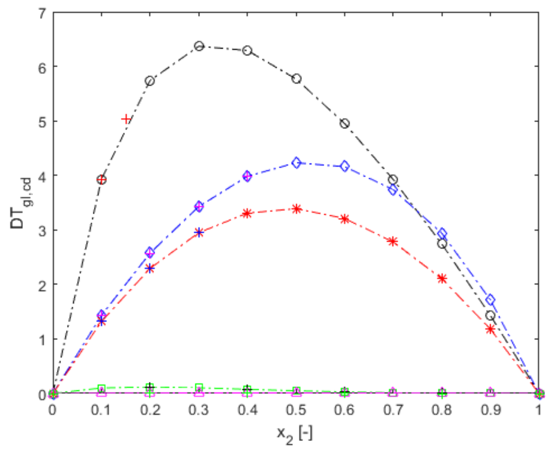

(b)

Figure 6.9. Calculated (model) vs theoretical temperature glides in (a) the evaporator and (b) the condenser for the selected mixtures with different mass fractions of the second component x_2 at $P_{exp,out} = 550$ kPa ($P_{cd,in} = 523$ kPa, $P_{ev,in} = 1949$ kPa).

6.4.2. Hot Fluid Inlet Temperature of 373 K

In Figure 6.10, the variations of performance indicators $\dot{W}_{net}$ and n_{th} of selected refrigerant blends with respect to the change of expander outlet pressure for various mass fractions are presented.

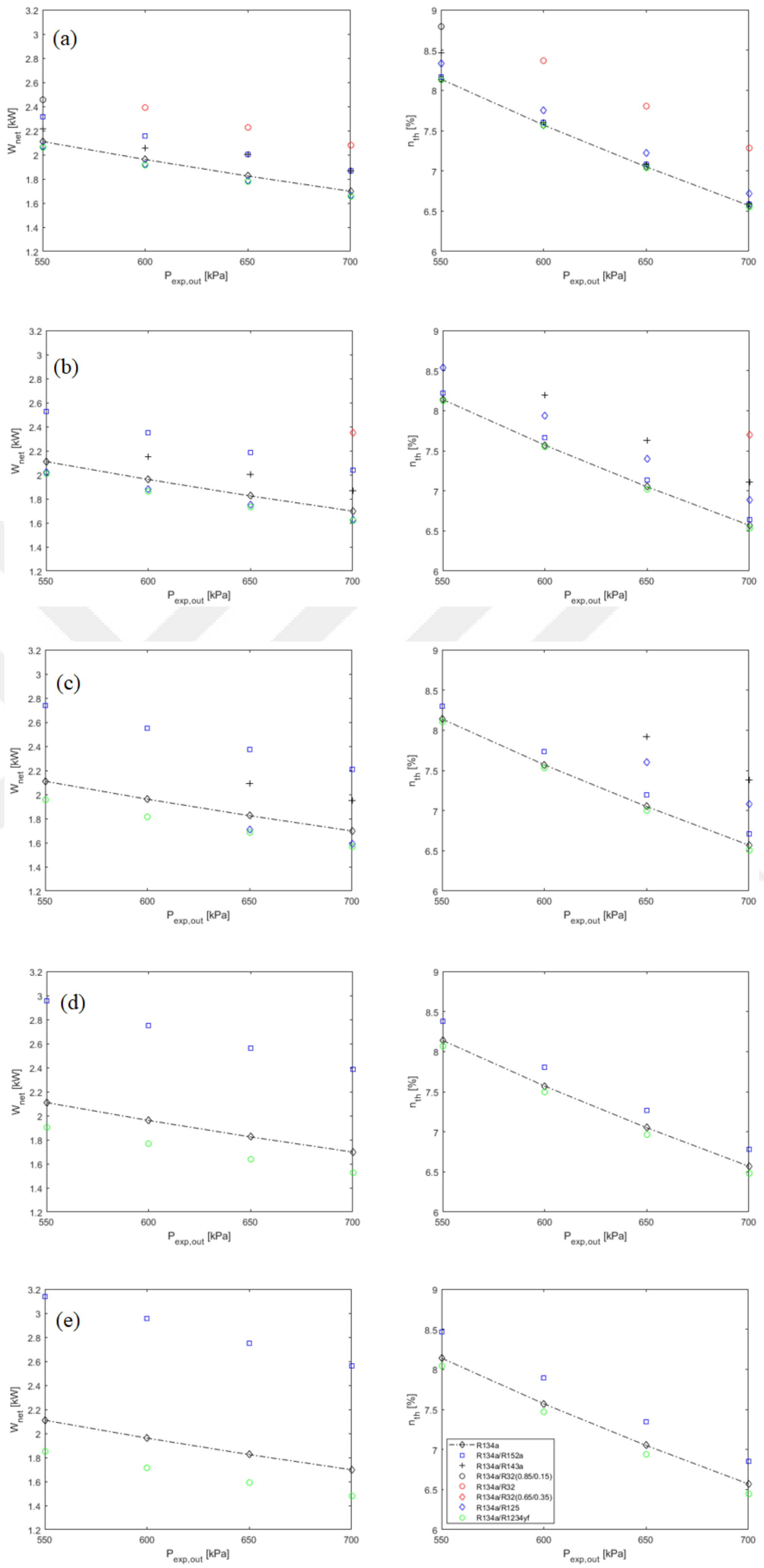

Figure 6.10. Performance indicators of R134a blends with varying expander outlet pressure (kPa) and mass fractions (a) 0.8/0.2 (b) 0.6/0.4 (c) 0.4/0.6 (d) 0.2/0.8 (e) 0.0/1.0 at a heat source temperature of 373 K.

As seen in Figure 6.10, five different R134a blends have been used in the analysis at first. However, the number of mixture blends that can be used is decreased with increasing mass fraction, x_2, due to the geometrical features of the heat exchangers, there are only two out of five R134a blends, R134a/R1234yf and R134a/R152a, have remained from the selected mixtures as the $x_2 = 1$ (see Figure 6.10-e).

Results provided in Figure 6.10 reveal that except R134a/R1234yf, the remaining four R134a blends including R134a/R143a, R134a/R32, R134a/R125, and R134a/R152a provide a better performance in terms of thermal efficiency than pure R134a case for all the expander outlet pressure conditions ranging between 550-700 kPa. Maximum achievable thermal efficiency is obtained for R134a/R32 (0.85/0.15) blend at $P_{exp,out} = 550$ kPa with 8.79%. However, when the mass fraction of R32 increases ($x_2 > 0.15$), the condenser area ($A_{tot,cnd} = 6.08$ m^2) could not compensate for the condensation temperature glide provided by R134a/R32 mixture, therefore, R134a/R32 mixture can only be used for a limited mass fraction of the second component ($x_2 \leq 0.15$). R134a/R143a is the mixture that gives the second-best performance. The highest thermal efficiency for R134a/R143a blend is obtained for R134a/R143a (0.7/0.3) with 8.64% when the expander outlet pressure is set to 550 kPa. Like R134a/R32 blend, the maximum achievable mass fraction of the second component of R134a/R143a is limited to $x_2 = 0.3$ when $P_{exp,out} = 550$ kPa since the condensation area becomes insufficient to provide a sub-cooled liquid mixture at the condenser outlet.

R134a/R32 and R134a/R143a are the top two best-performing blends that provide higher thermal efficiency than other mixtures for all selected expander outlet pressure values, although they have a limited applicable mass fraction of the second component. In contrast, R134a/R1234yf can be used for the whole composition including the pure fluid cases for R134a and R1234yf, yet R134a/R1234yf shows the worst performance for all mixture mass fractions for the whole expander outlet pressure variations. This stems from that although the condensation and evaporation pressures do not change meaningfully with the varying mass fractions of R134a/R1234yf blend, the enthalpy drop provided by the temperature difference between the inlet and the outlet of the expander becomes smaller with increasing mass fractions of R1234yf (see Figure E.1). Besides, the temperature differences provided by the expander also decrease with the increasing expander outlet pressure (see Figure E.2). Therefore, both the net power output and thermal efficiency values decrease with increasing mass fraction of R1234yf for the all-expander outlet pressure range. However, the evaporation and condensation temperature glides provided by R134a/R1234yf are remarkably close to 0 (see Figure 6.11) which means that R134a/R1234yf mixture shows azeotropic behavior. This phenomenon can be easily seen in Table C.4 in which the thermal efficiencies remain almost constant for R134a/R1234yf with the increasing mass fractions of R1234yf (In the case of pure R134a $n_{th} = 8.14\%$ whereas for pure R1234yf $n_{th} = 8.04\%$ at $P_{exp,out} = 550$ kPa).

In Figures 6.10a to 6.10e, the net power produced from the cycle values are also provided for each specific mass fraction. Figure 6.10 clearly shows that the maximum net power output is obtained by R134a/R152a blend. The highest net power outputs are obtained for R152a (pure) cases for each specific expander outlet pressure with a maximum of $\dot{W}_{net} =$ 3.17 kW as the expander outlet pressure is set to 550 kPa. R134a/R152a blend is the top-performing blend in terms of net power output for each specific expander outlet pressure condition as the mass fraction of the second component x_2 is either equal or higher than 0.4. The second high net power output that gives higher performance than R134a (pure) case is reached by R134a/R32 (0.85/0.15) with $\dot{W}_{net} = 2.45$ kW. R134a/R143a (0.7/0.3) with $\dot{W}_{net} = 2.26$ kW is the third best-performing blend that gives a higher net power output than pure R134a. However, due to the zeotropic behavior of R134a/R32 and R134a/R143a blends, the area needed to obtain a sub-cooled mixture surpasses the total condenser area limit $A_{tot,cd} = 6.08$ m^2, as the mass fraction of R32 increases beyond $x_2 > 0.15$ and R143a exceeds $x_2 > 0.3$.

The performance of the selected refrigerant mixtures is also evaluated as the same mass fraction is applied. The results presented in Table C.4 show the change in performance indicators n_{th} and $\dot{W}_{net}$ for the varying expander outlet pressures at each specific mass fraction. The highest net power output is obtained by R134a/R152a for all compositions that satisfy the condition $x_2 \geq 0.2$ including $x_2 = 0.2$ with 2.31 kW, $x_2 = 0.4$ with 2.52 kW, $x_2 = 0.6$ with 2.74 kW, $x_2 = 0.8$ with 2.95 kW, and $x_2 = 1$ with 3.17 kW. The highest thermal efficiencies in each specific mass fractions are obtained by R134a/R32 at $x_2 = 0.15$ with 8.79%, R134a/R125 with 8.33% at $x_2 = 0.2$, R134a/R143a with 8.64% at $x_2 = 0.3$ R134a/R125 with 8.54% at $x_2 = 0.4$, R134a/R152a with 8.30% at $x_2 = 0.6$, R134a/R152a with 8.38% at $x_2 = 0.8$, and R134a/R152a with 8.47% at $x_2 = 1$.

Like the previous case $\left(T_{hf,in} = 363\ K\right)$, the increase in the expander outlet pressure leads to a decrease in thermal efficiencies and net power outputs, yet it also provides an increase in maximum mass fraction limits of the second components of the selected blends. The result given in Table C.4 shows that as the expander outlet pressure is set to 600 kPa the maximum mass fraction limit of the second component x_2 of R134a/R143a increases from 0.3 to 0.5. An additional increase of 0.31% in thermal efficiency can be obtained by using R134a/R143a (0.5/0.5) instead of R134a/R143a (0.7/0.3) (see Table C.4).

When the expander outlet pressure reaches 650 kPa, the maximum achievable mass fraction of R32 is 0.3, whereas R143a and R125 are 0.6. Like the previous case $\left(T_{hf,in} = 363\ K\right)$, the highest achievable mass fractions for R143a and R125 are $x_2 = 0.75$ which are obtained at an expander outlet pressure of 700 kPa. The increase of the mass fraction of the second component of R134a/R143a to 0.75 can provide an additional increase of 0.21% in the thermal efficiency compared to R134a/R143a (0.4/0.6) at $P_{exp,out} = 700$ kPa. Besides, R134a/R143a (0.25/0.75) at $P_{exp,out} = 700$ kPa provides a better thermal efficiency than all R134 blends at this expander outlet pressure condition.

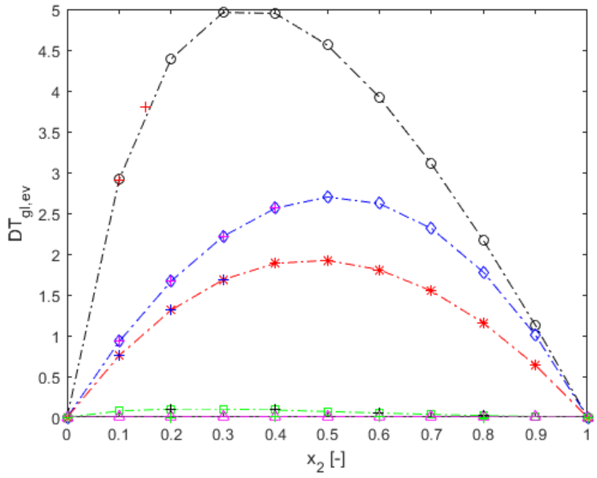

(a)

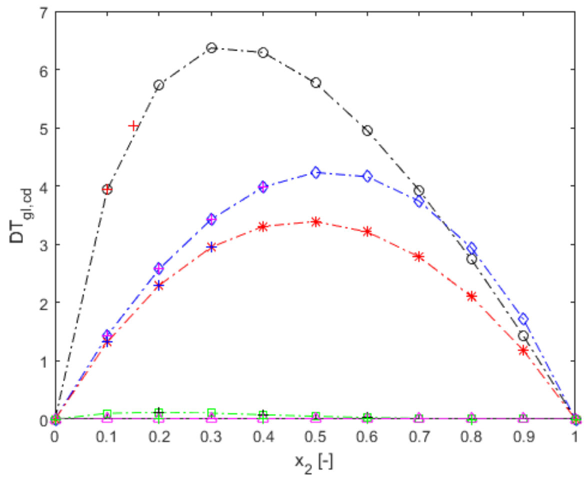

(b)

Figure 6.11. Calculated (model) vs theoretical temperature glides in (a) the evaporator and (b) the condenser for the selected mixtures with different mass fractions of the second component x_2 at $P_{exp,out} = 550$ kPa ($P_{cd,in} = 522$ kPa, $P_{ev,in} = 1949$ kPa).

6.4.3. Hot Fluid Inlet Temperature of 383 K

The variations of performance indicators of the selected refrigerant blends with respect to the change of expander outlet pressure for various mass fractions are shown in Figure 6.12.

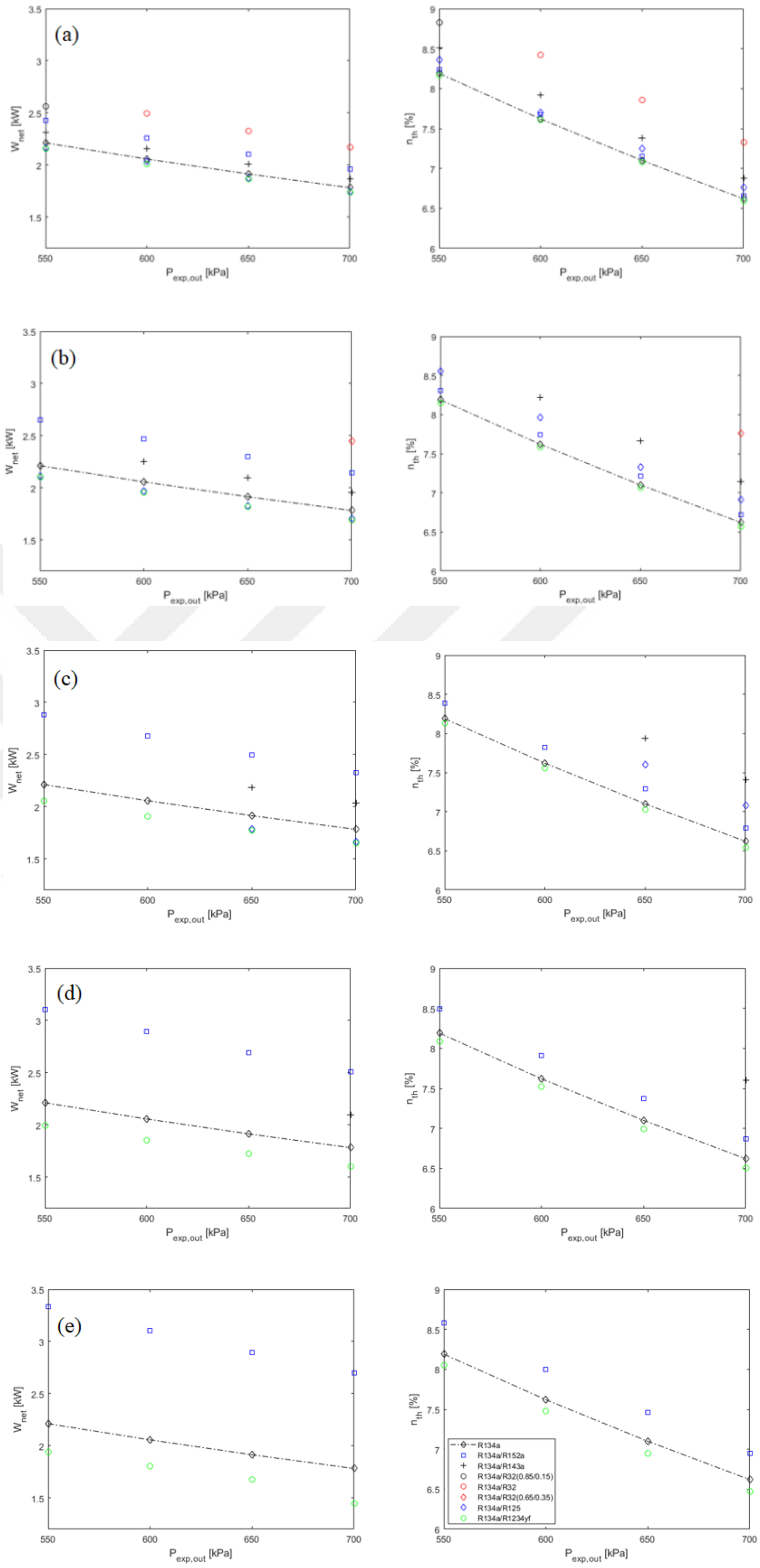

Figure 6.12. Performance indicators of R134a blends with varying expander outlet pressure (kPa) and mass fractions (a) 0.8/0.2 (b) 0.6/0.4 (c) 0.4/0.6 (d) 0.2/0.8 (e) 0.0/1.0 at a heat source temperature of 383 K.

Results shown in Figure 6.12 reveal that similar to the previous case, $T_{hf,in} = 373$ K, only two out of five blends including R134a/R152a and R134a/R1234yf are left from the selected R134a blends as the mass fraction of the second component $x_2 = 1$ (see Figure 6.12-e). Among the five selected refrigerant blends R134a/R32 is the top-performing mixture which provides the highest thermal efficiency. Figure 6.12 also reveals that all the selected refrigerant mixtures except R134a/R1234yf would provide a better performance than pure R134a for all selected expander outlet pressure range $P_{exp,out} = 550 - 700$ kPa. The maximum thermal efficiency is provided by R134a/R32 (0.85/0.15) blend with 8.84% at the expander outlet pressure of 550 kPa. Yet, similar to the previous case $T_{hf,in} = 373$ K, R134a/R32 can only be used as a limited mass fraction of R32 ($x_2 \leq 0.15$), due to the high condensation temperature glide which leads to the excessive increase of the area of condensation $A_{II,cd}$. This causes the insufficiency of the condenser areas to obtain a sub-cooled liquid mixture at the condenser outlets. R134a/R143a is the second best-performing blend that gives the highest thermal efficiency (R134a/R143a (0.7/0.3) with 8.67% at $P_{exp,out} = 550$ kPa). However, like R134a/R32 blend, the maximum allowable mass fraction of the second component of R134a/R143a is limited to $x_2 = 0.3$, since the condensation area becomes insufficient to provide sub-cooled liquid mixture at the condenser outlet. Yet, the maximum mass fraction limit of the second component (R143a) of R134a/R143a increases from $x_2 = 0.3$ to $x_2 = 0.75$ when the expander outlet pressure is selected as $P_{exp,out} = 700$ kPa.

R134a/R125 is the third top performing blend which provides higher thermal efficiencies than pure R134a case for the selected expander outlet pressure region $P_{exp,out} =$ 550-700 kPa (maximum achievable thermal efficiency is $n_{th} = 8.55\%$ obtained by R134a/R125(0.6/0.4) at $P_{exp,out} = 550$ kPa). However, the maximum mass fraction of the R125 component of R134a/R125 is limited to $x_2 = 0.4$ at $P_{exp,out} = 550$ kPa, $x_2 = 0.5$ at $P_{exp,out} = 600$ kPa and, $x_2 = 0.6$ at expander outlet pressures of 650 and 700 kPa. Therefore, as the mass fraction of the second component of R134a/R152a rises above $x_2 \geq$ 0.6, R134a/R152a becomes the top performing blend that provides higher thermal efficiency than the pure R134a case for $P_{exp,out} = 550$ kPa.

Unlike R134a/R143a and R134a/R32 mixtures, R134a/R152a mixture has a low temperature glide (see Figure 6.13) during phase change of the evaporation and the condensation since R152a has a boiling point ($T_{bp} = -24\,°C$) close to R134a ($T_{bp} = -26\,°C$). R134a/R152a is an azeotropic mixture and therefore it can be used for the pure fluid cases for both R134a and R152a components. The zeotropic mixtures such as R134a/R143a, R134a/R32, and R134a/R125 can only be used for a limited mass fraction of the second component due to the condensation area $A_{II,cd}$ limits. Therefore, R134a/R152a becomes the top-performing blend that provides the highest thermal efficiencies ($n_{th} = 8.49$ for R134a/R152a (0.2/0.8), and $n_{th} = 8.58$ for the pure R152a) when the mass fraction of the second component of R134a blends increases beyond $x_2 \geq 0.6$. Especially, as the expander outlet pressure of 550 kPa is used, the area required for the condensation $A_{II,cd}$ increases more rapidly with the increasing mass fraction of x_2 (see Figure E.3). When the expander outlet pressure is $P_{expout} \geq 650$ kPa, this effect is reduced. Due to the decrease in the required condensation areas at $P_{exp,out} = 650$ kPa and $P_{exp,out} = 700$ kPa cases, the maximum mass fraction limits of R32 for R134a/R32 increases to $x_2 = 0.35$ (see Figure E.3), whereas the mass fraction limits of R143a and R125 for R134a/R143a and R134a/R125 respectively increase to $x_2 = 0.75$ (see Figure E.4) and $x_2 = 0.6$ (see Figure E.5). Results clearly show that the superiority of the zeotropic mixtures depends on the condition that the temperature glide provided by the mixture should not lead to an excessive increase in the heat transfer areas of the evaporation or condensation.

Like R134a/R152a, R134a/R1234yf blend can be used for the whole composition including the pure fluid cases of R134a and R1234yf components. Yet, R134a/R1234yf shows the worst performance for all mixture mass fractions for the whole expander outlet pressure variations. Like the previous case ($T_{hf,in} = 373$ K), net power outputs and thermal efficiencies show a comparably slow decrease with an increasing mass fraction of R1234yf of R134a/R1234yf mixture (see Table C.5). However, due to the azeotropic behavior of R134a/R1234yf (providing a temperature glide close to 0; see Figure 6.13), the thermal efficiency values for R134a/R1234yf could not change meaningfully with the increasing mass fraction of the R1234yf component (see Table C.5; $n_{th} = 8.19\%$ for R134a (pure) whereas $n_{th} = 8.05\%$ for R1234yf (pure) at $P_{exp,out} = 550$ kPa).

In Figure 6.12a to 6.12e, the net power outputs are also shown for each specific mass fraction. Like the previous case ($T_{hf,in} = 373$ K), the maximum net power outputs for the mass fraction of the second components $x_2 \geq 0.4$ are obtained by the R134a/R152a blend.

The highest achievable net power output is reached by R152a (pure) case with $\dot{W}_{net} = 3.33$ kW at $P_{exp,out} = 550$ kPa. An additional 0.34 kW net power gain is provided compared to $T_{hf,in} = 363$ K case. R134a/R32 is the second blend that gives high net power output than R134a (pure) solution.

However, for the mass fractions of the second components; $x_2 \leq 0.15$ at $P_{exp,out} = 550$ kPa, $x_2 \leq 0.2$ at $P_{exp,out} = 600$ kPa, $x_2 \leq 0.29$ at $P_{exp,out} = 650$ kPa, and $x_2 \leq 0.35$ at $P_{exp,out} = 700$ kPa, R134a/R32 blend becomes the top-performing blend in terms of net power output (The maximum net power output of R134a/R32 blend is obtained by R134a/R32 (0.85/0.15) with $\dot{W}_{net} = 2.56$ kW). R134a/R143a is the third best-performing blend in terms of net power produced from the cycle. The highest net power output by using R134a/R143a blend is obtained by R134a/R143a (0.7/0.3) with $\dot{W}_{net} = 2.36$ kW. However, due to the zeotropic behavior of R134a/R32 and R134a/R143a blends, the area needed to obtain sub-cooled liquid mixture excess the total condenser area limit $A_{tot,cd} = 6.08$ m^2, as the mass fraction of R32 increases beyond $x_2 > 0.15$, and R143a exceeds $x_2 > 0.3$ at an expander outlet pressure of 550 kPa is selected.

The results provided in Table C.5 present the variation of performance indicators n_{th} and $\dot{W}_{net}$ for the varying expander outlet pressures at each specific mass fraction. The highest net power output is obtained by R134a/R152a for the mass fractions including $x_2 = 0.2$ with 2.43 kW, $x_2 = 0.4$ with 2.65 kW, $x_2 = 0.6$ with 2.87 kW, $x_2 = 0.8$ with 3.10 kW, and $x_2 = 1$ with 3.33 kW. However, R134a/R32 becomes the best performing blends for $x_2 \leq 0.15$ (R134a/R32 (0.85/0.15) provides $\dot{W}_{net} = 2.56$ kW). Maximum thermal efficiencies at each specific mass fraction are obtained by R134a/R32 with 8.84% at $x_2 = 0.15$, R134a/R143a with 8.51% at $x_2 = 0.2$, R134a/R143a with 8.67% at $x_2 = 0.3$, R134a/R125 with 8.55% at $x_2 = 0.4$, R134a/R152a with 8.30% at $x_2 = 0.6$, R134a/R152a with 8.38% at $x_2 = 0.8$, and R134a/R152a with 8.47% at $x_2 = 1$.

Like previous cases, $T_{hf,in} = 363$ K and $T_{hf,in} = 373$ K, the increase of the expander outlet pressure causes a decrease in thermal efficiencies and net power outputs, yet it also provides an increase in maximum mass fraction limits of the second component of the selected R134a blends. Table C.5 reveals that the maximum mass fraction limit of R143a of R134a/R143a mixture increases from 0.3 to 0.5 when $P_{exp,out} = 600$ kPa is selected instead of an expander outlet pressure of 550 kPa. An additional increase of 0.3% in thermal efficiency can be obtained by using R134a/R143a (0.5/0.5) instead of R134a/R143a (0.7/0.3) (see Table C.5).

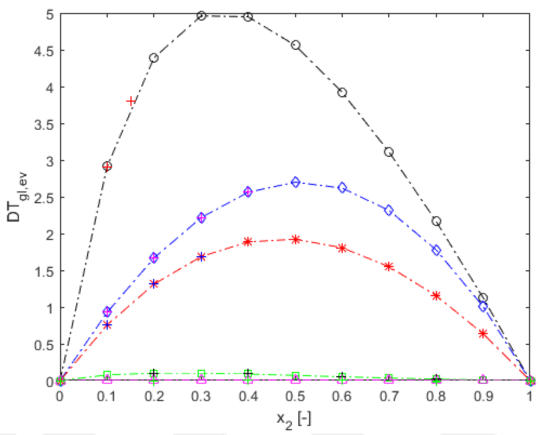

(a)

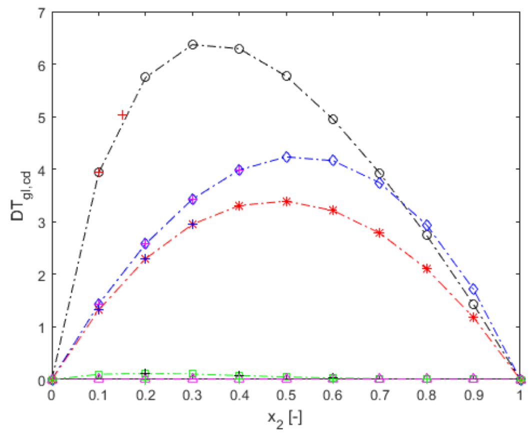

(b)

Figure 6.13. Calculated (model) vs theoretical temperature glides in (a) the evaporator and (b) the condenser for the selected mixtures with different mass fractions of the second component x_2 at $P_{exp,out} = 550$ kPa ($P_{cd,in} = 521$ kPa, $P_{ev,in} = 1949$ kPa).

6.4.4. Hot Fluid Inlet Temperature of 393 K

The variations of performance indicators of the selected refrigerant blends with respect to the change of the expander outlet pressure for various mass fractions are shown in Figure 6.14.

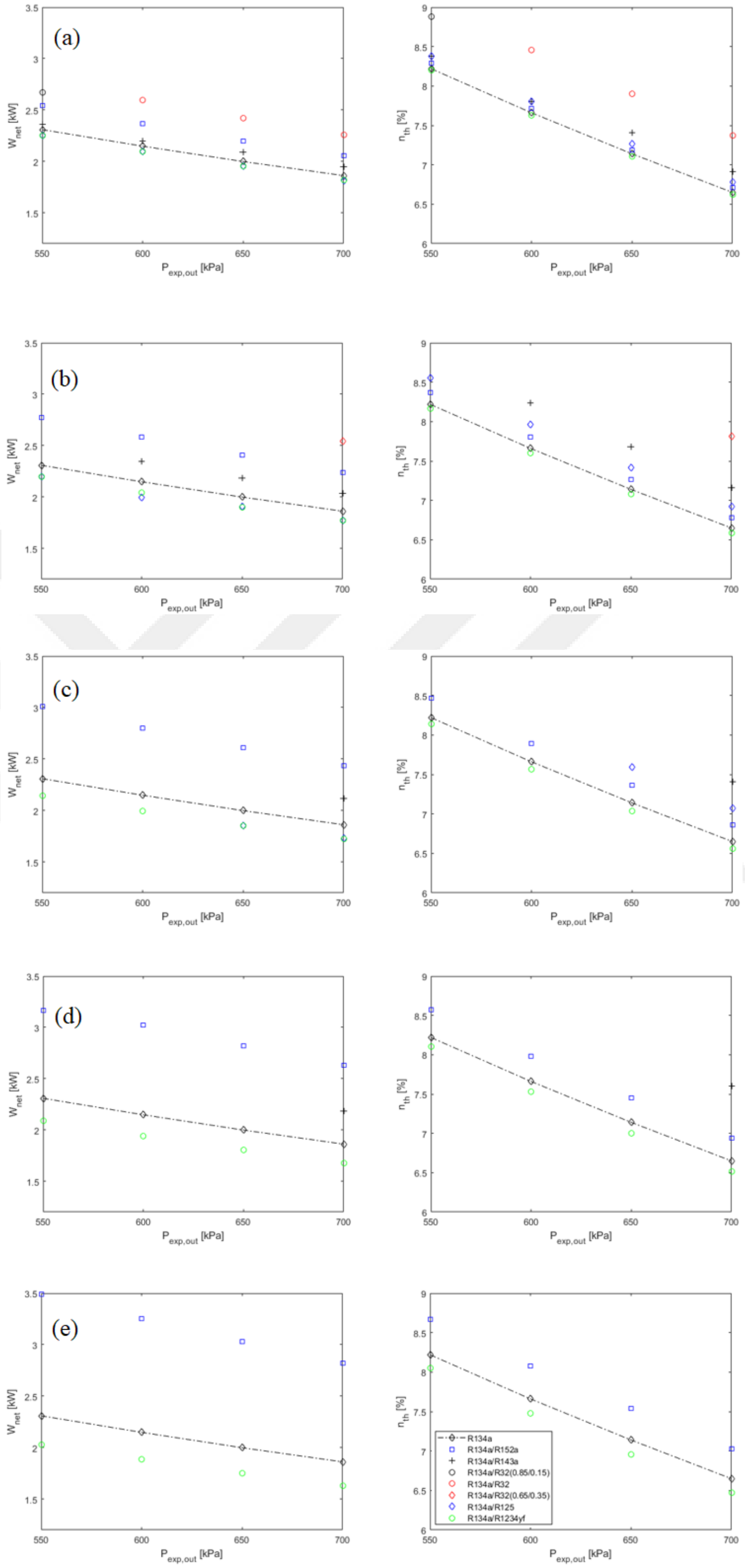

Figure 6.14. Performance indicators of R134a blends with varying expander outlet pressure (kPa) and mass fractions (a) 0.8/0.2 (b) 0.6/0.4 (c) 0.4/0.6 (d) 0.2/0.8 (e) 0.0/1.0 at a heat source temperature of 393 K.

Figure 6.14 shows that, like previous cases ($T_{hf,in} = 373$ K and $T_{hf,in} = 383$ K), there are only two out of five blends, R134a/R1234yf and R134a/R152a, have remained from the selected mixtures as the $x_2 = 1$ (see Figure 6.14-e). In terms of thermal efficiencies, R134a/R32 is the lead performing mixture that provides the best performance. Except R134a/R1234yf blend, all the selected refrigerant mixtures including R134a/R143a, R134a/R152a, R134a/R125, and R134a/R32 can provide higher thermal efficiencies than R134a (pure) case for the selected expander outlet pressure region $P_{exp,out} = 550 - 700$ kPa. Like previous cases, R134a/R32 (0.85/0.15) blend at $P_{exp,out} = 550$ kPa provides the highest achievable thermal efficiency with 8.88%. However, due to the high condensation temperature glide which causes an excessive increase in the condensation phase change area $A_{II,cd}$, the maximum achievable mass fraction of the R32 component of the R134/R32 mixture is limited to $x_2 \leq 0.15$. Like previous cases, the second high-performing blend which provides the best thermal efficiency is the R134a/R143a blend (R134a/R143a (0.7/0.3) with 8.69% at $P_{exp,out} = 550$ kPa). Yet, like the R134a/R32 blend the zeotropic behavior of R134a/R143a blend leads to a limitation of the mass fraction of R143a component. The condensation area of R134a/R143a becomes inadequate as the mass fraction of R143a rises above $x_2 > 0.3$. However, the increase of expander outlet pressure to 700 kPa, can lead to an increase of the maximum achievable mass fraction of the second component (R143a) of R134a/R143a from $x_2 = 0.3$ to $x_2 = 0.75$.

R134a/R125 is the third top-performing blend for all selected expander outlet pressure ranges (550-700 kPa) as the mass fraction of the second components of R134a blends is smaller than 0.4. However, when the mass fraction of R125 reaches 0.4, it becomes the best-performing blends providing the highest thermal efficiencies for all expander outlet pressure values ranging between 550 to 700 kPa (maximum thermal efficiency is obtained by R134a/R125 (0.6/0.4) with $n_{th} = 8.55\%$ at $P_{exp,out} = 550$ kPa). Interestingly, although R134a/R152a is the second worst performing blend among the five R134a blends, as the mass fraction of the second components of R134a blends exceeds $x_2 \geq 0.6$, it becomes the best-performing blends for all selected expander outlet pressure range.

As described in the previous case $T_{hf,in} = 383$ K, R134a/R152a has low evaporation and condensation temperature glides (see Figure 6.15), therefore it demands lower phase change areas of the evaporation and condensation compared to zeotropic mixtures such as

R134a/R125, R134a/R143a, and R134a/R32. Thus, R134a/R152a mixture can be used purely for both components of the mixture (R134a and R152a) due to the azeotropic behavior of the mixture. Zeotropic refrigerant blends such as R134a/R143a, R134a/R32, and R134a/R125 can only be used for the limited mass fraction of the second component due to the condensation area $A_{II,cd}$ limits. This makes the R134a/R152a mixture the top-performing blend in terms of thermal efficiencies as the mass fraction of the second component $x_2 \geq 0.6$ ($n_{th} = 8.47$ for R134a/R152a (0.4/0.6), $n_{th} = 8.57$ for R134a/R152a (0.2/0.8), and $n_{th} = 8.58$ for the pure R152a). Similar to the previous case $T_{hf,in} = 383$ K, the area of condensation increases drastically with the increasing mass fraction of x_2 for the zeotropic blends including R134a/R143a, R134a/R32, and R134a/R125, as the expander outlet pressure is selected as 550 kPa (see Figure E.6 to Figure E.8). Like the previous case, as the expander outlet pressure is $P_{expout} \geq 650$ kPa, this effect is reduced. Due to the decrease in the required areas of the condensation at $P_{exp,out} = 650$ kPa and $P_{exp,out} = 700$ kPa cases, the maximum mass fraction limits of R32 for R134a/R32 increases to $x_2 = 0.3$ at $P_{exp,out} = 650$ kPa, $x_2 = 0.35$ at $P_{exp,out} = 700$ kPa (see Figure E.6), whereas the mass fraction limits of R143a and R125 of R134a/R143a and R134a/R125 respectively increase to $x_2 = 0.75$ (see Figure E.7) and $x_2 = 0.6$ (see Figure E.8).

Like the previous case $\left(T_{hf,in} = 383 \text{ K}\right)$, R134a/R1234yf could be applied for the whole composition including the pure fluid cases for both components of the mixture (R134a and R1234yf). Yet, R134a/R1234yf is the worst-performing blend for all mixture mass fractions for the whole expander outlet pressure range. Like the previous case, net power outputs and thermal efficiencies show a comparably slow decrease with the increasing mass fraction of R1234yf of R134a/R1234yf mixture (see Table C.6). However, R134a/R1234yf is an azeotropic blend that provides a temperature glide close to 0 (see Figure 6.15), therefore the thermal efficiencies for the R134a/R1234yf do not change drastically with the increasing mass fraction of R1234yf component (see Table C.6; $n_{th} = 8.22\%$ for R134a (pure) whereas $n_{th} = 8.05\%$ for R1234yf (pure) at $P_{exp,out} = 550$ kPa).

The net power outputs are shown in Figure 6.14-(a) to Figure 6.14-(e) for each specific mass fraction of the selected mixtures. The maximum net power outputs are provided by R134a/R32 blends for the all selected expander outlet pressure values (550-700 kPa) when the mass fraction of the second component (R32) of the R134a/R32 blend is either equal or lower than 0.15 for $P_{exp,out} = 550$ kPa, 0.2 for $P_{exp,out} = 600$ kPa, 0.3 for $P_{exp,out} = 650$ kPa, and 0.35 for $P_{exp,out} = 700$ kPa (see Figure 17-a and Figure 17-b). The highest net power output values for $x_2 \leq 0.3$ are provided by R134a/R32 (0.85/0.15) with $\dot{W}_{net} = 2.67$ kW at an expander outlet pressure of 550 kPa. However, when the mass fraction of x_2 is greater than 0.4, R134a/R152a blend for the selected expander outlet pressure range. The highest achievable net power output is reached by R152a (pure) case with $\dot{W}_{net} = 3.49$ kW at $P_{exp,out} = 550$ kPa. An additional 0.49 kW net power gain is provided compared to $T_{hf,in} = 363$ K case. When x_2 ≥0.4, R134a/R32 becomes the second blend that gives high net power output than R134a (pure) solution. R134a/R143a is the third top-performing blend for the whole applicable mass fractions. R134a/R143a provides the maximum net power output for R134a/R143a (0.7/0.3) with $\dot{W}_{net} = 2.46$ at the expander outlet pressure of 550 kPa. Yet, due to zeotropic behaviour of R134a/R32 and R134a/R143a blends, the area needed to obtain sub-cooled liquid mixture excess the total condenser area limit $A_{tot,cd} = 6.08$ m^2, as the mass fraction of R32 increases beyond $x_2 > 0.15$ and R143a exceeds $x_2 > 0.3$ ($P_{exp,out} = 550$ kPa).

The results tabulated in Table C.6 show the change of n_{th} and $\dot{W}_{net}$ for the varying expander outlet pressures at each specific mass fraction. The highest net power output is obtained by R134a/R152a for the mass fractions including $x_2 = 0.2$ with 2.54 kW, $x_2 = 0.4$ with 2.77 kW, $x_2 = 0.6$ with 3.01 kW, $x_2 = 0.8$ with 3.16 kW, and $x_2 = 1$ with 3.49 kW. However, R134a/R32 becomes the best performing blends for $x_2 \leq 0.15$ at $P_{exp,out} = 550$ kPa (R134a/R32 (0.85/0.15) with $\dot{W}_{net} = 2.67$ kW), $x_2 \leq 0.2$ at $P_{exp,out} = 600$ kPa (R134a/R32 (0.8/0.2) with $\dot{W}_{net} = 2.59$ kW), $x_2 \leq 0.29$ at $P_{exp,out} = 650$ kPa (R134a/R32 (0.71/0.29) with $\dot{W}_{net} = 2.60$ kW), and $x_2 \leq 0.35$ at $P_{exp,out} = 700$ kPa (R134a/R32 (0.65/0.35) with $\dot{W}_{net} = 2.54$ kW). Maximum thermal efficiencies at each specific mass fraction are obtained by R134a/R32 with 8.88% at $x_2 = 0.15$, R134a/R143a with 8.54% at $x_2 = 0.2$, R134a/R143a with 8.69% at $x_2 = 0.3$, R134a/R125 with 8.55% at $x_2 = 0.4$, R134a/R152a with 8.47% at $x_2 = 0.6$, R134a/R152a with 8.57% at $x_2 = 0.8$, and R134a/R152a with 8.67% at $x_2 = 1$.

Like previous cases, the increase of the expander outlet pressure leads to a decrease in thermal efficiencies and net power outputs. The maximum mass fraction limits of the second component of the selected R134a blends with increased expander outlet pressure. Results provided in Table C.6 reveal that the maximum mass fraction limit of R143a of R134a/R143a blend increases to $x_2 = 0.5$ as the expander outlet pressure is selected as 600 kPa instead of 550 kPa. An additional increase of 0.29% in thermal efficiency can be obtained by using R134a/R143a (0.5/0.5) instead of R134a/R143a (0.7/0.3) (see Table C.6).

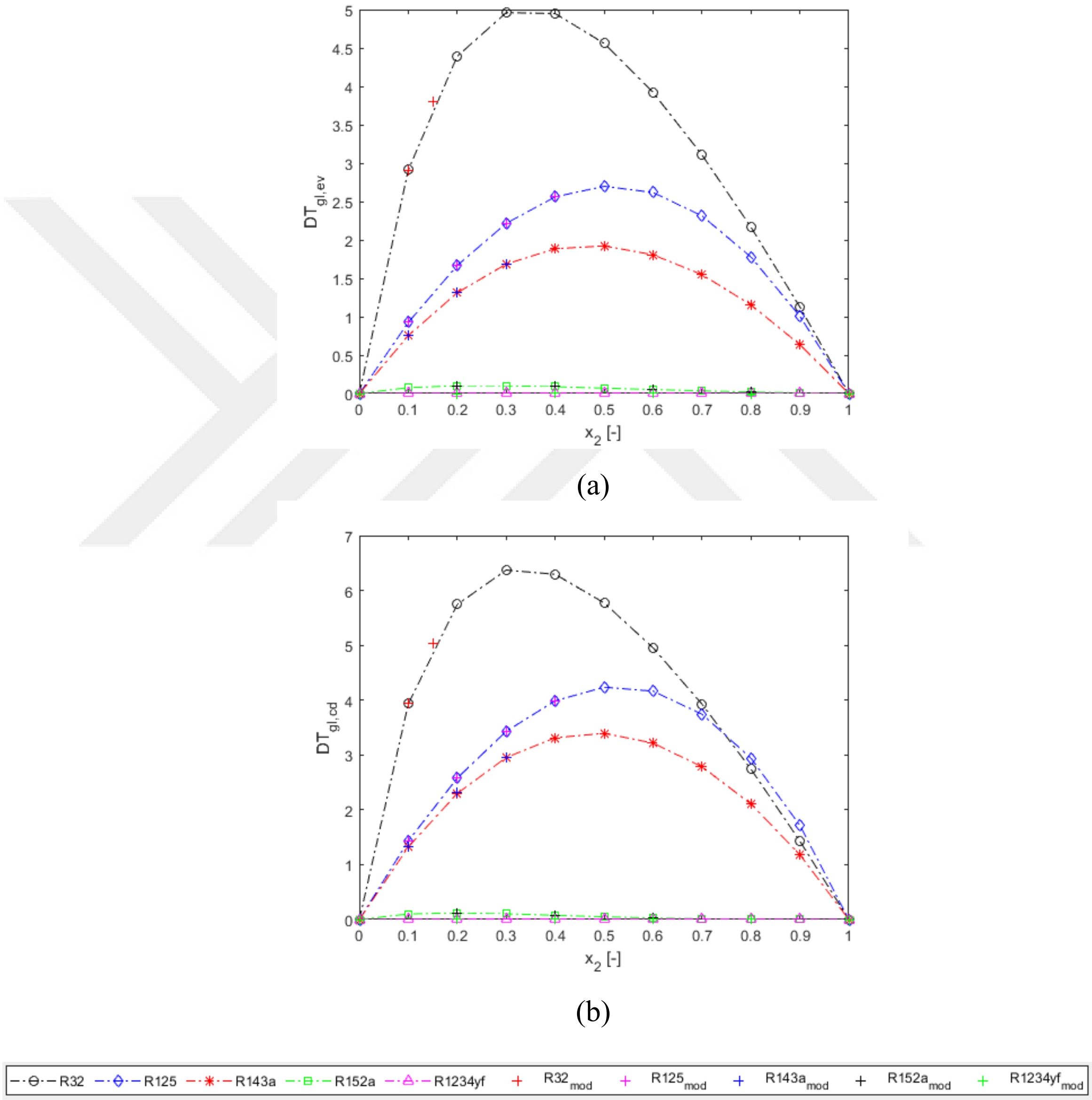

Figure 6.15. Calculated (model) vs theoretical temperature glides in (a) the evaporator and (b) the condenser for the selected mixtures with different mass fractions of the second component x_2 at $P_{exp,out} = 550$ kPa ($P_{cd,in} = 520$ kPa, $P_{ev,in} = 1949$ kPa).

7. SUMMARY & DISCUSSION

This study composes of two main parts. In the first part of the study, a comprehensive ORC model is built and validated using the tests conducted on a laboratory-scale ORC setup. The steady-state data are obtained at four different heat source temperatures, and the model is validated. In addition, a relative standard uncertainty analysis is conducted to assess the model accuracy for measured temperature, pressure, and flow rates.

The reliability of the experimental data is checked with repeatable experimental tests and standard deviation limits for the steady-state operation. Relative standard sensor uncertainties are given and compared to the measurement accuracy. Results indicated that the measurement uncertainties are close to or in the same order magnitude of the relevant sensor at each measurement point except for working fluid mass flow rate and pump outlet pressure for Exp-4.

For higher accuracy, pressure losses and temperature drop in pipelines are considered in sub-models. There is no iterative process in calculations of exit state properties. For the sub-model validation, a good match between test data and model output is observed for heat transfer rates in the evaporator and the condenser, the mass flow rate of R134a, and power consumed in the refrigerant pump. The sub-models predict the experimental data within ∓1% and∓2% error thresholds for all pressures and temperatures and ∓5% for the working fluid mass flow rate and power consumed in the pump. The highest calculated error is 5.15%, obtained for work consumed by the pump vs volumetric flow rate of the working fluid at Exp-2. The error of all remaining model predicted results, including pressure, temperature, mass flow rate of the working fluid, and work consumed by the pump are smaller than 2.5%.

Results tabulated in Table 5.4 show the model's prediction accuracy vs. the ones available in the literature. The interconnected cycle model predicts the pressures of the working fluid within ±1% and calculates the heat transfer rates within ±5% accuracy. The maximum deviation between the model-predicted temperature and the experimental result is 1.1 ℃ (within ∓2%) at the condenser inlet. The deviations for the remaining temperatures predicted at all sensors are less than 1 ℃, much lower than the maximum absolute error of 7 ℃ found in the literature [23]. The increased accuracy is achieved by incorporating piping pressure losses and temperature drops into the interconnected cycle model. Results tabulated in Table 5.5 show the effect of the pipe pressure drop and heat losses on the model's accuracy. The difference between the model prediction and the experimental measurement is calculated and tabulated in the table. The results show that the model that considers the losses predicts the temperature and the pressure more accurately, revealing the significance of the pipeline losses.

In the second part of the study, extensive parametric performance studies (Study-I and Study-II) are conducted starting from ten R134a blends with varying mass fractions with respect to the modified steady-state ORC model developed in Chapter 4. The performance of the selected refrigerant mixtures is examined in detail with respect to the change of hot fluid inlet temperatures (ranging between 363-403 K) and the expander outlet pressure. The main aim of the study is to find the optimal R134a blends and their mass fraction that gives the best performance in terms of net power produced from the cycle and cycle thermal efficiency for the given pressure and temperature fields.

The modified ORC model developed in the study considers the pipe losses in addition to the component sub-models to provide a better prediction accuracy. The heat exchanger model is modified for the refrigerant mixtures to take the temperature glide that occurs at the evaporation and condensation processes into account. The property calculations of selected mixture compounds are made by REFPROP v9.1, considering the liquid phase and vapor phase properties separately.

The validation of the modified ORC model proposed for the refrigerant mixture is made by statistically reliable experimental data obtained by R134a/R236fa with varying mass fractions for the hot fluid inlet temperatures of 90 ℃, 100 ℃ and 115 ℃. The experimental tests are conducted with similar set conditions for both pure fluid and mixture cases (i.e., hot fluid inlet temperature, refrigerant pump speed, and oil pump frequency) to show the cycle repeatability and data reliability. The sub-model validation results show that the modified heat exchanger model for refrigerant mixtures can predict the heat transfer rates within $\pm 10\%$ deviation from the test data for most cases.

The parametric performance study is divided into three parts. Firstly, best performing R134a blends, and their mass fraction are searched for hot fluid inlet temperatures of 363-

403 K for two different pump isentropic efficiency cases: $n_{pp,is} = 0.3$ (Study I-a) and $n_{pp,is} = 0.8$ (Study I-b). The main aim is to evaluate the performance of the selected R134a blends (R134a/R245fa, R134a/R227ea, R134a/R143a, R134a/R32, R134a/R125, R134a/R152a, R134a/R236fa, R134a/R236ea, R134a/R1234yf and R134a/R1234ze(e)) with respect to selected performance indicators: net power produced from the cycle and the cycle thermal efficiency.

In the second part of the parametric performance study, the performance search is made with respect to the expander outlet pressure changing between 550-700 kPa as the hot fluid inlet temperature varies between 363-393 K. The main aim is to determine the best-performing blends and their mass fraction in the selected temperature and pressure fields. The maximum achievable mass fraction limit of the second components and heat transfer area limitations of both the evaporator and the condenser are considered in the study to obtain a more realistic model. Based on the results provided in the first study, five out of ten R134a blends that performs best in terms of net power output and cycle thermal efficiency are selected as refrigerant mixture candidates for the Study-II. The thermodynamic constraints are defined in Chapter 5, The parametric performance evaluation of the five best performing refrigerant blends including R134a/R32, R134a/R125, R134a/R143a, R134a/R152a, and R134a/R1234yf with varying mass fractions are made for the hot fluid inlet temperatures of 363, 373, 383 and 393 K as the expander outlet pressure is changed between 550 to 700 kPa.

The results of Study I reveal that R134a/R32 is the best performing mixture among the ten R134a blends. The highest thermal efficiencies are 7.81% (Study I-a) and 8.49% (Study I-b) that are obtained for R134a/R32 (0.8/0.2) at hot fluid inlet temperature of 403 K. However, due to the zeotropic behavior of R134a/R32 blend, the maximum mass fraction limit of R32 component of R134a/R32 mixture is $x_{2,max} = 0.2$. Especially, the need for a high condensation area to compensate for the large temperature glide in the two-phase zone is the main cause that leads to the suppression of the total heat transfer area of the condenser. R134a/R143a, R134a/R125, and R134a/R152a are the other zeotropic mixtures that perform better than the pure R134a for the studied hot fluid inlet temperature range. Yet, like R134a/R32 blend, the maximum achievable mass fraction limits of the second component of R134a/R143a and R134a/R125 are $x_{2,max} = 0.5$, due to the excessive increase of the condensation areas stemming from the large condensation temperature glides.

Further, net power outputs of the selected R134a blends decrease with increasing mass fraction of x_2. Especially, net power outputs are in a tendency to decrease more for the zeotropic mixtures with high evaporation and condensation temperature glides including R134a/R245fa, R134a/R236ea, R134a/ R236fa, and R134a/R227ea. In contrast, for the refrigerant blends that show azeotropic behavior such as R134a/R1234yf and R134a/R1234ze(e), the decreasing trend of $\dot{W}_{net}$ reduces.

Net power output decreases with increasing mass fraction of the second component for most refrigerant mixtures selected. Especially, for the zeotropic mixtures with high evaporation and condensation temperature glides such as R134a/R245fa, R134a/R236ea, R134a/R236fa, R134a/R227ea, net power outputs are in tendency of decrease more compared to refrigerant mixtures which show near-azeotropic behavior (R134a/R1234yf and R134a/R1234ze). This is due to the reason that, when the evaporation or condensation temperature glide high compared to the temperature differences between the heat source and the heat sink, it results in a decrease in the evaporation pressure or an increase in condensation pressure [49].

Results of Study-I also reveal that the temperature at the evaporator outlet values for zeotropic blends R134a/R245fa, R134a/R236ea, and R134a/R236fa increase with the increasing mass fraction of the second component. However, these three blends are the worst performing blends in terms of net power outputs. For these blends with high condensation temperature glides, the condenser heat transfer area becomes inadequate to meet the condensation heat transfer demand of the zeotropic mixture which results in the deterioration of the heat transfer mechanism and the increase of the condenser outlet temperature. The smaller temperature difference during the expansion at the expander would lead to a smaller enthalpy drop. Net power outputs are only varied with respect to the change of enthalpy drop caused by the temperature difference, thus $\dot{W}_{net}$ values decrease as a function of the smaller enthalpy difference.

Like Study-I, two performance indicators including $\dot{W}_{net}$ and n_{th} are used for the second parametric performance study (Study-II). Results show that R134a/R32 and R134a/R143a are the top two blends providing higher thermal efficiency than other mixtures for all selected expander outlet pressure and hot fluid inlet temperature ranges.

Yet, in parallel to Study-I, they can only be used for the limited mass fraction of the second component of the mixture due to the high condensation area demands caused by the large condensation temperature glides they have. Besides, azeotropic blends such as R134a/R1234yf can be applied for the whole composition including pure fluid cases of each component of the mixture. Yet, R134a/R1234yf is the worst-performing blend for all mass fractions and the all-expander outlet pressure range, due to the smaller enthalpy drop at the expander.

The net power outputs are also evaluated for each specific mass fraction of the selected five R134a blends (Study-II). The results show that R134a/R152a is the best-performing blend in terms of net power output for the whole expander outlet pressure range (when $x_2 \geq 0.4$). The highest achievable net power outputs are provided by R152a (pure) cases for each specific expander outlet pressure value. R134a/R32 and R134a/R143a are the second and third best performing blends among the selected five R134a mixtures. However, when the mass fraction of $x_2 < 0.4$, R134a/R32 becomes the best-performing blend in terms of net power outputs, except for expander outlet pressure of 550 kPa.

Study-II also reveals that the increase of the expander outlet pressure value leads to a decrease in the cycle thermal efficiencies and power outputs. Yet, the corresponding maximum mass fraction limits of the second components of the mixtures increase with increasing expander outlet pressure. By increasing the expander outlet pressure, an additional increase of cycle thermal efficiencies is provided by increasing the mass fraction of the second components of the selected mixtures for each hot fluid inlet temperature value.

This study contributes to the literature through the detailed ORC model that includes connection pipes in addition to the regular components of the ORC (i.e., heat exchangers, pump, and expander). The modified ORC model developed in this thesis puts emphasize on the heat exchanger area limitation and the pipe losses which are significant for the parametric performance studies with refrigerant mixtures. Model validations for both pure fluid and refrigerant mixture cases are made by using statistically reliable data. Therefore, it contributes to the literature through a more realistic ORC model that can calculate performance indicators such as thermal efficiency and net power output values at the real component boundaries.

The parametric performance studies are also unique in terms of the strategy developed, and the extensive workspace it has. The extended parametric workspace searched in the study provides a more comprehensive approach for the selection of refrigerant mixtures including azeotropic and zeotropic blends. The modified ORC model developed in this study is also novel since it emphasizes the mass fraction limit of the second components of the selected mixtures. The model can freely be used in the parametric performance and optimization studies of different ORC configurations if actual geometries of each selected component are available.

8. CONCLUSIONS

This thesis provides an extensive study of the ORC modeling with component sub-models and connection pipes on pure fluids and zeotropic mixtures. The ORC model contributes to the literature through a detailed PHE modeling approach that can calculate the outlet temperatures and pressure drops using the inlet state conditions of each fluid for both the evaporator and condenser units. The model also includes pipe heat transfer and pressure drop correlations to predict the sensor point temperatures and pressures accurately.

The experimental part of the study is also unique since it provides a significant knowledge on the model capabilities for both pure fluids and zeotropic mixtures. Various test conditions (i.e., different heat source temperatures, working fluid pump speeds, oil pump frequencies) are used during the experimental studies to show the cycle repeatability and the data reliability not only for pure fluids but also for zeotropic mixtures. The main aim of the thesis is to understand the effect of using zeotropic mixtures instead of pure refrigerants on the ORC performance. Therefore, a comprehensive set of experiment which is composed of 24 different test cases are prepared to provide more insight on model validation of ORC with zeotropic mixtures. R236fa/R134a blend is used in the tests due to high zeotropic behavior of the mixture, and the applicability on the market. The experimental tests are carried out over two days in 6h and 8h operations. The data is collected in a continuous manner to understand to show the cycle repeatability, understand the transient behavior, and determine the steady-state zones of each test more accurately. The statistical means and standard deviations of each case proves the reliability of the experimental data.

The model validation studies are conducted for both pure fluid and zeotropic mixture models using the test data obtained by pure R134a and R236fa/R134a mixtures. The results show that the component sub-models for the evaporator can calculate the cycle temperatures and pressures within $\pm$5%, and heat transfer rates within $\pm$10% deviations from the experimental data for both the pure fluid and mixture cases. Similarly, the condenser sub-model can predict the cycle temperatures within $\pm$1%, and pressures within $\pm$3% deviations. The component sub-model validations results show that the ORC model provides an excellent accuracy on the pure fluids and good accuracy on the zeotropic mixtures.

In Chapter-6, extensive parametric performance studies are conducted to determine the best performing blends in terms of cycle power outputs and thermal efficiencies and the mass fraction limits of each mixture for the selected heat exchanger geometries and operating conditions. The study comprises of three studies (Study I-a, Study I-b, and Study II). In the first part of study, ten different R134a blends are used to determine the best performing R134a blends and their compositions for a hot fluid inlet temperature range of 363-403 K for the pump isentropic efficiencies of 0.8 (Study I-a) and 0.3 (Study I-b). The result show that four out of 10 refrigerant blends can contribute to the cycle performance including R134a/R32, R134a/R143a, R134a/R125a, and R134a/R152a, whereas R134a/R1234yf provides similar results to pure R134a. The result show that the use of zeotropic blends with more volatile second components such as R134a/R32, R134a/R143a and R134a/R125a can significantly contribute to the cycle performance as they provide large evaporation and condensation temperature glide during phase changes. Yet, the success of such zeotropic mixtures depends greatly on the allowable mass fraction limits of second components due to the geometrical constraints of the heat exchanger units. In addition, the near zeotropic blends with low boiling point differences such as R134a/R152a can slightly contribute to the cycle performance. The advantage of near such kind of near azeotropic blends is that they can be applied to a whole spectrum of compositions since they can’t need a larger evaporation and condensation areas.

In the second part of the study, the performance of five top performing blends from Study I are examined for more extended workspace that includes varying hot fluid inlet temperatures of 363, 373, 383 and 393 K, and expander outlet pressures of 550, 600, 650 and 700 kPa. The initial aim of the Study-II is to evaluate the performance of selected R134a blends in terms of net power outputs and thermal efficiencies, and to determine the maximum applicable mixture composition limits for each blend. The results show that R134a/R32 blend provides the best performance in terms of thermal efficiencies for all applicable mass fractions of R32 component, whereas R134a/R152a provides the best performance in terms of net power output as the mass fraction of R152a is higher than 0.4. In parallel to Study-I, azeotropic blends such as R134a/R1234yf can be applied for the whole composition including pure fluid cases of each component of the mixture. However, R134a/R1234yf is the worst-performing blend for all mass fractions and the all-expander outlet pressure range, due to the smaller enthalpy drop it provides at the expander.

The results provided in this part of study are significant since they not only showed the performance of the selected mixtures but also gave us information about the maximum reachable mass fraction limits of second components of each mixture.

REFERENCES

1. Rahbar, K., S. Mahmoud, R. K. Al-Dalah, N. Mozami and S. A. Mirhadizadeh, "Review of Organic Rankine Cycle for Small-scale Applications", *Energy Conversion and Management*, Vol. 134, pp. 135-155, 2016.

2. Ozdil, T., N. F. Segmen and A. Tantekin, "Thermodynamic Analysis of an Organic Rankine cycle (ORC) Based on Industrial Data," *Applied Thermal Engineering*, Vol. 91, pp. 43-52, 2015.

3. Satanphol, K., W. Pridasawas and B. Suphanit, "A Study on Optimal Composition of Zeotropic Working Fluid in an Organic Rankine Cycle (ORC) for Low Grade Heat Recovery", *Energy*, Vol. 123, pp. 326-339, 2017.

4. Nemati, A., H. Nami, F. Ranjbar and M. Yari, "A Comparative Thermodynamic Analysis of ORC and Kalina Cycles for Waste Heat Recovery: A Case study for CGAM cogeneration system", *Case Studies in Thermal Engineering*, Vol. 9, pp. 1-13, 2017.

5. Lecompte, S., H. Huisseune, M. V. D. Broek, B. Vanslambrouck, and M. D. Paepe, "Review of Organic Rankine Cycle Architectures for Waste Heat Recovery", *Renewable and Sustainable Energy Reviews*, Vol. 47, pp. 448-461, 2015.

6. Quoilin, S., M. V. D. Broek, S. Declaye, P. Dewallef and V. Lemort, "Techno-economic Survey of Organic Rankine Cycle (ORC) Systems", *Renewable and Sustainable Energy Reviews*, Vol. 22, pp. 168-186, 2013.

7. Quoilin, S., M. Orosz, H. Hemond and V. Lemort, "Performance and Design Optimization of a Low-cost Solar Organic Rankine Cycle for Remote Power Generation", *Solar Energy*, Vol. 85, No. 5, pp. 955-966, 2011.

8. Bellos, E., and C. Tzivanidis, " Parametric Analysis and Optimization of a Solar Driven Trigeneration System Based on ORC and Absorption Heat Pump", *Journal of Cleaner Production*, Vol. 129, pp. 535-542, 2017.

9. Ferrara, F., A. Gimelli and A. Luongo, " Small - scale Concentrated Solar Power (CSP)

Plant: ORCs Comparison for Different Organic Fluids", *Energy Procedia*, Vol. 45, pp. 217-226, 2014.

10. Tchanche, B. F., G. Papadakis, G. Lambrinos and A. Frangoudakis, "Fluid Selection for a Low-temperature Solar Organic Rankine Cycle", *Applied Thermal Engineering*, Vol. 29, No. 11, pp. 2468-2476, 2009.

11. Lu, Y., A. P. Roskilly, L. Jiang, and X. Yu, "Working Fluid Selection for a Small-scale Organic Rankine Cycle Recovering Waste Heat", *1st International Conference on Sustainable Energy and Resource Use in Food Chains*, Energy Procedia, Vol. 123, Windsor, United Kingdom, pp. 346-352, 2017.

12. Wei, D., X. Lu, Z. Lu and J. Gu, "Performance Analysis and Optimization of Organic Rankine Cycle (ORC) for Waste Heat Recovery", *Energy Conversion and Management*, Vol. 48, No. 4, pp. 1113-1119, 2007.

13. Dai, Y., J. Wang, and L. Gao, "Parametric Optimization and Comparative Study of Organic Rankine Cycle (ORC) for Low Grade Waste Heat Recovery", *Energy Conversion and Management*, Vol. 50, No. 3, pp. 576-582, 2009.

14. Oyewunmi, O. A., C. J. W. Kirmse, A. M. Pantaleo, and C. N. Markides, "Performance of Working Fluid Mixtures in ORC-CHP Systems for Different Heat-demand Segments and Heat-recovery Temperature Levels, *Energy Conversion and Management*, Vol. 148, pp. 1508-1524, 2017.

15. Algieri, A., and P. Morrone, "Energetic Analysis of Biomass-fired ORC Systems for Micro-scale Combined Heat and Power (CHP) generation. A Possible Application to the Italian Residential Sector", *Applied Thermal Engineering*, Vol. 71, No. 2, pp. 751-759, 2014.

16. Mascuch, J., V. Novotny, V. Vodicka, and Z. Zeleny, "Towards Development of 1-10 kW Pilot ORC Units Operating with Hexamethyldisiloxane and Using Rotary Vane Expander", Paper Presented at the *IV International Seminar on ORC Power Systems*, Vol. 129, No. 5, Milano, Italy, pp. 826-833, 2017.

17. Rech, S., S. Zandarin, A. Lazzaretto and C.A. Frangopoulos, " Design and Off - design

Models of Single and Two-stage ORC Systems on Board an LNG Carrier for the Search of the Optimal Performance and Control Strategy", *Applied Energy*, Vol. 204, pp. 221-241, 2017.

18. Manente, G., A. Toffolo, A. Lazzaretto, and M. Paci M., ’’ An Organic Rankine Cycle Off-design Model for the Search of the Optimal Control Strategy’’, *Energy*, Vol. 58, pp. 97-106, 2013.

19. Lecompte, S., H. Huisseune, M.V.D. Broek, B. Vanslambrouck, and M.D. Paepe , "Part-load Based Thermo-economic Optimization of the Organic Rankine Cycle (ORC) Applied to a Combined Heat and Power (CHP) System", *Applied Energy*, Vol. 111, pp. 871-881, 2013.

20. Mazzi, N., S. Rech and A. Lazzaretto, "Off-design Dynamic Model of a Real Organic Rankine Cycle System Fuelled by Exhaust Gases from Industrial Processes", *Energy*, Vol. 90, pp. 537-551, 2015.

21. Wang, J., Z. Yan, P. Zhao and Y. Dai, ‘’Off-design Performance Analysis of Solar-powered Organic Rankine Cycle’’, *Energy Conversion and Management*, Vol. 80, pp. 250-257, 2014.

22. Neto, R. de Oliveira, C.A.R. Sotomonte, C.J.R. Coronado, ‘’Off-design Model of an ORC System for Waste Heat Recovery of an Internal Combustion Engine’’, *Applied Thermal Engineering*, Vol. 195, pp. 1171-1188 2021.

23. Quoilin, S., V. Lemort and J. Lebrun, ‘’Experimental Study and Modeling of an Organic Rankine Cycle Using Scroll Expander’’, *Applied Energy*, Vol. 87, No. 4, pp. 1260-1268, 2010.

24. Lemort, V., S. Quoilin, C. Cuevas, and J. Lebrun, "Testing and Modeling a Scroll Expander Integrated into an Organic Rankine Cycle" , *Applied Thermal Engineering*, Vol. 29, No. 14, pp. 3094-3102, 2010.

25. Ziviani, D., S. Gusev, S. Lecompte, E.A. Groll, J. E. Braun, W.T. Horton, M. van der Brook, "Optimizing the Performance of Small-scale Organic Rankine Cycle that Utilizes a Single-screw Expander", *Applied Energy*, Vol. 189, pp. 416-432, 2017.

26. Fatigati, F., D. Vittorini, Y. Wang, J. Song, C. N. Markides and R. Cipollone, "Design and Operational Control Strategy for Optimum Off-design Performance of an ORC Plant for Low Grade Waste Heat Recovery", *Energies*, Vol. 13, No. 21, pp. 5846-5869 2020.

27. Quoilin, S., R. Aumann, A. Grill, A. Schuster, V. Lemort, and H. Spliethoff, "Dynamic Modeling and Optimal Control Strategy of Waste Heat Recovery Organic Rankine Cycles", *Applied Energy*, Vol. 88, pp. 2183-2190, 2011.

28. Dickes, R., O. Dumont, R. Daccord, S. Quoilin, V. Lemort, ‘’Modelling of Organic Rankine Cycle Power Systems in Off-design Conditions: An Experimentally Validated Comparative Study’’, *Energy*, Vol. 123, pp. 710-727, 2017.

29. Twomey, B.L., *Dynamic Simulation and Experimental Validation of an Organic Rankine Cycle Model*, Ph.D. thesis, The University of Queensland, 2016.

30. Lecompte, S., S. Gusev, B. Vanslambrouck and M.D. Paepe, "Experimental Results of a Small-scale Organic Rankine Cycle: Steady-state Identification and Application to Off-design Model Validation", *Applied Energy*, Vol. 226, No. 8, pp. 82-106, 2018.

31. Dickes, R., O. Dumont, L. Guillaume, S. Quoilin and V. Lemort, ‘’Charge-sensitive Modelling of Organic Rankine Cycle Power Systems for Off-design Performance Simulation’’, *Applied Energy*, Vol. 212, pp. 1262-1281, 2018.

32. Ziviani, D., B.J. Woodland, E. Georges, E.A. Groll, J.E. Braun and W.T. Horton WT, ‘’Development and a Validation of a Charge Sensitive Organic Rankine Cycle (ORC) Simulation Tool’’, *Energies*, Vol. 9, No. 9, pp. 389-425, 2016.

33. Moradi, R., H. Emanuele, V. Mauro, and L. Cioccolanti, ‘’Assumption Free Modeling of a Micro-scale Organic Rankine Cycle System Based on a Mass Sensitive Method’’, *Energy Conversion and Management*, Vol. 245, pp. 1145-1154, 2021.

34. Oh J., J. Park J. and H. Lee, ‘’Development of Fully Deterministic Simulation Model for Organic Rankine Cycle Operating Under Off-design Conditions’’, *Applied Energy*, Vol. 307, pp. 118-149, 2022.

35. Lemmon, E. W., M. O. MeLinden and M.L. Huber, "NIST Standard Reference Database 23, Version 9.1", *Applied Chemicals and Materials Division*, the United States Secretary of Commerce, Gaithersburg, the United States, 2013.

36. Woodland, B.J., J.E. Braun and W.T. Horton, "Experimental Testing of an Organic Rankine Cycle with Scroll Type Expander", paper presented in: *International Refrigeration and Air Conditioning Conference*, Purdue, the United States, pp. 11, 2012.

37. Garcia-Cascales, J.R., F. Vera-Garcia, J. M. Corberan-Salvador, and J. Gonzalvez-Macia, “Assessment of Boiling and Condensation Heat Transfer Correlations in the Modelling of Plate Heat Exchangers”, *International Journal of Refrigeration*, Vol. 30, No. 6, pp. 1029–1041, 2007.

38. Han, D.H., K.J. Lee and Y.H. Kim, “Experiments on the Characteristics of Evaporation of R410A in Brazed Plate Heat Exchangers with Different Geometric Configurations”, *Applied Thermal Engineering*, Vol. 23, No. 10, pp. 1209–1225, 2003.

39. Hayat, N., M. T. Ameen, M. K. Tariq, S. N. A. Shah, and A. Naveed, “Dual Objective Optimization of Organic Rankine Cycle (ORC) Systems Using Genetic Algorithm: a Comparison between Basic and Recuperative Cycles”, *Heat and Mass Transfer*, Vol. 53, No. 8, pp. 2577*2596, 2017.

40. Bekiloğlu, H.E., H. Bedir and G. Anlaş, "Organic Rankine Cycle Optimization with Explicit Designs of Evaporator and Radial Inflow Turbine", *Journal of Energy Resources Technology*, Vol. 142, No. 7, pp. 1-25, 2020.

41. Han D.H, Lee K.J, Kim Y.H, "The Characteristics of Condensation in Brazed Plate Heat Exchangers with Different Chevron Angles" , *Journal of Korean Physical Society*, Vol. 43, No. 1, pp. 66-73, 2003.

42. Churchill, S.W., and M. Bernstein, ‘‘A Correlating Equation for Forced Convection from Gases and Liquids to a Circular Cylinder in Crossflow’’, *Journal of Heat Transfer*, Vol. 99, No. 2, pp. 300-306, 1977.

43. Churchill, S. W., and H. H. S. Chu, ‘’Correlating Equations for Laminar and Turbulent

Free Convection from a Horizontal Cylinder'', *International Journal of Heat and Mass Transfer*, Vol. 18, No.9, pp. 1049-1053, 1975.

44. Incropera, F.P., D.P. DeWitt, *Fundamentals of Heat and Mass Transfer*, Sixth Edition, Hoboken, John Wiley, New Jersey, 2007.

45. Menon, E.S., *Transmission Pipeline Calculations and Simulations Manual*, First Edition, Elsevier Incorporation, Oxford, 2015.

46. Colebrook, C.F., ''Turbulent Flow in Pipes with Particular Reference to the Transition Region between the Smooth and Rough Pipe Laws'', *Journal of the Institution of Civil Engineers*, Vol. 11, No. 4, pp. 133-156, 1939.

47. Bao, J and L. Zhao, ''A Review of Working Fluid and Expander Selections for Organic Rankine Cycle'', *Renewable and Sustainable Energy Reviews*, Vol. 24, pp. 325-342, 2013.

48. Linke, P., A.I. Papadopoulos, and P. Seferlis, '' Systematic Methods for Working Fluid Selection and the Design, Integration and Control of Organic Rankine Cycles-A Review'', *Energies*, Vol. 8, No. 6, pp. 4755-4801, 2015.

49. Lecompte, S., B. Ameel, D. Ziviani, M. Van den Broek and M. da Paepe, ''Exergy Analysis of Zeotropic Mixtures as Working Fluids in Organic Rankine Cycles'', *Energy Conversion and Management*, Vol. 85, pp. 727-739, 2014.

50. Feng, Y., T. Hung, K. Greg, Y. Zhang, B. Li, and J. Yang J, ''Thermo-economic Comparison between Pure and Mixture Working Fluids of Organic Rankine Cycles (ORCs) for Low Temperature Waste Heat Recovery'', *Energy Conversion and Management*, Vol. 106, pp. 859-872, 2015.

51. Song, J., and C.W. Gu, ''Analysis of ORC Systems with Pure Hydrocarbons and Mixtures of Hydrocarbon and Retardant for Engine Waste Heat Recovery'' *Applied Thermal Engineering*, Vol. 89, pp. 693-702, 2015.

52. Sadeghi, M., A. Nemati, A. Ghavimi and M. Yari, ''Thermodynamic Analysis and Multi-objective Optimization of Various ORC Configurations Using Zeotropic Mixture,

Energy, Vol. 109, pp. 791-802, 2016.

53. Nondy, J. and T.K. Gogoi, ''Exergoeconomic Investigation and Multi-objective Optimization of Different ORC Configurations for Waste Heat Recovery: A Comparative Study'', *Energy Conversion and Management*, Vol. 245, No. 4, pp. 1145-1193, 2021.

54. Collings, P., Z. Yu, and E. Wang, '' A Dynamic Organic Rankine Cycle Using a Zeotropic Mixture as the Working Fluid with Composition Tuning to Match Changing Ambient Conditions'', *Applied Energy*, Vol. 171, pp. 581-591, 2016.

55. Wang, E., Z. Yu, and P. Collings, '' Dynamic Control Strategy of a Distillation System for a Composition Adjustable Organic Rankine cycle'', *Energy*, Vol. 141, pp. 1038-1051, 2017.

56. Liu, C., and T. Gao, ''Off-design Performance Analysis of Basic ORC, ORC Using Zeotropic Mixtures and Composition-adjustable ORC Under Optimal Control Strategy'', *Energy*, Vol. 171, No. 49, pp. 95-108, 2019.

57. Campana, F., M. Bianchi, L. Branchini, A. De Pascale, A. Peretto, M. Baresi and F.A, Rossetti, ''ORC Waste Heat Recovery in European Energy Intensive Industries: Energy and GHG savings'', *Energy Conversion and Management*, Vol. 76, pp. 244-252, 2013.

58. Al-Weshahi, Ȧ.M.A., B.F. Latrash, A.A. Anderson and B.B. Agnew, ''Working Fluid Selection of Low-grade Heat Geothermal Organic Rankine Cycle (ORC)'', *International Journal of Thermal Technologies*, Vol. 4, No. 1, pp. 6-12, 2014.

59. Bamovorat, G., B. Abadi and K.C. Kim, ''Investigation of Organic Rankine Cycles with Zeotropic Mixtures as a Working Fluid: Advantages and Issues, *Renewable and Sustainable Energy Reviews*, Vol. 73, pp. 1000-1013, 2017.

60. Z. Kang, J. Zhu, X. Lu, T. Li and X. Wu, ''Parametric Optimization and Performance Analysis of Zeotropic 1025 Mixtures for an Organic Rankine Cycle Driven by Low Medium Temperature Geothermal Fluids'', *Applied Thermal Engineering*, Vol. 89, pp. 323–331, 2015.

61. Lemmon, E.W., and R.T Jacobsen, ‘’Equations of State for Mixtures of R-32, R-125, R-134a, R-143a, and R-152a‘’, Journal of Physical and Chemical Reference Data, Vol. 33, No. 2, pp. 593-620, 2004.

62. Kunz, O., and W. Wagner., ‘’The GERG-2008 Wide-Range Equation of State for Natural Gases and Other Mixtures: An Expansion of GERG-2004’’, *Journal of Chemical & Engineering Data*, Vol. 57, No. 11, pp. 3032-3091, 2012.

63. Kunz, O., R. Klimeck, W. Wagner, and M. Jaeschke, ‘‘The GERG-2004 Wide-Range Equation of State for Natural Gases and Other Mixtures’’, *GERG Technical Monograph*, Düsseldorf, Germany, 2007.

64. H. Bell, I., ‘’Mixture Models for Refrigerants R-1234yf/134a, R-1234yf/1234ze(E), and R-134a/1234ze(E) and Interim Models for R-125/1234yf, R-1234ze(E)/227ea, and R-1234yf/152a’’, *Applied Chemicals and Materials Division*, National Institute of Standards and Technology, Boulder, the United States, 2022.

65. H. Bell, I., and E. W. Lemmon, ‘’Automatic Fitting of Binary Interaction Parameters for Multi-fluid Helmholtz-Energy-Explicit Mixture Models’’, *Journal of Chemical & Engineering Data*, Vol. 61, No. 11, pp. 3752-3760, 2016.

66. McLinden, M. O., E. W. Lemmon, and M. L. Huber, ‘’The Refprop Database for the Thermophysical Properties of Refrigerants’’, *20th International Congress of Refrigeration*, Washington, D.C., the United States, 2003.

67. Nimtz, M., M. Klatt and H. J. Krautz, ‘’Evaluation of the GERG-2008 Equation of State for the Simulation of Oxyfuel Systems’’, *Second Oxyfuel Combustion Conference,* Queensland, Australia, 2011.

68. Rowland, D., T. J. Hughes and E. F. May, ‘’Extending the GERG – 2008 Equation of State: Improved Departure Function and Interaction Parameters for (Methane +Butane)’’, *Journal of Chemical Thermodynamics*, Vol. 97, pp. 206-213, 2016.

69. Vetter, C., H. Wiemer, D. Kuhn, ‘’Comparison of Subcritical and Supercritical Organic Rankine Cycles for Power Generation from Low-temperature Low-enthalpy

Geothermal Wells, Considering Specific Net Power Output and Efficiency'', *Applied Thermal Engineering*, Vol. 51, No. 1, pp. 871-879, 2013.

70. Dai, X., L. Shi, Q. An, and W. Qian, ''Thermal Stability of Some Hydrofluorocarbons as Supercritical ORCs Working Fluids'', *Applied Thermal Engineering*, Vol. 128, pp. 1095-1101, 2017.

71. Qiu, G., ''Selection of Working Fluids for Micro-CHP Systems with ORC'', *Renewable Energy*, Vol. 48, pp. 565-570, 2012.

72. Wand, D., X. Ling, H. Peng, L. Liu, and L. Tao, ''Efficiency and Optimal Performance Evaluation of Organic Rankine Cycle for Low Grade Waste Heat Power Generation'', *Energy*, Vol. 50, No. 1, pp. 343-352, 2013.

73. Saleh, B., G. Koglbauer, M. Wendland and J. Fischer, ''Working Fluids for Low Temperature Organic Rankine Cycles'', *Energy*, Vol. 32, No. 7, pp. 1210-1221, 2007.

74. Zeyghami, M., ''Performance Analysis and Binary Working Fluid Selection of Combined-flash Binary Geothermal Cycle'', *Energy*, Vol. 88, pp. 765-774, 2015.

75. Gomez, J. M., J. P. Lamas, M. Martin, and J.M.P. Ortega, ''A multi-objective Optimization Approach for the Selection of Working Fluids of Geothermal Facilities: Economic, Environmental, and Social Aspects'', *Journal of Environmental Management*, Vol. 203, No. 3, pp. 962-972, 2017.

76. Moloney, F., E. Almatrafi and D.Y. Goswami, ''Working Fluid Parametric Analysis for Regenerative Supercritical Organic Rankine Cycles for Medium Geothermal Reservoir Temperatures'', *IV International Seminar on ORC Power Systems*, Energy Procedia, Tampa, the United States, pp. 15, 2017.

77. Bekiloğlu, H.E., H. Bedir and G. Anlaş, "Multi-objective Optimization of ORC Parameters and Selection of Working Fluid Using Preliminary Radial Inflow Turbine Design", *Energy Conversion and Management*, Vol. 183, pp. 833-847, 2019.

78. Calm, J. M., and G. C. Hourahan, ''Physical, Safety, and Environmental Data for Current and Alternative Refrigerants'', Refrigeration for Sustainable Development,

Current and Alternative Refrigerants'', Refrigeration for Sustainable Development, 23^{th} *International Congress of Refrigeration*, Paris, France, pp. 22, 2011.

79. Shu, G., Y. Gao, H. Tian, H. Wei, and X. Liang, ''Study of Mixtures Based on Hydrocarbons Used in ORC for Waste Heat Recovery'', *Energy*, Vol. 74, pp. 428-438, 2014.

80. Dai, X., L. Shi, Q. An, and W. Qian, ''Screening of Hydrocarbons as Supercritical ORCs Working Fluids by Thermal Stability'', *Energy Conversion and Management*, Vol. 126, pp. 632-637, 2016.

81. Feng, L., ''Exploration and Analysis of CO_2 + Hydrocarbons Mixtures as Working Fluids for Trans-critical ORC'', *Energy Procedia*, Vol. 129, pp. 145-151, 2017.

82. Fernandez, F.J., M.M. Prieto, I. Suorez, ''Thermodynamic Analysis of High Temperature Regenerative Organic Rankine Cycles Using Siloxanes as Working Fluids'', *Energy*, Vol. 36, No. 8, pp. 5239-5249, 2011.

83. Lai, N.A., M. Wendland and J. Fischer, ''Working Fluids for High Temperature Organic Rankine Cycles'', *Energy*, Vol. 36, pp. 199–211, 2011.

84. Mohsen S, A. Nemati, A. Ghavimi, and M. Yari, ''Thermodynamic Analysis and Multi-objective Optimization of Various ORC Configurations Using Zeotropic Mixtures'', *Energy*, Vol. 109, pp. 791-802, 2016.

85. Bekiloğlu, H. E., *Thermodynamic and Economic Analysis of ORC with Optimization of System Components*, M.S. Thesis, Boğaziçi University, 2019.

86. Xi, H., M. J. Li, Y. L. He, W. W. Wang, and Y.S. Li, ''Parametric Optimization of Zeotropic Mixtures Used in Low-temperature Organic Rankine Cycle for Power Generation'', *Turbine Technical Conference and Exposition*, Vol. 37, Düsseldorf, 2014.

87. Ahmed A.M. and R.I. Attila, ''Effect of Critical Temperature and Category of Zeotropic Mixture Working Fluids on the Thermal Performance in Subcritical ORC'', *International Journal of Thermofluids*, Vol. 20, pp. 1004-1010, 2023.

88. Wu, Y., Y. Zhu, and L. Yu, ‘’Thermal and Economic Performance Analysis of Zeotropic Mixtures for Organic Rankine Cycles’’, *Applied Thermal Engineering*, Vol. 96, pp. 57-63, 2016.

89. Feng, Y., T. Hung, K. Greg, Y. Zhang, B. Li, and J. Yang, ‘‘Thermo-economic Comparison between Pure and Mixture Working Fluids of Organic Rankine Cycles (ORCs) for Low Temperature Waste Heat Recovery, *Energy Conversion and Management*, Vol. 106, pp. 859-872, 2015.

90. Li, Y.R., M.T. Du, C.M. Wu, S.Y. Wu, and C. Liu, ‘’Potential of Organic Rankine Cycle Using Zeotropic Mixtures as Working Fluids for Waste Heat Recovery’’, Energy, Vol. 77, pp. 509-519, 2014.

91. Asma, A., E. Altun, H.E. Bekiloğlu, H. Bedir, and G. Anlaş, ‘’Steady-state Interconnected Cycle Modeling and Experimental Results of a Lab-scale ORC’’, *Applied Thermal Engineering*, Vol. 228, pp. 1205-1221, 2023.

APPENDIX A: EXPERIMENTAL RAW DATA AND UNCERTAINTIES

Experimental raw data and uncertainties are presented in this section.

Table A.1. Statistical values of reference steady-state zones (no time window).

Variable	Exp-1				Exp-2			
	Min	**Max**	**Ave**	**σ**	**Min**	**Max**	**Ave**	**σ**
$T_{pp,i}$(°C)	5.30	5.95	5.62	0.19	6.08	6.54	6.31	0.1
T_4(°C)	12.03	12.65	12.35	0.18	20.02	22.75	21.74	0.74
T_1(°C)	72.00	76.0	74.0	1.37	95.5	97.9	96.8	0.72
T_2(°C)	56.5	57.9	57.2	0.41	71.8	72.6	72.1	0.16
T_3(°C)	5.00	5.82	5.41	0.24	5.53	5.94	5.73	0.10
$T_{cw,in}$(°C)	3.87	5.89	4.86	0.66	3.55	5.52	4.78	0.56
T_8(°C)	6.65	8.40	7.53	0.47	5.01	6.57	5.92	0.42
$T_{hf,in}$(°C)	75.1	83.4	79.0	2.8	106.0	114.2	110.0	2.5
T_6(°C)	62.4	71.5	66.6	2.9	100.6	108.6	104.5	2.3
$P_{pp,i}$(bar)	5.033	5.722	5.364	0.183	6.107	6.507	6.364	0.097
P_1(bar)	13.765	15.394	14.612	0.412	16.274	16.850	16.635	0.134
P_2(bar)	5.121	5.739	5.406	0.170	6.136	6.523	6.377	0.097
P_3(bar)	4.973	5.652	5.293	0.184	6.044	6.440	6.295	0.097
P_4(bar)	13.723	15.310	14.548	0.402	16.107	16.691	16.475	0.132
$\dot{m}_{wf}$(kg/s)	0.084	0.166	0.122	0.016	0.035	0.064	0.048	0.005
$\dot{V}_{hf}$(m^3/h)	4.54	4.70	4.62	0.03	4.44	4.56	4.50	0.02
$\dot{V}_{cw}$(m^3/h)	8.49	8.60	8.54	0.02	8.53	8.64	8.59	0.02

Table A.1. Statistical values of reference steady-state zones (no time window). (cont.)

Variable	Exp-3				Exp-4			
	Min	**Max**	**Ave**	**σ**	**Min**	**Max**	**Ave**	**σ**
$T_{pp,i}$(°C)	6.08	6.50	6.31	0.09	5.75	6..27	6.04	0.13
T_4(°C)	19.55	20.42	20.00	0.22	15.42	16.20	15.89	0.19
T_1(°C)	88.6	91.3	90.0	0.82	81.2	85.1	83.2	1.18
T_2(°C)	67.8	68.4	68.1	0.12	63.76	65.1	64.5	0.34
T_3(°C)	5.47	5.98	5.74	0.13	5.31	5.93	5.64	0.18
$T_{cw,in}$(°C)	3.60	5.60	4.81	0.58	3.70	5.73	4.84	0.62
T_8(°C)	5.26	6.80	6.16	0.42	5.87	7.52	6.76	0.44
$T_{hf,in}$(°C)	96.3	104.8	100.1	2.6	85.9	95.0	90.1	2.9
T_6(°C)	89.7	98.4	93.8	2.5	76.7	86.5	81.4	2.9
$P_{pp,i}$(bar)	5.910	6.414	6.194	0.103	5.568	6.076	5.849	0.114
P_1(bar)	15.867	16.690	16.397	0.175	15.177	16.209	15.770	0.249
P_2(bar)	5.943	6.413	6.216	0.101	5.633	6.094	5.882	0.109
P_3(bar)	5.842	6.330	6.124	0.103	5.506	6.003	5.779	0.115
P_4(bar)	15.730	16.521	16.232	0.172	15.042	16.059	15.621	0.244
$\dot{m}_{wf}$(kg/s)	0.041	0.082	0.058	0.007	0.059	0.116	0.084	0.010
$\dot{V}_{hf}$(m^3/h)	4.44	4.59	4.51	0.02	4.50	4.64	4.57	0.022
$\dot{V}_{cw}$(m^3/h)	8.62	8.72	8.67	0.02	8.67	8.80	8.74	0.019

Table A.2 shows the relative standard uncertainty values for all pressure, temperature, and flow rate sensors of the ORC setup with the accuracy of each sensor. This analysis is significant to assess the reliability of the experimental tests and, thus, the validation study. For the sensor points with relative standard uncertainties more significant than sensor accuracy, replacing the relevant sensor with an accurate one does not change the experiment's reliability. However, if the vice versa relation between relative standard uncertainty and sensor accuracy is observed, the accuracy of the experiment and the model could be increased by replacing the relevant sensor ($\dot{V}_{cw}$, $\dot{V}_{hf}$) with a more accurate one. This experiment observes a close and/or same order of magnitude relation between relative standard uncertainty and sensor accuracy values for almost all pressure and temperature values. However, for the flow rate sensors, sensor accuracy (%) values for $\dot{V}_{cw}$, and $\dot{V}_{hf}$**,** are significantly higher than the relative standard uncertainty values of all experiments.

Absolute uncertainty values of the experimental tests are tabulated in Table A.3. In calculating absolute uncertainties, the following set of equations are used.

For enthalpy $h = h(T, P)$

$$U_h = \sqrt{\left(\frac{\partial h}{\partial T} U_T\right)^2 + \left(\frac{\partial h}{\partial P} U_P\right)^2}\,, \tag{A.1}$$

For density $\rho = \rho(T, P)$

$$U_\rho = \sqrt{\left(\frac{\partial \rho}{\partial T} U_T\right)^2 + \left(\frac{\partial \rho}{\partial P} U_P\right)^2}\,, \tag{A.2}$$

For heat transfer rate $\dot{Q} = \dot{m}(h_i - h_j)$

$$U_{\dot{Q}} = \sqrt{((h_i - h_j)U_{\dot{m}})^2 + (\dot{m}U_{h_i})^2 + (\dot{m}U_{h_j})^2}\,, \tag{A.3}$$

For mass flow rate $\dot{m} = \rho\dot{V}$

$$U_{\dot{m}} = \sqrt{\left(\dot{V}U_\rho\right)^2 + (\rho U_{\dot{V}})^2}\,, \tag{A.4}$$

where U denotes the absolute uncertainty, the values of $\frac{\partial h}{\partial T}$, $\frac{\partial h}{\partial P}$, $\frac{\partial \rho}{\partial T}$, and $\frac{\partial \rho}{\partial P}$ are calculated by REFPROP v9.1 for the working fluid (R134a). For the absolute uncertainty of the measured quantities, such as pressure, temperature, and volumetric flow rate, sensor accuracy is used.

Further, relative standard uncertainty calculation is made for pressure, temperature, and flow rate measurements. Table A.2 compares each sensor's calculated relative standard uncertainties and the sensor accuracy. The highest relative standard uncertainty is observed for the refrigerant pump outlet temperature of Exp-2 at 3.04%, followed by the mass flow rate of the working fluid of Exp-2 at 2.08%. Except these, all relative uncertainties are compatible with sensor accuracy values. The results are significant as they showed the reliability of the experimental data and gave us information about the modeling accuracy. The results illustrated that the highest errors in the experimental relative standard uncertainties are observed for the mass flow rate of the working fluid and temperature of the working fluid at the evaporator inlet.

Table A.2. Relative standard uncertainty (u_r) vs. sensor accuracy of the experiments.

Variable	**Relative standard uncertainty** (%)				**Acc (∓%)**
	Exp-1	**Exp-2**	**Exp-3**	**Exp-4**	
$T_{pp,i}$(°C)	0.23	0.93	0.42	0.36	-
T_1(°C)	0.12	0.07	0.11	0.17	-
T_2(°C)	0.11	0.10	0.03	0.21	-
T_3(°C)	0.24	0.31	0.27	0.19	-
T_4(°C)	0.26	3.04	0.86	0.72	-
$T_{cw,in}$(°C)	0.55	0.35	0.64	0.55	-
T_8(°C)	0.34	0.40	0.35	0.31	-
$T_{hf,in}$(°C)	0.32	0.28	0.26	0.41	-
T_6(°C)	0.29	0.20	0.29	0.41	-
$P_{pp,i}$(bar)	0.29	0.18	0.11	0.20	0.10%
P_1(bar)	0.28	0.10	0.07	0.17	0.10%
$P_{t,o}$(bar)	0.15	0.18	0.09	0.11	0.10%
P_2(bar)	0.25	0.21	0.11	0.17	0.10%
P_3(bar)	0.30	0.19	0.11	0.20	0.10%
P_4(bar)	0.29	0.08	0.06	0.17	0.10%
$\dot{m}_{wf}$(kg/s)	0.81	2.08	1.20	1.19	0.40%
$\dot{V}_{cw}$(m^3/h)	0.04	0.09	0.06	0.04	0.40%
$\dot{V}_{hf}$(m^3/h)	0.06	0.04	0.04	0.04	0.65%

Table A.3. Absolute uncertainty values of the experimental steady states.

Absolute Uncertainty	**Exp-1**	**Exp-2**	**Exp-3**	**Exp-4**
$U_{h,1}$ (kJ/kg)	0.1286	0.0826	0.1188	0.1702
$U_{h,2}$ (kJ/kg)	0.0643	0.0801	0.0237	0.1341
$U_{h,3}$ (kJ/kg)	0.0176	0.0244	0.0217	0.0149
$U_{h,4}$ (kJ/kg)	0.0452	0.9201	0.2428	0.1617
$U_{h,cw,in}$ (kJ/kg)	0.1135	0.0715	0.1304	0.1135
$U_{h,8}$ (kJ/kg)	0.1092	0.1009	0.0925	0.0882
U_{h,pp_i} (kJ/kg)	0.0176	0.0801	0.0367	0.0299
U_{h,pp_o} (kJ/kg)	0.0439	0.8126	0.2260	0.1367
U_{ρ,cd_cw}(kg/m^3)	0.0014	0.0007	0.0008	0.0009
U_{m,cd_cw} (kg/s)	0.0011	0.0022	0.0017	0.0011
U_{m,ev_hf} (kg/s)	0.0179	0.0169	0.0155	0.0239
U_{Q,ev_wf} (kW)	0.3478	0.1750	0.1905	0.0951
U_{Q,ev_hf} (kW)	0.5908	0.4967	0.4717	0.4808
U_{Q,cd_wf} (kW)	0.3586	0.1762	0.1984	0.0983
U_{Q,cd_cw} (kW)	0.0124	0.0107	0.0095	0.0090
$U_{W,pp}$ (kW)	0.0151	0.0423	0.0244	0.0098

Table A.4. Relative standard uncertainties for (a) pure fluid cases (b) R236fa/R134a mixture with varying composition (Case 10 to 18) (c) R236fa/R134a mixture with varying composition (Case 19 to 25).

	Relative Standard Uncertainty (%)								
Variable	**Case-1**	**Case-2**	**Case-3**	**Case-4**	**Case-5**	**Case-6**	**Case-7**	**Case-8**	**Case-9**
$T_{pp,i}$(K)	0.22	0.11	0.10	0.01	0.17	0.09	0.12	0.27	0.27
T_1(K)	0.39	0.87	1.02	0.76	0.90	0.65	0.15	0.19	0.19
T_2(K)	0.22	0.42	0.75	0.43	0.53	0.42	0.29	0.40	0.40
T_3(K)	0.32	0.11	0.10	0.01	0.17	0.09	0.14	0.20	0.20
$T_{ev,in}$(K)	0.17	0.17	0.14	0.02	0.19	0.12	0.15	0.19	0.19
$T_{cw,in}$(K)	0.4	0.10	0.09	0.01	0.18	0.10	0.19	0.01	0.01
T_8(K)	0.34	0.08	0.08	0.01	0.15	0.08	0.15	0.36	0.36
$T_{hf,in}$(K)	0.79	0.82	0.80	0.85	0.81	0.77	0.79	1.27	1.27
T_6(K)	0.81	0.77	0.70	0.71	0.73	0.67	0.69	1.13	1.13
$P_{pp,i}$(bar)	3.38	1.56	1.10	0.67	1.16	0.67	1.15	1.82	1.82
P_1(bar)	2.29	1.38	1.19	0.68	0.89	0.59	0.81	1.96	1.96
$P_{t,o}$(bar)	1.95	0.37	0.26	0.16	0.21	0.13	0.20	0.35	0.35
P_2(bar)	3.22	1.27	0.88	0.52	0.90	0.51	0.29	1.33	1.33
P_3(bar)	3.44	1.59	1.11	0.67	1.17	0.68	0.14	1.87	1.87
P_4(bar)	2.21	1.34	1.16	0.67	0.87	0.58	0.80	1.97	1.97
$\dot{m}_{wf}$(kg/s)	9.83	4.62	3.61	2.40	2.59	2.09	2.45	8.91	8.91
$\dot{V}_{hf}$(m^3/h)	0.46	0.55	0.72	0.72	0.82	0.94	1.01	1.16	1.16
$\dot{V}_{cw}$(m^3/h)	0.31	0.14	0.20	0.15	0.19	0.17	0.19	0.21	0.21

Table A.4. Relative standard uncertainties for (a) pure fluid cases (b) R236fa/R134a mixture with varying composition (Case 10 to 18) (c) R236fa/R134a mixture with varying composition (Case 19 to 25). (cont.)

	Relative Standard Uncertainty (%)								
Variable	**Case-10**	**Case-11**	**Case-12**	**Case13**	**Case-14**	**Case-15**	**Case-16**	**Case-17**	**Case-18**
$T_{pp,i}$(K)	0.16	0.12	0.22	0.05	0.11	0.14	0.04	0.03	0.06
T_1(K)	0.20	0.17	0.23	0.15	0.45	0.55	0.44	0.25	0.30
T_2(K)	0.60	0.56	0.73	0.46	0.33	0.39	0.48	0.69	0.75
T_3(K)	0.22	0.16	0.24	0.05	0.11	0.15	0.04	0.04	0.06
$T_{ev,in}$(K)	0.22	0.09	0.21	0.05	0.12	0.14	0.04	0.04	0.08
$T_{cw,in}$(K)	0.28	0.13	0.22	0.05	0.11	0.15	0.05	0.02	0.06
T_8(K)	0.26	0.12	0.61	0.05	0.10	0.14	0.05	0.02	0.06
$T_{hf,in}$(K)	0.80	0.78	0.79	0.67	0.58	0.67	0.74	0.79	0.81
T_6(K)	0.68	0.66	0.68	0.61	0.45	0.61	0.66	0.68	0.72
$P_{pp,i}$(bar)	2.80	1.58	2.67	1.11	1.07	1.33	1.74	2.63	3.44
P_1(bar)	2.14	1.94	2.52	1.48	0.79	0.95	1.56	2.76	3.09
$P_{t,o}$(bar)	0.45	0.44	0.52	0.28	0.26	0.30	0.43	0.86	0.79
P_2(bar)	1.01	0.97	1.43	0.60	0.79	1.02	1.22	1.78	2.42
P_3(bar)	2.73	1.59	2.73	1.10	1.05	1.35	1.77	2.67	3.49
P_4(bar)	2.01	1.82	2.40	1.38	0.75	0.90	1.48	2.64	2.93
$\dot{m}_{wf}$(kg/s)	4.24	4.39	3.71	2.13	1.51	1.77	2.29	4.05	4.12
$\dot{V}_{hf}$(m^3/h)	1.30	0.85	0.51	0.42	0.39	0.41	0.48	0.64	0.88
$\dot{V}_{cw}$(m^3/h)	0.24	0.16	0.16	0.16	0.15	0.17	0.15	0.14	0.14

Table A.4. Relative standard uncertainties for (a) pure fluid cases (b) R236fa/R134a mixture with varying composition (Case 10 to 18) (c) R236fa/R134a mixture with varying composition (Case 19 to 25). (cont.)

	Relative Standard Uncertainty (%)					
Variable	**Case-19**	**Case-20**	**Case-21**	**Case-22**	**Case-23**	**Case-24**
$T_{pp,i}$(K)	0.01	0.03	0.19	0.11	0.03	0.20
T_1(K)	0.69	0.76	0.37	0.92	0.37	1.64
T_2(K)	0.51	0.48	0.16	0.49	0.88	1.13
T_3(K)	0.01	0.02	0.22	0.12	0.03	0.20
$T_{ev,in}$(K)	0.02	0.03	0.18	0.09	0.04	0.26
$T_{cw,in}$(K)	0.01	0.03	0.27	0.12	0.03	0.19
T_8(K)	0.01	0.03	0.24	0.12	0.03	0.15
$T_{hf,in}$(K)	0.76	0.71	0.73	0.79	0.82	0.81
T_6(K)	0.67	0.61	0.77	0.72	0.72	0.79
$P_{pp,i}$(bar)	2.09	1.23	3.14	4.09	4.72	6.40
P_1(bar)	1.63	1.06	2.01	2.50	3.40	5.04
$P_{t,o}$(bar)	0.61	0.33	1.84	1.72	1.75	2.05
P_2(bar)	1.59	0.96	2.90	3.53	3.77	5.39
P_3(bar)	2.13	1.23	3.19	4.16	4.81	6.51
P_4(bar)	1.56	1.03	1.98	2.45	3.25	4.85
$\dot{m}_{wf}$(kg/s)	2.23	2.38	7.71	4.50	4.30	9.03
$\dot{V}_{hf}$(m^3/h)	0.66	1.26	0.94	1.19	0.60	0.47
$\dot{V}_{cw}$(m^3/h)	0.17	0.15	0.23	0.16	0.14	0.17

APPENDIX B: WORKING FLUID SCREENING AND PROPERTY ESTIMATION

B.1. Property Estimation of Refrigerant Mixtures

Refprop v9.1 uses the non-dimensional Helmholtz Energy Model to calculate mixture properties (i.e., enthalpy, entropy, isobaric heat capacity). In the database of Refprop v9.1, there are interaction parameters for 697 mixtures [65]. Table B.1 shows the equation of states together with the mixing rules of R134a blends used in this study.

Table B.1. Property calculation methods of selected refrigerant mixtures.

Refrigerant Mixture	Reference in NIST	Mixing Rule	Mixture EoS
R134a/R143a	[61]	KWT Lemmon & Jacobsen	Helmholtz Energy
R134a/R245fa	[62, 63]	KW0 Kunz & Wagner*	GERG-2008
R134a/R227ea	[61]	KWT Lemmon & Jacobsen	Helmholtz Energy
R134a/R1234yf	[62, 63, 64]	KW0 Kunz & Wagner*	GERG-2008
R134a/R1234ze	[64]	KW0 Kunz & Wagner	GERG-2008
R134a/R236ea	[62, 63]	KW0 Kunz & Wagner*	GERG-2008
R134a/R236fa	[62,63]	KW0 Kunz & Wagner*	GERG-2008
R134a/R32	[61]	KWT Lemmon & Jacobsen	Helmholtz Energy
R134a/R125	[61]	KWT Lemmon & Jacobsen	Helmholtz Energy
R134a/R152a	[61]	KWT Lemmon & Jacobsen	Helmholtz Energy

*No mixture data are available for the mixture. Estimated mixing parameters are used.

B.1.1. Helmholtz Energy Equation of State

Refprop v9.1 uses Helmholtz energy (a) to calculate the mixture properties which can be calculated by

$$a = a^{idmix} + a^{E}, \tag{B.1}$$

where a^{idmix} and a^{E} are respectively Helmholtz energy for ideal mixtures and the excess function for the mixture Helmholtz energy which can be formulated as [1]

$$a^{idmix} = \sum_{i=1}^{m} x_i[a_i^0(\rho, T) + a_i^r(\delta, \tau) + RTln(xi)], \tag{B.2}$$

$$\frac{a^E}{RT} = \alpha^E(\delta,\tau,x) = \sum_{i=1}^{m-1}\sum_{j=i+1}^{m} x_i x_j F_{ij} \sum_k N_k \delta^{d_k}\tau^{t_k}\exp(-\delta^{I_k}), \tag{B.3}$$

where ρ and T are the mixture density and the temperature, δ and τ are reduced mixture density and reduced temperature, a_i^0 and a_i^r are respectively ideal gas Helmholtz energy of component ''i'' and residual Helmholtz energy of component ''i'', and x_i is the mole fractions of the mixture components, N_k, t_k, d_k and I_k are the coefficients and exponents obtained from non-linear regression of the experimental data for selected mixtures.

$\delta = \rho/\rho_r$, and $\tau = T_r/T$ are reduced density and reduced temperature which can be calculated by

$$\rho_r = \left[\sum_{i=1}^{m}\frac{x_i}{\rho_{c_i}} + \sum_{i=1}^{m-1}\sum_{j=i+1}^{m} x_i x_j \xi_{ij}\right]^{-1}, \tag{B.4}$$

$$T_r = \sum_{i=1}^{m} x_i T_{c_i} + \sum_{i=1}^{m-1}\sum_{j=i+1}^{m} x_i x_j \zeta_{ij} , \tag{B.5}$$

where ξ_{ij} and ζ_{ij} are the mixture parameters that define the shapes of reduced temperature and density.

ξ_{ij} , ζ_{ij}, and F_{ij} are the mixture-dependent parameters that are fitted to each binary mixture data. Among these, ζ_{ij} is the most significant one which is used to capture the most key features of the selected refrigerant mixtures such as zeotropic or azeotropic behaviors. Normally, high-quality experimental mixture data should be available to obtain an accurate fit for these parameters. However, when the data is unavailable for the selected binary pair, Refprop uses a predictive model to calculate ζ_{ij}. The average deviation of the VLE data points is 4.5% when the empirical relation is used to calculate ζ_{ij}. If the experimental data exists, the absolute deviation of 4439 VLE data points is 1.77% [66].

The predictive empirical relation to calculate parameter ζ_{ij} is

$$\zeta_{ij}\frac{T_1^c}{T_2^c} = 40.4 - 25.3\ x\ 2^m\ ; m = \frac{T_1^c P_2^c \omega_2}{T_2^c P_1^c \omega_1}\,. \tag{B.6}$$

The ideal gas and residual Helmholtz energy which is required to determine single-phase thermodynamic properties are

$$\alpha^0 = \sum_{i=1}^{m} x_i \left[\frac{a_i^0(\rho, T)}{RT} + \ln(x_i) \right], \tag{B.7}$$

$$\alpha^r = \sum_{i=1}^{m} x_i \alpha_i^r(\delta, \tau) + \alpha^E(\delta, \tau, x) \,. \tag{B.8}$$

For simplicity, the dimensional form of ideal gas Helmholtz energy can be given as

$$\frac{a_i^0}{RT} = e_1 + \frac{e_2}{T} + ln\rho + (1 - c_0) lnT - \sum_k c_k \left[\frac{1}{t_k + 1} \right] \left[\frac{1}{t_k} \right] T^{t_k}$$
$$+ a_k ln \left[1 - exp\left(-\frac{b_k}{T} \right) \right], \tag{B.9}$$

where c_0, e_1, e_2, a_k and b_k for k=1-4 are the coefficients and exponents of the ideal gas equations for pure fluids.

Table B.2. Definition and calculation of mixture property in terms of Helmholtz energy derivations [66].

Mixture Property	Definition	Property calculation
Pressure (p)	$p(T, \rho, \bar{x}) = -(\partial a / \partial v)_{T, \bar{x}}$	$p = \rho RT \left[1 + \delta \left(\frac{\partial \alpha^r}{\partial \delta} \right)_\tau \right]$
Compressibility factor (Z)	$Z(T, \rho, \bar{x}) = p / \rho RT$	$Z = 1 + \delta \left(\frac{\partial \alpha^r}{\partial \delta} \right)_\tau$
Internal energy (u)	$u(T, \rho, \bar{x}) = a + Ts$	$\frac{u}{RT} = \tau \left[\left(\frac{\partial \alpha^0}{\partial \tau} \right)_\delta + \left(\frac{\partial \alpha^r}{\partial \tau} \right)_\delta \right]$
Enthalpy (h)	$h(T, \rho, \bar{x}) = u + Pv$	$\frac{h}{RT} = \tau \left[\left(\frac{\partial \alpha^0}{\partial \tau} \right)_\delta + \left(\frac{\partial \alpha^r}{\partial \tau} \right)_\delta \right] + \delta \left(\frac{\partial \alpha^r}{\partial \delta} \right)_\tau + 1$
Entropy (s)	$s(T, \rho, \bar{x}) = -(\partial a / \partial T)_{T, \bar{x}}$	$\frac{s}{R} = \tau \left[\left(\frac{\partial \alpha^0}{\partial \tau} \right)_\delta + \left(\frac{\partial \alpha^r}{\partial \tau} \right)_\delta \right] - \alpha^0 - \alpha^r$
Gibbs energy (G)	$G(T, \rho, \bar{x}) = h - Ts$	$\frac{G}{RT} = 1 + \alpha^0 + \alpha^r + \delta \left(\frac{\partial \alpha^r}{\partial \delta} \right)_\tau$

Table B.2. Definition and calculation of mixture property in terms of Helmholtz energy derivations [66]. (cont.)

Mixture Property	Definition	Property calculation
Fugacity (f)	$f_i(T,p,\bar{n}) = x_i p \varphi_i(T,p,\bar{n})$	$f_i = x_i \rho RT exp\left(\frac{\partial n\alpha^r}{\partial n_i}\right)_{T,V,n_j}$
Fugacity coefficient (φ)	$ln\varphi_i(T,p,\bar{n}) = \int_0^p \left(\frac{\hat{v}_i}{RT} - \frac{1}{p}\right) dp_{T,\bar{n}}$	$n\varphi_i = \left(\frac{\partial n\alpha^r}{\partial n_i}\right)_{T,V,n_j} - \ln\left(1 + \delta\left(\frac{\partial \alpha^r}{\partial \delta}\right)_\tau\right)$
Isobaric heat capacity (c_p)	$c_p(T,\rho,\bar{x}) = -(\partial h/\partial T)_{p,\bar{x}}$	$\frac{c_p}{R} = \frac{c_v}{R} + \frac{\left[1 + \delta\left(\frac{\partial \alpha^r}{\partial \delta}\right)_\tau - \delta_\tau\left(\frac{\partial^2 \alpha^r}{\partial \delta \partial \tau}\right)\right]}{\left[1 + 2\delta\left(\frac{\partial \alpha^r}{\partial \delta}\right)_\tau + \delta^2\left(\frac{\partial^2 \alpha^r}{\partial \delta^2}\right)\right]}$
Isochoric heat capacity (c_v)	$c_v(T,\rho,\bar{x}) = -(\partial u/\partial T)_{v,\bar{x}}$	$\frac{c_v}{R} = -\tau^2\left[\left[\left(\frac{\partial^2 \alpha^0}{\partial \tau^2}\right)_\delta + \left(\frac{\partial^2 \alpha^r}{\partial \tau^2}\right)_\delta\right]\right]$

Then, the properties expressed in terms of derivatives of Helmholtz energy and calculated. Table B.2 shows the definition and calculation of some mixture properties derived from Helmholtz energy.

B.1.2. GERG 2008 Equation of State

Ideal equations used in property estimation may lead to large errors for fluid mixtures with high complexity. Therefore, a more sophisticated equation of state model, which can accurately characterize complex mixtures, is needed [67]. GERG-2008 equation of state proposed by Kunz et al. [63] is one example of the non-cubic equation of states, especially used in applications of natural gas and their mixtures. GERG-2008 is an expanded version of GERG-2004, and it is explicit in Helmholtz's free energy as a function of temperature, density, and composition. It is valid for a temperature ranging from 60 to 700 K, and pressures up to 70 MPa. GERG-2008 involves the liquid and gas phase, supercritical region, and vapor-liquid equilibrium states for the mixtures of 21 different natural gas components including methane, nitrogen, carbon dioxide, propane, n-butane, ethane, n-pentane, iso-pentane, n-hexane, n-heptane, n-octane, n-nonane, n-decane, oxygen, hydrogen, carbon monoxide, water, hydrogen sulfide, argon, and helium [63].

Based on multi-fluid approximation GERG-2008 equation of state is explicit in Helmholtz free energy which can be formulated as [68]

$$\alpha(\delta, \tau, x) = \alpha^0(\rho, T, x) + \alpha^r(\delta, \tau, x)\,, \tag{B.10}$$

where ρ represents the density of the mixture, δ represents reduced density ($\delta = \rho/\rho_r$), T is the temperature, τ is the inverse reduced temperature ($\tau = T_r/T$), and x is the molar composition vector.

Equations given above represent the dimensionless form of Helmholtz free energy which is formulated as the summation of two different terms: the ideal gas contribution which is given by α^0, and residual part of the dimensionless Helmholtz energy represented by α^r term.

The mathematical representation of the ideal gas contribution, and the residual part are given as

$$\alpha^0(\rho, T, x) = \sum_{i=1}^{N} x_i[\alpha_{oi}^0(\rho, T) + ln(x_i)]\,, \tag{B.11}$$

$$\alpha^r(\delta, \tau, x) = \sum_{i=1}^{N} x_i \alpha_{oi}^r(\delta, \tau) + \Delta\alpha^r(\delta, \tau, x)\,, \tag{B.12}$$

where N is the number of constituents in the mixture, x_i is the mole fraction of each constituent in the mixture, α_{oi}^0 is the dimensionless Helmholtz energy of constituent $'i'$ in the ideal gas state, and $\Delta\alpha^r$ is the departure function represents the non-ideal contribution.

The dimensionless Helmholtz energy of component $'i'$ and departure function can be represented as

$$\begin{aligned} \alpha_{oi}^0 &= ln\left(\frac{\rho}{\rho_{c,i}}\right) \\ &+ \frac{R^*}{R}\left[n_{oi,1}^0 + n_{oi,2}^0 \frac{T_{c,i}}{T} + n_{oi,2}^0 ln\left(\frac{T_{c,i}}{T}\right)\right. \\ &+ \left.\sum_{k=4-6} n_{oi,k}^0 ln\left(\left|sinh\left(\vartheta_{oi,k}^0 \frac{T_{c,i}}{T}\right)\right|\right)\right]\,, \end{aligned} \tag{B.13}$$

$$\Delta\alpha^r = \sum_{i=1}^{N}\sum_{j=i+1}^{N} x_i x_j F_{ij}\alpha_{ij}^r\,(\tau,\delta)\,, \qquad \text{(B. 14)}$$

where F_{ij} is the scaling factor which is set to 1 if the departure term is fitted, and α_{ij}^r term is the departure function for the binary mixture $'ij'$.

The residual Helmholtz energy of constituent $'i'$ in the ideal gas state can be calculated by

$$\alpha_{oi}^r = \sum_{k=1}^{K_{pol,i}} n_{oi,k}\delta^{d_{oi,k}}\tau^{t_{oi,k}} + \sum_{k=K_{pol,i}+1}^{K_{pol,i}+K_{exp,i}} n_{oi,k}\delta^{d_{oi,k}}\tau^{t_{oi,k}}e^{-\delta^{c_{oi,k}}}\,, \qquad \text{(B. 15)}$$

where $n_{oi,k}$, $d_{oi,k}$, $t_{oi,k}$ and $c_{oi,k}$ are coefficients and exponents to calculate the residual part of Helmholtz energy for the mixture in the ideal gas state.

The residual Helmholtz energy of constituent $'i'$ in the non-ideal gas state can be calculated by

$$\alpha_{ij}^r = \sum_{k=1}^{K_{pol,ij}} n_{ij,k}\delta^{d_{ij,k}}\tau^{t_{ij,k}}$$
$$+ \sum_{k=K_{pol,i}+1}^{K_{pol,i}+K_{exp,i}} n_{ij,k}\delta^{d_{ij,k}}\tau^{t_{ij,k}} exp\left[-n_{ij,k}\left(\delta-\varepsilon_{ij,k}\right)^2 - \beta_{ij,k}\left(\delta-\gamma_{ij,k}\right)\right], \qquad \text{(B. 16)}$$

where $n_{ij,k}$, $d_{ij,k}$, $t_{ij,k}$, $\varepsilon_{ij,k}$, $\beta_{ij,k}$ and $\gamma_{ij,k}$ are coefficients and exponents required to determine the departure function for the non-ideal contribution of the binary mixture $'ij'$.

The mixture properties are captured by $x_i\alpha_{oi}^r$ term, and reduced functions are used in the determination of terms δ and τ. The departure function term is used to increase the accuracy of the model for mixtures, as the reduced functions are insufficient to mimic the behavior of the mixture. The value of this term should be set to zero when there is no experimental data for the selected mixture components.

In the determination of reduced density and temperature reduced functions for density and temperature, ρ_{red} and T_{red} are required.

Based on the quadratic mixing rule proposed by Klimeck, these functions can be represented as

$$\frac{1}{\rho_{red}(x)} = \sum_{i=1}^{N} {x_i}^2 \frac{1}{\rho_{c,i}} + \sum_{i=1}^{N-1} \sum_{J=\mathrm{i}+1}^{N} \frac{2x_i x_j}{\rho_{c,ij}} \,, \tag{B.17}$$

$$T_{red}(x) = \sum_{i=1}^{N} {x_i}^2 T_{c,i} + \sum_{i=1}^{N-1} \sum_{J=\mathrm{i}+1}^{N} 2x_i x_j T_{c,ij} \,, \tag{B.18}$$

where $\rho_{c,i}$ and $T_{c,i}$ are the critical density and temperature of each component.

The parameters $T_{c,ij}$ and $\rho_{c,ij}$ are represented by

$$\frac{1}{\rho_{c,ij}(x)} = \beta_{v,ij}\gamma_{v,ij} \frac{x_i + x_j}{\beta_{v,ij}^2 x_i + x_j} \frac{1}{8} \left(\rho_{c,i}^{-1/3} + \rho_{c,j}^{-1/3}\right)^3 \,, \tag{B.19}$$

$$T_{c,ij}(x) = \beta_{T,ij}\gamma_{T,ij} \frac{x_i + x_j}{\beta_{T,ij}^2 x_i + x_j} \left(T_{c,i} T_{c,j}\right)^{1/2} . \tag{B.20}$$

The accuracy of $T_{c,ij}$ and $\rho_{c,ij}$changes with respect to the variaton of binary interaction parameters including $\beta_{v,ij}$,$\gamma_{v,ij}$, $\beta_{T,ij}$,and $\gamma_{T,ij}$. The values of these parameters are set to unity when there is little or no available experimental data for the selected mixture.

This can reduce the set of equations into the following form proposed by Lorentz and Berthelot which can be given as [68]

$$\frac{1}{\rho_{c,ij}} = \frac{1}{8} \left(\rho_{c,i}^{-1/3} + \rho_{c,j}^{-1/3}\right)^3 \,, \tag{B.21}$$

$$T_{c,ij} = \left(T_{c,i} T_{c,j}\right)^{1/2} . \tag{B.22}$$

The properties of the refrigerant mixture can be calculated in the form of derivatives of the Helmholtz energy which can be given as

$$\Lambda_{ij}^{*} = \tau^{i} \delta^{j} \left(\frac{\partial (\alpha^{*})^{i+j}}{\partial \tau^{i} \partial \delta^{j}}\right) , \tag{B.23}$$

where * represents one of ideal gas, residual and total, Λ_{ij} is the mixture property derived from Helmholtz energy.

Table B.3. Working fluid candidates for R134a blends (Pre-screening).

Fluid	T_{cr}(°C)	P_{cr}(bar)	GWP[a] (100 years)	ODP[b]	Safety Data[c]	Fluid Type	References Used
(HCs)							
Propane	96	41.8	-20	0	A3	Wet	[2, 12, 13, 36, 37]
Isobutane	135	36.4	-20	0	A3	Dry	[2, 4, 30, 31, 46]
Isopentane	187	33.7	-20	0	A3	Dry	[30]
Neopentane	161	31.9	-20	0	n.a	Dry	[30]
Propene	91	45.3	-20	0	A3		[40]
Cyclopentane	358	27.6			A3		[10, 16]
Cyclohexane	280	40.7	-20	0	n.a	Dry	[5, 11, 30, 38, 39]
Butane	152	37.9	-20	0	A3	Dry	[6, 10, 16, 30, 33]
Octane	296	25.0	-20	0	n.a	Dry	[6, 30, 39]
Hexane	235	30.6	-20	0	n.a	Dry	[6, 10, 30, 38, 40]
Heptane	267	27.3	-20	0	n.a	Dry	[6, 30, 38, 39]
Pentane	196	33.6	-20	0	A3	Dry	[5, 10, 12, 30, 40]
Iso-hexane	225	30.4	-20	0	n.a	Dry	[30, 38, 39]
Benzene	289	48.8	-20	0	n.a	Dry	[5, 11, 30, 39]
Toluene	319	41.2	-20	0	n.a	Dry	[11, 16, 30, 38]
(HFCs)							
R11	197	43.7	4460	1	A1	Isentropic	[5, 11, 33]
R12	111	39.5	10200	1	A1	Isentropic	[2, 32, 36]
R32	78	57.8	716	0	A2	Wet	[30, 47]
R41	44	59.0	116	0	n.a	Wet	[37]
R125	66	36.3	3170	0	A1	Isentropic	[2]
R134a	101	40.6	1430	0	A1	Isentropic	[30, 34, 35, 36]
R143a	73	37.6	3800	0	A2	Wet	[2, 13, 30, 32, 37]
R152a	112	44.5	124	0	A2	Wet	[30]
R227ea	101	28.7	3220	0	A1	Dry	[2, 4, 6, 13, 30, 32]
R236fa	124	31.9	9810	0	A1	Dry	[2, 13, 30, 38]
R236ea	139	34.1	1200	0	A2	Dry	[30, 32, 33, 38, 39]
R245fa	153	36.1	950	0	B1	Dry	[2, 4, 6, 30, 31, 32]
R245ca	174	38.9	726	0	n.a	Dry	[2, 32, 33, 37,39]
R365mfc	187	32.7	804	0	n.a	Isentropic	[30, 38, 48]
PFCs							
RC318	114	27.8	10300	0	A1	Dry	[2, 32, 36, 38]
HFOs							
R1234yf	95	33.8	<4.4	0	A2	Isentropic	[30, 42, 43, 44]
R1234ze	110	36.3	6	0	A2	Isentropic	[30]
HCFCs							
R22	96	49.9	1760	0.055	A1	Wet	[2, 32]

Table B.3. Working fluid candidates for R134a blends (Pre-screening). (cont.)

Fluid	T_{cr}(°C)	P_{cr}(bar)	GWP[a] (100 years)	ODP[b]	Safety Data[c]	Fluid Type	References used
R123	183	36.6	79	0.02	B1	Dry	[5, 14, 31, 33, 38]
R124	122	36.2	527	0.022	A1	Wet	[32, 38]
R141b	204	42.1	630	0.11	A2	Isentropic	[11, 32, 33, 36]
R142b	137	40.6	2310	0.07	A2	Isentropic	[2, 46]

a: GWP relative to CO_2 [19], b: ODP relative to R11 [19]. c: ASHRAE Standard 34- A: low toxicity/B: high toxicity [30]no flammability/ 2: low flammability/ 3: high flammability [77]

APPENDIX C: PARAMETRIC PERFORMANCE STUDY RESULTS OF STUDY-I AND STUDY-II

Change of performance indicators for parametric performance studies are provided.

Table C.1. Variation of performance indicators for R134a blends with respect to varying hot fluid inlet temperature $T_{hf,in}$=363-403 K (Study I-a).

$T_{hf,in}$ (K)		363 K		373 K		383 K		393 K		403 K	
Mix. Ratio	**2nd Comp.**	W_{net} [kW]	n_{th} [%]	W_{net} [kW]	n_{th} [%]	W_{net} [kW]	n_{th} [%]	W_{net} [kW]	n_{th} [%]	W_{net} [kW]	n_{th} [%]
1.0/0.0	[-]	1.636	6.65	1.738	6.77	1.833	6.85	1.924	6.91	2.010	6.96
0.8/0.2	R152a	1.797	6.67	1.913	6.81	2.021	6.91	2.123	6.99	2.219	7.05
0.6/0.4		1.962	6.73	2.092	6.87	2.211	6.99	2.324	7.07	2.432	7.14
0.4/0.6		2.133	6.79	2.227	6.95	2.405	7.08	2.529	7.17	2.646	7.25
0.2/0.8		2.306	6.87	2.461	7.04	2.603	7.17	2.735	7.27	2.863	7.36
0.0/1.0		2.481	6.95	2.649	7.13	2.800	7.26	2.944	7.37	3.08	7.46
0.9/0.1	R143a	1.678	6.80	1.781	6.91	1.876	6.98	1.968	7.04	2.055	7.09
0.8/0.2		1.720	6.95	1.822	7.05	1.919	7.12	2.011	7.17	2.099	7.21
0.7/0.3		1.761	7.09	1.864	7.18	1.962	7.25	2.054	7.30	2.144	7.34
0.6/0.4		1.802	7.23	1.905	7.32	2.004	7.39	2.098	7.43	2.189	7.47
0.5/0.5		1.842	7.38	1.947	7.46	2.046	7.52	2.141	7.56	2.232	7.59
0.9/0.1	R32	1.845	7.11	1.951	7.22	2.050	7.30	2.146	7.36	2.238	7.41
0.8/0.2		2.046	7.50	2.157	7.60	2.261	7.69	2.362	7.76	2.459	7.81
0.9/0.1	R125	1.620	6.74	1.719	6.84	1.812	6.92	1.900	6.97	1.984	7.01
0.8/0.2		1.605	6.82	1.700	6.92	1.790	6.98	1.875	7.03	1.958	7.07
0.7/0.3		1.588	6.91	1.680	7.00	1.767	7.05	1.850	7.10	1.931	7.13
0.6/0.4		1.571	7.00	1.660	7.08	1.744	7.13	1.825	7.16	1.903	7.19
0.5/0.5		1.533	7.10	1.639	7.16	1.721	7.21	1.799	7.23	1.876	7.25
0.8/0.2	R236fa	1.493	6.36	1.634	6.48	1.686	6.57	1.772	6.63	1.855	6.68
0.6/0.4		1.345	6.01	1.444	6.14	1.533	6.23	1.617	6.30	1.697	6.34
0.4/0.6		1.186	5.56	1.287	5.72	1.377	5.82	1.459	5.90	1.536	5.95
0.2/0.8		n.a	n.a	1.118	5.19	1.209	5.33	1.291	5.43	1.367	5.49
0.0/1.0		n.a	n.a	n.a	n.a	1.022	4.71	1.110	4.85	1.186	4.94
0.8/0.2	R245fa	1.512	6.22	1.618	6.35	1.715	6.45	1.804	6.52	1.890	6.57
0.6/0.4		n.a	n.a	1.487	5.88	1.587	6.00	1.679	6.09	1.765	6.15
0.5/0.5		n.a	n.a	1.414	5.62	n.a	n.a	n.a	n.a	n.a	n.a
0.4/0.6		n.a	n.a	n.a	n.a	1.446	5.50	1.543	5.62	1.631	5.70
0.3/0.7		n.a	n.a	n.a	n.a	1.366	5.22	n.a	n.a	n.a	n.a
0.2/0.8		n.a	n.a	n.a	n.a	n.a	n.a	1.388	5.08	1.483	5.19
0.0/1.0		n.a	n.a	n.a	n.a	n.a	n.a	n.a	n.a	n.a	n.a
0.8/0.2	R236ea	1.494	6.31	1.595	6.43	1.687	6.51	1.774	6.58	1.857	6.63
0.6/0.4		1.344	5.89	1.444	6.03	1.535	6.12	1.620	6.19	1.700	6.24
0.4/0.6		n.a	n.a	1.285	5.55	1.376	5.67	1.460	5.75	1.538	5.81
0.2/0.8		n.a	n.a	n.a	n.a	1.204	5.12	1.289	5.23	1.357	5.39
0.0/1.0		n.a	n.a	n.a	n.a	n.a	n.a	1.098	4.60	1.181	4.71
0.8/0.2	R227ea	1.481	6.45	1.578	6.56	1.666	6.63	1.750	6.69	1.831	6.73
0.6/0.4		1.324	6.19	1.414	6.29	1.398	6.36	1.575	6.41	1.650	6.45
0.4/0.6		1.163	5.86	1.248	5.97	1.325	6.03	1.398	6.08	1.467	6.11
0.2/0.8		0.997	5.44	1.077	5.55	1.150	5.62	1.217	5.67	1.281	5.69
0.0/1.0		0.819	4.87	0.899	5.01	0.978	5.09	1.032	5.15	1.090	5.18
0.8/0.2	R1234yf	1.585	6.61	1.686	6.72	1.780	6.80	1.868	6.86	1.953	6.90
0.6/0.4		1.533	6.56	1.632	6.67	1.725	6.74	1.812	6.80	1.895	6.83
0.4/0.6		1.481	6.51	1.579	6.61	1.670	6.68	1.755	6.73	1.837	6.76
0.2/0.8		1.429	6.45	1.525	6.54	1.614	6.61	1.698	6.65	1.779	6.68
0.0/1.0		1.376	6.37	1.470	6.47	1.558	6.53	1.642	6.57	1.721	6.59
0.8/0.2	R1234ze	1.587	6.59	1.688	6.70	1.782	6.78	1.870	6.84	1.955	6.88
0.6/0.4		1.535	6.48	1.635	6.59	1.728	6.67	1.814	6.73	1.898	6.78
0.4/0.6		1.479	6.33	1.579	6.45	1.671	6.53	1.757	6.59	1.840	6.63
0.2/0.8		1.418	6.13	1.519	6.25	1.610	6.34	1.697	6.41	1.779	6.45
0.0/1.0		1.348	5.87	1.453	6.02	1.546	6.11	1.633	6.19	1.715	6.24

Table C.2. Variation of performance indicators for R134a blends with respect to varying hot fluid inlet temperature $T_{hf,in}$=363-403 K (Study I-b).

$T_{hf,in}$ (K)		363 K		373 K		383 K		393 K		403 K	
Mix. Ratio	2nd Comp.	W_{net} [kW]	n_{th} [%]	W_{net} [kW]	n_{th} [%]	W_{net} [kW]	n_{th} [%]	W_{net} [kW]	n_{th} [%]	W_{net} [kW]	n_{th} [%]
1.0/0.0	[-]	1.859	7.50	1.961	7.57	2.057	7.62	2.148	7.66	2.234	7.68
0.8/0.2	R152a	2.037	7.50	2.154	7.60	2.262	7.67	2.364	7.72	2.461	7.75
0.6/0.4		2.219	7.54	2.349	7.66	2.469	7.74	2.582	7.80	2.690	7.84
0.4/0.6		2.407	7.60	2.548	7.73	2.679	7.82	2.803	7.89	2.921	7.94
0.2/0.8		2.595	7.67	2.751	7.80	2.893	7.91	3.025	7.98	3.153	8.04
0.0/1.0		2.786	7.74	2.954	7.89	3.106	8.00	3.250	8.08	3.387	8.15
0.9/0.1	R143a	1.907	7.66	2.010	7.73	2.106	7.77	2.198	7.80	2.285	7.82
0.8/0.2		1.955	7.82	2.057	7.88	2.154	7.92	2.246	7.95	2.335	7.96
0.7/0.3		2.002	7.98	2.105	8.04	2.203	8.07	2.296	8.09	2.386	8.10
0.6/0.4		2.048	8.14	2.152	8.19	2.251	8.22	2.345	8.24	2.436	8.24
0.5/0.5		2.095	8.30	2.200	8.35	2.299	8.37	2.394	8.38	2.485	8.39
0.9/0.1	R32	2.074	7.92	2.180	8.00	2.280	8.05	2.376	8.09	2.468	8.11
0.8/0.2		2.281	8.29	2.392	8.37	2.496	8.42	2.597	8.46	3.694	8.49
0.9/0.1	R125	1.843	7.59	1.942	7.66	2.035	7.70	2.123	7.73	2.208	7.74
0.8/0.2		1.826	7.70	1.922	7.75	2.012	7.78	2.097	7.80	2.180	7.81
0.7/0.3		1.809	7.80	1.902	7.85	1.989	7.87	2.072	7.88	2.152	7.88
0.6/0.4		1.791	7.91	1.880	7.94	1.965	7.96	2.045	7.96	2.124	7.96
0.5/0.5		1.773	8.02	1.859	8.05	1.941	8.05	2.019	8.05	2.096	8.04
0.8/0.2	R236fa	1.713	7.23	1.813	7.31	1.906	7.36	1.992	7.39	2.075	7.41
0.6/0.4		1.560	6.90	1.659	6.99	1.749	7.04	1.833	7.08	1.913	7.09
0.4/0.6		1.397	6.48	1.498	6.60	1.588	6.66	1.670	6.70	1.747	7.72
0.2/0.8		n.a	n.a	1.323	6.09	1.415	6.19	1.497	6.24	1.573	6.27
0.0/1.0		n.a	n.a	n.a	n.a	1.222	5.58	1.310	5.67	1.386	5.73
0.8/0.2	R245fa	1.732	7.06	1.838	7.16	1.935	7.25	2.017	7.38	2.111	7.29
0.7/0.3		1.663	6.81	1.773	6.93	n.a	n.a	n.a	n.a	n.a	n.a
0.6/0.4		n.a	n.a	1.704	6.69	1.804	6.77	1.896	6.83	1.982	6.86
0.5/0.5		n.a	n.a	1.629	6.42	n.a	n.a	n.a	n.a	n.a	n.a
0.4/0.6		n.a	n.a	n.a	n.a	1.659	6.27	1.756	6.35	1.844	6.40
0.3/0.7		n.a	n.a	n.a	n.a	1.578	5.98	n.a	n.a	n.a	n.a
0.2/0.8		n.a	n.a	n.a	n.a	n.a	n.a	1.598	5.81	1.693	5.89
0.0/1.0		n.a	n.a	n.a	n.a	n.a	n.a	n.a	n.a	1.513	5.30
0.8/0.2	R236ea	1.712	7.16	1.813	7.24	1.905	7.30	1.993	7.33	2.075	7.35
0.6/0.4		1.555	6.76	1.656	6.85	1.747	6.91	1.832	6.95	1.912	6.97
0.5/0.5		1.471	6.51	n.a	n.a	n.a	n.a	n.a	n.a	n.a	n.a
0.4/0.6		n.a	n.a	1.490	6.38	1.582	6.46	1.666	6.51	1.744	6.54
0.3/0.7		n.a	n.a	1.400	6.10	n.a	n.a	n.a	n.a	n.a	n.a
0.2/0.8		n.a	n.a	n.a	n.a	1.403	5.92	1.488	5.99	1.566	6.03
0.0/1.0		n.a	n.a	n.a	n.a	n.a	n.a	1.289	5.36	1.372	5.44
0.8/0.2	R227ea	1.699	7.33	1.796	7.40	1.885	7.44	1.969	7.46	2.049	7.47
0.6/0.4		1.536	6.12	1.626	7.17	1.710	7.20	1.788	7.22	1.863	7.22
0.4/0.6		1.369	6.83	1.455	6.89	1.532	6.91	1.605	6.92	1.673	6.91
0.2/0.8		1.197	6.46	1.277	6.51	1.350	6.54	1.417	6.54	1.481	6.53
0.0/1.0		1.013	5.95	1.093	6.02	1.162	6.05	1.225	6.06	1.283	6.05
0.8/0.2	R1234yf	1.813	7.50	1.914	7.56	2.008	7.61	2.097	7.63	2.181	7.65
0.6/0.4		1.765	7.49	1.864	7.55	1.957	7.58	2.045	7.60	2.128	7.61
0.4/0.6		1.718	7.47	1.815	7.53	1.906	7.56	1.992	7.57	2.074	7.57
0.2/0.8		1.670	7.45	1.766	7.50	1.856	7.52	1.940	7.53	2.021	7.52
0.0/1.0		1.621	7.43	1.716	7.47	1.804	7.48	1.888	7.48	1.967	7.47
0.8/0.2	R1234ze	1.814	7.46	1.915	7.53	2.008	7.58	2.097	7.61	2.182	7.62
0.6/0.4		1.764	7.38	1.864	7.45	1.957	7.49	2.044	7.52	2.128	7.53
0.4/0.6		1.710	7.25	1.810	7.32	1.902	7.37	1.989	7.39	2.072	7.41
0.2/0.8		1.650	7.06	1.751	7.14	1.843	7.19	1.930	7.22	2.012	7.24
0.0/1.0		1.581	6.82	1.686	6.92	1.780	6.97	1.866	7.01	1.948	7.03

Table C.3. Variation of performance indicators for R134a blends with respect to varying expander outlet pressure $P_{exp,out}$ for heat source temperature $T_{hf,in} = 363$ K.

		$P_{exp,out}$=550 kPa		$P_{exp,out}$=600 kPa		$P_{exp,out}$=650 kPa		$P_{exp,out}$=700 kPa	
Mix. Ratio	**2nd Comp.**	W_{net} [kW]	n_{th} [%]	W_{net} [kW]	n_{th} [%]	W_{net} [kW]	n_{th} [%]	W_{net} [kW]	n_{th} [%]
1.0/0.0	[-]	2.001	8.06	1.859	7.50	1.728	6.98	1.608	6.49
0.8/0.2	R152a	2.192	8.07	2.037	7.50	1.895	6.98	1.762	6.50
	R143a	2.103	8.41	1.955	7.82	1.818	7.28	1.691	6.78
	R32	n.a	n.a	2.281	8.29	2.125	7.73	1.980	7.21
	R125	1.965	8.28	1.826	7.70	1.698	7.16	1.579	6.67
	R1234yf	1.952	8.06	1.813	7.50	1.684	6.97	1.566	6.49
0.7/0.3	R143a	2.154	8.58	2.002	7.98	1.861	7.43	1.733	6.92
	R32	n.a	n.a	n.a	n.a	2.275	7.97	2.157	7.50
	R125	1.947	8.39	1.809	7.80	1.682	7.26	1.565	6.76
0.6/0.4	R152a	2.388	8.10	2.219	7.54	2.064	7.02	1.921	6.54
	R143a	n.a	n.a	2.048	8.14	1.906	7.58	1.774	7.06
	R125	1.927	8.50	1.791	7.91	1.665	7.36	1.549	6.86
	R1234yf	1.902	8.06	1.765	7.49	1.639	6.96	1.524	6.47
0.5/0.5	R143a	n.a	n.a	2.095	8.30	1.950	7.74	1.814	7.21
	R125	n.a	n.a	1.773	8.02	1.649	7.47	1.533	6.96
0.4/0.6	R152a	2.588	8.16	2.407	7.60	2.239	7.08	2.083	6.59
	R143a	n.a	n.a	n.a	n.a	1.993	7.88	1.85	7.35
	R125	n.a	n.a	n.a	n.a	1.631	7.58	1.517	7.06
	R1234yf	1.851	8.05	1.718	7.47	1.595	6.94	2.481	6.46
0.3/0.7	R143a	n.a	n.a	n.a	n.a	n.a	n.a	1.896	7.49
	R125	n.a	n.a	n.a	n.a	n.a	n.a	1.500	7.17
0.25/0.75	R143a	n.a	n.a	n.a	n.a	n.a	n.a	1.915	7.56
	R125	n.a	n.a	n.a	n.a	n.a	n.a	1.492	7.23
0.2/0.8	R152a	2.790	8.23	2.595	7.67	2.416	7.14	2.248	6.65
	R1234yf	1.800	8.03	1.670	7.45	1.549	6.92	1.438	6.43
0.0/1.0	R152a	2.995	8.31	2.786	7.74	2.593	7.21	2.414	6.72
	R1234yf	1.775	8.01	1.621	7.43	1.504	6.90	1.395	6.41

Table C.4. Variation of performance indicators for R134a blends with respect to varying expander outlet pressure $P_{exp,out}$ for heat source temperature $T_{hf,in} = 373$ K.

		$P_{exp,out}$=550 kPa		$P_{exp,out}$=600 kPa		$P_{exp,out}$=650 kPa		$P_{exp,out}$=700 kPa	
Mix. Ratio	**2nd Comp.**	W_{net} [kW]	n_{th} [%]	W_{net} [kW]	n_{th} [%]	W_{net} [kW]	n_{th} [%]	W_{net} [kW]	n_{th} [%]
1.0/0.0	[-]	2.110	8.14	1.961	7.57	1.824	7.05	1.698	6.57
0.8/0.2	R152a	2.317	8.17	2.154	7.60	2.004	7.08	1.865	6.59
	R143a	2.162	8.30	2.057	7.88	1.915	7.37	1.782	6.84
	R32	n.a	n.a	2.392	8.37	2.229	7.80	2.078	7.28
	R125	2.067	8.33	1.922	7.75	1.788	7.22	1.664	6.72
	R1234yf	2.060	8.13	1.914	7.56	1.779	7.04	1.655	6.55
0.7/0.3	R143a	2.263	8.64	2.105	8.04	1.959	7.49	1.824	6.98
	R32	n.a	n.a	n.a	n.a	2.403	8.08	2.196	7.57
	R125	2.046	8.43	1.902	7.85	1.769	7.31	1.647	6.81
0.6/0.4	R152a	2.526	8.22	2.349	7.66	2.187	7.13	2.036	6.64
	R143a	n.a	n.a	2.152	8.19	2.003	7.63	1.866	7.11
	R125	2.023	8.54	1.880	7.94	1.749	7.40	1.628	6.89
	R1234yf	2.008	8.12	1.864	7.55	1.733	7.02	1.621	6.53
0.5/0.5	R143a	n.a	n.a	2.200	8.35	2.047	7.78	1.906	7.25
	R125	n.a	n.a	1.859	8.05	1.729	7.50	1.609	6.98
0.4/0.6	R152a	2.740	8.30	2.548	7.73	2.373	7.20	2.209	6.71
	R143a	n.a	n.a	n.a	n.a	2.091	7.92	1.948	7.38
	R125	n.a	n.a	n.a	n.a	1.709	7.60	1.591	7.08
	R1234yf	1.956	8.10	1.815	7.53	1.687	7.00	1.567	6.51
0.3/0.7	R143a	n.a	n.a	n.a	n.a	n.a	n.a	1.988	7.52
	R125	n.a	n.a	n.a	n.a	n.a	n.a	1.572	7.18
0.25/0.75	R143a	n.a	n.a	n.a	n.a	n.a	n.a	2.009	7.59
	R125	n.a	n.a	n.a	n.a	n.a	n.a	1.562	7.23
0.2/0.8	R152a	2.956	8.38	2.751	7.80	2.561	7.27	2.385	6.78
	R1234yf	1.903	8.07	1.766	7.50	1.640	6.97	1.524	6.48
0.0/1.0	R152a	3.173	8.47	2.954	7.89	2.751	7.35	2.563	6.85
	R1234yf	1.851	8.04	1.716	7.47	1.597	6.94	1.479	6.45

Table C.5. Variation of performance indicators for R134a blends with respect to varying expander outlet pressure $P_{exp,out}$ for heat source temperature $T_{hf,in} = 383$ K.

		$P_{exp,out}$=550 kPa		**$P_{exp,out}$=600 kPa**		**$P_{exp,out}$=650 kPa**		**$P_{exp,out}$=700 kPa**	
Mix. Ratio	**2nd Comp.**	**W_{net} [kW]**	**n_{th} [%]**	**W_{net} [kW]**	**n_{th} [%]**	**W_{net} [kW]**	**n_{th} [%]**	**W_{net} [kW]**	**n_{th} [%]**
1.0/0.0	[-]	2.212	8.19	2.057	7.62	1.914	7.10	1.782	6.62
0.8/0.2	R152a	2.431	8.24	2.262	7.67	2.105	7.15	1.960	6.66
	R143a	2.316	8.51	2.154	7.92	2.006	7.38	1.867	6.88
	R32	n.a	n.a	2.496	8.42	2.327	7.86	2.170	7.33
	R125	2.163	8.36	2.012	7.78	1.872	7.25	1.743	6.76
	R1234yf	2.159	8.17	2.008	7.61	1.868	7.08	1.738	6.60
0.7/0.3	R143a	2.368	8.67	2.203	8.07	2.050	7.52	1.910	7.01
	R32	n.a	n.a	n.a	n.a	2.506	8.14	2.356	7.63
	R125	2.139	8.45	1.989	7.87	1.851	7.33	1.724	6.83
0.6/0.4	R152a	2.654	8.31	2.469	7.74	2.299	7.21	2.141	6.72
	R143a	n.a	n.a	2.251	8.22	2.096	7.66	1.951	7.14
	R125	2.113	8.55	1.965	7.96	1.829	7.42	1.703	6.91
	R1234yf	2.106	8.15	1.957	7.58	1.820	7.06	1.693	6.57
0.5/0.5	R143a	n.a	n.a	2.299	8.37	2.140	7.80	1.994	7.27
	R125	n.a	n.a	1.941	8.05	1.806	7.50	1.682	6.99
0.4/0.6	R152a	2.879	8.39	2.679	7.82	2.495	7.29	2.325	6.79
	R143a	n.a	n.a	n.a	n.a	2.185	7.94	2.036	7.41
	R125	n.a	n.a	n.a	n.a	1.784	7.60	1.661	7.08
	R1234yf	2.053	8.13	1.906	7.56	1.772	7.03	1.648	6.54
0.3/0.7	R143a	n.a	n.a	n.a	n.a	n.a	n.a	2.077	7.54
	R125	n.a	n.a	n.a	n.a	n.a	n.a	1.640	7.17
0.25/0.75	R143a	n.a	n.a	n.a	n.a	n.a	n.a	2.098	7.60
	R125	n.a	n.a	n.a	n.a	n.a	n.a	1.629	7.22
0.2/0.8	R152a	3.107	8.49	2.893	7.91	2.694	7.37	2.510	6.87
	R1234yf	1.998	8.09	1.856	7.52	1.724	6.99	1.603	6.51
0.0/1.0	R152a	3.336	8.58	3.106	8.00	2.894	7.46	2.697	6.95
	R1234yf	1.944	8.05	1.804	7.48	1.676	6.95	1.557	6.47

Table C.6. Variation of performance indicators for R134a blends with respect to varying expander outlet pressure $P_{exp,out}$ for heat source temperature $T_{hf,in} = 393$ K.

		$P_{exp,out}$=550 kPa		$P_{exp,out}$=600 kPa		$P_{exp,out}$=650 kPa		$P_{exp,out}$=700 kPa	
Mix. Ratio	**2nd Comp.**	W_{net} [kW]	n_{th} [%]	W_{net} [kW]	n_{th} [%]	W_{net} [kW]	n_{th} [%]	W_{net} [kW]	n_{th} [%]
1.0/0.0	[-]	2.309	8.22	2.148	7.66	1.999	7.14	1.862	6.65
0.8/0.2	R152a	2.540	8.29	2.364	7.72	2.200	7.19	2.055	6.71
	R143a	2.415	8.54	2.246	7.95	2.092	7.41	1.949	6.91
	R32	n.a	n.a	2.597	8.46	2.422	7.90	2.259	7.37
	R125	2.255	8.38	2.097	7.80	1.953	7.27	1.743	6.76
	R1234yf	2.254	8.20	2.097	7.63	1.951	7.11	1.816	6.62
0.7/0.3	R143a	2.467	8.69	2.296	8.09	2.138	7.54	1.992	7.03
	R32	n.a	n.a	n.a	n.a	2.605	8.18	2.450	7.67
	R125	2.227	8.46	2.072	7.88	1.929	7.35	1.724	6.83
0.6/0.4	R152a	2.774	8.37	2.582	7.80	2.405	7.27	2.241	6.78
	R143a	n.a	n.a	2.345	8.24	2.184	7.68	2.034	7.16
	R125	2.199	8.55	1.995	7.96	1.905	7.42	1.703	6.91
	R1234yf	2.200	8.17	2.045	7.60	1.902	7.08	1.770	6.59
0.5/0.5	R143a	n.a	n.a	2.394	8.38	2.229	7.82	2.077	7.29
	R125	n.a	n.a	2.019	8.05	1.880	7.50	1.682	6.99
0.4/0.6	R152a	3.011	8.47	2.803	7.89	2.611	7.36	2.434	6.86
	R143a	n.a	n.a	n.a	n.a	n.a	n.a	2.120	7.41
	R125	n.a	n.a	n.a	n.a	1.856	7.59	1.661	7.08
	R1234yf	2.144	8.14	1.992	7.57	1.853	7.04	1.724	6.56
0.3/0.7	R143a	n.a	n.a	n.a	n.a	n.a	n.a	2.162	7.54
	R125	n.a	n.a	n.a	n.a	n.a	n.a	1.640	7.17
0.25/0.75	R143a	n.a	n.a	n.a	n.a	n.a	n.a	2.183	7.60
	R125	n.a	n.a	n.a	n.a	n.a	n.a	1.629	7.22
0.2/0.8	R152a	3.163	8.57	3.025	7.98	2.819	7.45	2.628	6.94
	R1234yf	2.089	8.10	1.940	7.53	1.803	7.00	1.678	6.52
0.0/1.0	R152a	3.490	8.67	3.250	8.08	3.029	7.54	2.823	7.03
	R1234yf	2.032	8.05	1.888	7.48	1.753	6.96	1.630	6.47

APPENDIX D: PARAMETRIC PERFORMANCE STUDY ADDITIONAL FIGURES AND TABLES OF STUDY-I

Additional results of parametric performance Study-I are provided in this section.

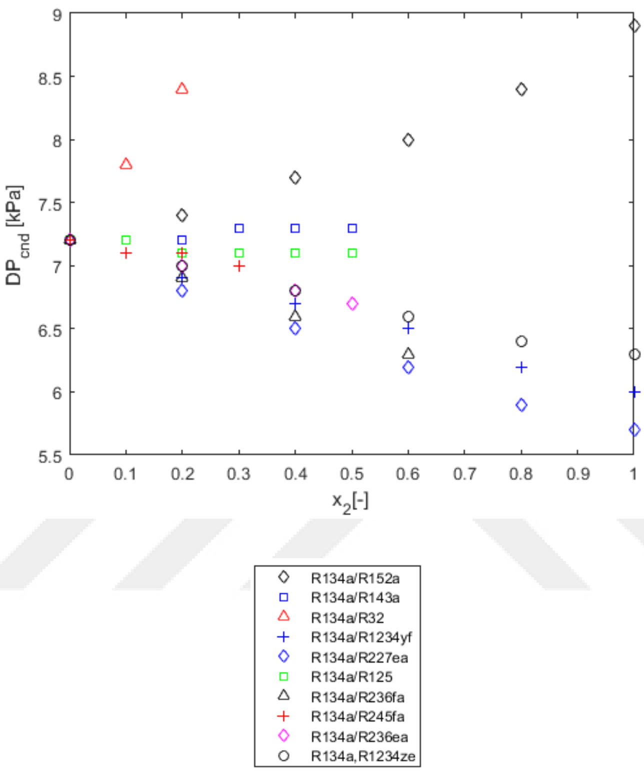

Figure D.1. Pressure difference between the inlet and the outlet of the condenser vs the mass fractions of the second component x_2 of the selected refrigerant mixtures at $T_{hf,in} = 363$ K for Study I-a (for R134a (pure): $P_{cnd,in} = 575.7$ kPa & $P_{cnd,out} = 568.5$ kPa).

Table D.1. Pressure difference and relative differences of the selected mixtures at $x_{2,max}$ with respect to reference case ($P_{cnd,in,ref} = 575.7$ kPa & $P_{cnd,out,ref} = 568.5$ kPa for pure R134a).

Mixture Name	$x_{2,max}$ **[-]**	$P_{cnd,in}$ **(kPa)**	$P_{cnd,out}$ **(kPa)**	ΔP_{cnd} **(kPa)**	$\Delta P_{cnd,in}$ **(kPa)**	$\Delta P_{cnd,out}$ **(kPa)**	**Rel. Diff.-I (%)**	**Rel. Diff.-II (%)**	**Rel. Diff.-II (%)**
R134a/R152a	1	564	555.1	8.9	11.7	13.4	1.55	2.03	2.36
R134a/R143a	0.5	572.8	565.5	7.3	2.9	3.0	1.27	0.50	0.53
R134a/R32	0.2	571.0	562.6	8.4	4.7	5.9	1.46	0.82	1.04
R134a/R125	0.5	576.9	569.8	7.1	1.2	1.3	1.23	0.21	0.23
R134a/R227ea	1	585.4	579.7	5.7	9.7	11.2	0.99	1.68	1.97
R134a/R236fa	0.6	580.7	574.4	6.3	5.0	5.9	1.09	0.87	1.04
R134a/R245fa	0.3	577.7	570.7	7.0	2.0	2.2	1.22	0.35	0.39
R134a/R236ea	0.5	579.9	573.2	6.7	4.2	4.7	1.16	0.73	0.83
R134a/R1234yf	1	578.0	572.0	6.0	2.3	4.5	1.04	0.40	0.79
R134a/R1234ze	1	578.4	572.1	6.3	2.7	3.6	1.09	0.47	0.63

*Ref. Diff-I: Change (of ΔP_{cnd} w.r.t $P_{cnd,in}$, Ref. Diff-II: Change of $\Delta P_{cnd,in}$ w.r.t $P_{cnd,in,ref}$, Ref. Diff-II: Change of $\Delta P_{cnd,out}$ w.r.t $P_{cnd,out,ref}$.

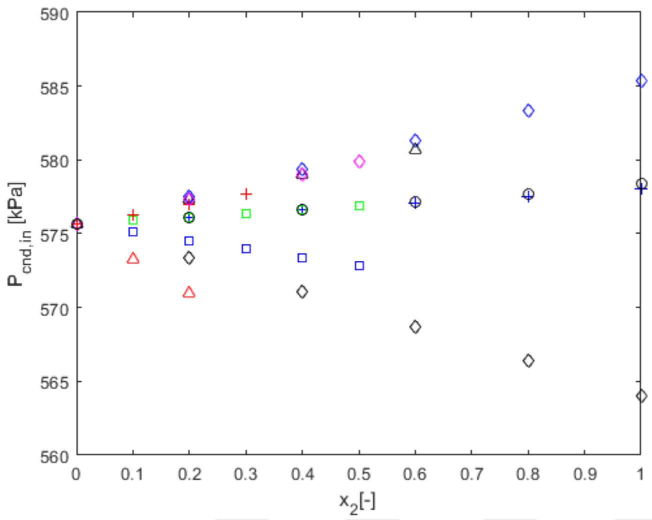

(a)

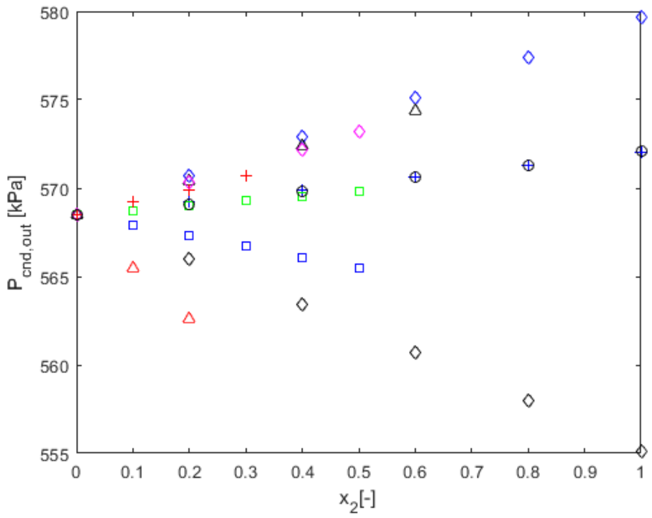

(b)

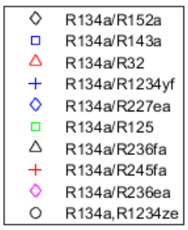

Figure D.2. Change of (a) condenser inlet pressure (b) condenser outlet pressure vs the mass fractions of the second component x_2 of the selected refrigerant mixtures at $T_{hf,in} = 363$ K for Study I-a (for R134a (pure): $P_{cnd,in} = 575.7$ kPa & $P_{cnd,out} = 568.5$ kPa).

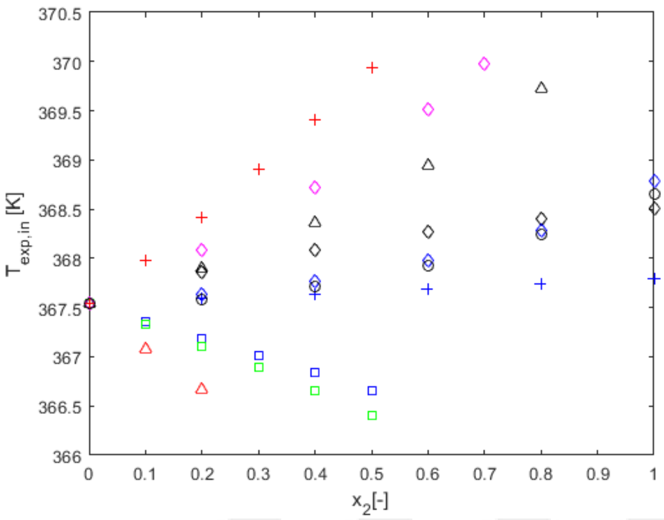

(a)

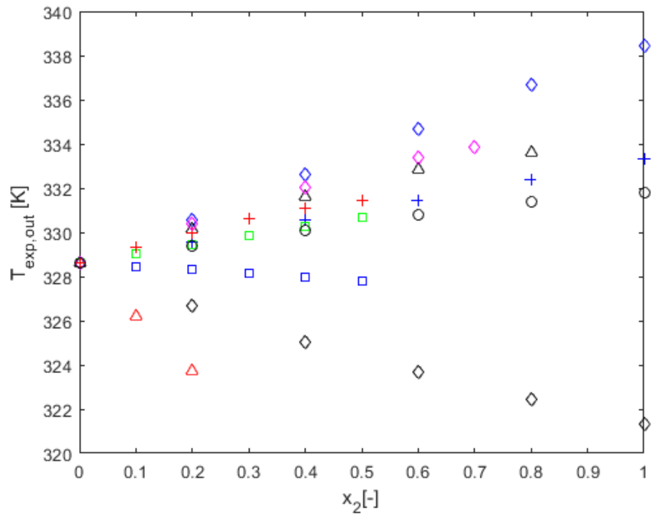

(b)

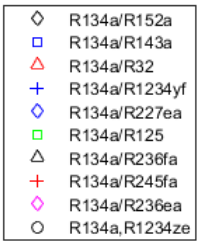

Figure D.3. Temperature variation at (a) the expander inlet (b) the expander outlet vs the mass fraction of the second components for the selected R134 blends ($T_{hf,in}$ = 373 K).

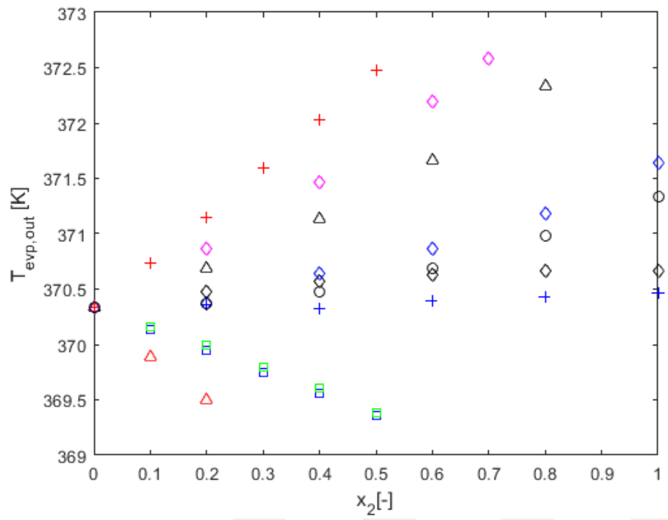

(a)

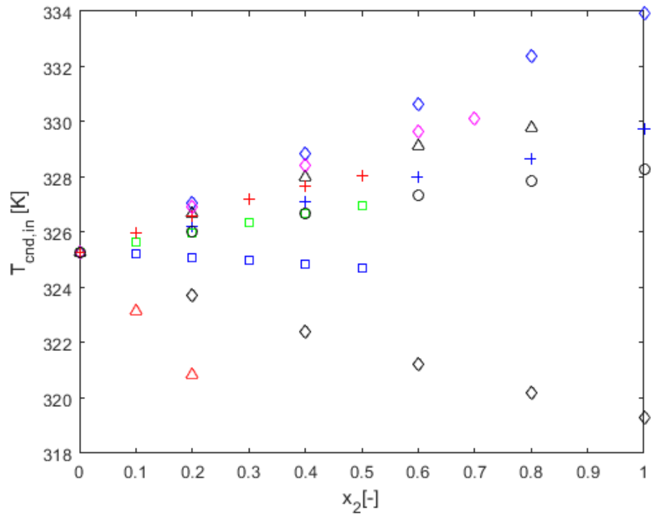

(b)

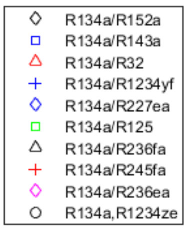

Figure D.4. Temperature at (a) the evaporator outlet (b) the condenser outlet vs the mass fraction of the second components for the selected R134 blends ($T_{hf,in} = 373$ K).

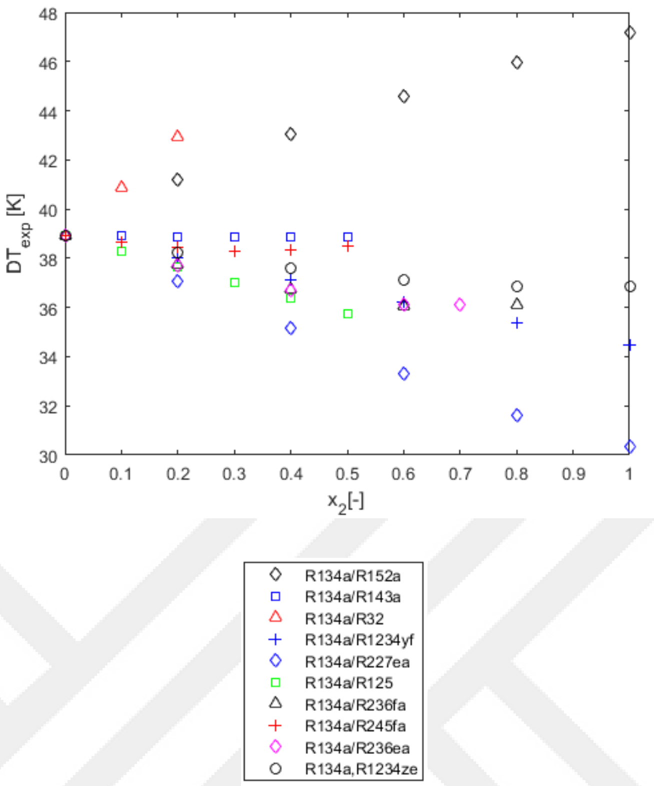

Figure D.5. Temperature drops at the expander vs the mass fraction of the second components for the selected R134 blends ($T_{hf,in} = 373$ K).

APPENDIX E: PARAMETRIC PERFORMANCE STUDY ADDITIONAL FIGURES OF STUDY-II

Additional results of parametric performance Study-I are provided in this section.

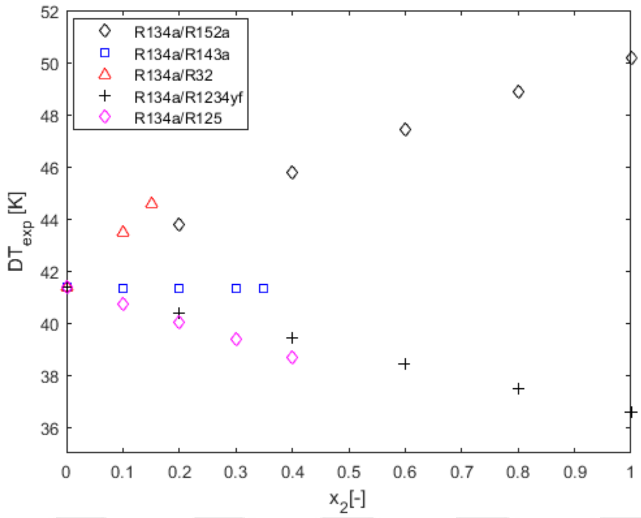

Figure E.1. Temperature drops at expander outlet vs the mass fraction of the second components for the selected R134 blends ($P_{exp,out} = 550$ kPa , $T_{hf,in} = 373$ K).

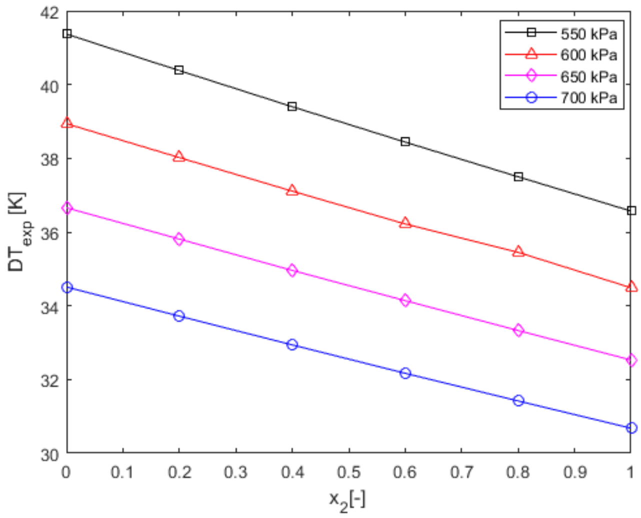

Figure E.2. Temperature drops at expander outlet vs the mass fraction of the second component for R134a/R1234yf ($P_{exp,out} = 550 - 700$ kPa, $T_{hf,in} = 373$ K).

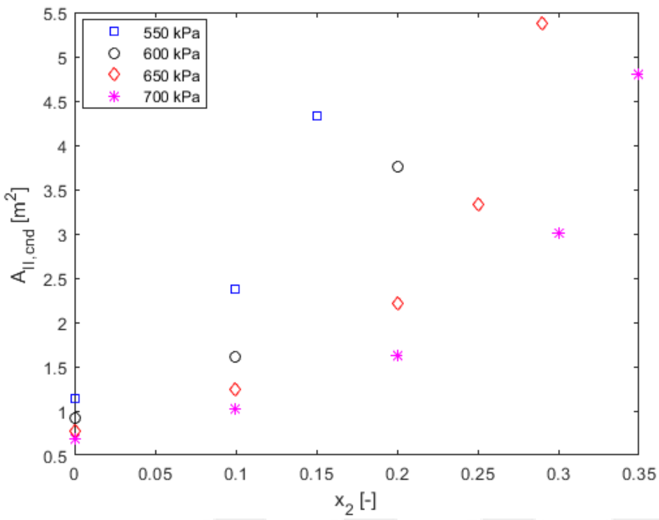

Figure E.3. The variation of the condensation phase change areas vs the mass fractions of the second components of R134a/R32 blends for varying expander outlet pressures at $T_{hf,in} = 383$ K.

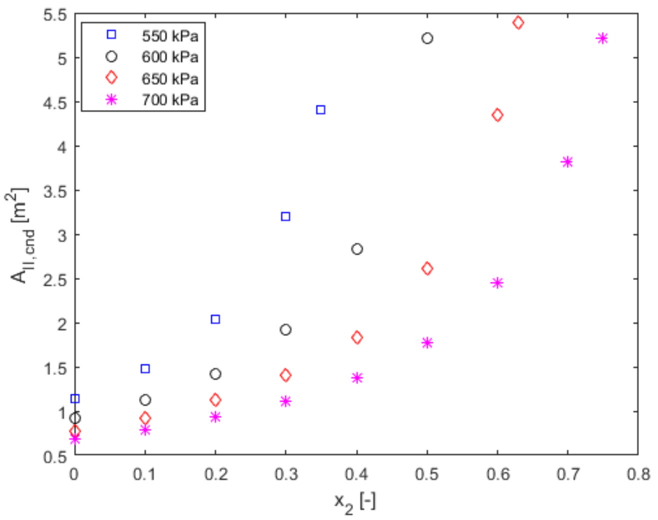

Figure E.4. The variation of the condensation phase change areas vs the mass fractions of the second components of R134a/R143a blends for varying expander outlet pressures at $T_{hf,in} = 383$ K.

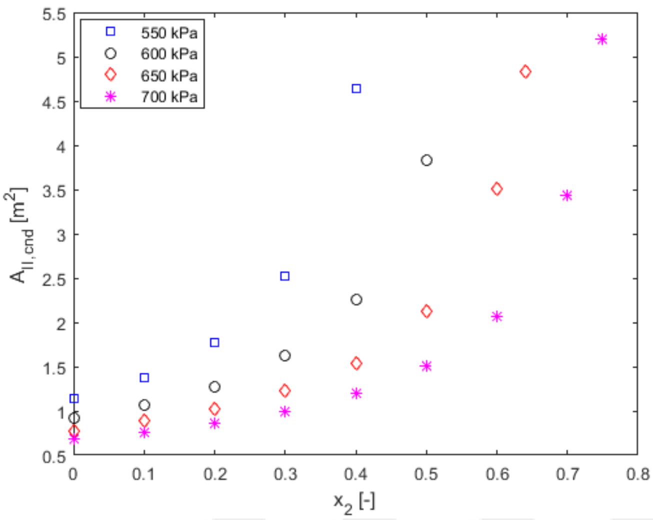

Figure E.5. The variation of the condensation phase change areas vs the mass fractions of the second components of R134a/R125 blends for varying expander outlet pressures at $T_{hf,in} = 383$ K.

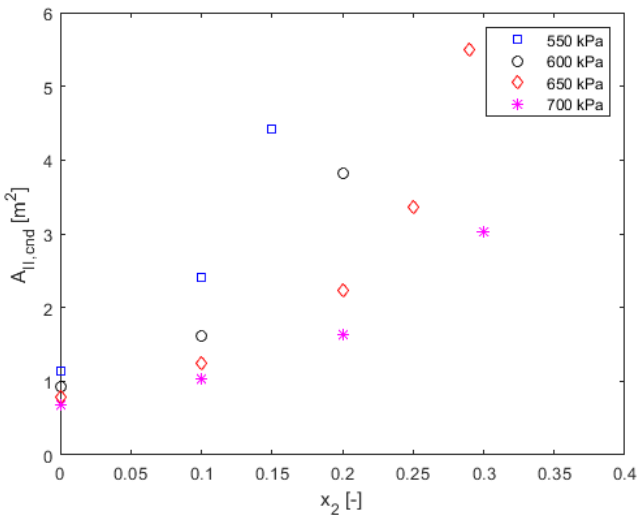

Figure E.6. The variation of the condensation phase change areas vs the mass fractions of the second components of R134a/R32 blends for varying expander outlet pressures at $T_{hf,in} = 393$ K.

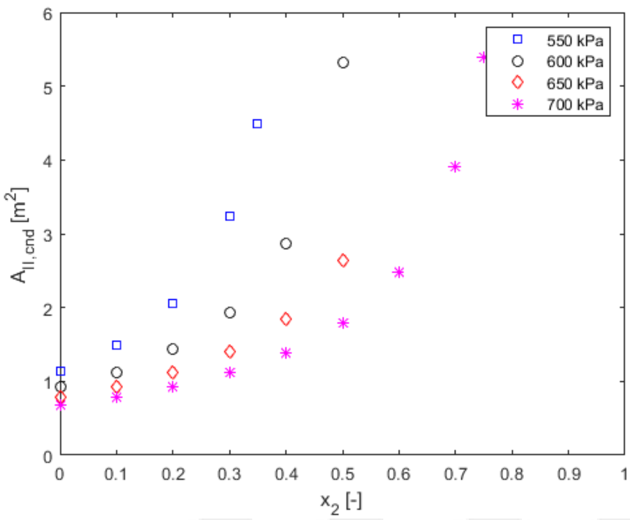

Figure E.7. The variation of the condensation phase change areas vs the mass fractions of the second components of R134a/R143a blends for varying expander outlet pressures at $T_{hf,in} = 393$ K.

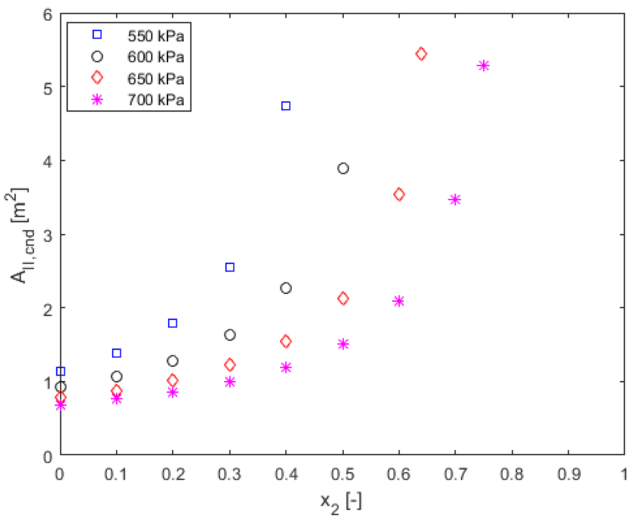

Figure E.8. The variation of the condensation phase change areas vs the mass fractions of the second components of R134a/R125 blends for varying expander outlet pressures at $T_{hf,in} = 393$ K.

APPENDIX F : PIPE GEOMETRIES OF ORC TEST SETUP AND MODEL INPUT

F.1. Pipe Geometries of the ORC Test Setup

Pipe geometries of the ORC test setup are provided in this section.

Table F.1. Pipe total lengths and elevations for each pipe section ($D_i = 22.1$ mm and $D_o = 25.4$ mm).

Pipe Section	Total Length (m) (Component Boundaries)	Total Elevation (m) Component Boundaries
Pipe (1): Pump to Evaporator	3.42	+0.07
Pipe (2): Evaporator to Throttle Valve	4.33	+0.63
Pipe (3): Expander to Condenser	7.90	0.00
Pipe (4): Condenser to Pump	3.08	-0.71

Table F.2. Pipe lengths and elevations between model components and sensors.

Pipe Section	Pipe Sub-section	Sensor Type	Total Length (m)	Total Elevation (m)
Pipe (1): Pump to Evaporator	Pipe(1a): Pump outlet to pump outlet sensor	T	2.12	+0.007
	Pipe(1b): Pump outlet to pump outlet sensor	P	2.25	+0.007
	Pipe(1c): Pump outlet to evaporator inlet sensor	T	2.77	+0.007
	Pipe(1d): Pump outlet to evaporator inlet	-	3.42	+0.007
Pipe (2): Evaporator to Throttle Valve	Pipe(2a): Evaporator outlet to evaporator outlet sensor	T	1.47	0.00
	Pipe(2b): Evaporator outlet to evaporator outlet sensor	P	1.63	0.00
	Pipe(2c): Evaporator outlet to throttle valve inlet	-	4.33	0.63
Pipe (3): Throttle Valve to Condenser	Pipe(3a): Throttle valve outlet to expander outlet sensor	P	1.00	0.00
	Pipe(3b): Throttle valve outlet to condenser inlet sensor	T	6.61	0.00
	Pipe(3c): Throttle valve outlet to condenser inlet sensor	P	6.78	0.00
	Pipe(3d): Throttle valve outlet to condenser inlet	-	7.90	0.00
Pipe (4): Condenser to Pump	Pipe(4a): Condenser outlet to condenser outlet sensor	P	0.58	0.00
	Pipe(4b): Condenser outlet to condenser outlet sensor	T	0.84	-0.13
	Pipe(4c): Condenser outlet to pump inlet sensor	T	1.61	-0.71
	Pipe(4d): Condenser outlet to pump inlet sensor	P	1.74	-0.71
	Pipe(4d): Condenser outlet to pump inlet sensor	-	3.08	-0.71

F.2. Number of Pipe Connection Elements and Loss Coefficients

Number of pipe connection elements of each pipe section and loss coefficients are presented in this section.

Table F.3. Number of pipe connection elements for each pipe section.

Pipe Number	Pipe Section	Number of pipe connection components								
		Elbows	Tee	Ball Valve	Needle Valve	Check Valve	Bend (90°)	Return Bend (180°)	Pipe Entrance	Pipe End
Pipe(1)	Pipe (1.a)	3	1	0	1	1	0	0	0	0
	Pipe (1.b)	3	1	0	1	1	0	0	0	0
	Pipe (1.c)	3	3	1	1	1	0	0	0	0
	Pipe (1.d)	5	4	2	1	1	1	0	0	0
Pipe(2)	Pipe (2.a)	1	1	1	0	0	0	0	0	0
	Pipe (2.b)	1	1	1	0	0	0	0	0	0
	Pipe (2.c)	6	8	2	0	0	0	0	0	0
Pipe(3)	Pipe (3.a)	0	0	0	0	0	0	0	0	0
	Pipe (3.b)	1	5	2	0	0	0	0	0	0
	Pipe (3.c)	1	5	2	0	0	0	0	0	0
	Pipe (3.d)	2	6	3	0	0	0	0	0	0
Pipe(4)	Pipe (4.a)	1	0	1	0	0	0	0	0	0
	Pipe (4.b)	1	0	1	0	0	0	0	0	0
	Pipe (4.c)	2	0	1	0	0	0	0	0	0
	Pipe (4.d)	2	2	2	0	0	2	0	0	0
Total		15	20	9	1	1	3	0	0	0

Table F.4. Loss coefficients (K) with respect to the type of pipe connection elements.

Type of Connection Elements	K	Note
Elbow	0.9	Regular (90° ,Threaded)
Tee	0.9 1.8	Line flow (Threaded) Branch flow (Threaded)
Ball valve	0.05	Fully open
Globe valve	8.2 6	Fully open Half open
Needle valve	2.5	Fully open
Check valve	2	Fully open
Bend (90°)	0.9	Smooth bend (90°)
Return Bend (180°)	1.5	Smooth turn bend (180°)
Union	0.08	Threaded
Pipe Entrance	0.5	Flush/square-edged entrance
Pipe End	1	-